TESIS DE LA UNIVERSIDAD DE ZARAGOZA

2024 475

Carlos Saenz Ezquerro

# Estudio de nanocomposites poliméricos y sus nanopartículas mediante simulación con dinámica molecular: influencia en las propiedades mecánicas y térmicas del material

Director/es
Laspalas Casanova, Manuel José
García Aznar, José Manuel



ISSN 2254-7606

Prensas de la Universidad
Universidad Zaragoza



ISSN 2254-7606

Universidad Zaragoza
1542

Tesis Doctoral

# ESTUDIO DE NANOCOMPOSITES POLIMÉRICOS Y SUS NANOPARTÍCULAS MEDIANTE SIMULACIÓN CON DINÁMICA MOLECULAR: INFLUENCIA EN LAS PROPIEDADES MECÁNICAS Y TÉRMICAS DEL MATERIAL


Autor

Carlos Saenz Ezquerro

Director/es

Laspalas Casanova, Manuel José
García Aznar, José Manuel

**UNIVERSIDAD DE ZARAGOZA**
**Escuela de Doctorado**


Programa de Doctorado en Ingeniería Mecánica

2024

Universidad Zaragoza
1542

# Tesis Doctoral

## ESTUDIO DE NANOCOMPOSITES POLIMÉRICOS Y SUS NANOPARTÍCULAS MEDIANTE SIMULACIÓN CON DINÁMICA MOLECULAR: INFLUENCIA EN LAS PROPIEDADES MECÁNICAS Y TÉRMICAS DEL MATERIAL


Autor

Carlos Sáenz Ezquerro

Director/es

José Manuel García Aznar
Manuel Laspalas

**UNIVERSIDAD DE ZARAGOZA**
**Escuela de Doctorado**


Programa de Doctorado en Ingeniería Mecánica

2024

# Estudio de **nanocomposites poliméricos y sus nanopartículas** mediante simulación con **dinámica molecular**: influencia en las **propiedades mecánicas y térmicas** del material


Tesis doctoral
**Carlos Sáenz Ezquerro**

Doctorado de Ingeniería Mecánica
Instituto Tecnológico de Aragón (ITA)
Multiescala en Ingeniería Mecánica y Biológica (M2BE)
Universidad de Zaragoza

Directores: José Manuel García Aznar y Manuel Laspalas


Zaragoza, 2024

Incluye artículo galardonado con **Premio Cahn 2023** en la revista *Journal of Materials Science*

Universidad Zaragoza
1542

ita Instituto Tecnológico de Aragón

*«Un objeto no resulta de la pluralidad de los átomos,*
*sino de la combinación de los átomos deviene cada objeto.»*
**Demócrito**, filósofo griego

*«Me explicó que nunca perdemos el cielo. Que lo llevamos dentro. Que todos los átomos que componen nuestro cuerpo algún día se formaron en el interior de las estrellas.»*
**Laura Esquivel**, escritora mexicana

# Agradecimientos

Esta tesis es el resultado de un largo camino, que se inició antes incluso de que yo fuera consciente de que iba a llegar al momento de escribir estas líneas. Es por ello por lo que, en primer lugar, quiero agradecer a la Dra. Cristina Crespo quien me embarcó en este viaje y siempre confió en mí.

También quiero agradecer a mis dos directores, el Dr. José Manuel García Aznar y el Dr. Manuel Laspalas, por haberme dado todo el apoyo y ayuda necesarios durante esta travesía. Ellos han sido los capitanes del barco, y con gran mérito.

A todos mis compañeros del Instituto Tecnológico de Aragón, que me han ofrecido un espacio de lugar y de tiempo donde he podido desarrollar todo este *pequeño Universo* que conforma mi tesis doctoral.

A mis amigos Rubén, Chavi, Carlitos, Pablo, Diego, Ángel, Alba y Raquel, los cuales me han ayudado a no naufragar, y a que este barco llegara al mejor de los puertos.

Y a mi familia, Josefa, Carmelo, Chema, Sonia, Armando y Carmelo, quienes son sempiternos, como lo son su amor y ayuda incondicional. Sin olvidar a mis abuelos Félix y Anselmo que, aunque ya no están en *este Universo*, con sus lecciones de vida se hicieron eternos.

# Presentación

La presente tesis doctoral titulada «Estudio de nanocomposites poliméricos y sus nanopartículas mediante simulación con dinámica molecular: influencia en las propiedades mecánicas y térmicas del material» se presenta como un compendio de publicaciones científicas previamente publicadas. A continuación, se enumeran las referencias completas de los cuatro trabajos publicados:

Prediction of the structure and mechanical properties of polycaprolactone-silica nanocomposites and the interphase region by molecular dynamics simulations: the effect of PEGylation [1]

***Carlos Sáenz Ezquerro***, *José Manuel García Aznar y Manuel Laspalas*

*Soft Matter*, 2022, 18, 2800

Monitoring interactions through molecular dynamics simulations: effect of calcium carbonate on the mechanical properties of cellulose composites [2]

***Carlos Sáenz Ezquerro***, *Manuel Laspalas, José Manuel García Aznar y Cristina Crespo Miñana*

*Cellulose*, 2023, 30, 705–726

Effects of Graphene Oxidation on Interaction Energy and Interfacial Thermal Conductivity of Polymer Nanocomposite: A Molecular Dynamics Approach [3]

*Francesco Maria Bellussi,* ***Carlos Sáenz Ezquerro***, *Manuel Laspalas y Agustín Chiminelli*

*Nanomaterials*, 2021, 11, 1709

Molecular modelling of graphene nanoribbons on the effect of porosity and oxidation on the mechanical and thermal properties [4]

***Carlos Sáenz Ezquerro***, *Manuel Laspalas, José Manuel García Aznar, Susana Castelar Ariza and Agustín Chiminelli*

*Journal of Material Science*, 2023, 58, 13295–13316

**Premio Cahn 2023**

# Contenidos


**1. Introducción ..... 1**

**2. Fundamentos de la dinámica molecular ..... 5**

2.1. Definición de la técnica ..... 7

2.2. Fundamentos teóricos ..... 7

2.3. Metodología ..... 11

2.4. Software/códigos de simulación ..... 16

**3. Dinámica molecular en la Ciencia de Materiales..... 19**

**4. Objetivos de la tesis ..... 25**

**5. Presentación de las publicaciones ..... 29**

5.1. Justificación de la unidad temática ..... 31

5.2. Publicación I: Estudio de interfases nanopartícula-polímero ..... 32

5.3. Publicación II: Análisis de cambios estructurales en el material mediante monitorización de interacciones ..... 36

5.4. Publicación III: Efecto de la modificación química de nanopartículas en las propiedades térmicas interfaciales de nanocomposites poliméricos ..... 39

5.5. Publicación IV: Estudio de propiedades de nanopartículas y efecto de modificaciones físico-químicas ..... 43

**6. Publicación I ..... 47**

**Prediction of the structure and mechanical properties of polycaprolactone–silica nanocomposites and the interphase region by molecular dynamics simulations: the effect of PEGylation**

**7. Publicación II ..... 63**

**Monitoring interactions through molecular dynamics simulations: effect of calcium carbonate on the mechanical properties of cellulose composites**

**8. Publicación III ..... 87**

**Effects of Graphene Oxidation on Interaction Energy and Interfacial Thermal Conductivity of Polymer Nanocomposite: A Molecular Dynamics Approach**

**9. Publicación IV ..... 103**

**Molecular modelling of graphene nanoribbons on the effect of porosity and oxidation on the mechanical and thermal properties**

**10. Discusión y conclusiones globales ..... 129**

10.1. Discusión global ..... 131

10.2. Conclusiones particulares ..... 132

10.3. Conclusiones globales ..... 134

10.4. Aportaciones originales ..... 135

10.5. Resultados de la tesis ..... 136

10.6. Trabajo futuro ..... 138

**Referencias ..... 139**

**Anexo A. Área temática y factor de impacto de las revistas ..... 149**

**Anexo B. Justificación de contribución del doctorando ..... 151**

# 1. Introducción

La ciencia de materiales es la disciplina científica que se encarga de investigar y establecer relaciones entre la estructura y las propiedades de los materiales. El constituyente microscópico más básico de los materiales son los átomos, y sus interacciones a nivel microscópico (en el orden de nanómetros y femtosegundos) van a determinar el comportamiento del material en la escala macroscópica (del orden o mayor que milímetros y milisegundos), siendo esta última escala la de interés para las aplicaciones tecnológicas y de la ingeniería. El paradigma estructura-propiedad se establece como un aspecto fundamental a resolver en cualquier sistema considerado en la ciencia de materiales, y establece la necesidad de estudiar y comprender los diferentes fenómenos que suceden en cada una de las diferentes escalas de longitud y tiempo de un material.

Para poder dar respuestas a este paradigma estructura-propiedad, se hace evidente, por tanto, la necesidad de estudiar un material desde sus propios átomos constituyentes, ya que las interacciones que se establezcan a este nivel del material tendrán consecuencias en las propiedades en las escalas superiores. Es en este punto donde las simulaciones atomísticas, que serán las protagonistas de esta tesis, tienen su papel principal. Precisamente la simulación se ha establecido como un puente de unión entre la teoría y el experimento, y en ocasiones es, de hecho, el único puente posible en aquellos aspectos del material donde las técnicas experimentales aún no han alcanzado a resolver, especialmente si se considera el material al nivel de la micro ($10^{-6}$ m) o nanoescala ($10^{-9}$ m). Las simulaciones atomísticas se establecen, por tanto, como una herramienta de apoyo al experimento, dando luz en aquellos puntos donde la experimentación no llega y pudiendo servir también como guía.

Ésta ha sido la motivación principal que ha llevado al estudio de cada uno de los diferentes materiales que se han considerado en esta tesis: profundizar en el estudio de estos sistemas en la escala microscópica con el objetivo de establecer relaciones entre algunas de sus propiedades microscópicas y su estructura molecular. Esta tesis se ha centrado principalmente en los materiales poliméricos reforzados con nanopartículas (los también denominados simplemente como nanocompuestos o *nanocomposites* en su término en inglés), incluyendo tanto el estudio del sistema combinado polímero + nanopartícula como solo el de sus nanopartículas. Los materiales que se han considerado han sido seleccionados por su relevancia e importancia en la ciencia de materiales, ya que han generado una atención considerable en las últimas dos décadas debido a su potencial de producir propiedades físicas, químicas y mecánicas superiores a los composites convencionales (aquellos en los que el refuerzo no tiene tamaño nanométrico). El estudio se ha orientado especialmente hacia el análisis de las propiedades mecánicas y térmicas de los materiales, entrando en aspectos tales como en la caracterización de las propiedades de la interfase,

que tiene una gran relevancia en el caso de los nanocompuestos, el análisis conformacional y el del mecanismo de fallo, entre otros aspectos analizados.

La tesis presenta en primer lugar un capítulo que describe, de forma resumida, los fundamentos de la técnica de la dinámica molecular y la metodología de trabajo aplicada durante el desarrollo de esta. Seguidamente se incluye un capítulo que presenta la situación de la dinámica molecular en la Ciencia de Materiales, con los principales hitos sobre su desarrollo histórico. A continuación, se establecen los objetivos planteados en la tesis y se presentan, de forma resumida, las diferentes publicaciones que componen la misma, en la que se describe brevemente el planteamiento llevado a cabo en cada una de las publicaciones y el contexto que ha motivado a su desarrollo. El cuerpo central de la tesis incluye cada una de las publicaciones originales, tal y como aparecen en las diferentes revistas científicas en las que fueron publicadas. Finalmente, la tesis concluye con un capítulo dedicado a la discusión global de resultados y de las principales conclusiones extraídas.

```
units   real
atom_style      full
boundary        p p p
processors      4 1 1

read_data       graphene_250x75A_xper.data


# FORCEFIELD-----------------------------------------------------

variable forcefield index COMPASS-TERSOFF_gewald
include ${forcefield}_forcefield.ff

# THERMO---------------------------------------------------------

timestep        0.5

thermo_style    custom step time etotal pe ke temp press
thermo  100
thermo
atom_m

# INIT                                                        ---

veloci

# CG DEFINITION OF BEADS-----------------------------------------

include CG_beads.mod

# CG CALCULATION OF COM------------------------------------------

include CG_com.mod

# CG CALCULATION OF BOND DISTANCES-------------------------------

include CG_bonds.mod

# BOND
DISTANCE ------------------------------------------------------
----------------------------------------

fix bond all ave/time 1 1 1000 v_bond1 v_bond2 v_bond3 v_bond4 v_bo
v_bond13 v_bond14 v_bond15 ave one file bonds.dump

fix     npt all npt temp 300.0 300.0 100.0 x 1.0 1.0 100.0 couple n
run     2000000
```

# 2. Fundamentos de la dinámica molecular

# 2.1. Definición de la técnica

La técnica de Dinámica Molecular (habitualmente abreviada en sus siglas en inglés como MD, por *Molecular Dynamics*) es un método de simulación computacional que se utiliza para estudiar el comportamiento y la evolución de sistemas atómicos y moleculares (o en general, de cualquier sistema compuesto por partículas discretas) a lo largo del tiempo [5]. Mediante esta técnica de simulación, un sistema material se modela en cuanto a sus partículas individuales, que habitualmente estarán constituidas por átomos o moléculas, y se calculan sus posiciones y velocidades en intervalos discretos de tiempo en base a un cálculo algorítmico. Estas simulaciones permiten analizar cómo las partículas interactúan entre sí y cómo se comportan en respuesta a fuerzas y condiciones específicas, como temperatura, presión y campos externos.

La dinámica molecular se utiliza en una variedad de campos científicos, incluyendo la química, la física, la biología, la materia condensada y la ciencia de materiales. Permite proporcionar información detallada sobre la estructura y las propiedades de sistemas a nivel molecular, lo que es esencial para comprender fenómenos como la difusión de partículas, las transiciones de fase, la reactividad química y las propiedades termodinámicas. Esta técnica se ha convertido en una herramienta valiosa para la investigación en la nanotecnología, la química computacional, el diseño de medicamentos y muchos otros campos científicos y de ingeniería.

# 2.2. Fundamentos teóricos

Se puede establecer que la dinámica molecular viene a ser el resultado de combinar las "tres mecánicas" (**Figura 1**): la mecánica clásica, la mecánica molecular y la mecánica estadística. De la mecánica clásica, o mecánica Newtoniana, toma la segunda ley de Newton que establece la relación existente entre la aceleración y la fuerza experimentada por las partículas del sistema. La mecánica molecular, por su parte, define las fuerzas que se generan entre las partículas del sistema, determinando la forma de los potenciales de interacción. Mientras que las propiedades de un sistema formado por la combinación e interacción de múltiples partículas discretas (sistema no continuo) se definen en base al promediado, de acuerdo con las ecuaciones definidas por la mecánica estadística.


**Figura 1 –** *La dinámica molecular (MD) es la conjunción de tres mecánicas.*

La segunda ley de Newton (**Ecuación 1**) establece que la fuerza es igual al producto de la masa por la aceleración,

$$\boldsymbol{F} = m \cdot \boldsymbol{a} = m\frac{d\boldsymbol{v}}{dt} = m \cdot \frac{d^2\boldsymbol{r}}{dt^2} \qquad (\mathbf{1})$$

y permite describir cómo las partículas del sistema se mueven en respuesta a las fuerzas que actúan sobre ellas. Es por tanto la base fundamental de la dinámica molecular, y es la relación que permitirá predecir el comportamiento de las partículas del sistema objeto de estudio.

Los potenciales interatómicos establecen la relación existente entre la fuerza o energía potencial que actúa sobre una partícula (átomo) del sistema y parámetros geométricos que se definen en base a las posiciones de las partículas, pudiendo ser distancias y/o ángulos, junto con constantes de ajuste. La forma y valores de las constantes que definen estos potenciales interatómicos se pueden derivar de teorías físicas o bien ajustarse a datos experimentales. En la **Figura 2** se muestra, de forma gráfica, un resumen de los principales tipos de interacciones atómicas que definen, o resultarán, en los diferentes potenciales interatómicos. El conjunto de los potenciales interatómicos que operan en un sistema queda recogido dentro de lo que se denomina campo de fuerza (en inglés *force field*, *FF*).

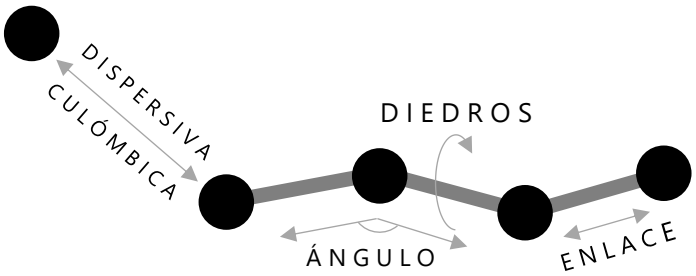


**Figura 2 –** *Principales tipos de interacción atómicas que definen los potenciales interatómicos del campo de fuerza.*

En un sistema compuesto por más de dos partículas no es posible predecir de forma determinista la evolución en el tiempo de dicho sistema. La integración de las ecuaciones Newtonianas, de las cuales resultaría la trayectoria del sistema en el tiempo $\mathbf{r}(t)$, no sería posible debido a la aparición de términos de interacción interpartícula. La trayectoria de las partículas en el sistema (es decir, su dinámica) se obtendría en su lugar de forma aproximada mediante la aplicación de algoritmos de integración. Existen varios tipos diferentes de algoritmos, siendo el algoritmo de Verlet [6] uno de los más empleados. Su formulación se resume a continuación (**Ecuaciones 2** y **3**):

$$\boldsymbol{r}(t+\delta t) = \boldsymbol{r}(t) + \delta t \cdot \boldsymbol{v}(t) + \frac{1}{2}\delta t^2 \cdot \boldsymbol{a}(t) + \cdots \qquad (\mathbf{2})$$

$$\boldsymbol{r}(t-\delta t) = \boldsymbol{r}(t) - \delta t \cdot \boldsymbol{v}(t) + \frac{1}{2}\delta t^2 \cdot \boldsymbol{a}(t) - \cdots \qquad (\mathbf{3})$$

Sumando ambas ecuaciones quedaría (**Ecuación 4**):

$$\boldsymbol{r}(t+\delta t) = 2\boldsymbol{r}(t) - \boldsymbol{r}(t-\delta t) + \delta t^2 \cdot \boldsymbol{a}(t) \qquad (\mathbf{4})$$

En el algoritmo de Verlet, $\mathbf{r}(t+\delta t)$ corresponde al vector posición del siguiente instante de tiempo, $\mathbf{r}(t)$ del instante actual y $\mathbf{r}(t-\delta t)$ del instante anterior de tiempo. El algoritmo de Verlet no depende de las velocidades de cada partícula, sino que calcula la posición de cada partícula en base a las posiciones de los dos instantes anteriores de tiempo y la aceleración $\mathbf{a}(t)$ (dependiente de las fuerzas que operan en cada partícula) del instante actual.

La trayectoria del sistema quedaría definida en base a fotogramas o *snaps* que contienen las posiciones de cada partícula y su velocidad. La separación temporal entre cada uno de estos fotogramas de la trayectoria del sistema es lo que se conoce como *timestep* (traducido como paso de tiempo), representado como $\delta t$, y la elección de su magnitud es crítica pues afecta a la precisión y a la eficiencia de la simulación. Un *timestep* largo implicaría resolver la trayectoria de las partículas con menor precisión (con saltos más grandes entre cada instante del cálculo), y podría dar lugar a comportamientos no realistas o incluso colisiones entre partículas que acabarían en un cálculo fallido. Por el contrario, un *timestep* corto generaría una trayectoria el sistema con mayor precisión y detalle, sin embargo, también reduciría mucho la eficiencia del cálculo e implicaría un mayor coste computacional. En este sentido el *timestep* debería ser lo suficientemente pequeño para capturar el comportamiento detallado de las partículas, pero lo suficientemente grande como para no requerir una cantidad prohibitiva de tiempo de cálculo. En cálculos atomísticos el *timestep* habitualmente se suele elegir como 1 femtosegundo (1 fs).

Toda simulación MD parte del establecimiento de unas condiciones iniciales. Estas condiciones establecen las posiciones y velocidades iniciales de cada partícula, y se deben

seleccionar de forma cuidadosa para no influir en los resultados del cálculo [7]. Las posiciones y velocidades de cada partícula, así como la fuerza (aceleración) que actúa sobre cada una, definirán la temperatura (T) y presión (P) del sistema. La temperatura del sistema está relacionada con el promedio temporal de la energía cinética K de acuerdo a la siguiente ecuación (**Ecuación 5**):

$$\langle K \rangle_{NVT} = \sum_{i=1}^{N} \frac{|\boldsymbol{p}_i|^2}{2m_i} = \frac{3}{2} N k_B T \quad \rightarrow \quad T = \frac{2\langle K \rangle_{NVT}}{3Nk_B} \qquad (\mathbf{5})$$

siendo $\mathbf{p_i}$ el momento lineal de la partícula i, $m_i$ la masa de la partícula i, N el número de partículas y $k_B$ la constante de Boltzmann. En el caso de la presión su cálculo se realiza en base a la siguiente expresión (**Ecuación 6**):

$$P = \frac{1}{V}\left[ N k_B T - \frac{1}{3} \sum_{i=1}^{N} \sum_{j=i+1}^{N} \boldsymbol{r_{ij}} \cdot \boldsymbol{f_{ij}} \right] \qquad (\mathbf{6})$$

donde V es el volumen del sistema, $\mathbf{r_{ij}}$ la distancia entre las partículas i y j, y $\mathbf{f_{ij}}$ la fuerza que actúa entre las partículas i y j. La temperatura y presión del sistema se controlan mediante el empleo de termostatos y baróstatos, los cuales se basan en algoritmos para ajustar las velocidades y posiciones del sistema (en este último caso mediante el ajuste de las dimensiones de la celda de simulación y el reescalado de las posiciones). En función de cómo se hayan ajustado estas variables se pueden distinguir diferentes tipos de ensamblados o colectividades termodinámicas tales como los que se listan en la siguiente figura (**Figura 3**):


**Figura 3 –** *Principales tipos de ensamblados o colectividades termodinámicas.*

# 2.3. Metodología

El plan de trabajo desarrollado para cada uno de los diferentes casos de estudio planteados en la tesis, los cuales se describen posteriormente de forma resumida en esta introducción y se abordan de forma detallada en cada uno de sus respectivos capítulos, presenta un esquema o formulación común. En el esquema mostrado en la **Figura 4** se resume de forma gráfica el método de trabajo planteado en la tesis.

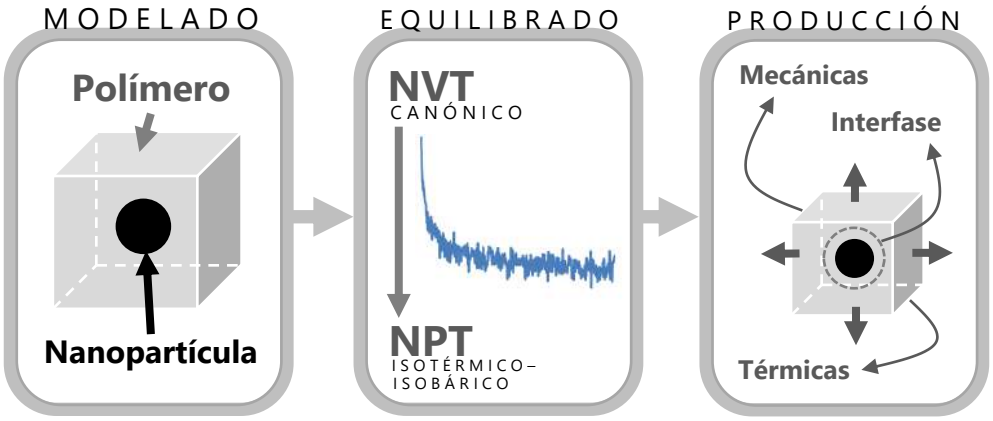


**Figura 4 –** *Resumen gráfico de la metodología de trabajo empleada en el desarrollo de la tesis.*

El proceso de trabajo comienza, en primer lugar, con el modelado a nivel atómico del sistema material objeto de estudio, esto es, de la nanopartícula y/o polímero. Este modelado requiere de un conocimiento de la composición química del sistema, para lo cual en algunos casos se debe acudir a bibliografía y/o bases de datos de materiales en los cuales se encuentre información cristalográfica (especialmente necesario en el caso de nanopartículas) o del modo de enlace de los átomos implicados en el sistema material. Para el modelado de polímeros (materia blanda) se tuvo que disponer de la fórmula molecular de su unidad característica, esto es, del monómero, y del tipo de enlaces implicados.

La celda de simulación del sistema material se preparó entonces en base a la información así evaluada, y esta celda contiene definidas las posiciones atómicas, tipología de átomos y enlaces (que incluye ángulos y diedros si se trata de enlaces covalentes). Normalmente esta primera configuración inicial que se establece no está equilibrada en términos termodinámicos, esto es, no representa un mínimo de energía el cual se requiere alcanzar previo a caracterizar las propiedades del sistema. El equilibrado del sistema se logra llevando a cabo sucesivas minimizaciones de energía e integración temporales, bien bajo el ensamblado canónico (NVT) o isotérmico-isobárico (NPT), según se requiera en función de la geometría y condiciones de contorno necesarias. En caso de requerir equilibrar el sistema, tanto en temperatura como en presión, el último equilibrado siempre se realizó bajo el

ensamblado NPT. Normalmente se considera que se ha alcanzado el mínimo cuando se obtiene una evolución constante (*plateau*) en el tiempo de la energía o de la densidad, suficientemente larga para asegurar que el propio sistema no experimenta reajustes y que se encuentra en el mínimo energético buscado. Habitualmente la etapa de equilibrado puede conllevar tiempos de simulación totales de 1-2 ns.

El tamaño de cada uno de los diferentes sistemas materiales estudiados, considerado como el número total de átomos, se elige de forma que sea estadísticamente significativo para la propiedad objeto de análisis. Esto es especialmente importante en el caso de evaluar tensiones atómicas o la presión del sistema, ya que suele ser la propiedad que, en proporción, presenta mayores niveles de fluctuación (en comparación por ejemplo a la temperatura o energía). La elección de sistemas pequeños puede conllevar a presiones y fluctuaciones muy altas, lo que se traduciría en determinaciones imprecisas de las propiedades mecánicas [7]. La geometría del sistema y su periodicidad también afectarán a esta elección.

El campo de fuerza (*force field*), que define las interacciones que se producen entre los átomos que componen el sistema, se elige en función de la naturaleza del material a modelar (polímero, nanopartícula…). En algunos de los estudios desarrollados en la tesis se realizó un cribado previo o ajuste de algunos de los parámetros del campo de fuerza (como, por ejemplo, valores de distancias de corte de algunos de los potenciales) para seleccionar las condiciones más idóneas y óptimas. En el caso concreto de los nanocompuestos, el campo de fuerza requirió de la combinación de dos campos de fuerza, uno para los átomos del componente polimérico y otro para los de la nanopartícula ya que, al tratarse de componentes de muy diferente naturaleza, normalmente un único campo de fuerza no es capaz de modelar correctamente los dos tipos de componentes. La conjunción de los dos campos se realiza definiendo, adicionalmente, los potenciales de interacción entre los átomos del polímero y de la nanopartícula mediante potenciales de Lennard-Jones 9-12 e interacciones electrostáticas tipo Coulomb, ya que esta combinación había mostrado buenos resultados en estudios anteriores [8], [9], [10].

Alcanzado el mínimo de energía, el sistema material ya está listo para la fase de caracterización o de producción de resultados (simulación). Durante las simulaciones de esta última etapa se determinan y/o monitorizan las diferentes propiedades en estudio, que en el desarrollo de esta tesis principalmente estuvieron relacionadas con tensiones atómicas (propiedades mecánicas) y con flujos de calor (propiedades térmicas), entre otras.

Las propiedades mecánicas de los modelos se caracterizaron empleando una aproximación cuasi-estática o de cuasi-equilibrio. Este método se basó en el descrito por Theodorou y

Suter [11] para el cálculo de propiedades mecánicas de polímeros amorfos, que consiste en la aplicación sucesiva de pequeños incrementos de deformación (positivos o negativos según corresponda a una tensión o compresión) en la celda de simulación. En total se aplican 6 tipos de deformación (**Figura 5**), 3 longitudinales en la dirección de los ejes cartesianos, y otros 3 de cizalladura en los planos que definen cada par de ejes (es decir, XY, XZ e YZ). Tras cada deformación los átomos inicialmente se reescalan a las nuevas posiciones, de forma proporcional, para posteriormente minimizar la geometría del sistema a las nuevas dimensiones de la celda, aplicando métodos de minimización. Se empleó el algoritmo FIRE (*fast inertial relaxation engine*) [12] para realizar esta minimización, al alcanzar convergencias más rápidas que mediante el método conjugado tradicional.

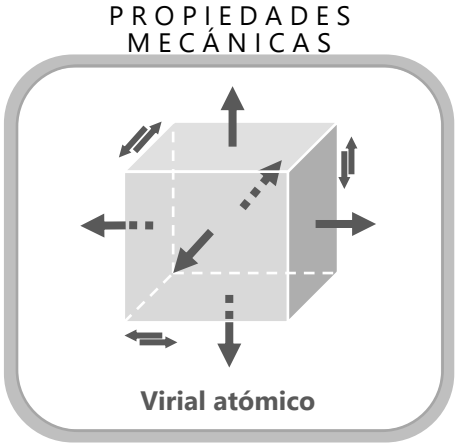


**Figura 5 –** *Método para el cálculo de propiedades mecánicas y tipos de deformaciones aplicadas al modelo molecular.*

La tensión resultante tras la minimización del sistema se calcula mediante el virial atómico $\sigma_{lm}$, que presenta la siguiente expresión para cada componente del tensor (**Ecuación 7**):

$$\sigma_{lm} = -\frac{1}{V}\sum_{i}\left(m^{i}u_{l}^{i}u_{m}^{i}\right) + \frac{1}{2}\sum_{i\neq j}\left(r_{l}^{ij}\right)\left(f_{m}^{ij}\right) \qquad (7)$$

donde $V$ es el volumen total del sistema, $m^i$ y $u^i$ denota la masa y velocidad del átomo i-ésimo, respectivamente, $r^{ij}$ se refiere a la distancia entre los átomos i-ésimo y j-ésimo, y $f^{ij}$ es la componente de la fuerza ejercida en el átomo i-ésimo por el átomo j-ésimo, mientras que $l$ y $m$ son las componentes de dirección. El primer término del virial atómico está relacionado con la energía cinética de los átomos, mientras que el segundo término se relaciona con la energía potencial y las fuerzas ejercidas entre los átomos. En condiciones estáticas, que es la aproximación considerada, el primero de los términos no contribuye a la tensión del sistema. A partir de la pendiente de la representación gráfica de cada componente del tensor $\sigma_{lm}$ frente al de deformación ($\varepsilon_{lm}$) se obtienen cada uno de los

coeficientes $C_{lm}$ que componen la matriz de rigidez $\mathbf{C}$, que para un material elástico lineal sería el mostrado en la **Ecuación 8** en notación contractuada:

$$\boldsymbol{C} = \begin{pmatrix} C_{11} & C_{12} & C_{13} & C_{14} & C_{15} & C_{16} \\ C_{21} & C_{22} & C_{23} & C_{24} & C_{25} & C_{26} \\ C_{31} & C_{32} & C_{33} & C_{34} & C_{35} & C_{36} \\ C_{41} & C_{42} & C_{43} & C_{44} & C_{45} & C_{46} \\ C_{51} & C_{52} & C_{53} & C_{54} & C_{55} & C_{56} \\ C_{61} & C_{62} & C_{63} & C_{64} & C_{65} & C_{66} \end{pmatrix} \qquad (\mathbf{8})$$

Esta matriz de rigidez se simplifica en materiales con simetría y algunos de sus coeficientes son igual a cero, siendo además solo parte de los restantes coeficientes independientes. Por ejemplo, para un material ortótropo, expresado en su sistema de direcciones principales, hay un total de 9 coeficientes independientes (**Ecuación 9**):

$$\boldsymbol{C} = \begin{pmatrix} C_{11} & C_{12} & C_{13} & 0 & 0 & 0 \\ C_{12} & C_{22} & C_{23} & 0 & 0 & 0 \\ C_{13} & C_{23} & C_{33} & 0 & 0 & 0 \\ 0 & 0 & 0 & C_{44} & 0 & 0 \\ 0 & 0 & 0 & 0 & C_{55} & 0 \\ 0 & 0 & 0 & 0 & 0 & C_{66} \end{pmatrix} \qquad (\mathbf{9})$$

Mientras que para un material isótropo sólo habría 2 coeficientes independientes (**Ecuación 10**):

$$\boldsymbol{C} = \begin{pmatrix} C_{11} & C_{12} & C_{12} & 0 & 0 & 0 \\ C_{12} & C_{11} & C_{12} & 0 & 0 & 0 \\ C_{12} & C_{12} & C_{11} & 0 & 0 & 0 \\ 0 & 0 & 0 & \dfrac{C_{11}-C_{12}}{2} & 0 & 0 \\ 0 & 0 & 0 & 0 & \dfrac{C_{11}-C_{12}}{2} & 0 \\ 0 & 0 & 0 & 0 & 0 & \dfrac{C_{11}-C_{12}}{2} \end{pmatrix} \qquad (\mathbf{10})$$

En los sistemas analizados normalmente no se asumió la simetría isótropa, sino que se consideró una simetría ortótropa inicialmente. A partir de la matriz de flexibilidad, $\mathbf{S}$, se obtienen el módulo elástico (E), coeficiente de Poisson (υ) y módulo de cizalladura (G) (**Ecuación 11**):

$$\boldsymbol{S} = \boldsymbol{C}^{-1} = \begin{pmatrix} 1/E_{11} & -v_{12}/E_{11} & -v_{13}/E_{11} & 0 & 0 & 0 \\ -v_{21}/E_{22} & 1/E_{22} & -v_{23}/E_{22} & 0 & 0 & 0 \\ -v_{31}/E_{33} & -v_{32}/E_{33} & 1/E_{33} & 0 & 0 & 0 \\ 0 & 0 & 0 & 1/G_{23} & 0 & 0 \\ 0 & 0 & 0 & 0 & 1/G_{31} & 0 \\ 0 & 0 & 0 & 0 & 0 & 1/G_{12} \end{pmatrix} \qquad (\mathbf{11})$$

En caso de isotropía, algunas de estas propiedades corresponderían a la misma magnitud, y por tanto, se podrían finalmente considerar valores promedio tal que (**Ecuaciones 12**, **13** y **14**):

$$E = \frac{E_{11} + E_{22} + E_{33}}{3} \qquad (\mathbf{12})$$

$$\upsilon = \frac{\upsilon_{12} + \upsilon_{13} + \upsilon_{21} + \upsilon_{23} + \upsilon_{31} + \upsilon_{32}}{6} \qquad (\mathbf{13})$$

$$G = \frac{G_{23} + G_{31} + G_{12}}{3} \qquad (\mathbf{14})$$

Algunos de los modelos generados también se caracterizaron en términos de la conductividad térmica (κ), para lo cual se empleó el método de Müller-Plathe [13]. Este método se basa en la aproximación reversible de no-equilibrio (RNEMD), mediante la imposición de un flujo de calor en el sistema cuya conductividad se desea determinar. La imposición de este flujo de calor se realiza mediante un procedimiento algorítmico en el cual se intercambia la energía cinética entre diferentes regiones de la celda de simulación, la cual se subdivide en capas. Este flujo de calor se determina en base a la siguiente fórmula (**Ecuación 15**):

$$\boldsymbol{J} = \frac{1}{2tA} \sum_{transfers} \frac{m}{2} \left( \boldsymbol{v}_{hot}^2 - \boldsymbol{v}_{cold}^2 \right) \qquad (\mathbf{15})$$

siendo t el tiempo de simulación, A el área de la sección transversal a través de la que se produce el flujo de calor, m la masa del átomo transferido, y $\mathbf{v}_{\text{hot}}$ y $\mathbf{v}_{\text{cold}}$ las velocidades de los átomos intercambiados. El sumatorio se aplica, de este modo, al total de átomos cuya velocidad se ha transferido por aplicación del algoritmo. La respuesta a este flujo de calor impuesto da lugar a un gradiente de temperatura a partir del cual se calcula la conductividad térmica, de acuerdo con la ecuación de conducción de calor (ley de Fourier) (**Ecuación 16**):

$$\kappa = \frac{-J}{dT/dx} \qquad (\mathbf{16})$$

donde dT/dx es el gradiente de temperatura del sistema en la dirección en la que se transfiere el flujo de calor. Para la aplicación de este método en la celda de simulación se realizan 20 subdivisiones, siendo las que se sitúan en los extremos las celdas "frías" y la situada en el centro la celda "caliente" (**Figura 6**). Por otro lado, la aplicación del algoritmo de Müller-Plathe requiere de la integración temporal en el ensamblado microcanónico (NVE), para asegurar la conservación de la energía del sistema.

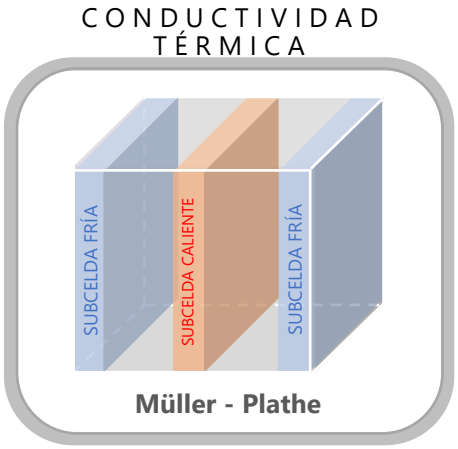


**Figura 6 –** *Método de Müller-Plathe para el cálculo de conductividad térmica del modelo molecular.*

## 2.4. Software/códigos de simulación

Existen infinidad de software o códigos de simulación que permiten llevar a cabo una simulación MD. Los códigos de simulación tienen definidos, de forma intrínseca, todos los diferentes procedimientos matemáticos establecidos en las bases de la dinámica molecular, brevemente descritos en los apartados anteriores, tales como los algoritmos de integración temporal, termostatos, baróstatos, ecuaciones de los campos de fuerza, por nombrar algunos ejemplos, así como las formulaciones para la obtención de propiedades del sistema (tales como flujos de calor, tensiones atómicas, etc.).

Algunos de estos códigos están más o menos especializados en la simulación de ciertos tipos de sistemas materiales. Por ejemplo, AMBER [14] y GROMACS [15] están especializados en simulaciones de sistemas biomoleculares (proteínas, ácidos nucleicos y carbohidratos), mientras que otros como LAMMPS [16] están más orientados a sistemas en estado sólido incluyendo la mesoescala.

Para el desarrollo de esta tesis se empleó el **código de simulación LAMMPS** (*Large-scale Atomic/Molecular Massively Parallel Simulator*). LAMMPS destaca frente a otros códigos por su versatilidad (los desarrolladores de software pueden incluso construir sus propias versiones), amplia comunidad de usuarios y estudios en los que se reporta su uso, lo cual da idea del potencial de éste para abarcar una amplia casuística. Este código fue desarrollado por científicos del *Sandia National Labs and Temple University*, bajo fondos del Departamento de Energía de los Estados Unidos, pero ha sido ampliado con paquetes o

librerías externas (tales como MOLECULE y REAXFF, por citar algunos ejemplos) para aumentar su funcionalidad y aplicación a diferentes sistemas y casuísticas [17]. LAMMPS es un código de simulación de propósito general, que puede usarse tanto en sistemas de biología, física, ciencia de materiales, química, bioquímica y otros campos para simular metales, semiconductores, polímeros, biopolímeros, entre otros. Ha sido optimizado para ser ejecutado en paralelo (especialmente bajo el protocolo MPI), mostrando un buen desempeño en las diferentes pruebas de rendimiento que se han realizado [18].

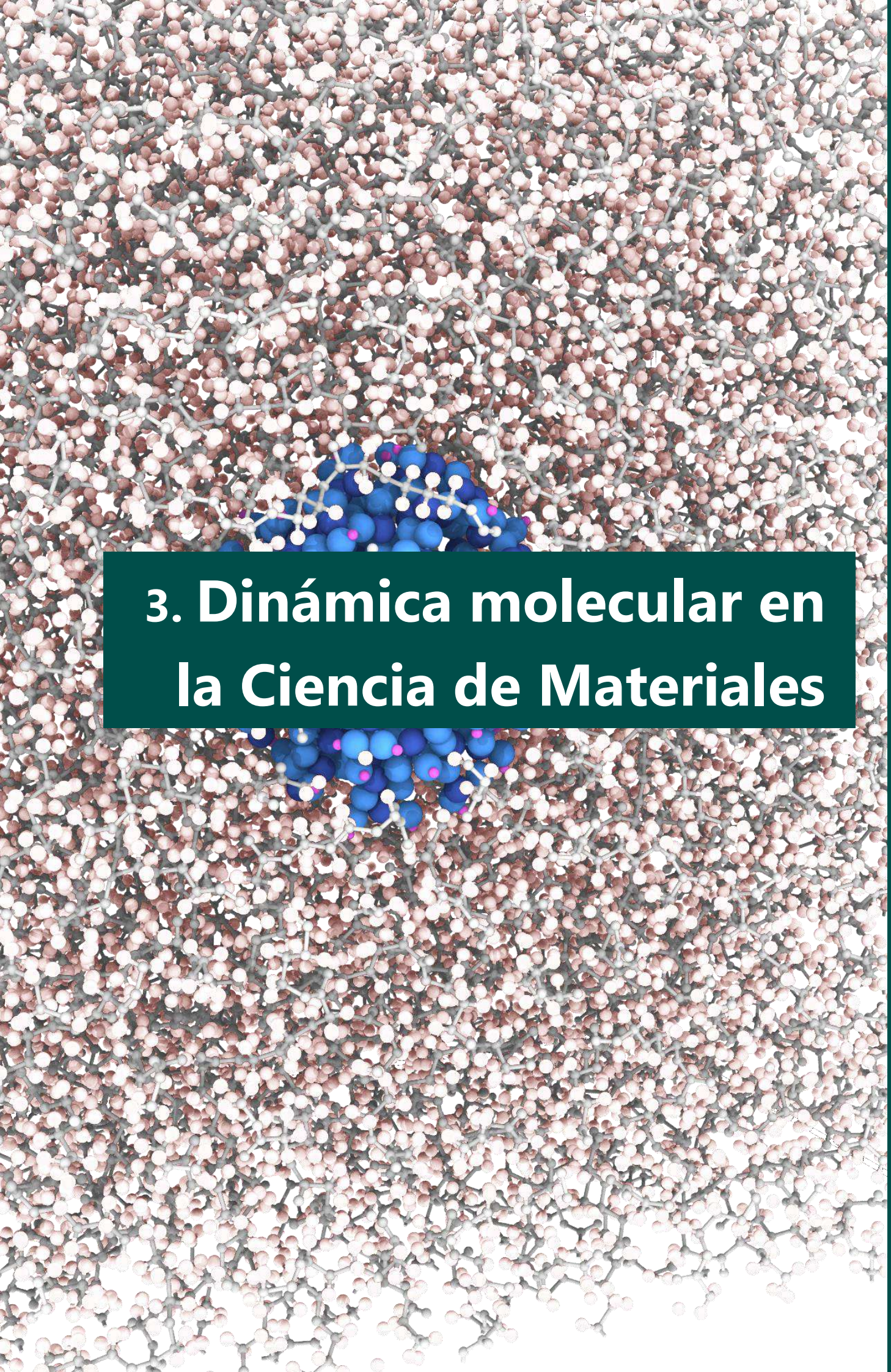

# 3. Dinámica molecular en la Ciencia de Materiales

Abordar el entendimiento básico de la estructura y fenómenos que suceden en los materiales, y las propiedades que de esto resulta, requiere de un análisis detallado a nivel microscópico del tipo de interacciones y de la energía subyacente. Las respuestas a este análisis se pueden extraer desde diferentes aproximaciones, partiendo la más fundamental de todas desde la resolución de la ecuación de Schrödinger tal como recogen los métodos *ab initio* o de la mecánica cuántica. Estos métodos se apoyan en la descripción de los sistemas materiales desde su estructura electrónica más fundamental, lo que da lugar a un mayor nivel de exactitud en las respuestas que de éstos se extraen, pero también hacen más compleja su propia resolución y su implementación completa es imposible hacerla para la mayoría de los sistemas de la ciencia de materiales y de la materia condensada, por lo que se debe recurrir a otras aproximaciones que simplifican la descripción del sistema [19].

En este punto se encuentra la dinámica molecular (MD), que simplifica la descripción del átomo a masas puntuales sin detalle de su estructura electrónica, donde su comportamiento físico obedece las leyes de la mecánica clásica Newtoniana. Al reducir drásticamente los grados de libertad con los que se describe cada átomo, los sistemas materiales que se pueden desarrollar mediante la dinámica molecular, alcanzan habitualmente las decenas de miles de átomos con los equipos de computación actuales, lo que permite tener un mayor detalle microscópico y suficiente población de partículas con las que poder modelizar las propiedades y fenómenos de un material de forma realista. Las simulaciones estándar MD permiten estudiar la trayectoria de un sistema del tamaño 1-100 Å en escalas de tiempo 1 fs– 100 ns [7], aunque en casos excepcionales y empleando potentes clúster de simulación se han llegado a reportar sistemas en el rango del micrómetro [20] y del milisegundo [21]. En esta escala de material el comportamiento de los átomos individuales se describe en base a campos de fuerza clásicos o semi-empíricos tales como COMPASS [22], AMBER [23] y OPLS[24], por citar algunos ejemplos representativos, basados en potenciales de interacción en los cuales las contribuciones electrónicas cuánticas no se consideran.

Las primeras simulaciones de dinámica molecular se llevaron a cabo a finales de la década de 1950 por Alder y Wainwright [25], [26], consistiendo en sistemas simples de moléculas gaseosas. El desarrollo de la técnica ha estado ligado al desarrollo de las propias capacidades de computación, al igual que a la formulación de los propios algoritmos de integración tal como el de Verlet [6], que sigue siendo el más popular a día de hoy, de tal modo que los avances en este campo permitieron también ir simulando sistemas cada vez más complejos, y realistas, llegando por ejemplo a la simulación de una proteína completa a finales de la década de 1970 [27]. También debe considerarse que el desarrollo de la propia técnica no solo ha estado ligado al de las propias capacidades de computación, sino también a la aceptación por parte de la comunidad científica de las bondades de la simulación como herramienta para predecir resultados en sistemas materiales [28]. Las simulaciones MD han demostrado ser una ayuda para interpretar experimentos, pero

también para predecir sus resultados. En este sentido cabría destacar el trabajo de Rahman y Stillinger [29] en 1971, en el cual se demostró que la estructura del agua líquida consistía en una red aleatoria de puentes de hidrógeno y que la difusión de las moléculas tenía lugar de forma continua y no a través de un mecanismo de "salto", como se creía hasta ese momento. Las simulaciones MD se han ido haciendo cada vez más populares en la ciencia de materiales y han comenzado a ganar más peso en las décadas recientes, por el fácil acceso a equipos de computación de alta capacidad (hoy en día incluso es posible realizar cálculos en equipos locales con coste modesto [30]) así como por haber demostrado ser un importante apoyo para el desarrollo experimental en la interpretación de resultados, sugerir nuevos experimentos y, cada vez más frecuentemente, predecir sus resultados.

Debido precisamente al rápido incremento de la capacidad computacional, los sistemas poliméricos, incluyendo sus sistemas híbridos (composites) cuando se combinan con un material de refuerzo, han sido objeto de intenso estudio mediante simulaciones de dinámica molecular en los últimos 50 años [31]. Los polímeros son una clase compleja de materiales que se presenta como un desafío para un científico computacional, ya que exhiben una serie de fenómenos en un amplio rango de escalas de longitud (que comienza desde el monómero, al nivel del angstrom, y se extiende hasta los nanómetros) y de tiempo (comenzando desde el femtosegundo y llegando hasta segundos, minutos o incluso años). Las simulaciones con modelos atomísticos normalmente se emplean para caracterizar interacciones en el nivel atómico en sistemas de morfología conocida, como por ejemplo para evaluar la compatibilidad entre el polímero y la fase dispersa , o la miscibilidad en el caso de mezclas de polímeros [32], [33], [34] o incluso con otro tipo de materiales [35], o también la energía y/o tensión superficial [36]. Las propiedades del sistema material derivan precisamente de las interacciones que se producen entre los diferentes átomos que constituyen el sistema, de ahí la importancia de realizar su análisis. Estas propiedades del material se pueden clasificar en dos grandes grupos: estáticas y/o de equilibrio; y dinámicas o de transporte.

La dinámica molecular ha demostrado ser una poderosa herramienta para la predicción de propiedades de equilibrio o termodinámicas en la fase condensada [37]. Durante el cálculo de propiedades de equilibrio, el sistema se mantiene en el mismo estado termodinámico (esto es, de energía, temperatura y presión) durante la fase de monitorización del parámetro objetivo, sin producir una perturbación que saque al sistema de este estado de equilibrio. La mecánica estadística ofrece entonces las soluciones matemáticas para el cálculo de la propiedad requerida en base al promedio estadístico. Este promedio asume la aplicación de la hipótesis ergódica [38], por la cual se establece que, para un sistema estacionario (esto

es, en equilibrio), el promedio temporal y el promedio sobre un conjunto estadístico de microestados arrojarán el mismo valor, esto es (**Ecuación 17**):

$$\lim_{\Delta t=\infty} \bar{x}_j^S = \lim_{N_S=\infty} \langle x_j^S \rangle \qquad (\mathbf{17})$$

O también [39] (**Ecuación 18**):

$$\langle G \rangle_{eq} = \bar{G} = \lim_{T\to\infty} \frac{1}{T} \int_0^T G(x_i) \qquad (\mathbf{18})$$

Aunque normalmente en el cálculo de propiedades de equilibrio no se produce una perturbación del sistema, en algunos métodos concretos sí que se aplica una perturbación suficientemente pequeña como para considerar al sistema en cuasi-equilibrio. Este es, por ejemplo, el método propuesto por Thedorou y Suter [11] para el cálculo de propiedades mecánicas de polímeros amorfos, el cual se describió con más detalle en el apartado 2.3 y el cual se empleó en el desarrollo de esta tesis para el cálculo de las propiedades mecánicas de los diferentes sistemas materiales considerados. En este método se aplican, sobre el sistema, una serie consecutiva de pequeñas perturbaciones en forma de incrementos de las dimensiones (deformación) para posteriormente reequilibrarlo mediante procedimientos de minimización energética (sin integración temporal). Este método ha sido ampliamente utilizado para calcular las propiedades mecánicas de sistemas poliméricos [40], [41] así como en otros materiales, con buenos resultados [42], [43].

En contraposición, las propiedades de transporte suelen calcularse mediante simulaciones de no equilibrio (lo que se conoce como *non-equilibrium molecular dynamics*, NEMD). Desde un punto de vista a nivel macroscópico, el transporte de propiedades tales como la masa y energía en respuesta a perturbaciones externas se describe a partir de ecuaciones fenomenológicas tales como la ley de Fick para el transporte de masa o la ley de Fourier para el transporte de calor. El método más directo para calcular estas propiedades a través de modelado molecular es mediante simulaciones de no-equilibrio en el que se monitorizan los flujos inducidos en el material (de energía, masa…) mediante campos o gradientes externos. Bajo este formalismo opera por ejemplo el método de Mülle-Plathé [13] para el cálculo de la conductividad térmica, descrito en al apartado 2.3, en el que se induce un gradiente de temperatura en el sistema mediante la imposición de un flujo de calor. También existen métodos NEMD descritos para el cálculo de propiedades mecánicas, en los cuales el sistema es sometido a una deformación constante bajo una determinada velocidad de deformación (*strain rate*) monitorizando la tensión del sistema. Sin embargo, los resultados obtenidos bajo este protocolo son altamente dependientes de la velocidad de deformación [44], [45], habitualmente balística (del orden de $10^9$s), alejados de los valores

habitualmente evaluados de forma experimental, lo cual no sucede mediante el método de minimización anteriormente mencionado.

Merece la pena destacar en ese punto el formalismo de Green-Kubo [46], [47], el cual permite el cálculo de propiedades de transporte empleando para ello las fluctuaciones de ciertas propiedades que se producen, de forma natural, durante el equilibrio de un sistema. Este formalismo establece las expresiones matemáticas exactas que relacionan transportes de coeficiente con la integral de la función de correlación correspondiente, como por ejemplo las que relacionan la conductividad térmica con la función de autocorrelación de la velocidad. Bajo las condiciones y procesado adecuado, tanto el método correspondiente NEMD como el de Green-Kubo conducirían a valores de propiedades equivalentes [48].

Es evidente que, ante el desarrollo de la técnica, la simulación mediante dinámica molecular supone una potente herramienta para el estudio de los materiales al servicio de la comunidad científica. Se ha establecido como un nexo de unión entre la experimentación y la teoría, en un microscopio computacional que permite llegar a la escala molecular del material de un modo convencional y práctico.

# 4. Objetivos

Esta tesis pretende contribuir en desarrollar las posibilidades que ofrece la técnica de simulación de dinámica molecular (MD) para explorar y ampliar el conocimiento sobre nanocompuestos poliméricos y sus nanopartículas, y más en concreto, en profundizar sobre la interfase nanopartícula-polímero, sus propiedades mecánicas y térmicas, y la relación de estas con la estructura del material.

De este modo se plantearon los siguientes **objetivos particulares** a conseguir en el desarrollo de la tesis:

- Aplicación de la técnica de dinámica molecular a una amplia variedad de sistemas materiales, para evaluar las posibilidades de adaptación a cada caso particular y las posibles limitaciones.

- Predecir las propiedades de interfases nanopartícula-polímero en nanocompuestos poliméricos, con especial atención en sus propiedades mecánicas y térmicas.

- Predecir el efecto de la adición de nanopartículas a materiales poliméricos (esto es, nanocompuestos) en cuanto a sus propiedades mecánicas y térmicas.

- Analizar los cambios estructurales que tienen lugar en un sistema material como consecuencia de la aplicación de tensiones y/o deformaciones, y su efecto en las propiedades mecánicas.

- Predecir las propiedades mecánicas y térmicas de nanopartículas, y evaluar el efecto en estas propiedades de su modificación química y física.

Bajo estas premisas, en el desarrollo de la tesis se han estudiado diferentes combinaciones de nanopartículas y materiales poliméricos a fin de conseguir uno o varios de los objetivos así planteados. La validación de los resultados obtenidos de las simulaciones MD se verificará en su comparativa con resultados obtenidos de forma experimental.

# 5. Presentación de las publicaciones

# 5.1. Justificación de la unidad temática

Esta tesis está compuesta por un compendio de cuatro publicaciones. Cada uno de estos trabajos se ha centrado en el estudio de un aspecto concreto de los **materiales nanocompuestos**, mostrándose en la **Figura 1** un resumen gráfico en el que se indica qué parte del material se ha analizado en cada una de las publicaciones.

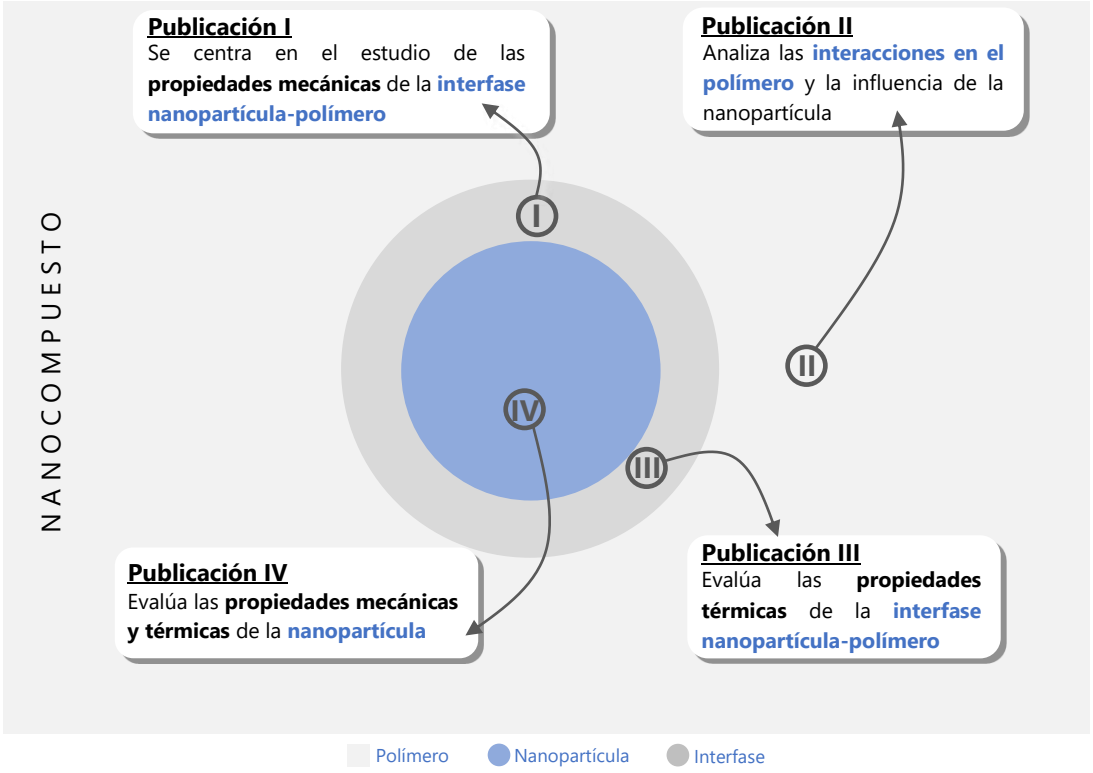


**Figura 1 –** *Resumen gráfico del contenido de la tesis.*

## 5.2. Publicación I: Estudio de interfases nanopartícula-polímero

Los compuestos poliméricos reforzados con nanopartículas han suscitado una gran atención en la ciencia de materiales en los años recientes, debido a su potencial para producir propiedades físicas, químicas y mecánicas superiores en el material. La influencia que las partículas de refuerzo de tamaño nanométrico (esto es, de las nanopartículas) tienen en las propiedades mecánicas del material que refuerzan resulta en algunos casos sorprendente, ya que la magnitud del efecto producido no se observa en los materiales compuestos convencionales a igualdad de porcentaje de refuerzo. La presencia de nanopartículas introduce una enorme cantidad de área interfacial [49] en la que las cadenas poliméricas sufren cambios de conformación y deformaciones a escala nanométrica. El contacto interfacial entre el polímero y la nanopartícula se manifiesta como una perturbación de la estructura (por ejemplo, se pueden encontrar cambios en su densidad, orientación o disposición de la cadena) y la dinámica del polímero. Es esta región de propiedades alteradas del polímero, o zona de transición entre la matriz polimérica y la partícula, lo que en la ciencia de materiales se conoce como interfase [50].

La importancia que la interfase tiene en las propiedades de los materiales compuestos reforzados con nanopartículas es lo que animó a llevar a cabo este primer estudio abordado en la tesis. De acuerdo con numerosos estudios encontrados en la literatura, las moléculas de polímero cercanas a la superficie de las nanopartículas experimentan una serie de cambios físicos en comparación con las propiedades de las moléculas de la región más alejada de la superficie (esto es, de la matriz polimérica). Estos estudios reportan, entre otros efectos, una dinámica interna de las moléculas de polímero más lenta, con una difusión reducida o insignificante de las moléculas absorbidas en la superficie [51], que da lugar a la formación de una capa vítrea de polímero [52]. Este confinamiento nanométrico de las moléculas de polímero se manifiesta, por ejemplo, en cambios en la temperatura de transición vítrea ($T_g$) de dichas moléculas confinadas, a la vez que presentan un mayor grado de heterogeneidad en comparación con las moléculas de la matriz [53].

Al considerar los modelos predictivos, las propiedades que exhiben los materiales compuestos reforzados con nanopartículas no pueden explicarse ni predecirse a partir de los modelos estándar de medios continuos o de campo medio de la mecánica continua [54]. En los modelos estándar de micromecánica habitualmente solo se consideran dos fases (fase continua y fase de refuerzo), sin embargo, cuando el refuerzo se encuentra en la dimensión de la nanoescala (esto es, se trata de nanopartículas), la superficie de la

nanopartícula-polímero aumenta de forma exponencial y hacen que el volumen de la interfase se deba tener en cuenta en los modelos [49]. Así, recientemente se han desarrollado nuevas formulaciones de estos modelos analíticos para inclusiones de tamaño nanométrico en las que los efectos superficie/interfase adquieren importancia y la interfase se considera como una tercera fase [55], [56], con un comportamiento mecánico diferente al del polímero de la matriz. En este punto es donde surge la principal dificultad de estos modelos, ya que ¿qué propiedades representativas se deben dar a esta interfase para introducirlas en los modelos?

Una posible respuesta a esta pregunta sería acudir a la caracterización experimental de la interfase nanopartícula-polímero. Para realizar esta caracterización se podría acudir a técnicas como la espectroscopia de RMN $^{1}H$ [52], [57], la dispersión de neutrones [58], [59] o la calorimetría DSC [60], entre otras, aunque a menudo se necesita de una combinación de varias para lograr resultados coherentes. Sin embargo, la obtención de resultados precisos y cuantitativos de materiales actualmente se limita a dispositivos que sólo son capaces de resolver hasta la microescala ($10^{-6}$ m), lo que está lejos del alcance realista de la escala de la interfase (del orden de $10^{-9}$ m). Además, dado que los distintas técnicas mencionadas miden la dinámica de las moléculas poliméricas o las magnitudes físicas relacionadas de forma diferente, no es sorprendente que no exista una cierta correlación entre los distintos resultados obtenidos con cada técnica.

Debido a las dificultades expuestas para llevar a cabo la caracterización experimental de la interfase con la suficiente resolución, la estrategia más atractiva consiste en estimar las propiedades de esta región mediante técnicas de simulación atomística, donde entraría en juego la dinámica molecular (MD) [61]. La estrategia más comúnmente aplicada para la determinación de las propiedades de la interfase suele ser la de aplicar algoritmos inversos en los que se comparan modelos MD y modelos de elementos finitos (en su abreviación en inglés, *finite elements* o FE) para asignar las propiedades equivalentes que tendría que tener la interfase [62], [63], [64], [65]. La mayoría de estos trabajos previos se han centrado en la caracterización de interfases de nanotubos de carbono y polímeros [66], [67], [68], aunque en los últimos años se han realizado grandes esfuerzos para modelar nanocompuestos reforzados con otro tipo de nanopartículas [64], [69], [70], [71], [72] e incluso metales [73], [74]. Una estrategia alternativa para la determinación de las propiedades de la interfase consiste en determinar las propiedades directamente de los modelos MD, sin tener que emplear el equivalente FE, pudiéndose encontrar en este sentido varios tipos de aproximaciones. Por ejemplo, en el estudio de Arash y colaboradores [66], las propiedades mecánicas de la interfase se obtienen mediante la división de la celda de simulación en subsecciones de las cuáles se calculan de forma local sus constantes elásticas. Una de las

principales desventajas o limitaciones de estos estudios es que no calculan gradientes de propiedades elásticas, sino que se determina una propiedad homogénea de la interfase. Sin embargo, en estudios posteriores tales como el de Fankhänel y colaboradores [75], empleando un método basado en las tensiones atómicas, se muestran resultados que permiten calcular un gradiente de rigidez a lo largo de la longitud de la interfase.

La importancia que la interfase tiene en los materiales nanocompuestos ha quedado, por tanto, puesta de manifiesto en la explicación anterior. Por esta razón, en este primer capítulo de la tesis se decidió abordar el estudio de un sistema material, compuesto por polímero y nanopartícula esférica, con el objetivo de determinar las propiedades mecánicas de la región de la interfase, basándose únicamente en los resultados de simulaciones de dinámica molecular (siguiendo de este modo la segunda de las estrategias descritas en el apartado anterior). En concreto, el sistema seleccionado estaba compuesto por la combinación de una matriz polimérica basada en policaprolactona (PCL) y nanopartículas de sílice como refuerzo (**Figura 2**). La estrategia que se siguió para caracterizar las propiedades de la interfase se basó en los perfiles de densidad polimérica y las fluctuaciones generadas por la presencia de la nanopartícula en la región de la interfase. Estas fluctuaciones de densidad se relacionaron posteriormente con fluctuaciones en las propiedades mecánicas, empleando modelos de correlación a partir de las cuales se pudieron determinar tanto perfiles de propiedades mecánicas como valores promedio.

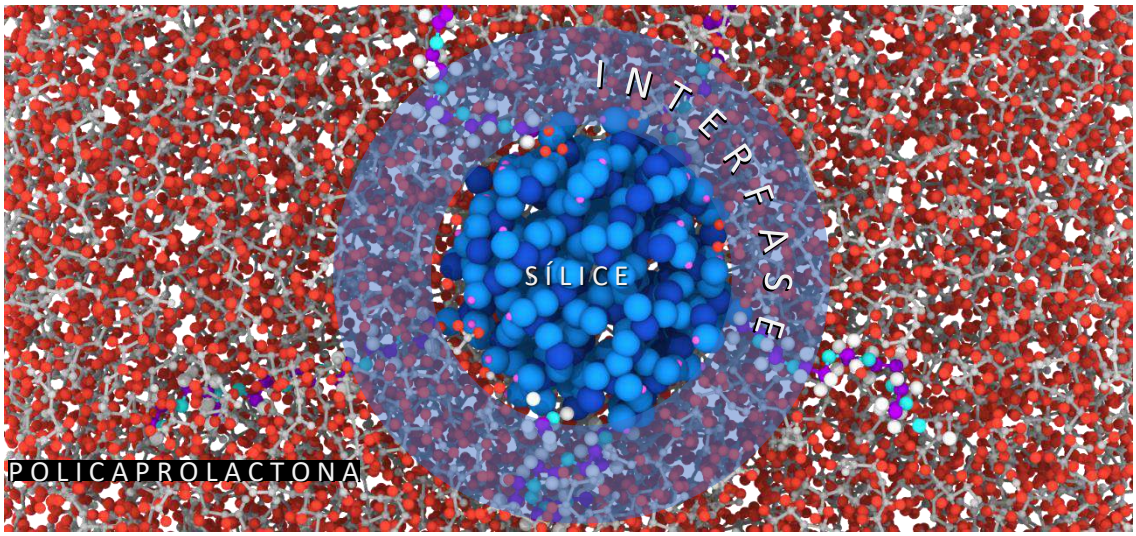


**Figura 2 –** *Detalle del modelo molecular de PCL con inclusión de $SiO_2$-PEG desarrollado en la Publicación I.*

Habitualmente las nanopartículas de sílice suelen funcionalizarse superficialmente mediante la introducción de diferentes grupos químicos [76], [77] con el objetivo de mejorar la compatibilidad con la matriz polimérica, por lo que en el estudio se analizaron dos tipos de nanopartículas de sílice: el primer tipo sin ninguna modificación superficial (puras o

"desnudas"); y un segundo tipo con una modificación superficial introducida mediante el *grafting* o anclaje covalente de cadenas cortas de polietilenglicol (PEG). De este modo, se pudo analizar la influencia que la modificación superficial de la nanopartícula tenía respecto a la interacción con la matriz, y respecto a las propiedades de la región de la interfase. Los modelos preparados (**Figura 3**) se caracterizaron principalmente en base a sus propiedades mecánicas elásticas (en el régimen de bajos niveles de deformación), mediante la aplicación de deformaciones basado en el método cuasi-estático y la posterior evaluación de las relaciones tensión-deformación [11].

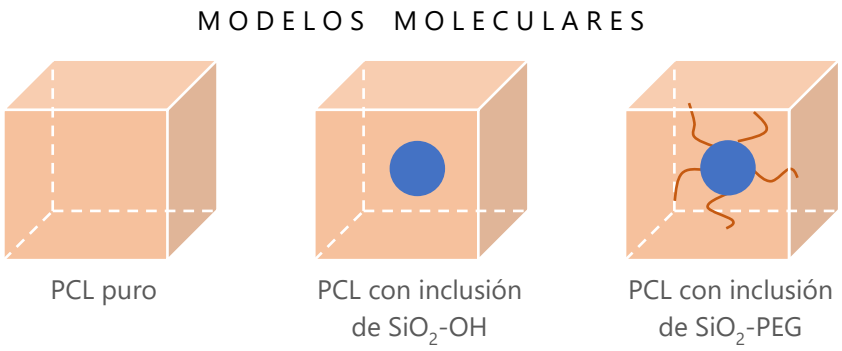


**Figura 3 –** *Listado esquemático del tipo de modelos moleculares desarrollados en la Publicación I.*

## 5.3. Publicación II: Análisis de cambios estructurales en el material mediante monitorización de interacciones

En el apartado 5.2 se ha indicado la influencia que la nanopartícula tiene sobre el polímero dentro de un material nanocompuesto, lo cual da lugar a la generación de una región de interfase alrededor de la nanopartícula con propiedades diferentes a las que tiene el polímero de la matriz (de una zona suficientemente alejada a la influencia de la nanopartícula). Este primer estudio se centró en la determinación de las propiedades mecánicas de la interfase, pero no se consideró el análisis de la posible influencia que la nanopartícula tiene al nivel de interacciones del polímero. En el estudio que se planteó a continuación, se pretendió profundizar al nivel de las interacciones del polímero y en el análisis de la influencia que la nanopartícula podría tener en este sentido.

Para este segundo trabajo se consideró una combinación diferente de polímero y nanopartícula a la empleada en el apartado 5.2. En concreto, se decidió analizar el sistema material basado en celulosa como matriz polimérica, y nanopartículas de carbonato de calcio como agente de refuerzo (**Figura 4**). La celulosa es una materia prima polimérica casi inagotable que presenta propiedades excepcionales [78] y se considera como el compuesto orgánico más abundante derivado principalmente de la biomasa [79]. Por su parte, el carbonato de calcio es uno de los minerales más abundantes de la Tierra [80] y puede encontrarse en rocas sedimentarias y minerales en forma de piedra, mármol e incluso sedimentos marinos. Por otro lado, es también uno de los biominerales más abundantes [81] ya que forma parte de corales, perlas, moluscos y el exoesqueleto de artrópodos [82], razones por las que se consideró la elección de estos dos materiales en este segundo capítulo.

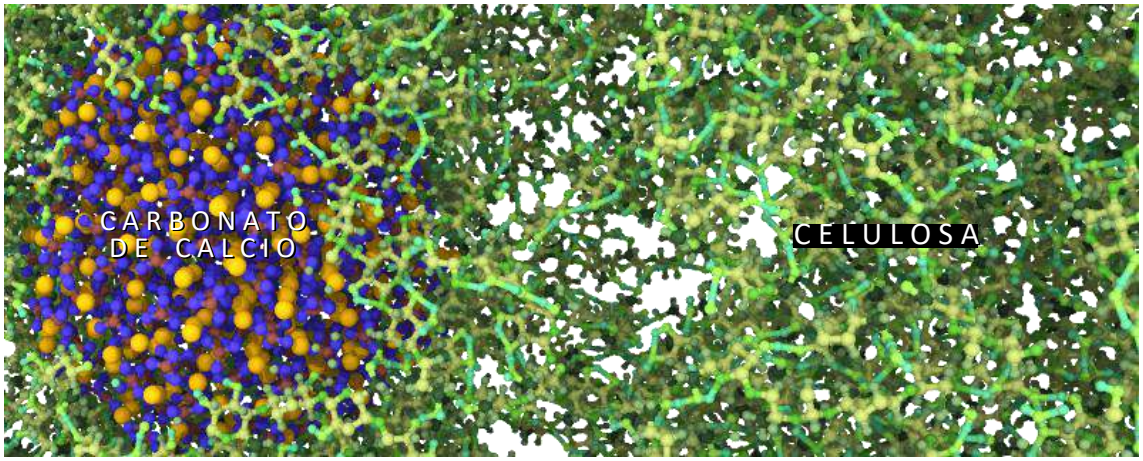


**Figura 4 –** *Detalle del modelo molecular de celulosa con inclusión de carbonato de calcio ($CaCO_3$) desarrollado en la Publicación II.*

Las aplicaciones industriales y comerciales de la celulosa y sus derivados abarcan una amplia gama de casos de uso: desde el envasado de alimentos [83], sensores de humedad y UV [79], terapia contra el cáncer [84], tratamiento de aguas residuales [85], captura de carbono [86], [87] o membranas selectivas [88], entre otros ejemplos. En los últimos años se ha dedicado especial atención al desarrollo de nanocompuestos basados en celulosa y nanopartículas inorgánicas como agentes de refuerzo, entre las que se pueden encontrar, por citar algunos ejemplos, sílice ($SiO_2$) [89], [90], dióxido de titanio ($TiO_2$) [91], [92], oro [93], partículas de caolín [94], [95], entre otros [96]. La adición de estos nanorefuerzos proporciona un material final con propiedades mejoradas respecto a la celulosa pura, tales como las propiedades mecánicas [94], antimicrobianas [93], ópticas [97] y conductividad térmica o eléctrica [98].

En el caso concreto de los nanocompuestos basados en carbonato cálcico ($CaCO_3$), se encuentran estudios que reportan una mejora de la resistencia mecánica, la biocompatibilidad [99] y la bioactividad [100], y las aplicaciones potenciales como materiales funcionales incluyen los campos biomédico [101], [102] y de pretratamiento del agua [103], [104]. No obstante, el uso de carbonato cálcico como agente de refuerzo en compuestos de celulosa, incluyendo también papel, todavía genera cierta controversia entre los diferentes estudios científicos, ya que el mecanismo de interacción entre la celulosa y el carbonato de calcio todavía no está bien establecido y es desconocido en muchos aspectos [105]. Algunos estudios indican que la presencia del carbonato de calcio puede interferir en la unión fibra-fibra (en el caso del papel) y, por tanto, disminuir la resistencia a la tracción del material [94], [106]. Algunos estudios encuentran, sin embargo, el efecto contrario de las partículas de carbonato cálcico en las propiedades mecánicas del papel [107], [108].

Debido a esta controversia, el segundo estudio desarrollado en la tesis trataría de aportar luz respecto al mecanismo de interacción celulosa-carbonato de calcio, el tipo de

interacciones implicadas y su relación respecto de las propiedades mecánicas del material final. De este modo, se construyeron modelos moleculares de celulosa reforzados con nanopartículas de carbonato de calcio de geometría esférica (**Figura 5**). Por un lado, se determinó la energía de interacción y la función de distribución radial (RDF) entre la matriz de celulosa y la nanopartícula de carbonato cálcico para evaluar cuantitativa y cualitativamente el tipo de interacción entre ambos componentes del sistema material. Por otro lado, se determinaron las propiedades mecánicas, tanto en la región elástica (mediante el cálculo de las constantes de rigidez) como a altas deformaciones, para determinar la deformación plástica remanente y la capacidad de recuperación del material. A lo largo de estas simulaciones se monitorizaron las interacciones por enlace de hidrógeno, así como la conformación de las moléculas de celulosa, mediante el análisis de los ángulos de torsión para evaluar el impacto de la deformación en los cambios estructurales a nivel molecular del material.

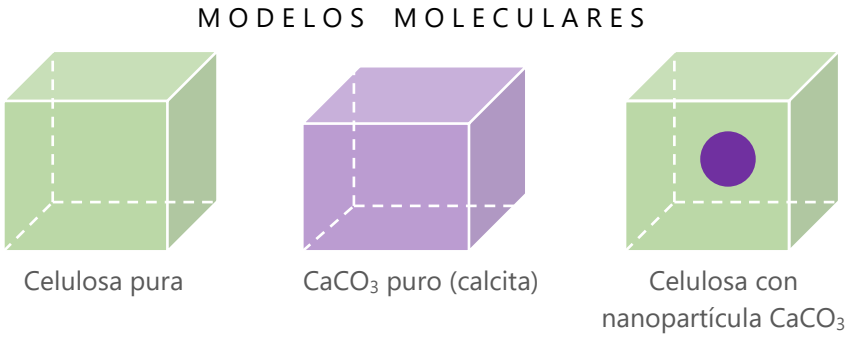


**Figura 5 –** *Listado esquemático del tipo de modelos moleculares desarrollados en la Publicación II.*

# 5.4. Publicación III: Efecto de la modificación química de nanopartículas en las propiedades térmicas interfaciales de nanocomposites poliméricos

Los anteriores trabajos se centraron fundamentalmente en el análisis de las propiedades mecánicas del material, bien desde el punto de vista de profundizar en el estudio de la interfase, o bien en el estudio pormenorizado de interacciones y conformaciones moleculares. Para ampliar la metodología de simulación MD al cálculo de otras propiedades, en este tercer capítulo se decidió centrar el estudio en las propiedades de conductividad térmica de nanocompuestos poliméricos, y en particular en la que tiene lugar a través de la interfase polímero-nanopartícula (**Figura 6**), ya que determinará en un alto grado el nivel de refuerzo producido sobre este tipo de propiedades en el material compuesto final.

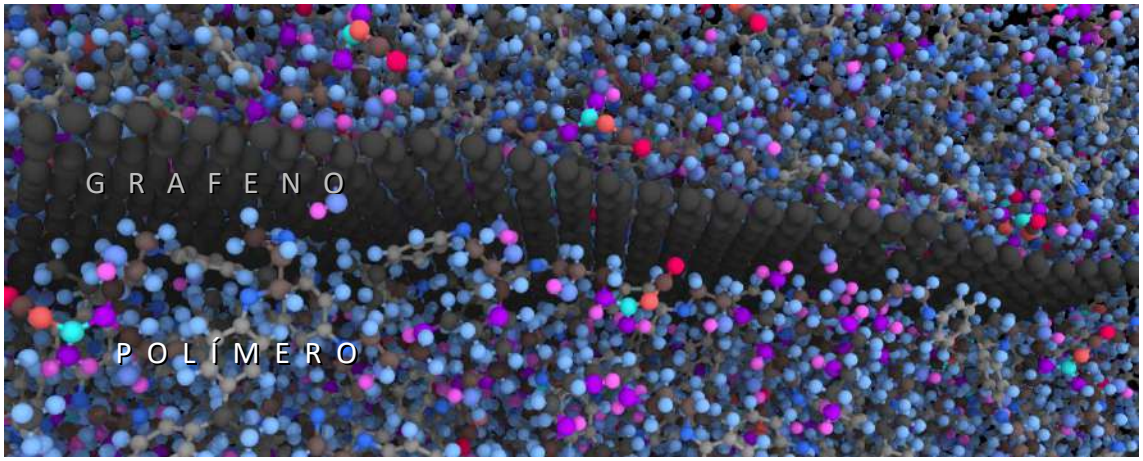


**Figura 6 –** *Detalle de la región de la interfase en el modelo molecular de resina epoxi (EPO) con grafeno puro desarrollado en la Publicación III.*

Para este tercer trabajo se eligieron nanocompuestos basados en nanopartículas de grafeno que, a diferencia de las empleadas en los sistemas materiales de los anteriores capítulos, presentan una morfología 2D o laminar. Este tipo de nanorefuerzos han experimentado un enorme interés en las últimas dos décadas (desde que se descubrieron en el año 2004 por Geim y Novoselov [109]) por sus excepcionales propiedades. El grafeno consiste en una lámina del espesor de un átomo constituida por átomos de carbono de hibridación $sp^2$ unidos covalentemente y que forman redes cristalinas hexagonales ideales en forma de colmena [110], [111]. Esta estructura molecular origina un enlace π de largo alcance y es responsable de sus extraordinarias propiedades mecánicas [112], [113], eléctricas [114],

[115] y térmicas [116]. Las aplicaciones y propiedades del grafeno se han estudiado intensamente y abarcan la ingeniería biomédica [117], la electrónica [118], [119], y la aeroespacial [120], entre otras. No obstante, las formas oxidadas del grafeno, que principalmente incluyen al óxido de grafeno (GO) y el óxido de grafeno reducido (rGO), suelen preferirse con respecto a la estructura pura, ya que son más activas frente a la modificación química y presentan una mayor separación entre capas que el grafeno puro [121], debido a la presencia de grupos polares (es decir, grupos que contienen oxígeno). Las variedades oxidadas del grafeno presentan además una cinética electrocrómica mejorada [122], una menor resistencia a la transferencia de calor a través de la interfase [3] y un mayor carácter hidrofílico [123], [124] que la forma pura [125], [126], [127].

Las excepcionales propiedades que presenta el grafeno y sus derivados suscitaron su aplicación como agente de refuerzo en nanocomposites poliméricos [128]. Debido a la elevada área superficial de interfase por unidad de volumen que pueden aportar las nanopartículas de grafeno, en numerosos estudios se describen incrementos excepcionales de propiedades mecánicas incluso a bajos porcentajes de refuerzo. Por citar un ejemplo, en el estudio de Yan y colaboradores [129] reportan incrementos del módulo de Young de hasta seis veces mayor al del polímero puro con tan solo un 0,94% en peso de grafeno. En la revisión de Papageorgiou y colaboradores [113] se puede encontrar una extensa revisión con diferentes combinaciones de matriz y derivados de grafeno, y el nivel de refuerzo conseguido en cada caso.

Las propiedades térmicas del grafeno son incluso más extraordinarias que las mecánicas, ya que el grafeno con una estructura perfecta tiene la mayor conductividad térmica entre todos los materiales conocidos (se reportan valores entre 3000–4000 W/m·K)[130], [131], [132], propiedad que comparte con el diamante. Pese a estas sobresalientes propiedades térmicas del grafeno, cuando se aplica como refuerzo a composites poliméricos suelen aparecer dos tipos de problemas que hacen que la conductividad no sea tan elevada como se esperaría [133]. Por un lado la presencia de bordes (lo que se conoce como efecto del borde), defectos y modificación química en el grafeno producen una dramática reducción de su conductividad. Otro tipo de problemas se deben a la preparación en sí del nanocompuesto, que debido a la morfología 2D del grafeno y su elevada área interfacial suelen dar lugar a una mala dispersión, impidiendo conseguir todo el potencial del nanorefuerzo. Por otro lado, se debe asegurar además un buen acoplamiento entre la matriz polimérica y el nanorefuerzo al nivel de la interfase para conseguir el mayor incremento en la conductividad térmica en el material compuesto final.

Otro aspecto que se debe considerar respecto al potencial de refuerzo del grafeno en la conductividad térmica es el del fenómeno de percolación. El fenómeno de percolación

térmica, tal como se entiende en la ciencia de materiales, se produce debido al flujo de fonones dentro de un material en el cual existe algún tipo de mecanismo de interconexión, y se refiere a la transición abrupta de aislante a conductor que se produce al incrementar el porcentaje del nanorefuerzo en el material [134]. El límite en el cual se produce esta transición se conoce como umbral de percolación, en el cual se establece una red interactiva entre las nanopartículas de grafeno y que da lugar a un incremento notable en las propiedades térmicas. En el caso de la percolación eléctrica el fenómeno se conoce bien y está bien apoyado por diferentes teorías [135], [136], incluyendo efectos cuánticos tales como la conductividad por efecto túnel [137], [138]. La existencia de la percolación térmica todavía genera, no obstante, cierta controversia ya que el mecanismo de transporte se basa en fonones a diferencia del de la percolación eléctrica, que se basa en "saltos" de electrones bien por contacto directo interfacial o por efecto túnel. De hecho, el umbral de percolación, considerado como porcentaje en peso del grafeno, puede ser diferente para la conductividad térmica y eléctrica al estar originados por diferentes efectos y mecanismos físicos [134], [139].

Este escenario suscitó al desarrollo del estudio descrito en esta tercera publicación de la tesis (**Figura 7**). Al considerarse que los principales factores que pueden limitar el potencial de refuerzo de la conductividad térmica del grafeno son una mala dispersión y una elevada resistencia interfacial polímero–nanopartícula, el estudio se centró en la evaluación de la energía de interacción y en el cálculo de la resistencia interfacial (también conocida como resistencia de Kapitza, $R_K$). La capacidad de dispersión del grafeno, dentro de la matriz polimérica, va a depender en un alto grado del tipo de interacción que se establezca con ésta, de modo que cuanto más favorable sea, mayor será su posibilidad y capacidad de dispersión. Del mismo modo, también podría entenderse que una mala interacción polímero-grafeno daría lugar a una mayor aglomeración entre las propias nanopartículas de grafeno y, por consiguiente, disminuiría su potencial efecto de refuerzo. En el estudio se quiso comprobar la influencia tanto del tipo de matriz polimérica, para lo que consideraron tres tipos de matrices poliméricas, como del tipo de modificación química del grafeno (entendida en este caso como oxidación). Respecto de la matriz se escogió ácido poliláctico (PLA) por tratarse de un polímero biobasado y de naturaleza eminentemente polar, polipropileno (PP) por su naturaleza hidrofóbica (o mayormente apolar) opuesta a la del PLA, y resina epoxi (EPO) que, a diferencia de los polímeros anteriores, es un polímero termoestable que presenta entrecruzamiento en su estructura molecular. Por otro lado, se escogieron tres tipos diferentes de grafeno. En primer lugar, el que podría denominarse como grafeno puro o prístino (G) que no contiene ningún tipo modificación química o grupo funcional (solo contiene átomos de carbono), y a continuación se eligieron óxido de grafeno (GO) y óxido de grafeno reducido (rGO), los cuales presentan diferentes grados de

oxidación entre sí (modificación química mediante grupos basados en oxígeno). El cálculo de la conductividad térmica a través de la interfase (resistencia de Kapitza, $R_K$) se basó en un método de no equilibrio (NEMD), siendo la perturbación aplicada la generación de un incremento de temperatura de la nanopartícula (grafeno). A partir de la monitorización de la diferencia de temperatura nanopartícula-polímero durante el reequilibrado térmico del sistema se calculó el valor de $R_K$.

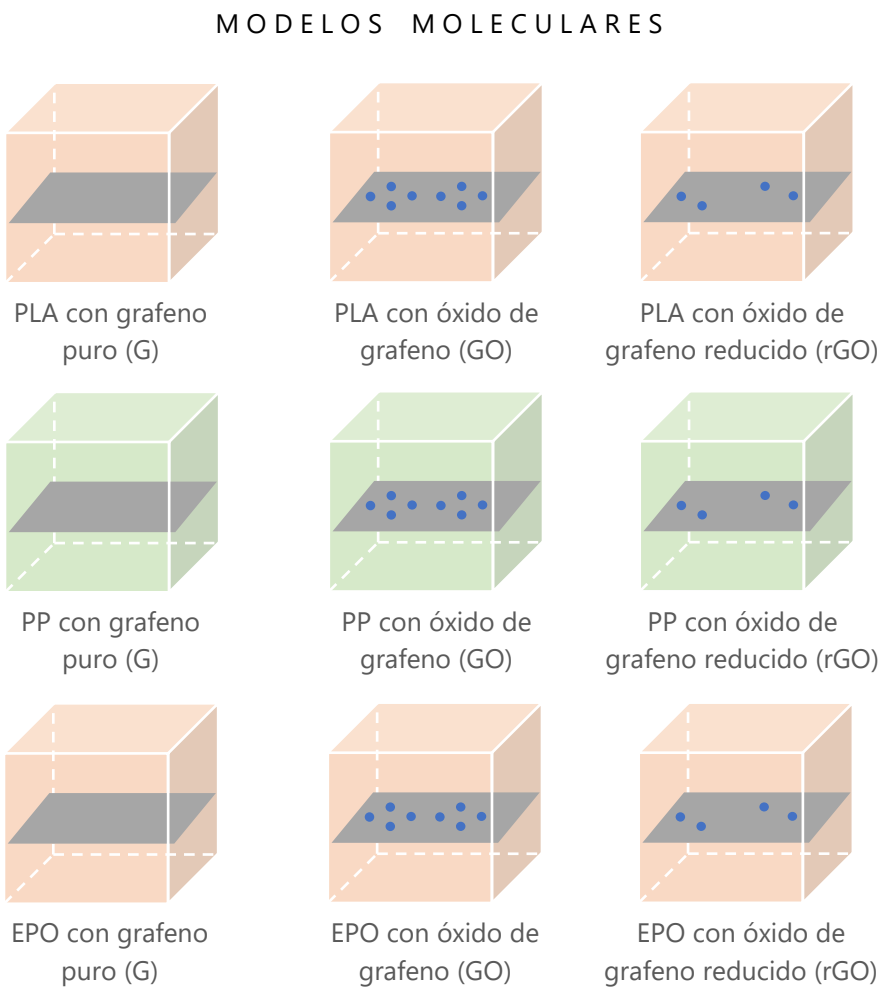


**Figura 7 –** *Listado esquemático del tipo de modelos moleculares desarrollados en la Publicación III.*

## 5.5. Publicación IV: Estudio de propiedades de nanopartículas y efecto de modificaciones físico-químicas

En los trabajos anteriores, el objeto de análisis de los diferentes sistemas materiales estudiados se centró principalmente en el estudio de la interfase nanopartícula-polímero, sus propiedades mecánicas y térmicas, y las interacciones implicadas entre ambos componentes del sistema. Para ampliar la metodología aplicada y completar el estudio de todo el sistema de nanocomposite, en este cuarto y último de los trabajos se planteó centrar el estudio únicamente en la nanopartícula, sin considerar el componente polimérico. Al igual que sucede con las propiedades de la interfase, la determinación de las propiedades de las nanopartículas requiere, en muchos casos, de técnicas experimentales avanzadas tales como la nanoindentación [140] y la nanocompresión [141], los únicos dos tipos de ensayos que hasta la fecha permiten determinar las propiedades mecánicas de nanopartículas. De este modo, la simulación mediante dinámica molecular se establece como una estrategia alternativa en la caracterización de nanopartículas [142], estableciendo métodos computacionales que reproducen o mimetizan en muchas ocasiones a los propios ensayos experimentales [143].

Este cuarto trabajo se centró, de este modo, en el estudio de las propiedades mecánicas y térmicas de nanopartículas de grafeno (**Figura 8**). En este sentido, las propiedades de las nanopartículas de grafeno están intrínsecamente ligadas a su grado de oxidación y nivel de porosidad. A nivel experimental, tanto el nivel de oxidación como la porosidad del grafeno se pueden modular o, dicho de otro modo, dependen del proceso de síntesis por el que se han obtenido. La síntesis del óxido de grafeno suele llevarse a cabo tratando el grafeno puro o el grafito con ácidos y agentes oxidantes fuertes, tales como el permanganato y el ácido sulfúrico (método Hummers) [144], [145]. Este tratamiento genera oxidación en las nanopartículas de grafeno, mediante la introducción de grupos hidroxilo (C-OH) y oxirano (C-O-C) en la superficie de la lámina, además de grupos carboxílicos (C-COOH) y carbonilo (C-C=O) en las posiciones de los bordes [146], [147]. Otra característica estructural importante de las formas oxidadas del grafeno es la presencia de defectos estructurales en forma de poros o vacantes que normalmente se producen por un exceso de oxidación y/o por la exfoliación laminar [148], [149]. En el estudio de Li y colaboradores [150] se demostró, precisamente mediante simulaciones MD, que la presencia de defectos en forma de

agujeros en la lámina de grafeno disminuía la resistencia interfacial entre el polímero y el grafeno en sistemas de nanocomposite.

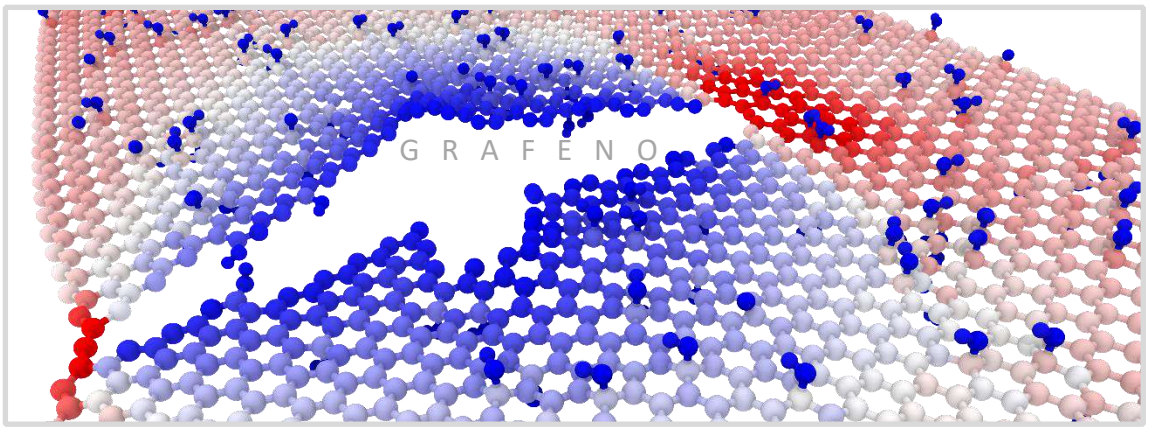


**Figura 8 –** *Detalle de modelo molecular de nanopartícula de grafeno desarrollada en la Publicación IV.*

Las propiedades y la estructura de los derivados oxidados del grafeno están afectadas, por tanto, por la cantidad y distribución de los grupos polares y por la porosidad de la lámina (defectos de vacante). Dicho de otro modo, las propiedades del grafeno se pueden modular, a través de la cantidad de grupos polares y de poros en su estructura según requiera la aplicación. En este sentido se han descrito varios métodos para sintetizar grafeno con porosidad controlada, como la síntesis por plantilla [151], [152] y la activación química/térmica [153], [154]. El grafeno puro presenta un extraordinario modulo elástico de hasta 1 TPa, tal y como revelan los estudios experimentales realizados mediante nanoindentación [112], así como una excepcional conductividad térmica de 3000–4000 W/m·K [130], [131], [132]. No obstante, estas propiedades se ven drásticamente disminuidas debido a la oxidación del grafeno [155], [156].

La estudiada relación entre las propiedades del grafeno con respecto a su nivel de oxidación y porosidad es lo que suscitó al planteamiento de este cuarto estudio. Más concretamente, se estableció como objetivo analizar el mecanismo molecular por el cual estos dos factores afectaban a las propiedades mecánicas y térmicas de las nanopartículas de grafeno. Bajo esta premisa se desarrollaron una serie de modelos atomísticos de nanocintas (GNR) (en inglés *nanoribbons*) basados en grafeno puro (G) y óxido de grafeno (GO) con diferentes porcentajes de poros (es decir, de defectos de vacantes). Las nanocintas de grafeno son estructuras que tienen una elevada relación longitud frente a anchura, la cual habitualmente se encuentra por debajo de los 100 nm, característica que las dota de ciertas propiedades debido a efectos de confinamiento y de borde en comparación a partículas ordinarias de grafeno [157]. También se las conoce como grafeno cuasi-monodimensional debido a su particular geometría. Por citar algunos ejemplos, se ha visto que a anchuras por debajo de

los 10 nm, los GNR se convierten en semiconductores debido a la separación de las bandas electrónicas de conductividad, pudiendo actuar de este modo como transistores [158], [159]. Incluso se describen estados cuánticos exóticos en conjunciones de nanocintas [160] o estados biexcitónicos que los hacen candidatos potenciales en fotónica y optoelectrónica [161]. No obstante, estas aplicaciones requieren de nanocintas estructuralmente perfectas y lo suficientemente estrechas para conseguir sus exóticas propiedades.

El objetivo de este cuarto estudio no fue el de analizar la influencia de la anchura en las propiedades de las nanocintas, sino el de evaluar la influencia de la oxidación y porosidad en sus propiedades mecánicas y térmicas, así como los mecanismos moleculares que afectan a dichas propiedades. Para el estudio se prepararon un total de 14 modelos diferentes de GNR (**Figura 9**), divididos entre los de grafeno puro (G) y óxido de grafeno (GO), con porcentajes crecientes de porosidad desde el 0% hasta un 6%. Se escogió una anchura de 75 Å y una longitud periódica de 250 Å. En concreto estos modelos se caracterizaron en términos de su módulo de Young, la relación de Poisson, la resistencia a la tracción y la deformación a la rotura, a partir de simulaciones MD cuasi-estáticas, utilizando el enfoque de minimización de energía, a partir del cual también se evaluó el mecanismo de fallo. Además, la conductividad térmica se calculó mediante el método de Müller-Plathe [58], basándose en este caso en un enfoque de no equilibrio. Dado que la conductividad térmica depende íntimamente del mecanismo de transmisión de fonones, también se determinaron las funciones de densidad de estados (DOS) junto con el camino libre medio (MFP) del fonón para ayudar en la descripción de los resultados encontrados de conductividad térmica.

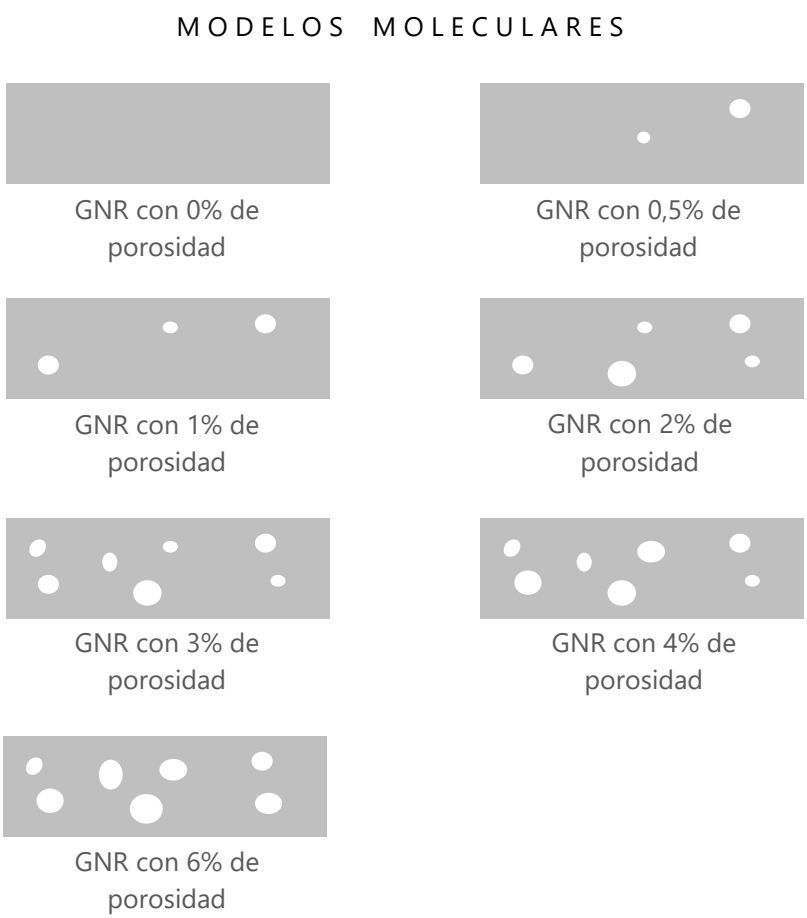


**Figura 9 –** *Listado esquemático del tipo de modelos moleculares desarrollados en la Publicación IV.*

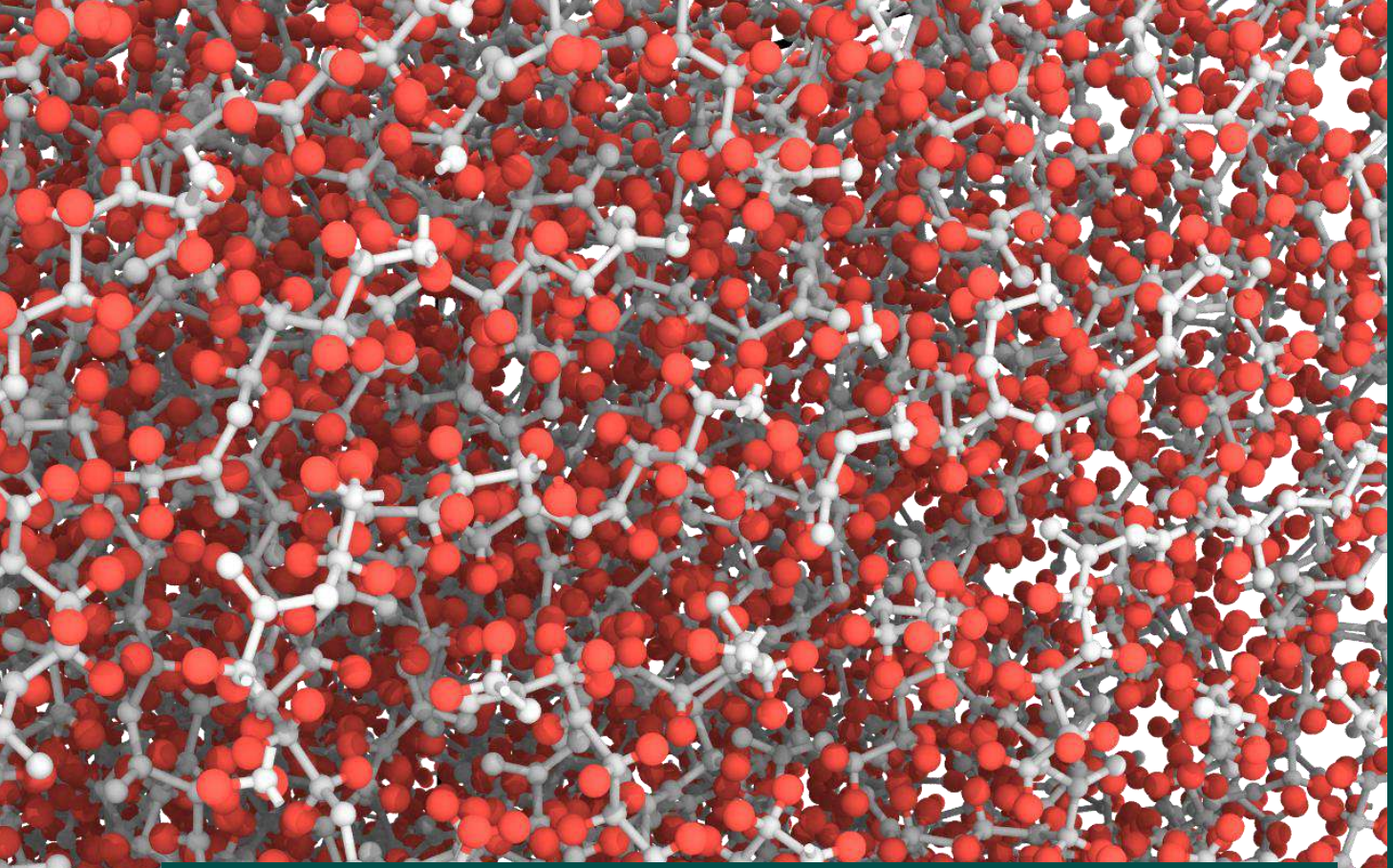

# 6. Publicación I

**Prediction of the structure and mechanical properties of polycaprolactone-silica nanocomposites and the interphase region by molecular dynamics simulations: the effect of PEGylation**

**Soft Matter,**
**DOI:** 10.1039/d1sm01794b
**Factor de impacto en 2022**: 3,4
**Área temática**: Materials Science, Multidisciplinary
**Cuartil JCR (2022):** Q3



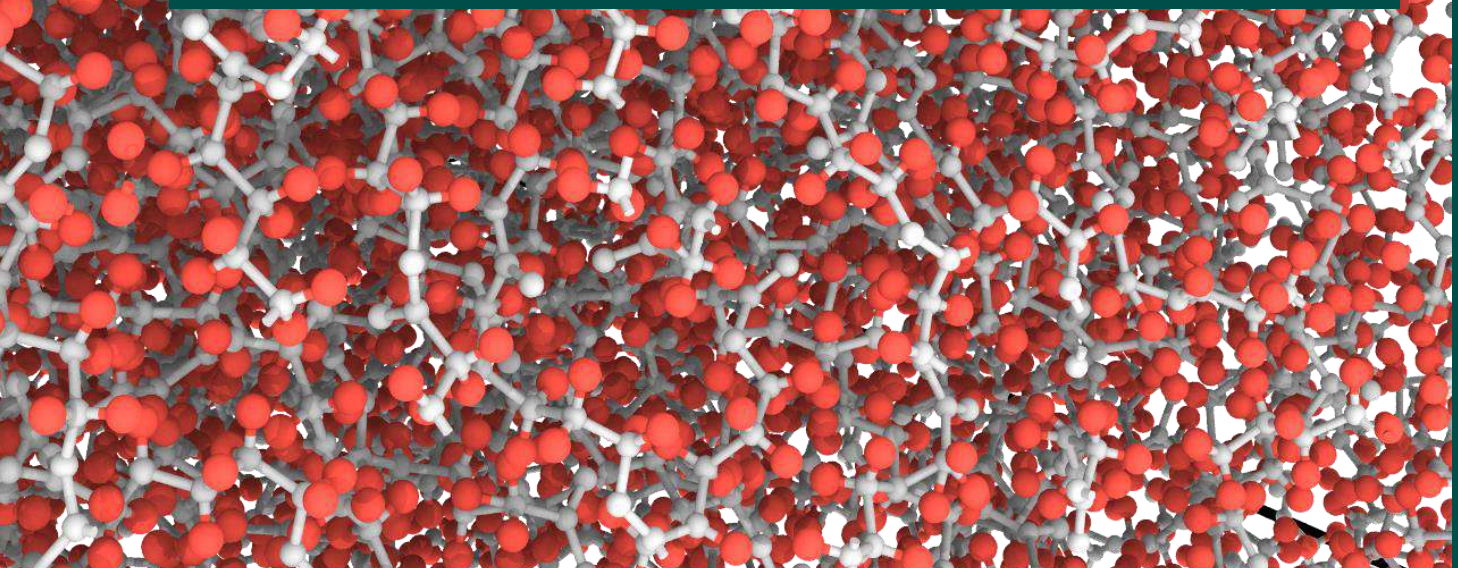

Soft Matter

PAPER



Cite this: *Soft Matter*, 2022, **18**, 2800

# Prediction of the structure and mechanical properties of polycaprolactone–silica nanocomposites and the interphase region by molecular dynamics simulations: the effect of PEGylation

Carlos Sáenz Ezquerro, *[a] José Manuel García Aznar [b] and Manuel Laspalas [a]

Polymer/silica (PS) nanocomposites are, among numerous combinations of inorganic/organic nanocomposites, one of the most important materials reported in the literature and have been employed in a wide variety of applications. Due to this great interest in the scientific and industry community, knowledge about their physiochemistry allows for a better understanding of their development and improvement. One area of interest found in biopolymers is silica, where silica nanoparticles can be used to increase their mechanical properties and give them higher opportunities to replace synthetic plastics. With this aim in mind, molecular dynamics (MD) simulations were used to predict the structure and mechanical properties of the interphase region and nanocomposite systems of polycaprolactone (PCL), a common poly(hydroxy acid) type biopolymer, reinforced with silica nanoparticles. Two types of nanoparticles were studied to assess the effect of PEGylation: hydroxyl (ungrafted) and polyethylene glycol (PEG) (grafted or PEGylated) functionalized silica. The interaction energy between the nanoparticle and the polymeric matrix was determined, showing an increase of the affinity between each component due to the PEGylation of the nanoparticle. Through the analysis of polymer density profiles, the structure and thickness of the interphase region were determined, and it was observed that PEGylation increased the interphase thickness from 10.80 Å to 13.04 Å while it decreased the peak and average polymer density of the interphase region. Using compressed and expanded molecular models of the neat PCL polymer, the mechanical properties of the interphase region were related to its density through an interpolation model, and mechanical property profiles were obtained, from which the average values of the Young's modulus, Poisson's ratio and shear modulus of the interphase region were calculated. Finally, the mechanical properties of the nanocomposites were determined by molecular mechanics simulations, showing that the silica nanoparticles increased the stiffness of the composite system to about 7–8% with respect to that of the neat polymer, having a 2.09% weight of bare silica or 2.82% weight of PEGylated silica. PEGylation did not show an additional effect on the overall mechanical properties. A mean field micromechanics model (Mori–Tanaka) corroborated the properties calculated for the interphase region using MD simulations. It was concluded that the PEGylation of the nanoparticle improved the affinity, and thus the dispersion, of the silica nanoparticles towards the PCL matrix, but with no further increase in the mechanical properties of the composite.

Received 21st December 2021,
Accepted 8th March 2022

DOI: 10.1039/d1sm01794b

rsc.li/soft-matter-journal

## 1. Introduction

Nanoparticle reinforced polymeric composites have generated considerable attention among materials scientists and engineers due to their potential of producing superior physical, chemical, and mechanical properties. The influence of nano-scale size fillers on elastic properties is, however, somewhat surprising because this type of effect is not observed in conventional composite materials.[1] The presence of nanoparticles introduces an enormous amount of interfacial area, in which polymer chains undergo conformational changes and deformations at the nanoscale.[2,3] The interfacial contact between the polymer and nanoparticle manifests itself as a perturbation of the structure (*e.g.*, density,

[a] *Aragon Institute of Technology ITAINNOVA, María de Luna 7-8, Zaragoza 50018, Spain. E-mail: csaenz@itainnova.es; Tel: +34-976-011-868*
[b] *Aragon Institute of Engineering Research (I3A), University of Zaragoza, Zaragoza 50018, Spain*

 

chain orientation or arrangement) and the dynamics of the polymer.[4–6] This region of altered polymer properties is commonly termed as the interphase in the literature.

The polymer molecules near the surface of such nano-scale fillers experience a series of physical changes in comparison with the properties of those in the bulk region far from the filler surface.[7] Slower internal dynamics, with reduced or negligible diffusion of the molecules absorbed onto the surface,[8] have been reported, with the formation of a glassy polymer layer.[9] This nanometric confinement of polymers usually undergoes a change in the glass transition temperature ($T_g$) of such confined molecules[10,11] and also experiences a higher degree of heterogeneity compared to the molecules in the bulk region.[12]

The magnificent reinforced properties of nanocomposites cannot been explained or predicted from standard continuum mechanics mean field models.[13–16] The influence of the interphase on the mechanical properties of the composite is specially critical when the reinforcement is in the nanoscale dimension,[17,18] which cannot be considered with standard two-phase micromechanics models. Recently, new formulations of these analytical models for nanoscale size inclusions have been developed, in which surface/interphase effects become important.[19,20] In these extended analytical models, the interphase is considered as a third phase, with a mechanical behavior different from that of the bulk polymer.[21] Several studies have shown better performance of these three-phase models with respect to the related two-phase model in the determination of the mechanical properties of nanoreinforced polymers,[22–25] but then the main modelling difficulties are focused on the representative properties of this interphase to be introduced in the model.

The experimental characterization of polymer surfaces and interphases in many cases requires special techniques, such as $^1$H NMR spectroscopy,[7,9] neutron scattering[26–28] or DSC calorimetry,[29] and others,[30] and often only a combination of different techniques could be helpful.[31] To date, the accuracy and repeatability of basic force/displacement measurements taken by probe microscopy (a technique which made possible for the first-time imaging and manipulation of materials at the level of individual atoms) have been a subject of debate. Because of this uncertainty, it appears that accurate and quantitative material testing is currently limited to devices that resolve only down to the microscale ($10^{-6}$ m).[32] In addition, since the different methods probe chain dynamics or derived quantities in different ways, a certain level of disagreement between the different results is not surprising.[7] Due to the difficulties in the experimental characterization of the interphase region, the most appealing strategy is to estimate the properties of this region by atomistic simulation techniques, such as molecular dynamics (MD)[33] or related coarse-graining (CG) approaches.[34] A majority of previous studies have focused on the characterization of carbon nanotube–polymer reinforcements,[24,35,36] although in recent years great effort has been made to model nanoclay and nanoparticle-reinforced nanocomposites.[4,5,22,37,38] Through molecular modelling, it is possible to assess the effect of chemical modification on the properties of materials without additional experiments. The properties of the interphase region are influenced dramatically by their composition and types of chemical groups that are present.[28] The grafting of molecules on the surface of one of the two components involved in the interphase is one way to modulate the properties of this region through the introduction of new chemical groups, and the reinforcement effect of nanoinclusion can be tuned by modifying the filler–polymer interfacial properties.[39,40]

A particular group of materials that have attracted a lot of attention in recent years is biopolymers.[41] These materials encompass a broad band of applications such as food packaging,[42,43] medical devices,[44] tissue engineering,[45] coatings[46] and others.[47] Nevertheless, the strength, stability and other mechanical attributes of biopolymers are lower compared to those of synthetic or petroleum-based polymers.[41] An alternative to compensate for these properties of biopolymers is to enhance their performance through the addition of micro- or nano-reinforcements. Among the numerous types of fillers, silica nanoparticles were found to be useful candidates for improving the mechanical performance of polymeric materials.[48] Silica nanoparticles are found in a variety of forms (*e.g.* amorphous, crystalline, porous, non-porous, *etc.*)[49] and are characterized by a large surface area, ease of functionalization[50] and biocompatibility.[51] Silica reinforced composites have been employed in medical equipment,[52–54] flame-retardant materials,[55,56] optical devices, photo-resistant materials, proton exchange membranes and chemosensors.[57,58] Besides, the surface modification of silica nanoparticles *via* chemical grafting of polymers or oligomers[59] has been reported to lead to a stronger interaction between the nanosilica and the matrix to bring a tuneable interfacial interaction.[60] Thus, considering the increasing interest in biopolymers and their related reinforced composites, in the present study, full atomistic models of silica nanoparticles dispersed in the polycaprolactone matrix (PCL) were modeled to predict the structure and mechanical properties of the interphase region. In fact, two types of nanoparticles were studied, ungrafted and PEGylated, in order to assess also the effect of surface modification of silica nanoparticles *via* PEGylation, as a representative chemical grafting modification of the surface of the silica nanoparticle, on the interaction energy and mechanical properties using classical MD simulations.

## 2. Methodology

The simulation methodology consisted of modeling, equilibration and further characterization of different molecular systems. A summary of the methodology is shown in Fig. 1. Briefly, in the first step, the PCL polymer chain and the silica crystalline network, from which the ungrafted and PEGylated nanoparticles were generated, were modelled atomistically. These components were combined to obtain the neat PC and nanocomposite RVE models, which were later equilibrated and finally characterized to determine their interaction energy, density profiles and elastic constants.

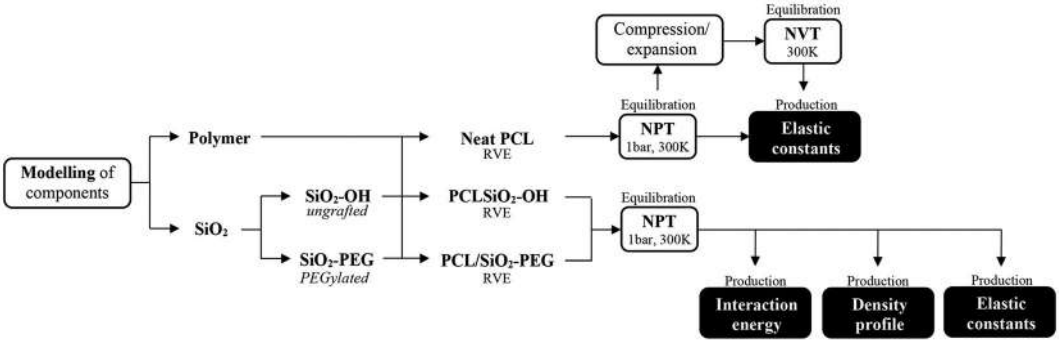


Fig. 1 Summary of simulation methodology.

### 2.1. Modeling of relaxed systems

Full atomistic models of polymer nanocomposites were developed by the inclusion of silica nanoparticles (grafted and ungrafted) in a PCL matrix. First, the neat polymeric matrix of PCL was modeled by equilibrating 160 chains with a degree of polymerization of 20 in a cubic cell. The molecular weight of 2284.9 Da for these molecules represented a low molecular weight PCL according to commercial grades of PCL polymers.[61,62] The structure of the monomer is shown in Fig. 2, which also includes the partial charges of the atoms. The initial geometry of the monomer and the partial charges of the atoms were obtained by molecular mechanics optimization using the MMF94 force field.[63] These charges were later adjusted in order to obtain a neutral polymer molecule. Initially, fully spread polymer chains were put on a simulation cell and allowed them to move freely in a canonical ensemble (*NVT*) at 300 K for 100 ps. After this initial simulation, a constant pressure–constant temperature (*NPT*) algorithm was subsequently applied for 300 ps in order to adjust the volume of the system under conditions of 300 K and 1 atm and obtained a relaxed state model of the neat polymer. The time step was fixed at 1 fs and periodic boundaries were applied to a cell box. MD simulations were performed using the LAMMPS simulation package[64] and the parameters for atom stretching, bending, torsion and van der Waals interactions were taken from the AMBER[65] or OPLS-AA force field.[66] The silica parameters were obtained from the PCFF force field[67] and the reference study by Lopes *et al.*[68]

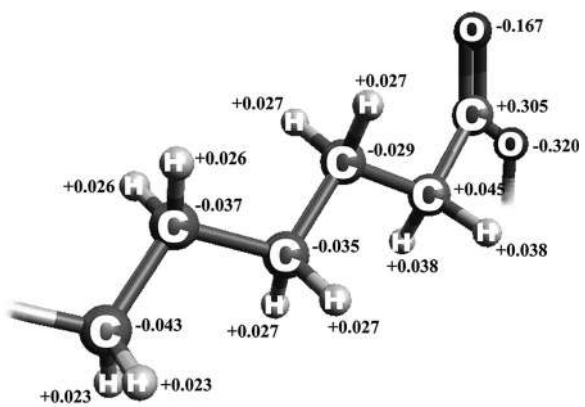


Fig. 2 Optimized geometries of the monomer and atomic partial charges (values in eV).

The silica core was constructed from a lattice of crystalline silica following a strategy similar to that described in the study of Ndoro *et al.*[4] The crystalline lattice of silica ($SiO_2$) was obtained by replication of a unit cell of α-quartz over three dimensions and later equilibrated by time integration first under the *NVT* ensemble at 300 K for 100 ps and subsequently under the *NPT* ensemble at 300 K and 1 atm for 300 ps. To construct a nanoparticle of 1 nm radius and center located at the central point within this lattice, all silicon atoms lying outside this sphere were initially removed. All oxygen atoms that were not connected to the retained silicon atoms were also removed and that the oxygen atoms remaining at the surface were saturated with hydrogen to satisfy their chemical bonding, which created silanol groups (Si–O–H) over the surface of the nanoparticle. This initial adjustment of the silica core surface rendered the ungrafted nanoparticle ($SiO_2$–OH). This nanoparticle was equilibrated again under the *NVT* ensemble at 300 K to allow the silica atoms to accommodate the new geometry. Grafting of polyethylene glycol (PEG) chains on the silica surface was performed by replacing some of the hydrogen atoms of silanol groups randomly located over the surface of the nanoparticle, which gave place to new Si–O–C bonds. A total of 8 PEG chains with a degree of polymerization of 8 were grafted, which supposed a grafting density of 0.80 chain per $nm^2$, a typical value found in experimental PEGylated silica nanoparticles,[69–71] and this nanoparticle was identified as $SiO_2$–PEG. This nanoparticle was equilibrated only once and it was embedded in the PCL matrix to avoid the PEG chains to take the mushroom (*i.e.*, ball-shaped) conformation.[70] The initial charges of the silicon and oxygen atoms in the crystalline lattice of +1.02 and −0.51 eV, respectively, were later adjusted to ensure a sum of zero over all nanoparticle atoms both in $SiO_2$–OH and $SiO_2$–PEG. Fig. 3 shows the pictures of rendered images of the modeled nanoparticles.

Nanocomposites of grafted (PCL/$SiO_2$–OH) and PEG-grafted (PCL/$SiO_2$–PEG) silica were obtained by the inclusion procedure. This was performed by creating a cavity in the midst of the neat polymer displacing the polymer chains and inserting the nanoparticle. The weight fractions of the nanoparticle in the modeled composite system were 2.09% for PCL/$SiO_2$–OH and 2.82% for

 

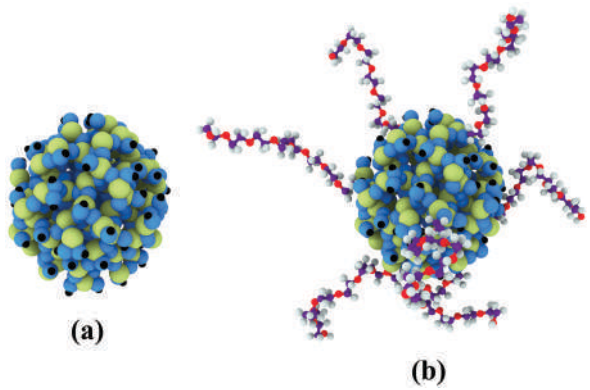


Fig. 3 Partial models of (a) ungrafted ($SiO_2$–OH) and (b) PEG-grafted silica ($SiO_2$–PEG) nanoparticles.

PCL/$SiO_2$–PEG. These hybrid organic–inorganic systems were equilibrated by applying first a time integration under the canonical (*NVT*) ensemble for 100 ps at 300 K, in which the nanoparticle atoms (including PEG chains in the case of the $SiO_2$–PEG nanoparticle) were initially kept frozen. Later, the nanoparticle atoms were allowed to move and the full nanocomposite system was again time integrated under the *NVT* ensemble for 100 ps. Finally, these systems were time integrated under the isothermal–isobaric (*NPT*) ensemble for 300 ps at 300 K and 1 atm to obtain relaxed systems. In the case of the PCL/$SiO_2$–PEG system, the conformation of the PEG chains within the polymer was mainly brush (*i.e.* extended chains), since this nanoparticle was not equilibrated in the isolated state as was explained before.[70] The fully relaxed molecular models of nanocomposites are shown in Fig. 4. A partial slice of the cell box was performed in these pictures to better show the inserted nanoparticle.

### 2.2. Method for calculating the interaction energy

The interaction energy defines the energy of a system involved in the interaction between its components (in terms of its potential energy). In the material systems studied, here, these components are PCL and silica nanoparticles (ungrafted or PEG-grafted). This interaction energy ($E_i$) can be calculated by considering the energy of the system and the energy of the isolated components as indicated below:

$$E_i = E_{total} - (E_{PCL} + E_{SiO_2}) \quad (1)$$

where $E_{total}$ is the potential energy of the whole system, $E_{PCL}$ is the energy of the PCL polymer matrix without the silica nanoparticle and $E_{SiO_2}$ is the energy of the silica nanoparticle without the polymer matrix, both calculated within the nanocomposite system. In the case of the PEGylated silica nanoparticle ($SiO_2$–PEG), PEG chains were also included for the calculation of the $E_{SiO_2}$ term. The potential energy has contributions from bonds, angles, dihedrals, and van der Waals and Coulombic interactions.

### 2.3. Method for generating density profiles

Once the relaxed atomic models were obtained, production runs for generating density profiles of the polymer around the nanoparticle were conducted in the first place. For this purpose, it was necessary that the nanoparticle silica core atoms were fixed in its position, which indicate freezing of the silica core atoms. It should be noted that the fluctuations of atoms due to thermal vibrations (*i.e.*, the vibration of bonds and angles) would have introduced uncertainty in the radial profiles since the surface of the nanoparticle would have not been exactly at the same distance from the center of the simulation cell due to these deviations at each time step. Simulations at 300 K using an *NVT* algorithm were then carried out for 50 ps, while sampling the atomic coordinates every 10 ps (10 000 time steps). The radial density profiles were then calculated by sorting the atoms into spherical bins of thickness 0.32 Å around the silica nanoparticle and averaged through every sampled time step. Silica core atoms were not included in the density analysis. In the case of the neat PCL system, the sorting of atoms was performed using orthogonal bins of thickness 0.32 Å parallel to the $Z$ direction of the simulation box.

### 2.4. Method for calculating elastic constants

The mechanical properties of the neat polymer and nanocomposites systems were evaluated by performing deformation simulations from which stress–strain relationships were evaluated. The method was based on molecular mechanics.[72,73] The resulting stress–strain responses were used to determine the engineering constants of the equivalent continuum material under the scope of linear elasticity (*i.e.*, at small strains). For any linear elastic material, the stiffness matrix in a contracted

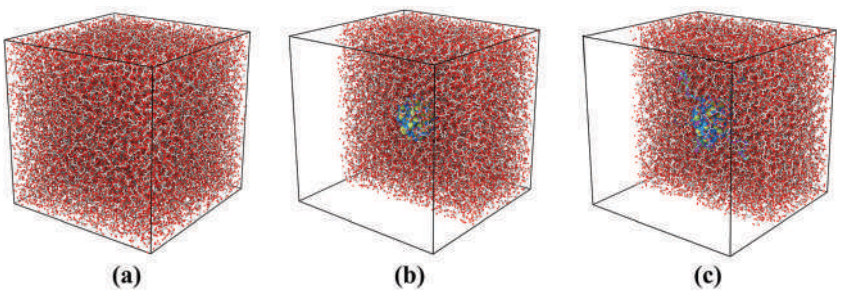


Fig. 4 Atomistic models of the (a) neat polymer, (b) polymer matrix with an inclusion of PCL/$SiO_2$–OH (ungrafted) and (c) polymer matrix with an inclusion of PCL/$SiO_2$–PEG (grafted).

notation is written as

$$C = \begin{pmatrix} C_{11} & C_{12} & C_{13} & C_{14} & C_{15} & C_{16} \\ C_{21} & C_{22} & C_{23} & C_{24} & C_{25} & C_{26} \\ C_{31} & C_{32} & C_{33} & C_{34} & C_{35} & C_{36} \\ C_{41} & C_{42} & C_{43} & C_{44} & C_{45} & C_{46} \\ C_{51} & C_{52} & C_{53} & C_{54} & C_{55} & C_{56} \\ C_{61} & C_{62} & C_{63} & C_{64} & C_{65} & C_{66} \end{pmatrix} \quad (2)$$

where $C_{ij}$ are the stiffness coefficients related to $i$ stress with the $j$ strain components. In materials with symmetries expressed in their principal axis system (*i.e.*, isotropic, orthotropic), this stiffness matrix simplifies and some of the coefficients are equal to zero, being only part of the remaining coefficients independent (*i.e.*, 9 independent coefficients for an orthotropic material and 2 for an isotropic one). For an orthotropic material, the stiffness matrix would take the form

$$C = \begin{pmatrix} C_{11} & C_{12} & C_{13} & 0 & 0 & 0 \\ C_{12} & C_{22} & C_{23} & 0 & 0 & 0 \\ C_{13} & C_{23} & C_{33} & 0 & 0 & 0 \\ 0 & 0 & 0 & C_{44} & 0 & 0 \\ 0 & 0 & 0 & 0 & C_{55} & 0 \\ 0 & 0 & 0 & 0 & 0 & C_{66} \end{pmatrix} \quad (3)$$

The calculation of the elastic stiffness matrix by means of molecular mechanics simulations was carried out considering a static or equilibrium approach.[73] After obtaining relaxed structures by applying time integration simulations under the isothermal–isobaric assembly (*NPT*), the structures were subjected to a set of 6 types of deformation cycles (three uniaxial tension and compression pairs, and three pure shear pairs), controlled by the corresponding strain vectors, with the deformed component taking a chosen small value while the other components of the vector were kept fixed at zero (*i.e.* changing one cell parameter while maintaining the rest of the cell parameters fixed), and applying a minimization after each deformation stage without changing the cell parameters (see Fig. 5). The deformation was applied in cycles of positive and negative deformation increases, with an amplitude of 0.003 (0.3%) up to a total deformation of 0.009 (0.9%). The minimization of the structures was performed using the FIRE method (fast inertial relaxation engine)[74] for 10 000 iterations. The response of the system at each state of deformation was sampled in terms of stress during the equilibration time after the initial 6 ps, where the system was allowed to relax, and was defined in the form of virial stress as,

$$\sigma_{ij} = -\frac{1}{V}\sum_{k}\left(m^k u_i^k u_j^k\right) + \frac{1}{2}\sum_{l\neq k}\left(r_i^{kl}\right)\left(f_j^{lk}\right) \quad (4)$$

where $V$ is the total volume of the system of atoms, $m^k$ and $u^k$ denote the mass and velocity of the $k$-th atom, respectively, $r^{kl}$ refers to the distance between the $k$-th and $l$-th atoms, and $f^{kl}$ is the force exerted on the $l$-th atom by the $k$-th atom. The first term in the virial equation is related to the kinetic energy of the atoms, while the second is related to the potential energy (forces exerted between the atoms). Under static conditions, which was the approximation considered here, the first term has no contribution to stress. Each component of the stiffness matrix was obtained from the slope of the stress *versus* the strain plot for each $\sigma_{ij}$ component of the virial stress. Due to the symmetry of the systems under a study (*i.e.* spherical nanoparticles), it was expected an isotropic behavior, but this condition was not imposed and only an orthotropic material was initially assumed. Then, the compliance matrix $S$ which was obtained by the inversion of the stiffness matrix $C$ as

$$S = C^{-1} = \begin{pmatrix} 1/E_{11} & -\nu_{12}/E_{11} & -\nu_{13}/E_{11} & 0 & 0 & 0 \\ -\nu_{21}/E_{22} & 1/E_{22} & -\nu_{23}/E_{22} & 0 & 0 & 0 \\ -\nu_{31}/E_{33} & -\nu_{32}/E_{33} & 1/E_{33} & 0 & 0 & 0 \\ 0 & 0 & 0 & 1/G_{23} & 0 & 0 \\ 0 & 0 & 0 & 0 & 1/G_{31} & 0 \\ 0 & 0 & 0 & 0 & 0 & 1/G_{12} \end{pmatrix} \quad (5)$$

where $E_{ij}$, $\nu_{ij}$ and $G_{ij}$ are the elastic modulus, Poisson's ratio and shear modulus. The moduli obtained for each direction were finally compared and the average values were obtained by considering an isotropic behaviour as stated in the following:

$$E = \frac{E_{11} + E_{22} + E_{33}}{3} \quad (6)$$

$$\nu = \frac{\nu_{12} + \nu_{13} + \nu_{21} + \nu_{23} + \nu_{31} + \nu_{32}}{6} \quad (7)$$

$$G = \frac{G_{23} + G_{31} + G_{12}}{3} \quad (8)$$

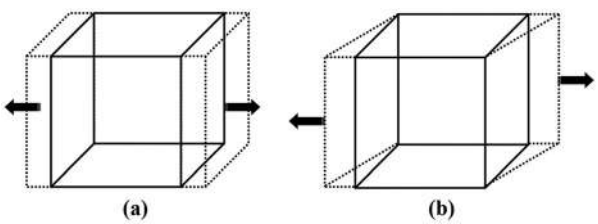


Fig. 5 Schematic diagrams of un-strained (solid line) and strained (dotted line) shapes of the system cell in (a) uniaxial tension and (b) shear deformation simulations.

Table 1 Analysis of density

| Force field | Density (g cm$^{-3}$) | Error[a] (%) |
|---|---|---|
| AMBER | 0.956 ± 0.066 | −16.5 |
| OPLS-AA | 1.057 ± 0.068 | −7.7 |

[a] Experimental value: 1.145 g cm$^{-3}$.

# 3. Results

## 3.1. Selection of the force field

Initially, the modeled neat polymer system was subjected to two types of force fields, AMBER and OPLS-AA, with the aim of assessing the best set of bonded and non-bonded atomic interaction parameters to reproduce polycaprolactone properties. After the *NVT* and *NPT* equilibration stages, the density of the systems under the conditions of 300 K and 1 atm was sampled in a *NPT* simulation and compared with the experimental value (1.145 g cm$^{-3}$ at 300 K). This is shown in Table 1. Although in both force fields the density of neat polycaprolactone was underrated, the best prediction in the density was obtained with the OPLS-AA force field which gave a result of 1.057 g cm$^{-3}$ and which supposed a deviation from the experimental value of −7.7%. The AMBER force field resulted in a deviation of −16.5% from the experimental value, which is higher than that with the OPLS-AA force field. Odegard *et al.*[75] also found better performance of OPLS-AA in comparison with the AMBER force field in the mechanical properties of polyimide; so, considering these results, the OPLS-AA force field was applied in subsequent simulations.

## 3.2. Interaction energy

The interaction energy between the PCL matrix and silica nanoparticles is summarized in Table 2. The van der Waals and Coulombic components of the interaction energy have also been calculated. The results are given in either absolute values or normalized by the area involved in the interaction. This area was calculated as the surface of the silica nanoparticle determined using the surface mesh tool from the OVITO software, considering only the silica core atoms, which is based on the alpha-shaped algorithm.[76,77] The ungrafted ($SiO_2$–OH) and grafted nanoparticles showed a favorable or attractive interaction towards the PCL polymer, as indicated their negative values of the interaction energy. It was observed that, in both types of nanoparticles, the van der Waals component was dominant over the Coulombic (electrostatic) interactions. Besides, the grafting of PEG chains in the silica nanoparticle increased the interaction energy due to a drastic increase of the van der Waals component. These results indicated thus that PEGylation increases the interaction between the PCL polymer matrix and the nanoparticle. MD studies in the literature also showed a favorable interaction between PCL and ungrafted silica nanoparticles.[78] In the same way, several studies have demonstrated that the grafting of polymers in silica nanoparticles improved the miscibility and dispersion of silica nanoparticles within the polymeric matrix,[59,79] which would be in agreement with the increase of the interaction energy found due to the grafting of PEG chains in the present study.

## 3.3. Polymer density around nanoparticles

The polymer density profiles for neat PCL and silica nanocomposites are shown in Fig. 6. Silica atoms (Si, O and H) were not included in the profiles, although, in the case of the PCL/$SiO_2$–PEG composite, two profiles with and without PEG chain atoms were obtained for comparison. In this way, PEG chains could be considered as a part of the polymer. The neat polymer exhibited a constant density throughout the simulation box, with deviations from a mean value of 1.057 g cm$^{-3}$ due to the thermal vibrations of the atoms. When a silica nanoparticle, grafted or ungrafted, was inserted within the polymer, the polymer density was perturbed from that encountered in the neat system or the bulk polymer matrix. With both the ungrafted (PCL/$SiO_2$–OH) and grafted (PCL/$SiO_2$–PEG) silica nanoparticles, it was observed that the polymer tended to accumulate around the nanoparticle in the form of dense layers. This behavior was similar to those found in previous studies with polymer–silica hybrids[4,5,37,38] and resembles the behavior of a fluid that wets a surface reasonably well.[80] In the region immediately in contact with the nanoparticle (at distances around 12.5 Å), a layer of the polymer with the highest density was found, with peaks of density of 1.810 g cm$^{-3}$ and 1.588 g cm$^{-3}$ for the ungrafted and grafted systems, respectively. After this dense layer of the polymer, a region of depletion of the polymer was observed at distances close to 15 Å, with density values lower than those of the bulk matrix or the neat polymer, where there is no nanoparticle effect. In the PCL/$SiO_2$–PEG system, it was observed that the density profile was very similar in form and changes were minor when including and not including the PEG chains in the radial profiles, except that a little higher increase in the density was observed when including PEG chains. Previously, it was obtained that the PEGylation of the silica nanoparticle increased the interaction energy between the nanoparticle and the PCL polymer, but this fact did not reflect in a higher polymer density around the PEGylated nanoparticle compared to the ungrafted one. Smith *et al.*,[37] who studied the effect of functionalization of silica nanoparticles with trimethylsiloxane (TMS) moieties in the poly(dimethylsiloxane) (PDMS) density,

Table 2 Interaction energy between nanoparticles and PCL

| | | | van der Waals component | | Coulombic component | |
|---|---|---|---|---|---|---|
| Interaction | $E_i$, (J 10$^{-18}$) | $E_i$, (J m$^{-2}$) | J m$^{-2}$ | % | J m$^{-2}$ | % |
| PCL/$SiO_2$–OH | −5.32 ± 0.22 | −0.412 ± 0.017 | −0.332 ± 0.012 | 81 | −0.080 ± 0.005 | 19 |
| PCL/$SiO_2$–PEG | −8.09 ± 0.14 | −0.633 ± 0.017 | −0.546 ± 0.016 | 86 | −0.087 ± 0.006 | 14 |

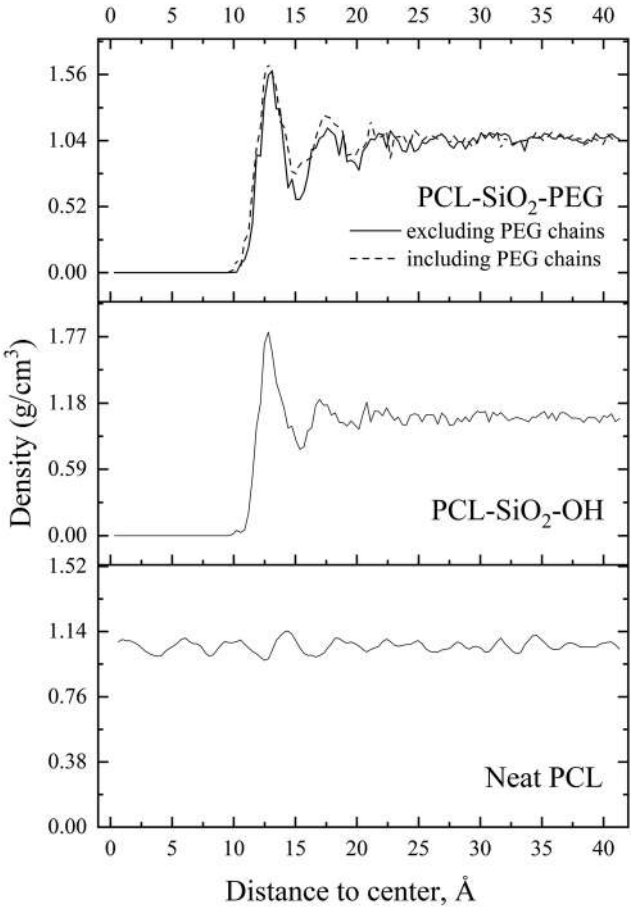


Fig. 6 Radial density profiles of the polymer around the nanoparticle for neat PCL and nanocomposites.

obtained similar results. It should be considered that the presence of the PEG chains in the interphase region (in the form of extended chains) occupies a part of the volume of this region, so that the PCL chains would have a certain degree of steric hindrance to get close to the silica surface.

The polymer density profiles were also analyzed and splitted into atomistic C, H and O profiles, as shown in Fig. 7. From these profiles, the affinity of the nanoparticle to a certain type of element can be deduced. This affinity was calculated in terms of the relative density of the peak with respect to the bulk matrix where the nanoparticle had no influence. These values of the relative peak density are summarized in Table 3. For the PCL/$SiO_2$–OH system, it was observed that the affinity of the silica nanoparticle was specially high to carbon and oxygen atoms, whereas there was no appreciable affinity to hydrogen. In this sense, note that a relative density of hydrogen of 1.13 indicated that the density of this element near the nanoparticle surface was nearly the same than that at the bulk matrix. From these atomistic profiles, the presence of a little peak in the oxygen density at 10.24 Å was striking, which indicated that a small fraction of the oxygen atom was in close contact with the silica surface and at the same depth than hydroxyl groups. The greater affinity to the oxygen and carbon atoms of the silica nanoparticle was repeated in the PEG grafted nanoparticle, although, in this case, the peak density values were lower than those of the ungrafted nanoparticle due to the steric hindrance effect of the grafted PEG chains. When considering the PEG atoms to the density, changes were minor and the same tendency was observed. Note that the increase in the relative density of oxygen was due to the higher content of this element in PEG chains than that in the PCL polymer. These results would suggest that higher oxidized polymers, *i.e.* with a greater content of oxygen or a lower content of hydrogen, would have higher affinity to silica nanoparticles, either bare or PEGylated. Several experimental studies found that bare silica fillers interacted favorably with polymers capable of acting as hydrogen bond acceptors,[8] supporting the results found here.

From the polymer density profiles, the interphase thickness could also be determined following a statistical procedure based on the accumulated standard deviation (ASD) of the density profiles.[81] Briefly, the ASD calculation is based on the fluctuations that occur in the polymer density and is calculated as shown in the following formula:

$$\mathrm{ASD}(d) = \sqrt{\frac{\sum_{d}^{h} (\rho(d) - \bar{\rho})^2}{n-1}}; \quad h > d \tag{9}$$

where $d$ is the distance with respect to the center of the silica nanoparticle, $h$ is the highest distance defined in the profile (*i.e.*, a cutoff distance), $\rho(d)$ is the density at a distance $d$, and $\bar{\rho}$ is the average density in the interval of distances ($d$, $h$). When the ASD was plotted *versus* the distance center of the nanoparticle, the profiles were obtained as shown in Fig. 8. As can be observed from these profiles, at sufficiently high distances, the ASD remained constant at the value of the bulk matrix, but, when approximating to the nanoparticle at lower distances, the ASD started to increase due to the influence of the nanoparticle. The distance at which this increase was produced was defined as the interphase upper limit, as have been pointed out in the profiles shown in Fig. 8. This point was calculated quantitatively considering the statistical deviations of the ASD at the bulk region by defining the critical value of the ASD as

$$\mathrm{ASD}_{\mathrm{critical}} = \overline{\mathrm{ASD}}_{\mathrm{bulk}} + \sqrt{\frac{\sum_{\mathrm{bulk}} \left(\mathrm{ASD}(d) - \overline{\mathrm{ASD}}\right)^2}{n-1}} \tag{10}$$

where $\overline{\mathrm{ASD}}_{\mathrm{bulk}}$ is the average ASD observed at the bulk region (*i.e.*, at distances far enough from the nanoparticle surface) and the ASD(d) refers to the value of the ASD at a distance $d$ in this bulk region. The second term in eqn (9) considered thus the fluctuations of the ASD in the bulk region due to statistical noise, and the distance at which the ASD($d$) was higher than this $\mathrm{ASD}_{\mathrm{critical}}$ was defined as the interphase upper limit. On the other hand, the interphase thickness was calculated considering the nanoparticle surface at 10 Å as the lower interphase limit. The interphase thickness values are shown in Table 4. The interphase thickness of the PCL/$SiO_2$–OH composite was 10.80 Å, which was similar to other reported values in either

 

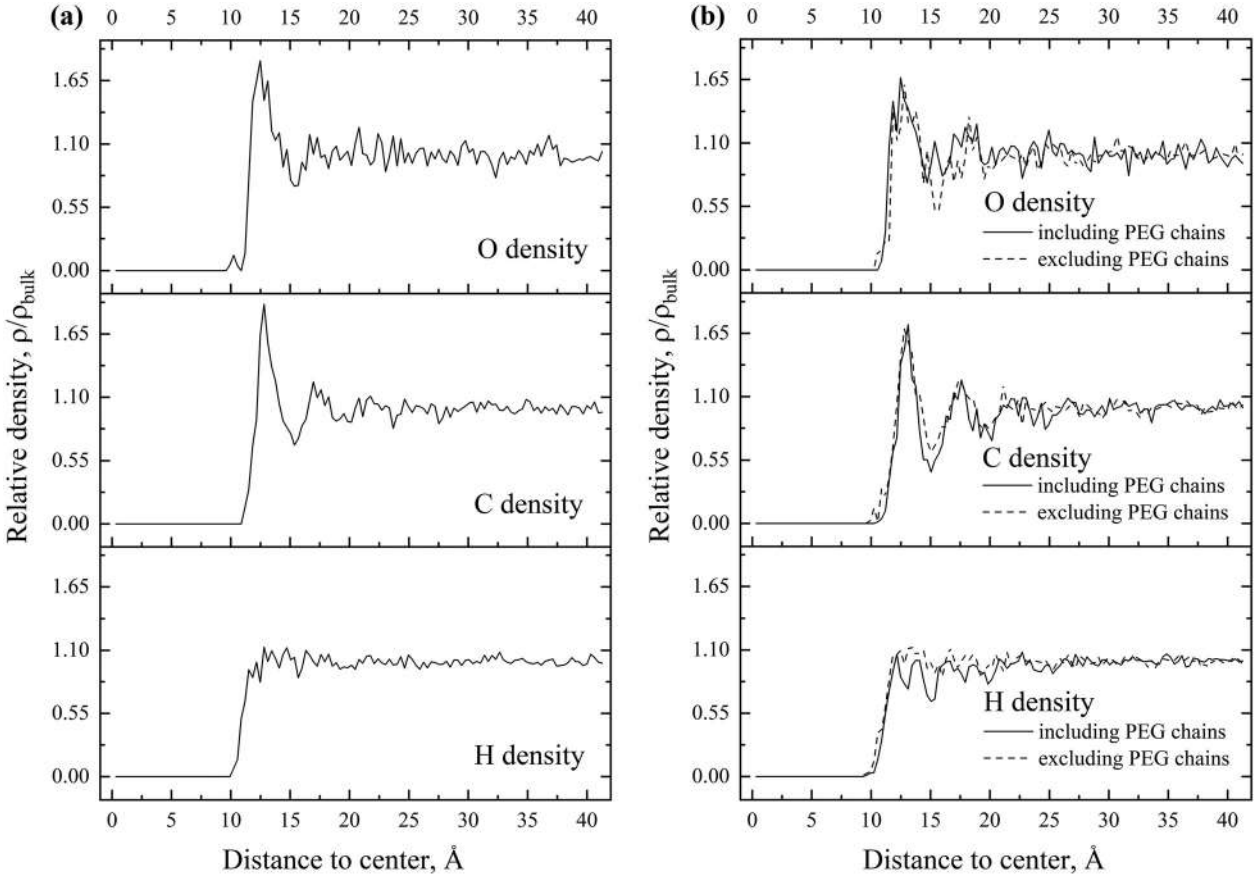


Fig. 7 Radial density profiles of elements around the nanoparticle for (a) PCL/$SiO_2$–OH and (b) PCL/$SiO_2$–PEG composites.

Table 3 Relative peak densities in nanocomposites (with respect to the bulk matrix density, $\rho_{peak}/\rho_{bulk}$, unitless)

| | | Relative peak density, $\rho_{peak}/\rho_{bulk}$ | | | |
|---|---|---|---|---|---|
| System | | Polymer | Carbon (C) | Hydrogen (H) | Oxygen (O) |
| PCL/$SiO_2$–OH | | 1.72 | 1.91 | 1.13 | 1.82 |
| PCL/$SiO_2$–PEG | Excluding PEG chains | 1.52 | 1.73 | 1.08 | 1.62 |
| | Including PEG chains | 1.56 | 1.68 | 1.13 | 1.67 |

theoretical[22] or experimental[7] studies for the polymer–silica interphase thickness. For the PCL/$SiO_2$–PEG composite, the interphase thickness extended to 13.04 Å when PEG chains were considered in the analysis, which was higher than that of the ungrafted nanocomposite. These results of the interphase thickness are in the range of values obtained in the literature *via* MD simulations.[82] If PEG chains were not considered in the analysis, this value was lower (12.08 Å) than that observed including PEG chains but higher than that in the ungrafted nanoparticle. For further analysis, it would be more realistic to consider the value including PEG chains since they form a part of the interphase region. From these profiles of the accumulated SD, it was even possible to observe the layer structure of the polymer near the nanoparticle surface, as was evidenced from the presence of successive steps in the region between 10 and 20 Å from the nanoparticle center. It was possible to identify between 2 and 3 layers of polymer in each nanocomposite system, as have been identified in Fig. 8. The average value of the polymer density in the interphase region was also calculated from the polymer density profiles considering the interphase thickness, as shown in Table 4. The average density was lower than that of the bulk polymer matrix due to the existence of the van der Waals gap between the nanoparticle and PCL and fluctuations of the density in the interphase region.

### 3.5. Elastic mechanical properties of the interphase through MD simulations

Using the compressed and expanded models of the pure polymer, it was possible to determine the elastic mechanical properties of the PCL polymer as a function of its density. The results of this characterization are plotted in Fig. 9, in which standard deviation bars are also plotted. It was observed that either the Young's ($E$) modulus or shear ($G$) modulus increased

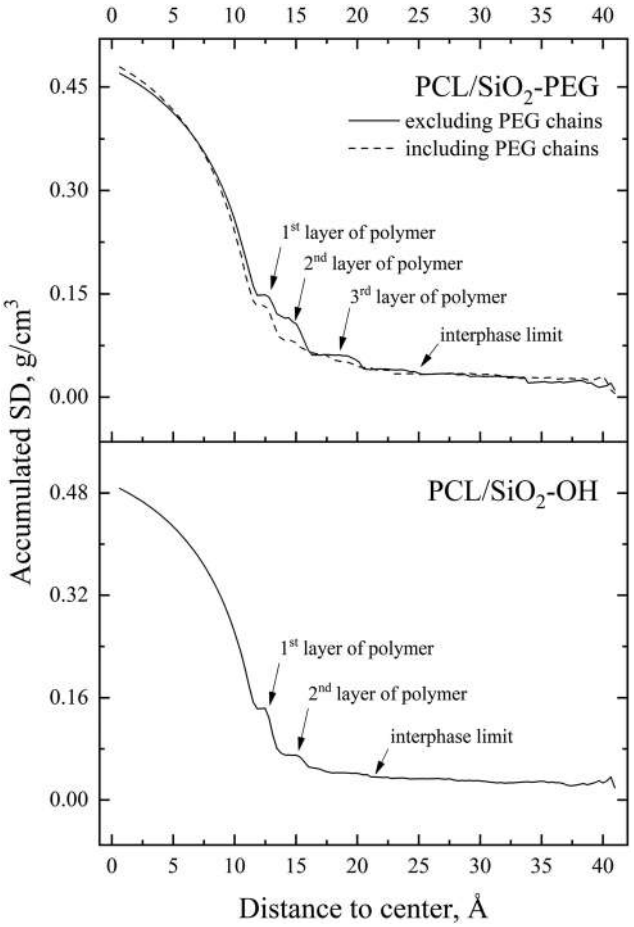


Fig. 8 Accumulated standard deviation (SD) of polymer density profiles.

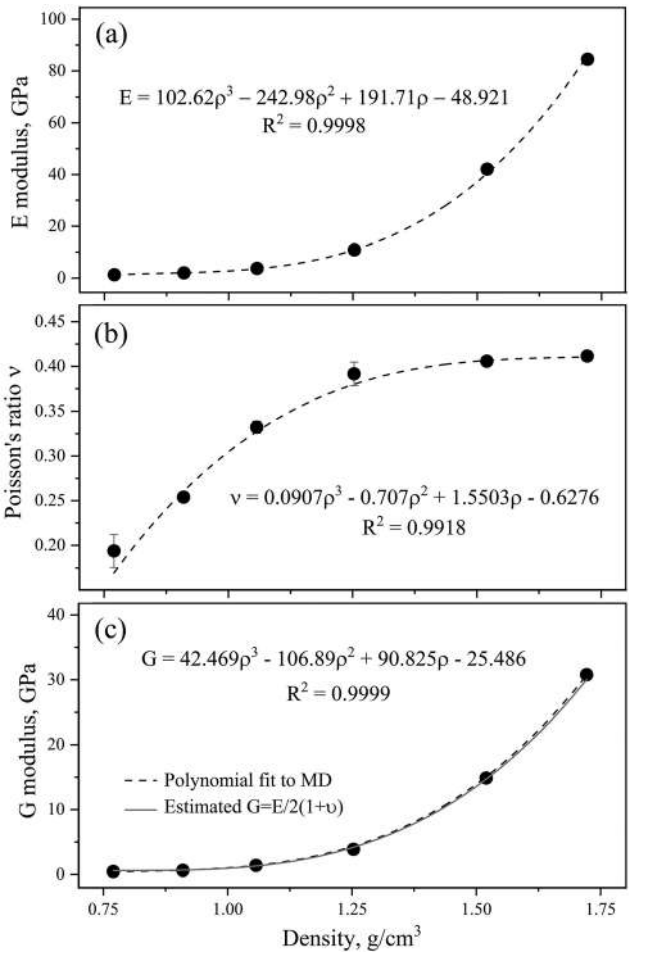


Fig. 9 (a) Young's modulus ($E$), (b) Poisson's ratio and (c) shear modulus ($G$) of the PCL polymer *versus* the density and 3rd order polynomial fitting for a density range between 0.75 and 1.75 g cm$^{-3}$.

Table 4 Average density and thickness of the interphase region

| System | | Density (g cm$^{-3}$) | Thickness (Å) |
|---|---|---|---|
| PCL/$SiO_2$–OH | | 0.98 | 10.80 |
| PCL/$SiO_2$–PEG | Excluding PEG chains | 0.89 | 12.08 |
| | Including PEG chains | 0.99 | 13.04 |

rapidly with the density, while the Poisson's ratio tended to an asymptote at around 0.40. The three plots *versus* density were well fitted to a 3rd order polynomial within the studied range. Herasati *et al.*[25] carried out an equivalent study of nanocomposite models of polyvinylchloride (PVC) with carbon nanotubes (CNT) and obtained the same behavior of the $E$ modulus and Poisson's ratio against the density of the polymer. In Fig. 9c, together with the polynomial fitting curve, the curve for the estimated value of the $G$ modulus was also shown considering an elastic and isotropic behavior, $G = E/2(1 + \nu)$. As it can be observed, the estimated $G$ curve was very close to the polynomial fitting (*i.e.* generated from the MD results), which indicated thus a perfect elastic behavior of the neat polymer within the studied range of density (*i.e.* from 0.75 to 1.75 g cm$^{-3}$). Using the polynomial fitting and density profiles around the nanoparticle, which were previously described, it was possible to generate the corresponding elastic mechanical property profiles as shown in Fig. 10. In the case of the PCL/$SiO_2$–PEG system, a simplification was made and the extrapolation of the density to elastic mechanical properties was made considering that the interphase region was only composed of the PCL polymer (the PEG chains supposed approximately the 10% by the weight of the interphase region). The existence of polymer density peaks in the interphase region was reflected in these elastic mechanical radial profiles as sharp peaks in the case of the Young's and shear moduli, due to the exponential relationship found between these two properties and the density. In the case of Poisson's ratio, the perturbations in the interphase region with respect to bulk matrix properties were of lower magnitude than with the moduli. These profiles revealed in this way the heterogeneity of the interphase region since different properties could be associated depending on its distance to the surface of the nanoparticle. In our study, a homogenization of the properties of the interphase was decided to apply in order to manage with this heterogeneity. Thereby, taking these radial profiles and the interphase thickness determined by the ASD method, as shown in Table 4, the

 

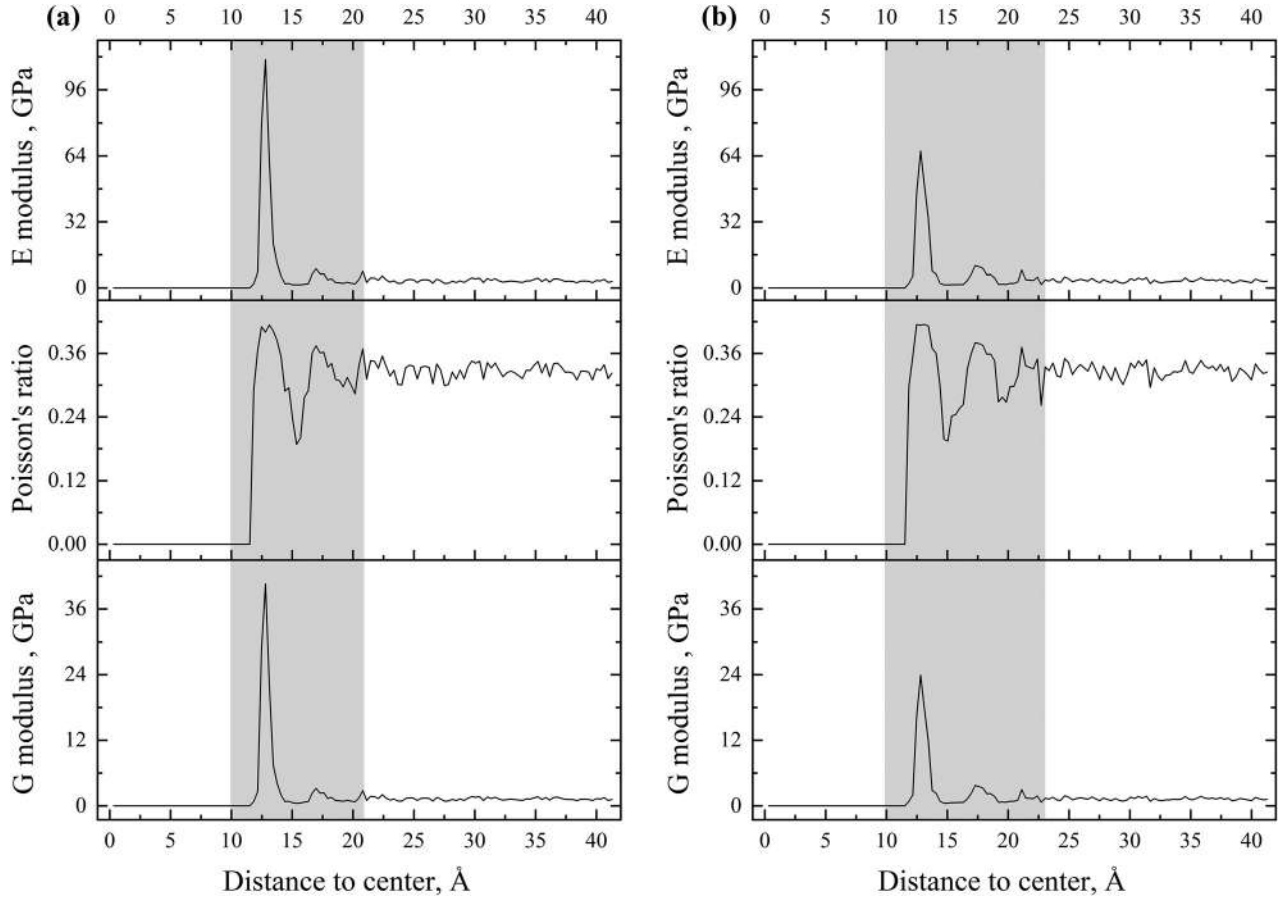


Fig. 10 Radial profiles of the elastic mechanical properties around the nanoparticle in (a) PCL/$SiO_2$–OH and (b) PCL/$SiO_2$–PEG systems (shading indicates the interphase region).

average values of the elastic mechanical properties of the interphase region of nanocomposite systems were estimated. These values were obtained considering weighted averages with respect to the volume of the bins that conformed the interphase region and are summarized in Table 5. In the same way, the properties of the bulk matrix region, far from the nanoparticle surface, were estimated. The interphase region presented thus a clear increase of the rigidity in comparison with the bulk matrix (which presented the same property values as those of the neat PCL polymer), due to the increase observed in the Young's and shear moduli and decrease of the Poisson's ratio. These results reflected the glassy nature of the polymer in the interphase region, because of the perturbation produced by the interaction with the silica nanoparticle. The $E_i/E_m$ relationship would take values of 4.4 and 2.4 for PCL/$SiO_2$–OH and PCL/$SiO_2$–PEG, respectively, which are in agreement with other values found in the literature for silica nanocomposites.[20,82]

Table 5 The average mechanical properties of the interphase region and the bulk matrix in nanocomposites obtained from radial profiles

| System | Region | Young's modulus, $E$ (MPa) | Poisson's ratio, $\nu$ | Shear modulus, $G$ (MPa) |
|---|---|---|---|---|
| PCL/$SiO_2$–OH | Interphase | 8694 | 0.30 | 3135 |
| | Bulk matrix | 3446 | 0.33 | 1251 |
| PCL–$SiO_2$–PEG | Interphase (including PEG chains) | 7313 | 0.30 | 2614 |
| | Bulk matrix | 3519 | 0.33 | 1275 |

### 3.4. Elastic mechanical properties of material systems through MD simulations

The elastic mechanical properties of material systems were obtained from the calculation of the stiffness matrices, which are shown in Fig. 11, whereas results in terms of the elastic constants $E$, $\nu$ and $G$ are summarized in Table 6. The calculated Young's modulus for neat PCL was 3704 MPa, which was higher than the experimental values commonly found in the range of 50–1500 MPa for this polymer.[83–85] Farazin *et al.*,[86] who also studied the mechanical properties of PCL nanocomposites by MD simulations, obtained an elastic modulus of 3.3 GPa, which was close to that obtained in the present study. The situation with the shear modulus was similar to that with the elastic modulus, since the experimental values of the shear modulus were around 500 MPa.[87] Although it was evident that the MD simulations overestimate the elastic and shear moduli in the case of PCL polymers in comparison with the experiments, the aim of MD calculations developed at the present study was to predict relative properties between the different

$$\textbf{(a)}\quad C = \begin{pmatrix} 5.6 & 2.7 & 2.8 & 0.2 & 0.2 & 0.2 \\ 2.7 & 5.4 & 2.7 & 0.1 & 0.2 & 0.1 \\ 2.7 & 2.7 & 5.5 & 0.1 & 0.1 & 0.1 \\ 0.0 & 0.0 & 0.0 & 1.4 & 0.0 & 0.0 \\ 0.0 & 0.0 & 0.0 & 0.0 & 1.4 & 0.0 \\ 0.0 & 0.0 & 0.0 & 0.0 & 0.0 & 1.4 \end{pmatrix}$$

$$\textbf{(b)}\quad C = \begin{pmatrix} 5.8 & 2.8 & 3.0 & 0.2 & 0.2 & 0.2 \\ 2.7 & 5.8 & 2.8 & 0.1 & 0.1 & 0.2 \\ 3.0 & 2.9 & 6.0 & 0.2 & 0.2 & 0.3 \\ 0.0 & 0.1 & 0.0 & 1.4 & 0.0 & 0.0 \\ 0.1 & 0.0 & 0.1 & 0.0 & 1.5 & 0.0 \\ 0.1 & 0.1 & 0.1 & 0.0 & 0.0 & 1.5 \end{pmatrix}$$

$$\textbf{(c)}\quad C = \begin{pmatrix} 5.6 & 2.7 & 2.8 & 0.2 & 0.2 & 0.1 \\ 2.7 & 5.6 & 2.8 & 0.4 & 0.3 & 0.3 \\ 2.8 & 2.8 & 6.0 & 0.2 & 0.2 & 0.2 \\ 0.0 & 0.2 & 0.0 & 1.4 & 0.0 & 0.0 \\ 0.1 & 0.1 & 0.1 & 0.0 & 1.5 & 0.0 \\ 0.1 & 0.1 & 0.1 & 0.1 & 0.1 & 1.5 \end{pmatrix}$$

Fig. 11 Stiffness matrices obtained for the (a) neat PCL, (b) PCL/$SiO_2$–OH and (c) PCL/$SiO_2$–PEG systems.

Table 6 Elastic mechanical properties of nanocomposite systems

| System | Young's modulus, $E$ (MPa) | Poisson's ratio, $\nu$ | Shear modulus, $G$ (MPa) |
|---|---|---|---|
| Neat PCL | 3704 ± 78 | 0.332 ± 0.007 | 1394 ± 19 |
| PCL/$SiO_2$–OH | 3996 ± 39 | 0.325 ± 0.018 | 1479 ± 40 |
| PCL/$SiO_2$–PEG | 3971 ± 195 | 0.314 ± 0.014 | 1475 ± 61 |

nanocomposite systems and the influence of nanoparticle inclusion and nanoparticle PEGylation in the mechanical behavior of PCL. The calculated value for the Poisson's ratio was, in contrast, close to the expected value at around 0.33.[88] The Young's modulus ($E$) and shear modulus ($G$) were increased by 7–8% and 6%, respectively, after the inclusion of both types of silica nanoparticles in the PCL matrix. This stiffening of the composite systems in comparison with the neat polymer also manifested in a decrease of the Poisson's ratio by 2–5% after the inclusion of the nanoparticles. These results showed that the PEGylation of the silica nanoparticle did not have a significant effect on the overall mechanical properties of the nanocomposite models. Although it was observed that PEGylation decreases the stiffness of the interphase region due its lower polymer density; on the other hand, PEGylation increased the interphase thickness due to the higher interaction. Both effects compensated and the overall stiffness of the composite was equivalent as with the non-PEGylated nanoparticle. In Table 7, the elastic modulus of the composites was estimated using the Mori–Tanaka model[14] for an equivalent RVE of the studied composite models, using the values of the E modulus and Poisson's ratio obtained from the MD simulations of the interphase region and matrix region (in the case of the $SiO_2$ particle, a modulus of 70.5 GPa and a Poisson's ratio of 0.17 were used according to the bibliography).[89] As can be observed, this model predicted the same E modulus for each nanocomposite system and corroborated the results obtained from the MD simulations, showing that the properties calculated for the interphase region, either the thickness or mechanical properties, were coherent. Several experimental studies found in the literature confirmed these results in the same way. Calandrelli *et al.*,[90] who studied the mechanical properties of polycaprolactone reinforced with fumed silica (ungrafted silica), found that with nanoparticle reinforcements of 1.0% and 3.0% in weight, the Young's modulus was increased by +13% and +31%, respectively. On the other hand, Moussaif *et al.*[91] studied the reinforcement of PCL composites with PEGylated silica nanoparticles and obtained an increase of +33.3% at 3.0% loading of the nanoparticle, similar to that found for the ungrafted silica nanoparticle by Calandrelli *et al.*[90] These results agreed with the results found in the MD simulations presented here, in the sense that similar increases were found for both types of nanoparticles.

Considering either the results from the MD simulations or the experiments,[59] there is evidence that the PEGylation of silica nanoparticles just improved the dispersion of nanoparticles, which was explained by the higher interaction energy between the nanoparticle and the PCL matrix obtained after the PEGylation of the nanoparticle. Kim *et al.* demonstrated that only for a sufficiently stronger polymer–particle surface interaction strength the presence of particles will result in mechanical reinforcement beyond simple hydrodynamics predictions, due to the better dispersion of the nanoparticles.[9] This means that if the nanoparticles were well dispersed, either the neat nanoparticles or the PEGylated ones would give the same mechanical performance to the composite. Nevertheless, if problems with the dispersion of the silica nanoparticles were detected during the experimental preparation of the composites, the MD simulations have shown that the PEGylation of the nanoparticles would improve its dispersion due to the increase of the interaction energy. In drug delivery studies, PEG coating has demonstrated to shield the surface of the nanoparticles from aggregation, opsonization and phagocytosis,[92] and some authors have found that coatings of PEG even suppressed the adhesion between solid microspheres.[79,93]

Table 7 Estimation of the elastic modulus of composites systems using the Mori–Tanaka model

| System | $SiO_2$ volume ($nm^3$) | Interphase volume ($nm^3$) | Matrix volume ($nm^3$) | Predicted Young's modulus, $E$ (MPa) | Predicted Poisson's ratio, $\nu$ |
|---|---|---|---|---|---|
| PCL/$SiO_2$–OH | 4.19 | 33.51 | 534.09 | 3720 | 0.327 |
| PCL/$SiO_2$–PEG | 4.19 | 47.04 | 520.56 | 3752 | 0.326 |

## 4. Conclusion

Full-atom models of nanocomposite systems made up of ungrafted and PEGylated silica nanoparticles dispersed in the polycaprolactone matrix were developed to study the structure and mechanical properties of the interphase region and nanocomposite systems. It was observed that the grafting of PEG chains in the silica nanoparticle increased the interaction energy due to a drastic increase of the van der Waals component. The presence of the silica nanoparticle manifested in a perturbation in the polymer density profiles when compared to that encountered in the bulk polymer matrix, since it was observed that the polymer tended to accumulate around the nanoparticle in the form of dense layers. The polymer density profiles also suggested that higher oxidized polymers, *i.e.* with a greater content of oxygen or a lower content in hydrogen, would have higher affinity to silica nanoparticles. The interphase thickness, which was estimated from the ASD plots, was increased due to the PEGylation of the nanoparticle. Using compressed and expanded models of the pure polymer, it was possible to have an estimation of the mechanical properties of the interphase region by relating to its density in terms of Young's modulus, Poisson's ratio and shear modulus. Thus, the lower polymer density found in the PEGylated nanoparticle interphase also resulted in lower stiffness for the interphase region of this nanocomposite system. Finally, the mechanical properties of the nanocomposites were determined by molecular mechanics simulations, showing that the presence of the silica nanoparticle increased the stiffness of the nanocomposite although its PEGylation did not show an additional effect on the overall mechanical properties. In addition, the properties of the interphase region (*i.e.* thickness and mechanical properties) calculated by MD simulations from the density radial profiles for these nanocomposite models were corroborated using the Mori–Tanaka model. It was concluded that PEGylation improved the affinity, and thus the dispersion, of the silica nanoparticles towards the PCL matrix, but with no further increase of the mechanical properties of the composite.

## Author contributions

CSE and ML conceived the project. CSE performed the simulations and analyzed the results. JMGA supervised the project and methodology. ML contributed to the validation of the results performing the micromechanical analysis. CSE wrote the manuscript with input from all the authors.

## Conflicts of interest

There are no conflicts to declare.

## Acknowledgements

This work was partly granted by the FSE Operative Programme for Aragon (2014–2020).

## References

1 A. Adnan, C. T. Sun and H. Mahfuz, *Compos. Sci. Technol.*, 2007, **67**, 348–356.
2 M. Roy, J. K. Nelson, R. K. MacCrone, L. S. Schadler, C. W. Reed and R. Keefe, *IEEE Trans. Dielectr. Electr. Insul.*, 2005, **12**, 629–643.
3 M. Roy, C. W. Reed, R. K. MacCrone, L. S. Schadler, J. K. Nelson, R. Keefe and W. Zenger, *Proceedings of 2005 International Symposium on Electrical Insulating Materials, 2005. (ISEIM 2005)*, 2005, vol. 1, pp. 223–226.
4 T. V. M. Ndoro, E. Voyiatzis, A. Ghanbari, D. N. Theodorou, M. C. Böhm and F. Müller-Plathe, *Macromolecules*, 2011, **44**, 2316–2327.
5 A. Ghanbari, T. V. M. Ndoro, F. Leroy, M. Rahimi, M. C. Böhm and F. Müller-Plathe, *Macromolecules*, 2012, **45**, 572–584.
6 A. Ghanbari, M. Rahimi and J. Dehghany, *J. Phys. Chem. C*, 2013, **117**, 25069–25076.
7 Y. Golitsyn, G. J. Schneider and K. Saalwächter, *J. Chem. Phys.*, 2017, **146**, 203303.
8 A. Kusmin, S. Gruener, A. Henschel, N. de Souza, J. Allgaier, D. Richter and P. Huber, *Macromolecules*, 2010, **43**, 8162–8169.
9 S. Y. Kim, H. W. Meyer, K. Saalwächter and C. F. Zukoski, *Macromolecules*, 2012, **45**, 4225–4237.
10 M. Alcoutlabi and G. B. McKenna, *J. Phys.: Condens. Matter*, 2005, **17**, R461–R524.
11 A. Serghei, H. Huth, C. Schick and F. Kremer, *Macromolecules*, 2008, **41**, 3636–3639.
12 S. Ok, M. Steinhart, A. Şerbescu, C. Franz, F. Vaca Chávez and K. Saalwächter, *Macromolecules*, 2010, **43**, 4429–4434.
13 J. Eshelby, *Proc. R. Soc. Lond. Ser.: Math. Phys. Sci.*, 1957, **241**, 376–396.
14 T. Mori and K. Tanaka, *Acta Metall.*, 1973, **21**, 571–574.
15 J. C. Halpin and J. L. Kardos, *Polym. Eng. Sci.*, 1976, **16**(5), 344–352.
16 Y. Benveniste, *Mech. Mater.*, 1987, **6**, 147–157.
17 J. Cho, M. S. Joshi and C. T. Sun, *Compos. Sci. Technol.*, 2006, **66**, 1941–1952.
18 S. Saber-Samandari and A. Afaghi Khatibi, *Key Eng. Mater.*, 2006, **312**, 199–204.
19 H. L. Duan, J. Wang, Z. P. Huang and B. L. Karihaloo, *Proc. R. Soc. Math. Phys. Eng. Sci.*, 2005, **461**, 3335–3353.
20 J. C. Martinez-Garcia, A. Serraïma-Ferrer, A. Lopeandía-Fernández, M. Lattuada, J. Sapkota and J. Rodríguez-Viejo, *Nanomaterials*, 2021, **11**, 830.
21 A. P. Sokolov, V. N. Shchetinin and M. Y. Kozlov, *Math. Models Comput. Simul.*, 2021, **13**, 347–359.
22 G. M. Odegard, T. C. Clancy and T. S. Gates, *Polymer*, 2005, **46**, 553–562.
23 S. F. Ferdous, Md. F. Sarker and A. Adnan, *Polymer*, 2013, **54**, 2565–2576.
24 B. Arash, Q. Wang and V. K. Varadan, *Sci. Rep.*, 2014, **4**, 6479.
25 S. Herasati, L. C. Zhang and H. H. Ruan, *Int. J. Solids Struct.*, 2014, **51**, 1781–1791.

26 M. Krutyeva, A. Wischnewski, M. Monkenbusch, L. Willner, J. Maiz, C. Mijangos, A. Arbe, J. Colmenero, A. Radulescu, O. Holderer, M. Ohl and D. Richter, *Phys. Rev. Lett.*, 2013, **110**, 108303.

27 T. Glomann, G. J. Schneider, J. Allgaier, A. Radulescu, W. Lohstroh, B. Farago and D. Richter, *Phys. Rev. Lett.*, 2013, **110**, 178001.

28 T. Glomann, A. Hamm, J. Allgaier, E. G. Hübner, A. Radulescu, B. Farago and G. J. Schneider, *Soft Matter*, 2013, **9**, 10559–10571.

29 P. Klonos, A. Kyritsis and P. Pissis, *Polymer*, 2016, **84**, 38–51.

30 B. Carroll, S. Cheng and A. P. Sokolov, *Macromolecules*, 2017, **50**, 6149–6163.

31 M. Stamm, *Polymer Surfaces and Interfaces*, Springer, 2008, pp. 1–16.

32 T. Gates, G. Odegard, S. Frankland and T. Clancy, *Compos. Sci. Technol.*, 2005, **65**, 2416–2434.

33 W. Xu, Q. H. Zeng, A. B. Yu and D. R. Paul, *Mater. Sci. Forum*, 2010, **654–656**, 1654–1657.

34 Q. H. Zeng, A. B. Yu and G. Q. Lu, *Prog. Polym. Sci.*, 2008, **33**, 191–269.

35 J. Gou, B. Minaie, B. Wang, Z. Liang and C. Zhang, *Comput. Mater. Sci.*, 2004, **31**, 225–236.

36 A. Liu, K. W. Wang and C. E. Bakis, *Compos. Part Appl. Sci. Manuf.*, 2011, **42**, 1748–1755.

37 J. S. Smith, O. Borodin, G. D. Smith and E. M. Kober, *J. Polym. Sci., Part B: Polym. Phys.*, 2007, **45**, 1599–1615.

38 H. Eslami, M. Rahimi and F. Müller-Plathe, *Macromolecules*, 2013, **46**, 8680–8692.

39 J. Oberdisse, *Soft Matter*, 2006, **2**, 29–36.

40 J. Oberdisse and B. Deme, *Macromolecules*, 2002, **35**, 4397–4405.

41 A. George, M. R. Sanjay, R. Srisuk, J. Parameswaranpillai and S. Siengchin, *Int. J. Biol. Macromol.*, 2020, **154**, 329–338.

42 R. Grujić, D. Vujadinović and D. Savanović, in *Advances in Applications of Industrial Biomaterials*, ed. E. Pellicer, D. Nikolic, J. Sort, M. Baró, F. Zivic, N. Grujovic, R. Grujic and S. Pelemis, Springer International Publishing, Cham, 2017, pp. 139–160.

43 R. Porta, M. Sabbah and P. Di Pierro, *Int. J. Mol. Sci.*, 2020, **21**, 4942.

44 R. Rebelo, M. Fernandes and R. Fangueiro, *Procedia Eng.*, 2017, **200**, 236–243.

45 J. Velema and D. Kaplan, *Adv. Biochem. Eng. Biotechnol.*, 2006, **102**, 187–238.

46 A. J. Nathanael and T. H. Oh, *Polymers*, 2020, **12**, 3061.

47 B. Aaliya, K. V. Sunooj and M. Lackner, *Int. J. Biobased Plast.*, 2021, **3**, 40–84.

48 M. Kaseem, Z. Ur Rehman, S. Hossain, A. K. Singh and B. Dikici, *Polymers*, 2021, **13**, 3036.

49 R. Narayan, U. Nayak, A. Raichur and S. Garg, *Pharmaceutics*, 2018, **10**, 118.

50 A. Liberman, N. Mendez, W. C. Trogler and A. C. Kummel, *Surf. Sci. Rep.*, 2014, **69**, 132–158.

51 H. Jaganathan and B. Godin, *Adv. Drug Delivery Rev.*, 2012, **64**, 1800–1819.

52 A. G. B. Castro, M. Diba, M. Kersten, J. A. Jansen, J. J. J. P. van den Beucken and F. Yang, *Mater. Sci. Eng., C*, 2018, **85**, 154–161.

53 M. Ke, J. A. Wahab, B. Hyunsik, K.-H. Song, J. S. Lee, M. Gopiraman and I. S. Kim, *RSC Adv.*, 2016, **6**, 4593–4600.

54 C. E. Plazas Bonilla, S. Trujillo, B. Demirdögen, J. E. Perilla, Y. Murat Elcin and J. L. Gómez Ribelles, *Mater. Sci. Eng., C*, 2014, **40**, 418–426.

55 A. Bifulco, D. Parida, K. A. Salmeia, S. Lehner, R. Stämpfli, H. Markus, G. Malucelli, F. Branda and S. Gaan, *Composites, Part C*, 2020, **2**, 100022.

56 T. Kashiwagi, J. R. Shields, R. H. Harris Jr. and R. D. Davis, *J. Appl. Polym. Sci.*, 2003, **87**, 1541–1553.

57 M. Montalti, E. Rampazzo, N. Zaccheroni and L. Prodi, *New J. Chem.*, 2012, **37**, 28–34.

58 Y. Su, *React. Funct. Polym.*, 2006, **66**, 967–973.

59 N. Tsubokawa, *Polym. J.*, 2007, **39**, 18.

60 H. Zou, S. Wu and J. Shen, *Chem. Rev.*, 2008, **108**, 3893–3957.

61 K. Y. Lim, B. C. Kim and K. J. Yoon, *Polym. J.*, 2002, **34**, 313–319.

62 Polycaprolactone – an overview | ScienceDirect Topics, https://www.sciencedirect.com/topics/chemical-engineering/polycaprolactone (accessed January 21, 2022).

63 T. A. Halgren, *J. Comput. Chem.*, 1996, **17**, 490–519.

64 S. Plimpton, *J. Comput. Phys.*, 1995, **117**, 1–19.

65 S. J. Weiner, P. A. Kollman, D. T. Nguyen and D. A. Case, *J. Comput. Chem.*, 1986, **7**, 230–252.

66 W. L. Jorgensen, D. S. Maxwell and J. Tirado-Rives, *J. Am. Chem. Soc.*, 1996, **118**, 11225–11236.

67 H. Sun, *Abstr. Pap. Am. Chem. Soc.*, 1992, **203**, 291.

68 P. E. M. Lopes, V. Murashov, M. Tazi, E. Demchuk and A. D. MacKerell, *J. Phys. Chem. B*, 2006, **110**, 2782–2792.

69 I. Fukuda, S. Mochizuki and K. Sakurai, *Colloids Surf., B*, 2016, **146**, 642–648.

70 L. Shi, J. Zhang, M. Zhao, S. Tang, X. Cheng, W. Zhang, W. Li, X. Liu, H. Peng and Q. Wang, *Nanoscale*, 2021, **13**, 10748–10764.

71 D. Selli, S. Motta and C. Di Valentin, *J. Colloid Interface Sci.*, 2019, **555**, 519–531.

72 D. Theodorou and U. Suter, *Macromolecules*, 1986, **19**, 379–387.

73 D. N. Theodorou and U. W. Suter, *Macromolecules*, 1986, **19**, 139–154.

74 E. Bitzek, P. Koskinen, F. Gähler, M. Moseler and P. Gumbsch, *Phys. Rev. Lett.*, 2006, **97**, 170201.

75 G. M. Odegard, T. C. Clancy and T. S. Gates, *46 th AIAA/ASME/ASCE/AHS/ASC Structures, Structural Dynamics, and Materials Conference*, 2005, pp. 1–12.

76 A. Stukowski, *Model. Simul. Mater. Sci. Eng.*, 2009, **18**, 015012.

77 H. Edelsbrunner and E. Mucke, *ACM Trans. Graph.*, 1994, **13**, 43–72.

78 N. M. Mahani, *Mater. Res.*, 2020, **23**, e20200188.

79 S. Upadhyayula, T. Quinata, S. Bishop, S. Gupta, N. R. Johnson, B. Bahmani, K. Bozhilov, J. Stubbs, P. Jreij,


 

P. Nallagatla and V. I. Vullev, *Langmuir*, 2012, **28**, 5059–5069.
80 K. Bucior, L. Yelash and K. Binder, *Phys. Rev. E: Stat. Nonlin. Soft Matter Phys.*, 2009, **79**, 031604.
81 C. Sáenz Ezquerro, M. Laspalas, A. Chiminelli, F. Serrano and C. Valero, *Fibers*, 2018, **6**, 54.
82 J. Choi, H. Shin, S. Yang and M. Cho, *Compos. Struct.*, 2015, **119**, 365–376.
83 N. Al Habis, A. El Moumen, M. Tarfaoui and K. Lafdi, *Arab. J. Chem.*, 2020, **13**, 3210–3217.
84 S. Eshraghi and S. Das, *Acta Biomater.*, 2010, **6**, 2467–2476.
85 D. Kurniawan, F. M. Nor, H. Y. Lee and J. Y. Lim, *Proc. Inst. Mech. Eng. [H]*, 2011, **225**, 1015–1020.
86 A. Farazin, F. Aghadavoudi, M. Motififard, S. Saber-Samandari and A. Khandan, *J. Appl. Comput. Mech.*, 2020, **7**(4), 1907–1915.
87 A. J. Harmata, C. L. Ward, K. J. Zienkiewicz, J. C. Wenke and S. A. Guelcher, *J. Mater. Res.*, 2014, **29**, 2398–2407.
88 E. Armanios and J. Reeder, *American Society for Composites/ American Society for Testing And Materials Committee D30: Nineteenth Technical Conference*, DEStech Publications, Inc., 2004.
89 Azom, AZoM.com.
90 L. Calandrelli, M. Annunziata, F. Della Ragione, P. Laurienzo, M. Malinconico and A. Oliva, *J. Mater. Sci.: Mater. Med.*, 2010, **21**, 2923–2936.
91 N. Moussaif, S. Irusta, C. Yagüe, M. Arruebo, J. G. Meier, C. Crespo, M. A. Jimenez and J. Santamaría, *Polymer*, 2010, **51**, 6132–6139.
92 J. S. Suk, Q. Xu, N. Kim, J. Hanes and L. M. Ensign, *Adv. Drug Delivery Rev.*, 2016, **99**, 28–51.
93 Y. Zare, *Compos. Part Appl. Sci. Manuf.*, 2016, **91**, 127–132.

# 7. Publicación II

**Monitoring interactions through molecular dynamics simulations: effect of calcium carbonate on the mechanical properties of cellulose composites**

**Cellulose,**
**DOI:** 10. 1007/ s10570- 022- 04902-1
**Factor de impacto en 2022**: 5,7
**Área temática**: Materials Science, Paper & Wood
**Cuartil JCR (2022):** Q1

Cellulose
https://doi.org/10.1007/s10570-022-04902-1

ORIGINAL RESEARCH

# Monitoring interactions through molecular dynamics simulations: effect of calcium carbonate on the mechanical properties of cellulose composites

**Carlos Sáenz Ezquerro · Manuel Laspalas · José Manuel García Aznar · Cristina Crespo Miñana**

Received: 11 May 2022 / Accepted: 15 October 2022


**Abstract** This study describes the preparation and characterization of full atomistic models of amorphous cellulose and calcium carbonate ($CaCO_3$) nanocomposite to assess its mechanical properties within and beyond the elastic limit via molecular dynamics simulations. The interactions by hydrogen bond and conformation of the cellulose molecules from the assessment of torsional angles were specifically monitored during the tensile stretching simulations to get deep understanding of the possible structural changes produced in the material during the deformation. On the one hand, the results showed a favorable interaction of the cellulose matrix with the calcium carbonate nanoparticle, with the electrostatic contribution being dominant over the van der Waals component. The determined mechanical elastic constants indicated that the inclusion of the $CaCO_3$ nanoparticle provided an increase on the rigidity of the composite system of 15%, 18% and 19% in the Young, shear or bulk modulus, respectively. On the other hand, using extension and compression simulations, the recovery capacity of the material systems was also assessed in terms of plastic deformation. The elastoplastic behavior was observed for either the neat or the $CaCO_3$ nanocomposite, with an elastic limit around 2.5%. The results also showed that the presence of the $CaCO_3$ nanoparticle produced higher values of plastic deformation in the composite material compared to the neat cellulose system and thus decreased the flexibility of the material. A hysteresis mechanism was identified together with irreversible conformational changes on the cellulose molecules which would explain the plastic deformation observed on the cellulosic systems. It was concluded that the higher plastic deformations observed in the nanocomposite system would be a result of the disruption of the network of hydrogen bonds and the associated decrease on the number of possible interactions.

**Supplementary Information** The online version contains supplementary material available at https://doi.org/10.1007/s10570-022-04902-1.

C. Sáenz Ezquerro · M. Laspalas · C. Crespo Miñana
Aragon Institute of Technology ITAINNOVA, María de Luna 7-8, 50018 Zaragoza, Spain
e-mail: csaenz@itainnova.es

J. M. García Aznar (✉)
Aragon Institute of Engineering Research (I3A), University of Zaragoza, 50018 Zaragoza, Spain
e-mail: jmgaraz@unizar.es

Published online: 22 November 2022

## Graphical Abstract

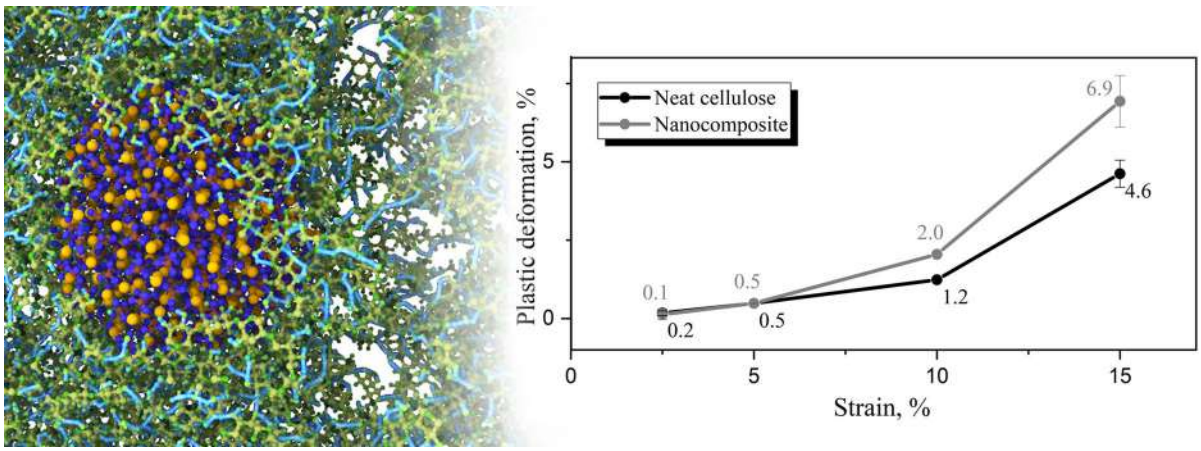


**Keywords** Molecular dynamics · Cellulose · Calcium carbonate · Mechanical properties · Hydrogen bonds

## Introduction

Cellulose is an almost inexhaustible polymeric raw material with outstanding properties (Klemm et al. 2005) and is remarkably considered to be the most abundant organic compound mainly derived from biomass (Ummartyotin and Manuspiya 2015). With an annual production estimated to be over $7.5 \times 10^{10}$ tons (Li et al. 2018), is the most abundant biomass resource in the world. The industrial and commercial applications of cellulose and its derivatives cover a wide range of use cases. From food packaging (Liu et al. 2021), humidity and UV sensors (Ummartyotin and Manuspiya 2015), cancer therapy (Jian et al. 2014), wastewater treatment (Kalidhasan et al. 2012), carbon capture (Gebald et al. 2014; Sepahvand et al. 2020) or selective membranes (Hou et al. 2020), among others.

Particular attention has been dedicated in the recent years to the development of nanocomposites based on cellulose and inorganic nanoparticles as fillers, such as $SiO_2$ (Pinto et al. 2008; Sheykhnazari et al. 2016), $TiO_2$ (Garusinghe et al. 2018; Hamad et al. 2020), gold (Rie and Thielemans 2017), kaolin particles (Fahmy and Mobarak 2008; Torvinen et al. 2017), among others (Alves et al. 2019). The combination of both components provides a final material with improved properties, such as mechanical (Fahmy and Mobarak 2008), antimicrobial (Rie and Thielemans 2017), optical (Hynninen et al. 2021) and thermal or electrical conductivity (Phiri et al. 2018). Among the different inorganic fillers, in the past years great effort has been paid to the synthesis and applications of cellulose nanocomposites filled with calcium carbonate ($CaCO_3$) due to its relating properties such as mechanical strength, biocompatibility, and biodegradation, and bioactivity, and potential applications including biomedical, antibacterial and water pre-treatment fields as functional materials (Ma et al. 2016). Calcium carbonate is one of the most abundant biomineral (Meldrum 2003) as formed in corals, pearls, molluscs and the exoskeleton of arthropods (Vilela et al. 2010). In the field of paper, which is the most important cellulose-based material in terms of worldwide production tons (Bajpai 2013), calcium carbonate is the dominant filler in the production of wood-free uncoated paper (Chen et al. 2011) due to its high number of benefits (economical, environmental, improves paper brightness, opacity, porosity, etc.) (Holik et al. 2013). Nevertheless, the use of calcium carbonate as filler can interfere with the fibre–fibre bonding and thus decrease the tensile strength of the filled paper (Maloney et al. 2005; Fahmy and Mobarak 2008). Some studies have reported, in contrast, the opposite effect of calcium carbonate particles on the mechanical performance of paper (Chen et al. 2011; Mohamadzadeh-Saghavaz et al. 2014). Due to this controversy, further study should be performed to clarify the real relationship between calcium carbonate and cellulose materials.

From an environmental point of view, the pollution problems associated with the use of non-degradable plastic packaging materials are demanding the finding of solutions to replace them with biodegradable alternatives. At this point, the development of eco-friendly cellulose solvents (Isobe et al. 2013; Krysztof et al. 2018) has allowed to the fabrication of various regenerated cellulose (RC) based films and hydrogels, which establish an attractive biodegradable substitute for common packaging materials (Huang and Wang 2022). This kind of cellulose derivatives, obtained from the regeneration of dissolved cellulose, have modulated chemical and physical properties and exhibits an amorphous nature compared to the natural occurring high crystalline cellulose (Ciolacu et al. 2010). Besides, their porous structure allow for the incorporation of functional fillers which can expand their performance and applications (Ardila-Diaz et al. 2020; Salama and Abdel Aziz 2020; Xu et al. 2021; Shaghaleh et al. 2021). Calcium carbonate, which was successfully incorporated in regenerated cellulose films by the precipitation method (Zhu et al. 2020), increased the tensile strength when the optimum concentration was added to the film.

Theoretical modelling of cellulose materials, which comprises ab initio calculations (Kubicki et al. 2013; Uto and Yui 2018), molecular dynamics (MD) simulations (Li et al. 2017; Zhao et al. 2019) and coarse-grained (CG) approaches (Mehandzhiyski and Zozoulenko 2021), allows for a deep understanding of the phenomena occurring at the atomistic or molecular level, which later manifests in their macroscopic properties. Molecular modelling has played an important role over the years for the understanding of molecular-scale phenomena since it offers a level of detail that surpasses what can be reached by experimental methods (Wohlert et al. 2022). Such modelling methods can be used to predict the effect of chemical modifications, such us grafting (Wang et al. 2019), the thermal decomposition (Paajanen et al. 2021) or the dissolution process (Bering et al. 2022) of cellulose, among others phenomena, without the need of experimental input. In the specific field of composites, MD simulations are usually used to predict the mechanical properties of the material (Pashmforoush et al. 2020; Ren et al. 2021) or the effect of different additives on its flexibility (Chen et al. 2004a, b, 2007).

Considering the importance of calcium carbonate as filler of cellulose-based or paper related materials and the increasing interest on the packaging industry for the regenerated cellulose based films, the present study describes the modelization performed, through MD simulations, of an amorphous cellulose (AC) composite filled with calcium carbonate nanoparticles, with the aim of studying the effect of such nanoparticles on its mechanical properties, either in the elastic region or beyond the elastic limit in the plastic regime. On the one hand, the interaction energy and radial distribution function (RDF) between the cellulose matrix and the calcium carbonate nanoparticle were determined to assess the type of interaction quantitatively and qualitatively. On the other hand, the elastic stiffness constants were determined using molecular mechanics simulations and, with the aim of assessing the recovery capacity of the materials, the modelled molecular systems were subjected to a series of extension and compression simulations from which the remanent plastic deformation could be determined. The hydrogen bond interactions and conformation of cellulose molecules through the analysis of torsion angles were also monitored during these simulations to check for possible structural changes in the material.

## Methods

### Computational implementation

All calculations presented in the following study were performed using the LAMMPS simulation code (Plimpton 1995). The interactions between cellulose atoms were modeled through a Class II potential as stated next:

$$
\begin{aligned}
E_{pot} = & \sum_{b}\left[K_2(r-r_0)^2 + K_3(r-r_0)^3 + K_4(r-r_0)^4\right] \\
& + \sum_{\theta}\left[H_2(\theta-\theta_0)^2 + H_3(\theta-\theta_0)^3 + H_4(\theta-\theta_0)^4\right] \\
& + \sum_{\phi}\left[V_1\left[1-cos(\phi-\phi_1^0)\right] + V_2\left[1-cos(2\phi-\phi_2^0)\right] + V_3\left[1-cos(3\phi-\phi_3^0)\right]\right] \\
& + \sum_{\chi} K_\chi \chi^2 + \sum_{b}\sum_{b'} F_{bb'}(b-b_0)(b'-b_0') \\
& + \sum_{b}\sum_{\theta} F_{b\theta}(b-b_0)(\theta-\theta_0) \\
& + \sum_{b}\sum_{\phi}(b-b_0)\left[V_1 cos\phi + V_2 cos2\phi + V_3 cos3\phi\right] \\
& + \sum_{b'}\sum_{\phi}(b'-b_0')\left[V_1 cos\phi + V_2 cos2\phi + V_3 cos3\phi\right] \\
& + \sum_{\theta}\sum_{\phi}(\theta-\theta_0)\left[V_1 cos\phi + V_2 cos2\phi + V_3 cos3\phi\right] \\
& + \sum_{\phi}\sum_{\theta}\sum_{\theta'} K_{\phi\theta\theta'} cos\phi(\theta-\theta_0)(\theta'-\theta_0') \\
& + \sum_{i>j}\frac{q_i q_j}{\varepsilon r_{ij}} + \sum_{i>j}\left[\frac{A_{ij}}{r_{ij}^9} - \frac{B_{ij}}{r_{ij}^6}\right]
\end{aligned}
$$

where $K_i$, $H_i$, $V_i$, and $F_i$ are force constants, r is the distance between atoms, b is the bond length, θ and φ are bond and torsion angles, $q_i$ is the partial charge of a given atom, and $A_{ij}$ and $B_{ij}$ are the van der Waals parameters. The value of these parameters has been defined based on the COMPASS force field, specified in H. Sun's work (Sun 1998). The previous potentials describe well the interaction between atoms in organic or small inorganic molecules, and have been validated for the mechanical simulation of cellulose (Tanaka and Iwata 2006; Bazooyar et al. 2012),

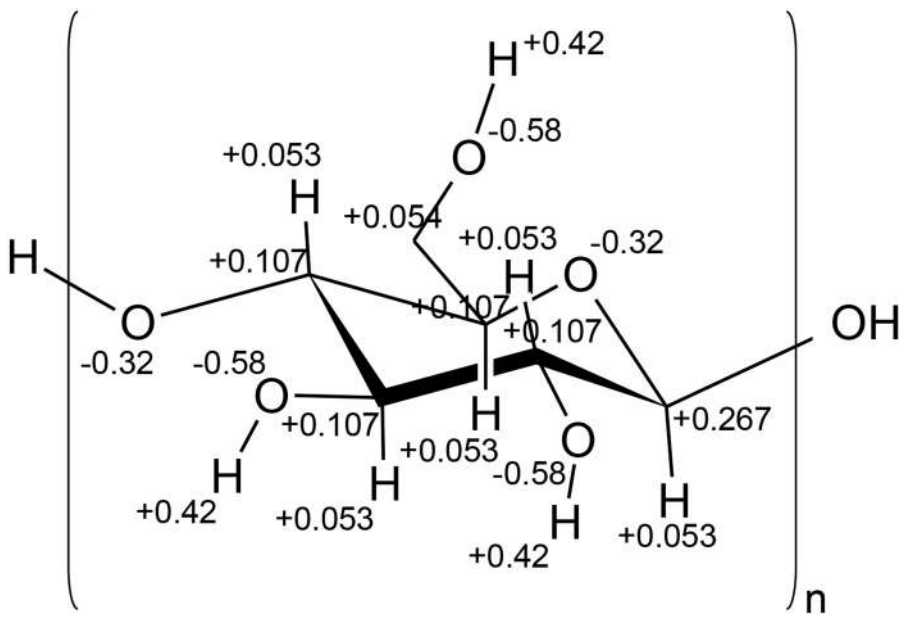


**Fig. 1** Structure and partial atomic charges of cellulose molecules (n = 40). The molecular structure of the cellulose monomer (i.e., glucose residue) is represented and the partial atomic charge, in relative terms with respect to an electron charge, is indicated for each atom in the structure

but they are not usually accurate for inorganic compounds. For ionic solids the interactions between ions are better described using other exponential potentials, such as those involved in the force field developed by Raiteri et al. (Raiteri et al. 2010; Raiteri and Gale 2010), which was used in the present study to model the interactions between atoms within the calcium carbonate in the present study. The force field described by Raiteri et al. combines the sum of a Buckingham potential and coulombic interactions:

$$E_{pot} = A \cdot exp\left(-\frac{r}{\rho}\right) - \frac{C}{r^6} + \sum_{i>j} \frac{q_i q_j}{\varepsilon r_{ij}}$$

where A and ρ are factors associated with the exponential term of the Buckingham potential, and C is a coefficient associated with attractive dispersion forces between oxygen atoms of carbonate ions (set to zero for all other interactions between Ca, C and O). The partial atomic charges for the calcium carbonate atoms were taken directly as defined in the Raiteri

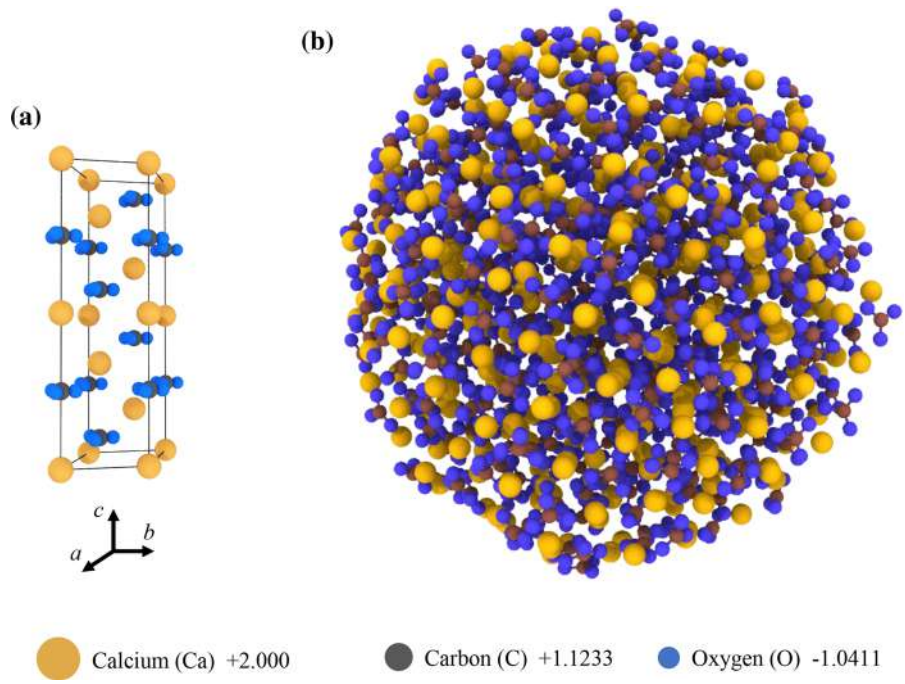


**Fig. 2** **a** Unit cell of calcium carbonate (calcite, $CaCO_3$) showing partial atomic charges and **b** model of 2 nm radius calcium carbonate nanoparticle ($Ca_{439}(CO_3)_{439}$). In first place the atomic structure of the unit cell of calcium carbonate based on calcite is shown, including partial atomic charges, and in second place a render of the modeled calcium carbonate nanoparticle is represented

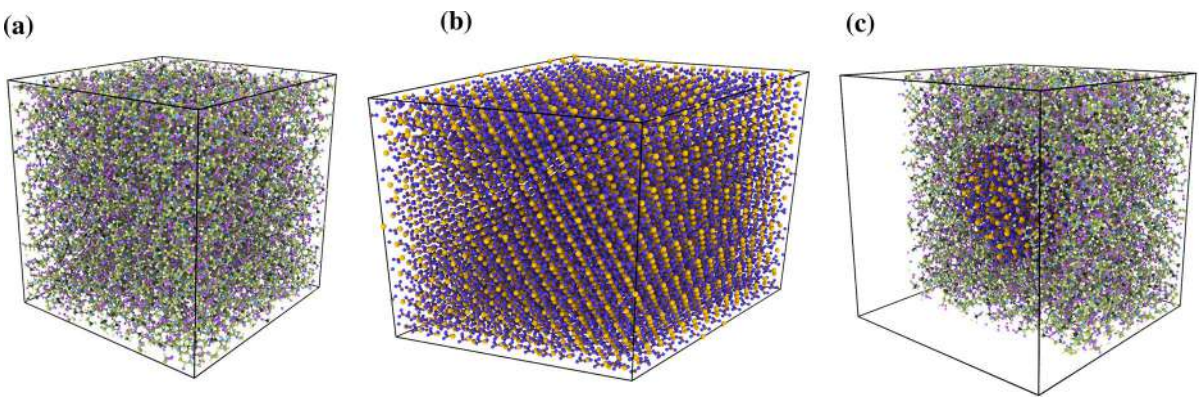


**Fig. 3** Molecular systems employed for the characterization: **a** neat cellulose (amorphous), **b** neat calcium carbonate (calcite) and **c** nanocomposite models. The renders of three molecular models are depicted by detailed render images (perspective view).

force field. The interactions between cellulose and calcium carbonate atoms were directly modeled from van der Waals interactions using the Lennard–Jones 9–12 potential with the parameters defined in the COMPASS force field, since previous study showed good results with this combination (Ylikantola et al. 2013; Zhao et al. 2019; Pashmforoush et al. 2020). Likewise, the long-distance coulombic interactions (> 10.5 Å) were calculated by coupling an Ewald solver (Particle Mesh Ewald, PME), which uses the reciprocal images of the models. In all the simulations the Nosé-Hoover thermostat (Nosé 1984; Hoover 1985) was used to maintain the systems at 300 K of temperature, the time step was set at 0.5 fs and the Verlet algorithm was used to update the positions of the atoms.

System preparation

Initially, the molecular models of oligomers of cellulose were built by bonding 40 units of β-D-glucopyranose by O-β(1 → 4)-glycosidic bonds, resulting in a chain with a degree of polymerization with n = 40 (i.e., number of glucose residues) (French 2017). The partial atomic charges were generated considering the charge increments of the COMPASS force field (Sun 1998). Figure 1 shows the partial charges of the cellulose structure generated. In this study no ionic groups (such as carboxyl) were included in the molecules of cellulose (i.e. standard cellulose without any degree of oxidation). The model of neat amorphous cellulose matrix was initially generated by randomly adding 38 chains of the cellulose oligomers in the simulation cell under periodic boundary conditions (PBC). To equilibrate this molecular system, first it was time integrated under the NVT canonical ensemble at 300 K during 75 ps to let the molecules of cellulose to relax and accommodate the volume of the simulation box. Further the system was subjected to 5 cycles of minimization and time integration under the isothermal-isobaric ensemble (NPT) up to a total of 4 ns at 300 K to get a fully relaxed system (i.e., with zero stress). A rendering of this model is shown in Fig. 3a.

The calcium carbonate model was based on the crystalline structure of calcite, whose hexagonal unit cell together with the atomic partial charges is shown in Fig. 2. Either the cell parameters, atomic coordinates and the partial atomic charges were taken from the study described by Raiteri et al. (Raiteri et al. 2015). By replicating the unit cell of the calcite in the three directions of space it was obtained a crystal lattice that, after equilibration in the isothermal-isobaric ensemble (NPT) during 1 ns at 300 K, gives rise to the model of pure calcite (Fig. 3b). The density of the calcite model in the equilibrium state was determined as 2.611 g/cm$^3$. Compared to the experimental density values determined for amorphous calcium carbonate of 1.62 g/cm$^3$ (Liu et al. 2010) and that for the calcite polymorph of 2.71 g/cm$^3$ (DeFoe and Compton 1925), the calculated density value revealed a high crystallinity degree of the developed model. On the other hand, the unit cell parameters calculated for this model were 4.99 Å, 5.16 Å and 16.95 Å for *a*, *b* and *c* respectively. The experimental values determined for calcite were reported as 4.99 Å and 17.062 Å for *a* and *c* respectively (Bearchell and Heyes 2002; Raiteri et al. 2015), which were very close to the values determined for the developed model and were thus in agreement with its high crystallinity.

The $CaCO_3$ nanoparticle model was generated by isolating a spherical region of 2 nm radius in the previously developed pure calcite lattice model. The isolation procedure was made using LAMMPS commands and checking that the stoichiometry of calcium carbonate was not altered after the isolation of atoms. The formula of the isolated nanoparticle was $Ca_{439}(CO_3)_{439}$. The nanoparticle was later placed on a simulation box and equilibrated under the canonical ensemble (NVT) during 1 ns at 300 K to let the atoms equilibrate under the new geometry. A picture of the stabilized $CaCO_3$ nanoparticle is shown in Fig. 2b. Finally, the nanocomposite model was built by placing randomly a total of 38 cellulose chains around the equilibrated $CaCO_3$ nanoparticle within a simulation box with PBC, which supposed a 15.1% in weight of nanofiller reinforcement. This model was relaxed by applying a total of 4 cycles of minimization and time integrated under the isothermal-isobaric ensemble (NPT) at 300 K up to a total of 2 ns. A rendering of this model can be seen in Fig. 3c. It should be noted that although only one nanoparticle was inserted in the generated nanocomposite model, this system was simulated under the PBC conditions, so it was implicitly equivalent to a system with infinite number of nanoparticles dispersed in an amorphous cellulose matrix (Sharma et al. 2019).

### Interaction energy and radial distribution function (RDF)

The interaction energy defines the energy of a system (in terms of its potential energy) involved in the interaction between its components, which here would be cellulose and calcium carbonate ($CaCO_3$). This interaction energy ($E_i$) can be calculated considering the energy of the system and the energy of the isolated components as indicated below:

$$E_i = E_{total} - (E_{cellulose} + E_{CaCO3}) \quad (1)$$

where $E_{total}$, is the potential energy of the whole system, $E_{cellulose}$ is the energy of the cellulose matrix without the nanoparticle and $E_{CaCO3}$ is the energy of the calcium carbonate nanoparticle without the cellulose matrix. The potential energy has contributions from bonds, angles, dihedrals, van der Waals and coulombic interactions. The radial distribution function (RDF), also called pair correlation function g(r), was calculated according to next formula:

$$g_{ij}(r) = \frac{n_{ij}(r)}{4\pi r^2} \quad (2)$$

where $n_{ij}(r)$ is the number of pair atoms i-j within the range $(r - \Delta r/2, r + \Delta r/2)$, and r the distance between the atoms.

### Assessment of hydrogen bond interaction

According to IUPAC (International Union of Pure and Applied Chemistry) (Arunan et al. 2011), hydrogen bonds are formed between an electronegative atom (i.e. the acceptor atom) and a hydrogen atom bonded to a second electronegative atom (i.e. the donor atom) (McNaught and Wilkinson 1997). In the force field chosen in this study (i.e. a combination of COMPASS and Raiteri potentials) the hydrogen bond interaction is considered in the van der Waals and Coulomb interactions of the atoms involved in the bond (i.e. it is considered as a mean field approximation), but not in a specific energy term. For this reason, the contribution of hydrogen bonding to the system in energy terms cannot be measured directly, but otherwise it is possible to have an estimate of the number of hydrogen bonds in the system considering the distance between the acceptor atom and the hydrogen atom. In the present study, the criterion to establish the formation of a hydrogen bond interaction was based in the distance between the involved atoms. As it was established in the work from MacLeod and Rosei (MacLeod and Rosei 2011), the nature of hydrogen bond can be classified according to its energy as very strong, strong and weak (Nishiyama et al. 2008). Besides its energy, the distance between the hydrogen and donor atoms are also affected by the strength of the hydrogen bond and this fact was taken into account in the present study. Two types of hydrogen bonds were assessed from the material systems under study: strong hydrogen bonds were considered when the distance between the acceptor atom and hydrogen was lower than 2.0 Å; on the other hand, weak hydrogen bonds were considered when this distance was in the range 2.0 – 3.0 Å. As was previously indicated, the acceptor and donor atoms must be of high electronegativity, which in the considered material systems could only be the oxygen (O) atoms of hydroxyl (–OH) and/or ether groups (–O–) present in the cellulose chains, and the oxygen atoms present in the carbonate ions of the $CaCO_3$ nanoparticle. In order to quantify the number of hydrogen bonds, the OVITO software (Stukowski 2009) was used considering a maximum cut-off of 2.0 Å or 3.0 Å between the donor and acceptor atoms, depending on the type of hydrogen bond. This software also allows to distinguish bonds between different molecules, and this fact was considered to calculate intramolecular, intermolecular and total number hydrogen bonds.

### Mechanical properties

The mechanical properties in the elastic region of the different models prepared were evaluated in terms of the 6×6 elastic stiffness matrix, C. For any linear elastic material the stiffness matrix in contracted notation can be written written as:

$$C = \begin{pmatrix} C_{11} & C_{12} & C_{13} & C_{14} & C_{15} & C_{16} \\ C_{21} & C_{22} & C_{23} & C_{24} & C_{25} & C_{26} \\ C_{31} & C_{32} & C_{33} & C_{34} & C_{35} & C_{36} \\ C_{41} & C_{42} & C_{43} & C_{44} & C_{45} & C_{46} \\ C_{51} & C_{52} & C_{53} & C_{54} & C_{55} & C_{56} \\ C_{61} & C_{62} & C_{63} & C_{64} & C_{65} & C_{66} \end{pmatrix} \quad (3)$$

where $C_{ij}$ are the stiffness coefficients relating i stress with j strain components. In materials with symmetries expressed in their principal axis system, the stiffness matrix simplifies and some of the coefficients are equal to zero, being the rest independent (9 for an orthotropic material, 2 for an isotropic one). The calculation of the

elastic stiffness matrix by means of molecular mechanics simulations was carried out considering a static or equilibrium approach. After obtaining relaxed structures by applying time integration simulations under the isothermal-isobaric assembly (NPT), the structures were subjected to a set of 6 types of deformation cycles (three uniaxial stress and compression pairs, and three pure shear pairs), controlled by the corresponding strain vectors, with the deformed component taking a small value while the other components of the vector were kept fixed at zero (i.e. changing one cell parameter while maintaining the rest of the cell parameters fixed), and applying a minimization after each deformation stage without changing the cell parameters. The deformation was applied in cycles of positive and negative deformation increments, with amplitude of 0.003 (0.3%) up to a maximum of 0.009 (0.9%). Before the elastic matrix calculation, a pre-minimization procedure was initially applied to the models using the FIRE method (Fast Inertial Relaxation Engine) (Bitzek et al. 2006) for 10,000 iterations. The response of the system at each state of deformation was sampled in terms of the stress during the equilibration time after the initial 6 ps, where the system was allowed to relax, and was defined in the form of virial stress as,

$$\sigma_{ij} = -\frac{1}{V}\sum_{k}\left(m^k u_i^k u_j^k\right) + \frac{1}{2}\sum_{l\neq k}\left(r_i^{kl}\right)\left(f_j^{lk}\right) \tag{4}$$

where V is the total volume of the system of atoms, $m^k$ and $u^k$ denote the mass and velocity of the k-th atom, respectively, $r^{kl}$ refers to the distance between the k-th and l-th atoms, and $f^{kl}$ is the force exerted on the l-th atom by the k-th atom. The first term in the virial equation is related to the kinetic energy of the atoms, while the second is related to the potential energy (forces exerted between the atoms). In static conditions, which is the approximation considered here, the first term has no contribution to stress. Each component of the stiffness matrix was obtained from the slope of the stress versus strain plot for each $\sigma_{ij}$ component of the virial stress:

$$C = \begin{pmatrix} \Delta\sigma_{11}/\Delta\varepsilon_{11} & \Delta\sigma_{11}/\Delta\varepsilon_{22} & \Delta\sigma_{11}/\Delta\varepsilon_{33} & \Delta\sigma_{11}/\Delta\gamma_{12} & \Delta\sigma_{11}/\Delta\gamma_{13} & \Delta\sigma_{11}/\Delta\gamma_{23} \\ \Delta\sigma_{22}/\Delta\varepsilon_{11} & \Delta\sigma_{22}/\Delta\varepsilon_{22} & \Delta\sigma_{22}/\Delta\varepsilon_{33} & \Delta\sigma_{22}/\Delta\gamma_{12} & \Delta\sigma_{22}/\Delta\gamma_{13} & \Delta\sigma_{22}/\Delta\gamma_{23} \\ \Delta\sigma_{33}/\Delta\varepsilon_{11} & \Delta\sigma_{33}/\Delta\varepsilon_{22} & \Delta\sigma_{33}/\Delta\varepsilon_{33} & \Delta\sigma_{33}/\Delta\gamma_{12} & \Delta\sigma_{33}/\Delta\gamma_{13} & \Delta\sigma_{23}/\Delta\gamma_{23} \\ \Delta\sigma_{12}/\Delta\varepsilon_{11} & \Delta\sigma_{12}/\Delta\varepsilon_{22} & \Delta\sigma_{12}/\Delta\varepsilon_{33} & \Delta\sigma_{12}/\Delta\gamma_{12} & \Delta\sigma_{12}/\Delta\gamma_{13} & \Delta\sigma_{12}/\Delta\gamma_{23} \\ \Delta\sigma_{13}/\Delta\varepsilon_{11} & \Delta\sigma_{13}/\Delta\varepsilon_{22} & \Delta\sigma_{13}/\Delta\varepsilon_{33} & \Delta\sigma_{13}/\Delta\gamma_{12} & \Delta\sigma_{13}/\Delta\gamma_{13} & \Delta\sigma_{13}/\Delta\gamma_{23} \\ \Delta\sigma_{23}/\Delta\varepsilon_{11} & \Delta\sigma_{23}/\Delta\varepsilon_{22} & \Delta\sigma_{23}/\Delta\varepsilon_{33} & \Delta\sigma_{23}/\Delta\gamma_{12} & \Delta\sigma_{23}/\Delta\gamma_{13} & \Delta\sigma_{23}/\Delta\gamma_{23} \end{pmatrix} \tag{5}$$

The compliance matrix S was obtained from the inversion of the stiffness matrix C. Assuming an approximately orthotopic behavior, the elastic constants can be directly derived from the compliance matrix component as:

$$S = C^{-1} = \begin{pmatrix} 1/E_{11} & -\nu_{12}/E_{11} & -\nu_{13}/E_{11} & 0 & 0 & 0 \\ -\nu_{21}/E_{22} & 1/E_{22} & -\nu_{23}/E_{22} & 0 & 0 & 0 \\ -\nu_{31}/E_{33} & -\nu_{32}/E_{33} & 1/E_{33} & 0 & 0 & 0 \\ 0 & 0 & 0 & 1/G_{23} & 0 & 0 \\ 0 & 0 & 0 & 0 & 1/G_{31} & 0 \\ 0 & 0 & 0 & 0 & 0 & 1/G_{12} \end{pmatrix} \tag{6}$$

On the other hand, the stress–strain curve was generated by applying small consecutive (positive) longitudinal strain increments to the structure under study. These increments were applied in two stages: initially 20 deformation increments equal to 0.003 are applied, and later 25 deformation increments equal to 0.005 were applied, which in total makes a final model deformation equal to 0.185. After each increase in deformation, the model was minimized using the FIRE (Fast Inertial Relaxation Engine) algorithm for 10,000 iterations and the model stress was calculated using the virial. Subsequently, the stress was plotted against the deformation to generate the corresponding stress–strain curve.

## Plastic deformation assessment through extension and compression (recovery) simulations

Molecular mechanics simulations were used to estimate the plastic deformation remaining in the systems under study after the application of a certain finite strain. The methodology was based on that described by Chen et al. (2004a). In this type of simulations, the relaxed systems are first deformed up to a given final strain value by the application of consecutive small deformation increment steps. The application of a series of small consecutive steps of deformation

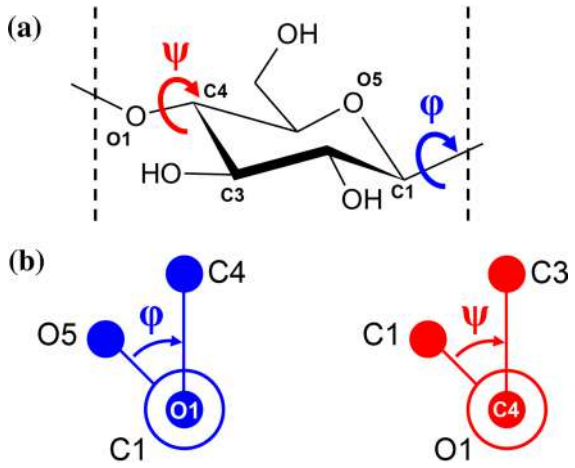


**Fig. 4** **a** Location of torsional angles φ and ψ in glycosidic bonds of cellulose. **b** Definition of atoms involved in φ and ψ angles according to Newman projection representation. The torsional angles φ and ψ are defined graphically in the representation of the cellulose monomer (AGU), together with its definition in the Newman projections

instead of the application a unique large deformation step allows the system to accommodate after each deformation increment, avoiding thus the generation of unrealistic overstresses that conducted to an unreliable estimation of the properties of the system. The deformation of the system is conducted by changing the box dimensions in the direction under study while keeping the rest of dimensions fixed (e.g. the box dimension X is changed in order to apply a $\varepsilon_{11}$ strain on each model). The atomic coordinates are remapped after each increment of deformation and further minimized by the application of molecular mechanics using the FIRE (Fast Inertial Relaxation Engine) algorithm (Bitzek et al. 2006) for 10,000 iterations to accommodate the atoms in an energy minimized structure. The systems were deformed up to four different final strains in separated simulations, i.e. 2.5%, 5%, 10% and 15%. Once the systems were deformed up to one of these final target deformations, then they were compressed by application of a series of deformation decrements in the opposite way back to 0% of strain. During the extension simulations, the deformation was applied initially in increments of 0.3% up to a total 4.2% and later in increments of 1.0%, as in the case of the compression simulations. The stress of the system and the number of hydrogen bond interactions were monitored at each stage of deformation to reproduce the stress–strain and hydrogen bonds versus strain curves.

**Table 1** Interaction energy assessment

| Interaction | Total, (J/m$^2$) | Van der Waals | | Coulombic | |
|---|---|---|---|---|---|
| | | J/m$^2$ | % | J/m$^2$ | % |
| Cellulose-$CaCO_3$ | −1.119 | −0.159 | 14 | −0.960 | 86 |

The first column indicates the type of interaction evaluated and the next columns the resulted total energy (in J/m$^2$), the van der Waals energy in J/m$^2$ and percentage, and the last two columns indicate the Coulombic energy in J/m$^2$ and percentage

## Conformational analysis

The conformation of cellulose molecules was assessed from the analysis of the torsional angles involved in the glycosidic bonds, which determine the relative orientation between two adjacent glucopyranose rings. These torsional angles (i.e. dihedral) are referred as φ (phi) and ψ (psi) (Sankaranarayanan et al. 2015; Nivedha et al. 2016), and were defined as follows:

$$\varphi \rightarrow O5 - C1 - O1 - C4' \tag{7}$$

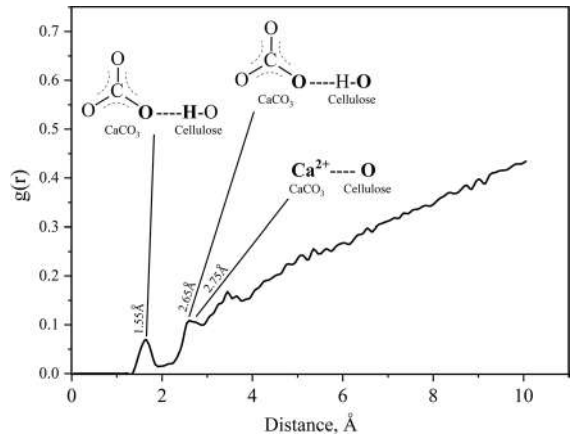


**Fig. 5** Radial distribution function (RDF) of interaction between cellulose and calcium carbonate nanoparticle. In this graph it is depicted a representation of the pair interactions associated to each one of the peaks by considering the molecular structures of the groups in the nanocomposite model

$$\psi \rightarrow C1 - O1 - C4' - C3' \tag{8}$$

Figure 4 shows a graphic representation of the definition of φ and ψ angles, indicating the orientation for the calculus of the angle value according to Newman projection representations:

## Results and discussion

### Interaction between cellulose and calcium carbonate

The interaction energy between cellulose and calcium carbonate was calculated from the nanocomposite model as shown in Table 1. The van der Waals and Coulombic components have also been calculated, and the results have been normalized by the area involved. The negative value of the total interaction energy indicated that the cellulose and the calcium carbonate had an attractive interaction, i.e., there is compatibility between both components. On the one hand, it is observed that the Coulombic component is dominant compared to the van der Waals component in the interaction between cellulose and calcium carbonate, which indicated that the electrostatic interactions dominated over the dispersive forces. The radial distribution function (RDF) determined between cellulose and the calcium carbonate nanoparticle (see Fig. 5) showed two specific interactions at 1.55 Å and 2.65 Å, which were due to the electrostatic interaction between the hydroxyl group in the cellulose molecules and the oxygen atom of the carbonate ion, and a third specific interaction at 2.75 Å due to the electrostatic interaction between the calcium ion and the oxygen atoms in cellulose (either in hydroxyl or ether). These results are in agreement with experimental studies described in the literature in which a good absorption and interaction between cellulose and calcium carbonate has been reported (Dalas et al. 2000; Vilela et al. 2010). On the other hand, Fimbel and Siffert (Fimbel and Siffert 1986) determined that the adsorption of carbonate on cellulose was mainly governed by the electrostatic interaction energy, which is in agreement with the results presented here and validate, at least qualitatively, the models developed in the present study. The electrostatic mechanism of interaction between calcium carbonate and cellulose would also explain the selectivity found on the precipitation of calcium carbonate towards the carboxyl group on the surface of cellulose fibers (Vilela et al. 2010), since these chemical groups are partially dissociated in water.

**(a)**

$$C = \begin{pmatrix} 13.6 & 4.8 & 4.6 & 0.0 & -0.1 & 0.0 \\ 4.8 & 12.6 & 4.5 & 0.2 & -0.1 & 0.3 \\ 4.5 & 4.4 & 12.2 & 0.1 & -0.2 & 0.3 \\ -0.1 & 0.2 & 0.2 & 4.2 & 0.1 & -0.1 \\ -0.2 & -0.1 & -0.2 & 0.1 & 4.1 & 0.1 \\ -0.1 & 0.3 & 0.2 & -0.1 & 0.1 & 3.9 \end{pmatrix}$$

**(b)**

$$C = \begin{pmatrix} 15.8 & 6.1 & 5.6 & 0.2 & 0.4 & 0.1 \\ 6.0 & 15.5 & 5.4 & 0.2 & 0.0 & -0.5 \\ 5.5 & 5.4 & 14.0 & -0.1 & 0.3 & -0.4 \\ 0.2 & 0.2 & 0.0 & 5.2 & -0.1 & 0.0 \\ 0.4 & 0.0 & 0.3 & -0.1 & 4.6 & 0.1 \\ 0.1 & -0.5 & -0.3 & 0.1 & 0.1 & 4.6 \end{pmatrix}$$

**Fig. 6** Elastic matrix obtained from MD simulations for the **a** pure cellulose and **b** nanocomposite systems. The stiffness matrices for the neat cellulose and nanocomposite matrix are represented, showing the specific value of the 6×6 coefficients calculated from the MD simulations

### Evaluation of the elastic mechanical properties

The elastic stiffness matrix obtained for the pure cellulose and nanocomposite systems are shown in Fig. 6, whereas a summary of the main elastic constants obtained from the stiffness matrix are collected in Table 2. The values obtained for pure cellulose are consistent with those reported in the

**Table 2** Summary of elastic matrix constants

| Model | $E_{11}$, (GPa) | $E_{22}$, (GPa) | $E_{33}$, (GPa) | $\nu_{12}$ | $\nu_{13}$ | $\nu_{23}$ | $G_{12}$, (GPa) | $G_{13}$, (GPa) | $G_{23}$, (GPa) | K, (GPa) |
|---|---|---|---|---|---|---|---|---|---|---|
| Neat cellulose | 11.0 | 10.1 | 9.9 | 0.29 | 0.27 | 0.27 | 4.2 | 4.1 | 3.9 | 7.9 |
| $CaCO_3$ nanocomposite | 12.4 | 12.2 | 11.2 | 0.29 | 0.28 | 0.27 | 5.2 | 4.6 | 4.6 | 9.4 |

The first column of the table indicates the type of model evaluated. Next to these columns are collected the properties of these models in terms of elastic constants $E_{11}$ (in GPa), $E_{22}$ (in GPa), $E_{33}$ (in GPa), Poisson's ratio $\nu_{12}$ (unitless) $\nu_{13}$ (unitless), $\nu_{23}$ (unitless), and shear modulus $G_{12}$ (in GPa), $G_{13}$ (in GPa) and $G_{23}$ (in GPa)

literature (Chen et al. 2004a). The Young's modulus of pure cellulose on the tensile stress conditions are reported in the range 12–27 GPa (Quesada Cabrera et al. 2011), or even lower depending on the type of sample and preparation (5–9 GPa) (Hancock et al. 2000). This modulus is very dependent on the crystallinity of the cellulose, amongst other factors such as relative humidity and porosity (Hancock et al. 2000), i.e. on the relative orientation of the cellulose molecules. According to the contiguity model (Ganster et al. 1994), the volume fraction of crystals $V_C$ (i.e. crystallinity) could be calculated as

$$V_C = \frac{\overline{E} - \overline{E}_a}{\Theta \cdot \left(\overline{E + E_a \cdot \xi}\right)} \tag{9}$$

where $\overline{E}$ is the mean longitudinal modulus of the material, $\overline{E}_a$ is the amorphous modulus, $\xi$ is the contiguity parameter and $\Theta$ is defined by the expression

$$\Theta = \frac{\overline{E}_c - \overline{E}_a}{\overline{E}_a + \xi \cdot \overline{E}_a} \tag{10}$$

where $\overline{E}_c$ is the crystalline modulus of cellulose. Taking the values of 128GPa (Sakurada et al. 1962) and 5 GPa (Eichhorn and Young 2001) for the crystalline and amorphous moduli and a value of 5 for the contiguity parameter (Eichhorn and Young 2001), the volume fraction of crystals $V_c$ for the pure cellulose model developed in the present study would be of 0.19, i.e. a crystallinity of 19%, considering an average elastic modulus $\overline{E}$ of 10.3 GPa. In other words, the pure cellulose model developed in this study is essentially amorphous with low degree of orientation or alignment between the molecules, which is the source of crystallinity in cellulose materials. In the same direction, the Poisson's ratio is also very dependent on the crystallinity and phase as stated by Nakamura et al. (Nakamura et al. 2004) who determined values of 0.38, 0.30 and 0.46 for the Poisson's ratio for different cellulose crystalline forms. In the present study, an average value of 0.28 was determined for the Poisson's ratio, which would be in agreement with the reported experimental values considering also the low crystallinity of 19% estimated for this model.

The inclusion of the calcium carbonate nanoparticle on the cellulose matrix clearly had an impact on its elastic mechanical properties. Either the Young's, shear or bulk modulus were increased to 11.9 GPa, 4.8 GPa and 9.4 GPa in average, which supposed an increment of 15%, 18% and 19% respectively compared to the neat cellulose. The Poisson's ratio was not changed and the nanocomposite system showed a value of 0.28 as the neat cellulose model. In the papermaking industry, it is usually recognized that the strength properties of paper, whose structure is a network of cellulose fibers, are reduced by increasing the paper ash content (i.e. the calcium carbonate content) (Mohamadzadeh-Saghavaz et al. 2014). This fact is usually related to the deterioration of the fibre-to-fibre bond (Mohamadzadeh-Saghavaz et al. 2014), among other mechanisms. Nevertheless, the MD results presented here are in the opposite direction, considering either

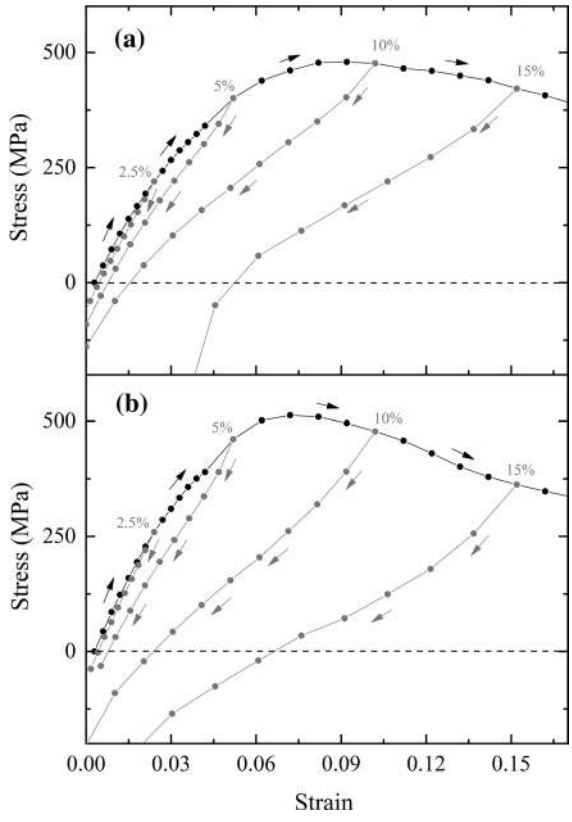


**Fig. 7** Stress–strain curves during extension and compression simulations for **a** neat cellulose and **b** $CaCO_3$ composite. The curves shown in this figure are the stress versus strain values obtained during the extension and compression simulations of the neat cellulose and calcium carbonate nanocomposite systems

the interaction energy and mechanical properties. This duality observed in the behavior of calcium carbonate towards the performance of its cellulose composites could be explained by the strength factor that relates with the mechanical properties of a material made of fibers (Sáenz Ezquerro et al. 2019), which is stated as:

$$\text{Strength factor} = \text{RBA}_{\text{m}} \cdot (\text{density of interactions}) \tag{11}$$

where $\text{RBA}_{\text{m}}$ is the relative bonded area between the fibers of the material system. This factor establishes that the strength in a fibrous material is a combination of the area in contact between the fibers and the number of interactions per unit of area in the material. The MD simulations showed that there exists a favorable interaction between the cellulose and the calcium carbonate, so the limiting parameter in the strength factor would be the $\text{RBA}_{\text{m}}$ (i.e. the area in contact). Precisely, Chen et al. (2011) indicated that the form of the calcium carbonate affected the strength properties of paper depending on how the calcium carbonate particles adapted and embedded between the fibers. In other words, the form of calcium carbonate (e.g. whiskers, spheres) affected thus to the effective area in contact between fibers which would explain, depending on the global balance of the area in contact, why calcium carbonate could improve or deteriorate the strength properties of cellulose-based fibrous materials. For this reason, several experimental studies also found an improvement on the mechanical properties of paper due to the reinforcing of calcium carbonate particles (Chen et al. 2011; Mohamadzadeh-Saghavaz et al. 2014), which confirmed the results of the MD simulations presented here.

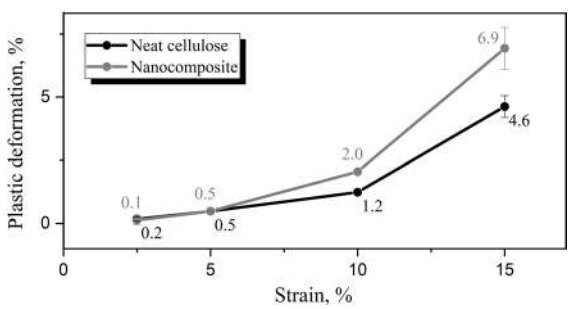


**Fig. 8** Plastic deformation after extension and compression simulations. In this graph the plastic deformation that remain after the extension and compression simulations of either the neat cellulose or calcium carbonate nanocomposite model is represented for each level of applied strain

## Strain recovery assessment through extension and compression simulations

The elastic mechanical properties shown previously were obtained at low deformations of the material. The next type of simulations were obtained by extending the simulations to higher deformations and then compressed back to the initial state. In Fig. 7 the stress–strain curves generated during these extension and compression simulations for the pure cellulose and nanocomposite systems are shown. As it was previously described, the systems were initially deformed (strained) in separated extension simulations up to four different final deformations (2.5%, 5.0%, 10% and 15%) and after that the systems were compressed back to the initial dimensions. During the extension simulations at low levels of deformation (below 2.5%) either the neat cellulose or the nanocomposite systems exhibited a linear stress–strain behavior (i.e., elasticity), which was also observed in the compression curve, since it was very close to the extension curve (i.e., no hysteresis mechanism). When the applied strain in the extension simulation was higher than 2.5% the compression curve did not follow the extension curve and tended to be further away (i.e., not superposed), which indicated that there existed a hysteresis mechanism. This fact also implied that the state at which the stress of the system became zero during the compression simulations had a different length than the original, exhibiting thus a permanent or plastic deformation. In Fig. 8 the results of plastic deformation versus applied strain are plotted. Below applied strains of 5.0% the remanent plastic deformation of both material systems was below 0.5%, which indicated an elastic behavior at this range of deformations. Nevertheless, when the applied strain increased the plastic deformation increased as well over 1.0%, which indicated that the elastic limit had been overcome and the materials experienced an elastoplastic behavior. Besides, the presence of the calcium carbonate nanoparticle produced an additional increase on the remanent plastic deformation of the material after the extension and compression simulations respect to the neat cellulose. In other words, the presence of calcium carbonate nanoparticle

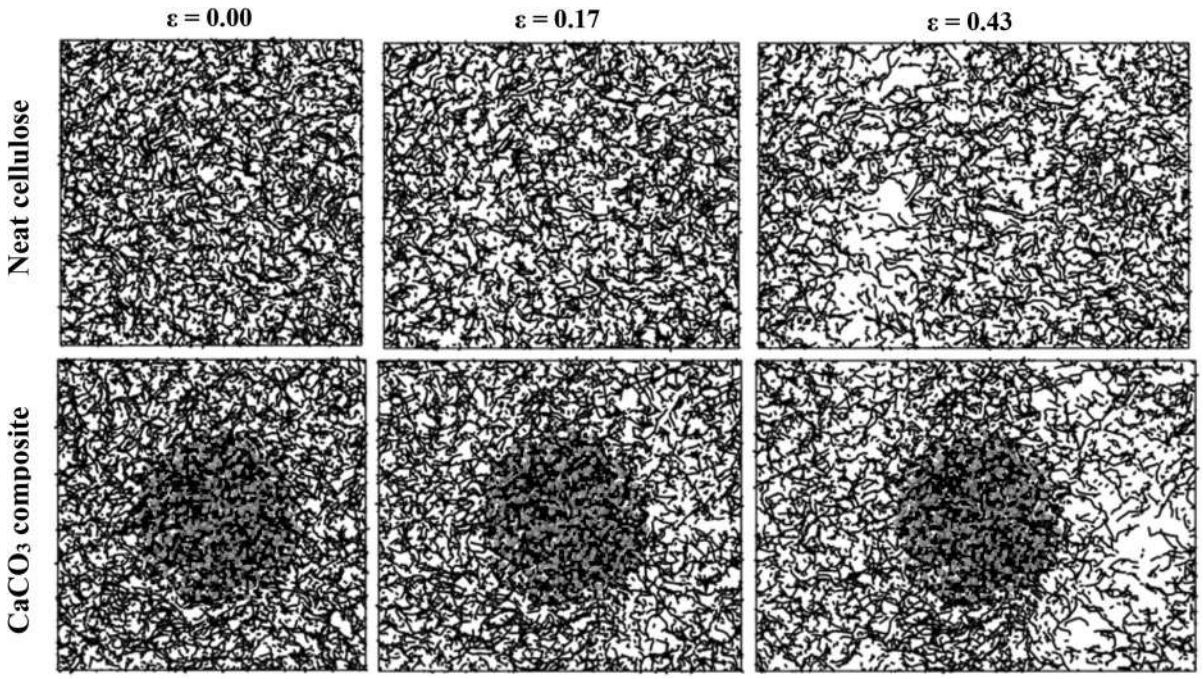


**Fig. 9** Graphic representation of hydrogen bond interactions during extension simulations. A rendering of the hydrogen bond network obtained at different levels of deformation during the extension simulations is shown for the neat cellulose and calcium carbonate nanocomposite models, respectively

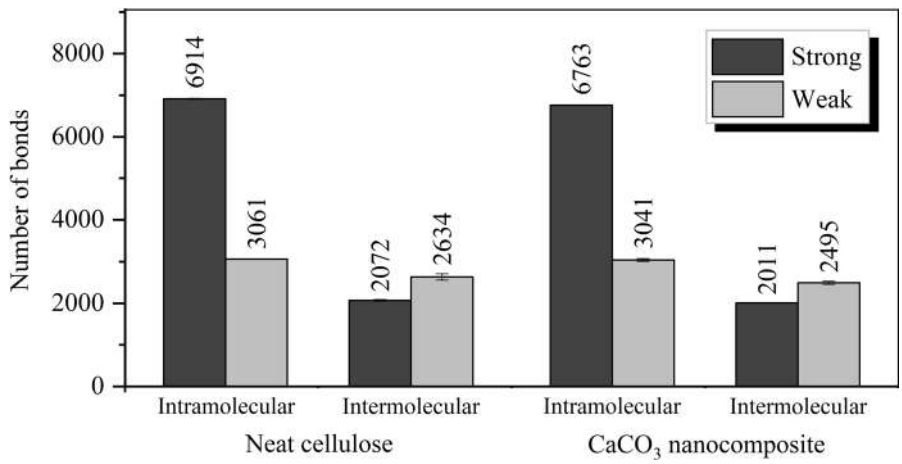


**Fig. 10** Average number of hydrogen bonds at equilibrium state. A column graphic is shown in which the average number of hydrogen bonds of the neat cellulose and calcium carbonate nanocomposite model is plotted, in terms of intramolecular and intermolecular

decreased the flexibility of the cellulosic material system. This type of simulations were also carried out by Chen et al. (2004a, b, 2007) to assess the flexibility of cellulose models and the effect of different cross-linking moieties. These authors obtained a similar curve for the neat cellulose system either in terms of calculated stress and strain values, and even predicted similar plastic deformation of the material as has been obtained in the present study after the extension and compression simulations using a different force field (Chen et al. 2004a).

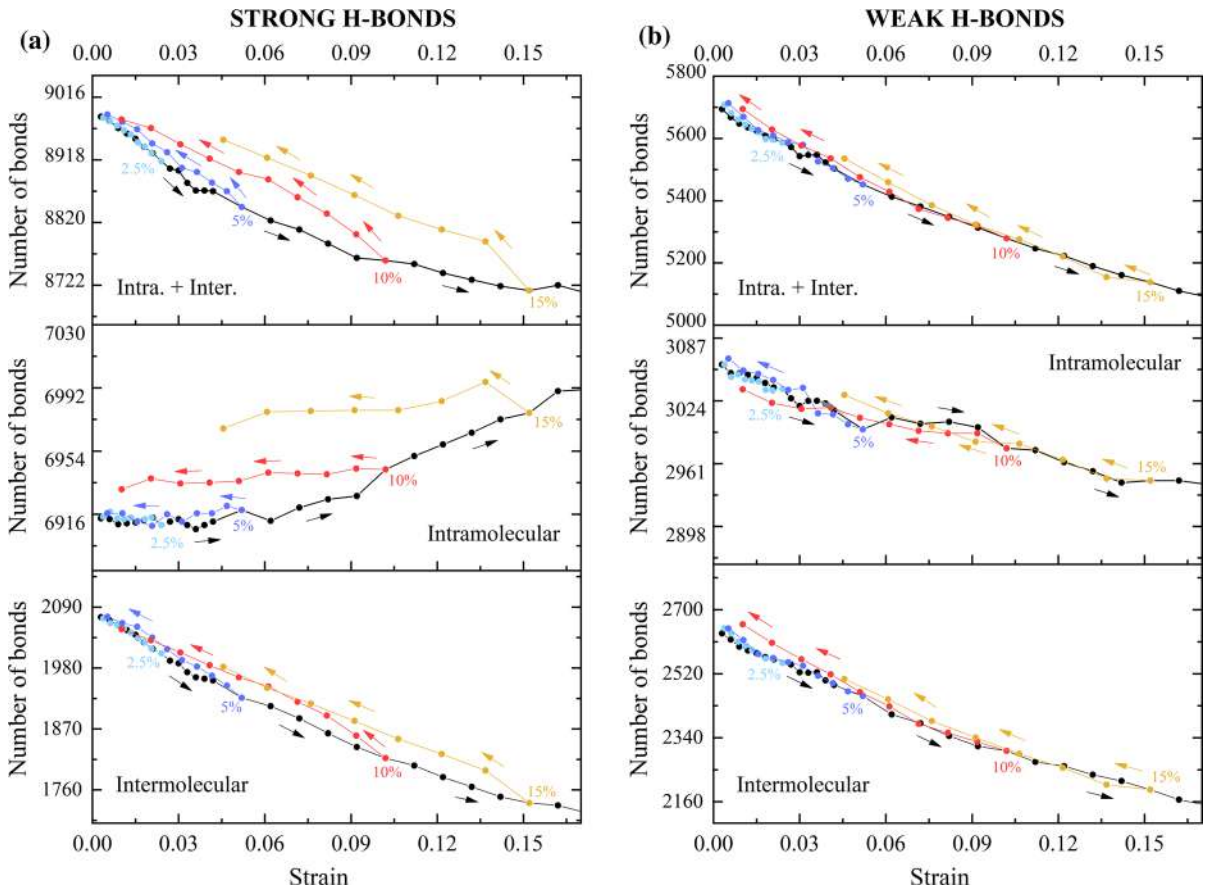


**Fig. 11** Number of **a** strong and **b** weak hydrogen bond interactions during extension and compression simulations for pure cellulose. In this figure a total of six graphics are plotted, each one showing the evolution of the number of hydrogen bonds during the extension and compression simulations of the neat cellulose model in terms of strong and weak bonds, and split into intramolecular, intermolecular and total number of bonds in each case

## Assessment of hydrogen bond interactions during extension and compression simulations

Together with the stress, the number of hydrogen bonds was also monitored during the extension and compression simulations. As was pointed out previously, two types of hydrogen bonds (i.e. weak and strong) were considered depending on the distance between the acceptor atom and hydrogen. In Fig. 9 a graphic representation of the evolution of hydrogen bonds, considering the total number obtained by the sum of strong and weak interactions, at different strain states during the extension simulations is shown for the neat and nanocomposite systems. In this representation it is possible to observe the formation of failure regions in form of cavities in which there were no hydrogen bonding when increasing the deformation of the material systems, and which were responsible of the decrease of the stress in the system. From Fig. 10, where the total number of hydrogen bonds is summarized, it can be observed that the majority of the hydrogen bonds corresponded to the intramolecular interactions, which agreed with other molecular dynamic simulation studies (Ren et al. 2021). On the other hand, it was observed a decrease of around 3% in the total number of hydrogen bonds, which comes from the sum of either strong and weak bonds, due to the presence of the $CaCO_3$ nanoparticle in comparison with the neat cellulose, indicating thus that the calcium carbonate was less active towards the hydrogen bond formation than the cellulose itself. This effect of calcium carbonate on the hydrogen

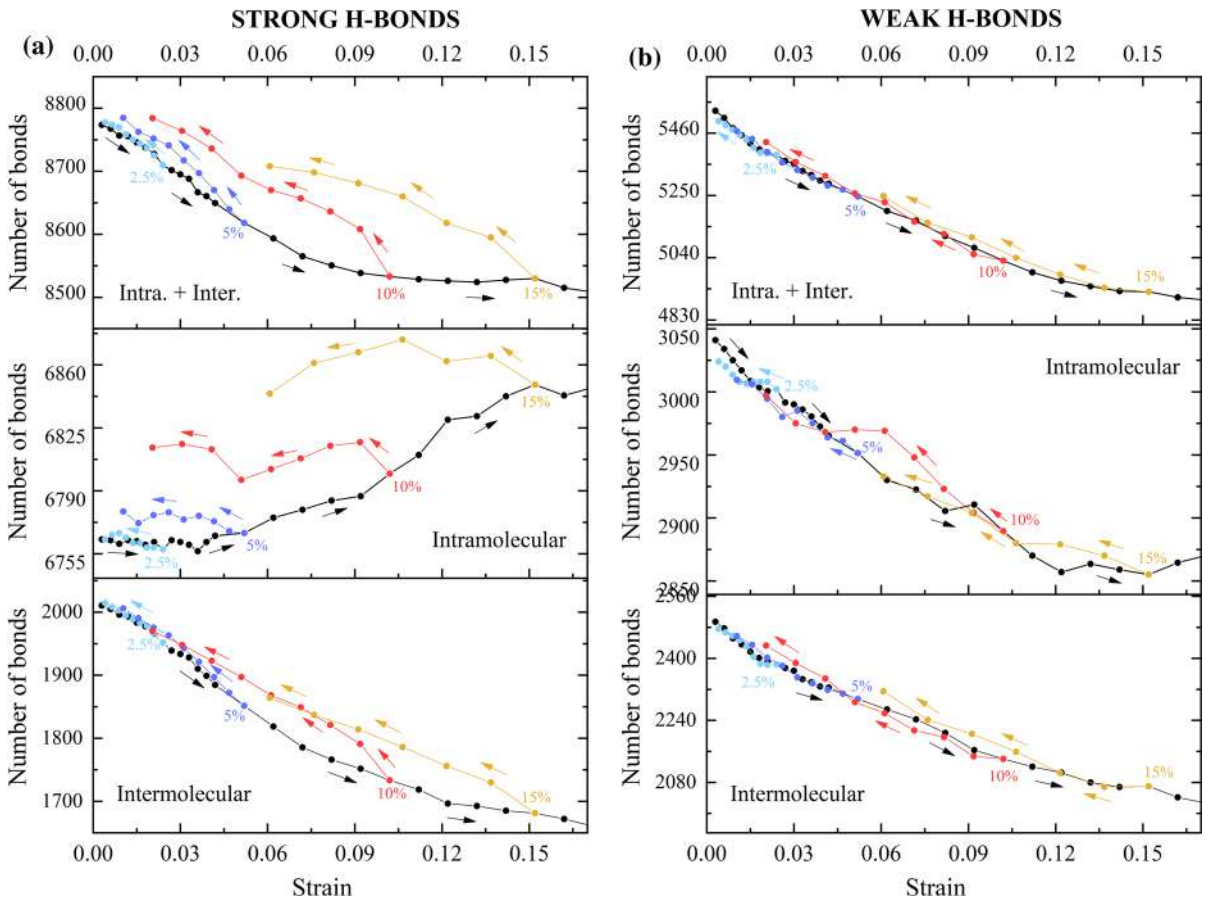


**Fig. 12** Number of **a** strong and **b** weak hydrogen bond interactions during extension and compression simulations for $CaCO_3$ composite. In this figure a total of six graphics are plotted, each one showing the evolution of the number of hydrogen bonds during the extension and compression simulations of the calcium carbonate nanocomposite model in terms of strong and weak bonds, and split into intramolecular, intermolecular and total number of bonds in each case

bonding of cellulose has been applied experimentally in other studies found on the scientific literature to increase the adsorption capacity of fluff pulp (Xu et al. 2017).

The evolution of the number of hydrogen bonds during the recovery simulations is plotted in Fig. 11 and Fig. 12 for the neat and nanocomposite systems respectively. In these figures up to six plots can be found, since the assessment of hydrogen bonds was split into strong and weak, regarding to its length distance, and then divided into total, intramolecular and intermolecular attending to the position of the hydrogen bond in the molecules. The tendency observed in the evolution of the number of hydrogen bonds was similar in either the neat cellulose or calcium carbonate composite, except for the fact that the number of bonds in the composite system was below the neat cellulose system as indicated previously. The important points to check in these curves were the tendency on the number of bonds respect to the deformation (i.e., negative or positive), and how the extension and compression curves superpose each other (i.e., presence or not of a hysteresis mechanism). In the case of the strong hydrogen bonds (Fig. 11a and Fig. 12a) it was observed that the intramolecular bonds tended to increase while the deformation increased, while the opposite tendency was observed for the intermolecular bonds. When the systems were compressed back to the relaxed state, a hysteresis effect was observed in the intramolecular bonds, while the evolution of intermolecular bonds was parallel to the original curve, although not totally superposed. The

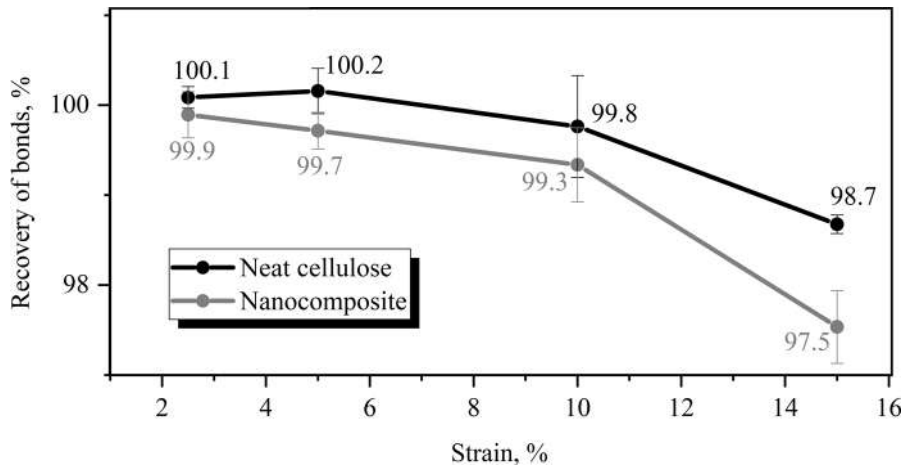


**Fig. 13** Summary of recovery of total (weak + strong) number of hydrogen bonds after extension and compression simulations. In this graph the recovery of hydrogen bonds at each strain is plotted for the neat cellulose an nanocomposite systems

positive tendency and hysteresis mechanism found in the intramolecular bonds indicated that the deformation of the material produced a reorganization of the molecules into a new conformation which was maintained even after the systems were compressed back (i.e., the original geometry was no recovered). This fact was especially important at deformations higher than 5%. The evolution of the total number of bonds was dominated by the intermolecular ones, since they showed a similar tendency. When considering the weak bonds (Fig. 11b and Fig. 12b), the situation was simpler than that found with the strong bonds. The number of hydrogen bonds, either intramolecular or intermolecular, always decreased while the extension deformation increased, and no hysteresis effect was found later since the compression curve was superposed with the extension curve. Given that the hysteresis mechanism is related to a non-reversible process, the fact that the hysteresis was mainly found only in the strong intramolecular hydrogen bonds indicated in this way that the deformation process would have produced irreversible conformational changes within the cellulose molecules, since these type of hydrogen bonds are mainly located between hydroxyl and/or ether groups located at close positions in the molecule (e.g., O2-H···O3 or O2-H···O5) (Nishiyama et al. 2008). The conformational analysis was assessed trough the phi (φ) and psi (ψ) angles as it is described later in the text.

Comparing the initial and final number of hydrogen bonds it was possible to calculate the recovery of hydrogen bonds as:

$$Recovery\ H.Bond(\%) = \frac{N}{N_0} \cdot 100 \tag{12}$$

where $N$ is the number of hydrogen bonds of the system where the stress became zero during the compression simulation and $N_0$ is the initial number of hydrogen bonds of the system. A value of recovery over 100% indicates that new bonds were created after the deformation process, while a value below 100% reflects that there was produced a loss of hydrogen bonds respect to the original number. A summary of the recovery of hydrogen bonds in terms of the total number of bonds, obtained from the sum of weak and strong interactions, is plotted in Fig. 13. At deformations below 5% the curves of both materials (i.e. neat cellulose and nanocomposite) were statistically similar, but at deformations higher than 5% the nanocomposite system exhibited lower recovery values, coherent with the results of plastic deformation described previously A deeper analysis of hydrogen bonds recovery can be found in the supplementary material (Fig. S1). In summary, the calcium carbonate nanoparticle did not affected significatively the behavior of the hydrogen bonds towards the deformation as has been described previously, so the higher plastic deformation and lower hydrogen bond recovery values observed in the nanocomposite system in comparison with the neat cellulose would be explain due to a disruption of the network of hydrogen bonds and the associated decrease on the number of possible interactions with the calcium carbonate nanoparticle.

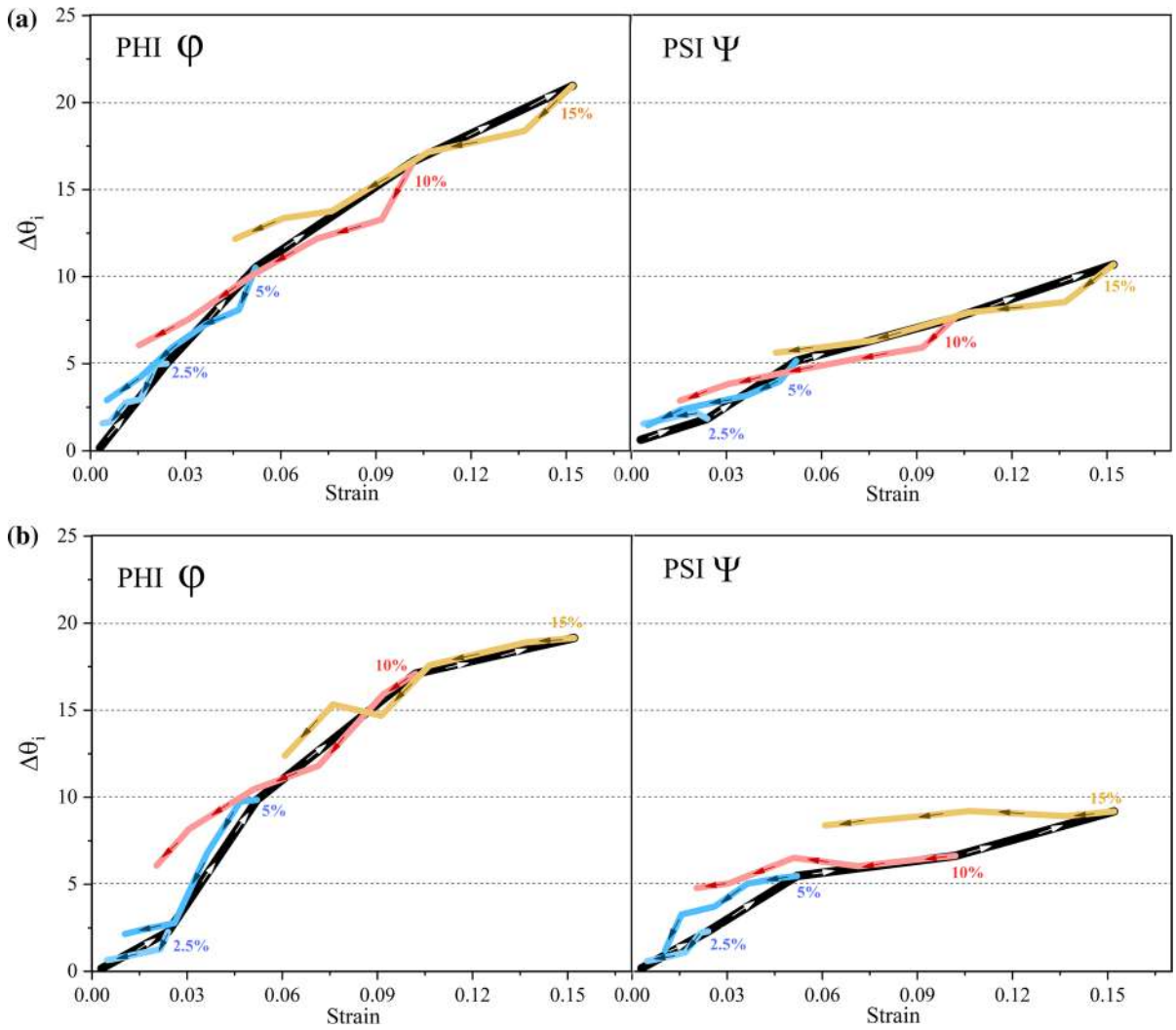


**Fig. 14** Variation (delta values $\Delta\Theta_i$) of φ and ψ angles during the extension (black line) and compression (color lines) simulations for **a** neat cellulose and **b** $CaCO_3$ nanocomposite. In this figure curves showing the evolution of the variation of φ and ψ torsional angles are plotted during the extension and compression simulations for the neat cellulose and nanocomposite

## Conformational analysis

The conformation analysis was made in the basis of the values of φ (phi) and ψ (psi) torsional angles, as were defined in Fig. 4. Initially, the phi-psi map (i.e. the Ramachandran plots) were obtained from each of the relaxed structures, as it is shown in Fig. S2 (see supplementary material). A total of 31,121 points make up each plot and each data point represents the combination of φ and ψ angles occurring in a glycosidic bond of the cellulose molecules. The plots were similar in both systems, indicating that the calcium carbonate nanoparticle had no significant effect on the conformation of cellulose molecules in the composite system. In both systems the torsional angles were mainly found at two consecutive oval regions in the ranges of φ/ψ of approximately (−225, −120)/(−150, −15) and (−120, −15)/(−150, −15). These values were similar to those found for cellobiose using quantum mechanical calculations at B3LYP/6-31+G(d) level (French et al. 2021).

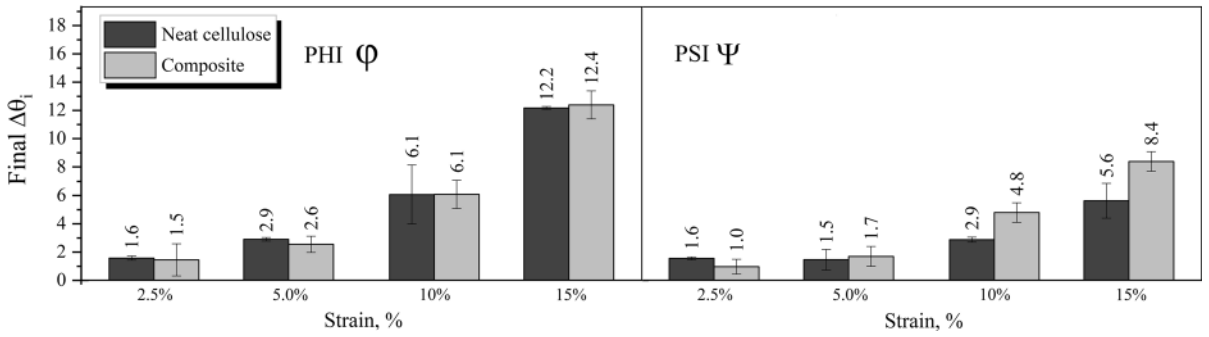


**Fig. 15** Final values of $\Delta\Theta_i$ for φ and ψ angles after extension and compression simulations**.** In this graph the final values of $\Delta\Theta_i$ for φ and ψ torsional angles after the deformation process are plotted

During the extension and compression simulations, the values of φ and ψ were also monitored at the different deformation states to check for possible conformation changes of the cellulose molecules. These changes were calculated as delta values ($\Delta\Theta_i$) respect to the initial values of the φ and ψ angles as stated next,

$$\Delta\Theta_i(\varepsilon) = abs\left(\Theta_0 - \Theta_\varepsilon\right) i = \varphi, \psi \tag{13}$$

where $\Theta_i$ refers to φ or ψ angles, ε is the deformation, abs indicate the absolute value, $\Theta_0$ the angle value at the relaxed state (i.e. $\varepsilon = 0$) and $\Theta_\varepsilon$ is the angle value at the ε deformation. These delta values were averaged over all the monitored φ/ψ angles and the average was plotted versus the applied deformation as shown in Fig. 14. As can be observed, during the extension simulation the delta value $\Delta\Theta_i$ increased while the strain increased in both systems and both torsional angles, indicating that there was produced a finite change in the conformation of the cellulose molecules due to this deformation. The variations found in φ angles were higher than those produced in the ψ angles. When the systems were compressed back, the delta value $\Delta\Theta_i$ decreased, i.e. the torsional angles tended to their initial values. Nevertheless, as occurred with the hydrogen bonds, the final values of $\Delta\Theta_i$ (i.e. the recovery of the torsional angles) depended on the applied deformation. The final values of $\Delta\Theta_i$ after the extension and compression simulations have been summarized in Fig. 15. As can be seen, the final $\Delta\Theta_i$ increased with the deformation or, in other words, the recovery of the conformation of the molecules (i.e. their original torsional angle values) was lower when the applied deformation increased, with an exponential tendency for both types of torsional angles. These results agreed with the evolution observed in the strong intramolecular hydrogen bonds (i.e., those mainly located at close positions within a molecule) and explained the hysteresis mechanism associated with this type of bonds at deformations higher than 5%. No significative differences were observed between the neat and nanocomposite systems, which indicated that the calcium carbonate nanoparticle not affected to the conformation of cellulose molecules itself. In brief, the results of the assessment of torsional angles revealed that the tensile deformation of the cellulosic materials, either neat and nanocomposite, produced irreversible conformational changes within the cellulose molecules which contributed to the plastic deformation in the systems.

## Concluding remarks

The present study addressed the preparation and characterization of amorphous cellulose composites molecular models to analyze the effect of the presence of a calcium carbonate ($CaCO_3$) nanoparticle on its mechanical properties, either in the elastic region or beyond the elastic limit in the plastic regime, for which the hydrogen bond interactions and torsional angles were monitored to understand in a molecular level the deformation process. It was observed that the interaction of the cellulose matrix with the calcium carbonate nanoparticle was favorable (i.e., attractive), with the electrostatic contribution being dominant

over the van der Waals component as was obtained either from the analysis of the interaction energy or RDF. The crystallinity of 19% for the neat cellulose model was calculated from the values of the mechanical elastic constants using the contiguity model equations, which was in agreement with the calculated Poisson's ratio value. In addition, the elastic constants determined for the neat calcium carbonate model also agreed with the reported values in the literature. The inclusion of the $CaCO_3$ nanoparticle gave place to an increase on the rigidity of the composite system, which indicated that the calcium carbonate would potentially contribute to an improvement of the mechanical properties of the cellulose composite. Extension and compression simulations were in the same way conducted to study the effect of tensile deformation on the recovery capacity of the material systems in terms of remanent plastic deformation. At strains below 5% either the neat cellulose or $CaCO_3$ nanocomposite exhibited an elastic behavior (i.e., lineal stress–strain relationship), with the remanent plastic deformation taking nearly-zero values. Nevertheless, when the applied strain was higher than 5%, an elastoplastic behavior was observed in both material systems, and the plastic deformation increased. The presence of the $CaCO_3$ nanoparticle produced higher values of plastic deformation in the composite material compared to the neat cellulose system and decreased thus the flexibility of the material. Through the analysis of the evolution of hydrogen bond interactions and torsional angle conformation during the extension and compression simulations, it was possible to identify the presence of a hysteresis mechanism on the strong intramolecular bonds (i.e., short hydrogen bonds located at close positions within the same molecule), and thus the presence of irreversible conformational changes on the cellulose molecules which would explain the plastic deformation observed after the deformation process. The $CaCO_3$ nanoparticle affected mainly to the number of overall hydrogen bond interactions due to its lower hydrogen bond formation capacity, but not to the evolution of hydrogen bond interactions or to the conformation of cellulose molecules during the deformation process, so the higher plastic deformations observed in the nanocomposite material would be a result of the disruption of the network of hydrogen bonds and the associated decrease on the number of possible interactions.

**Acknowledgments** This work has been granted by Spanish Ministry of Science, Innovation and Universities—State Research Agency—PREFIJO project RTC-2017-6258-5.

**Author contributions** All authors contributed to the study conception and design. Modeling, data collection and analysis were performed by CSE. The first draft of the manuscript was written by CSE and all authors commented on previous versions of the manuscript. All authors read and approved the final manuscript.

**Funding** Open Access funding provided thanks to the CRUE-CSIC agreement with Springer Nature. This work has been granted by Spanish Ministry of Science, Innovation and Universities—State Research Agency—PREFIJO project RTC-2017-6258-5.

**Declarations**

**Competing interest** The authors have no relevant financial or non-financial interests to disclose.



## References

Alves L, Ferraz E, Gamelas JAF (2019) Composites of nanofibrillated cellulose with clay minerals: a review. Adv Colloid Interface Sci 272:101994. https://doi.org/10.1016/j.cis.2019.101994

Ardila-Diaz LD, de Oliveira TV, de Soares NFF (2020) Development and evaluation of the chromatic behavior of an intelligent packaging material based on cellulose acetate incorporated with polydiacetylene for an efficient packaging. Biosensors 10:59. https://doi.org/10.3390/bios10060059

Arunan E, Desiraju GR, Klein RA et al (2011) Definition of the hydrogen bond (IUPAC Recommendations 2011). Pure Appl Chem 83:1637–1641. https://doi.org/10.1351/PAC-REC-10-01-02

Bajpai P (2013) Recycling and deinking of recovered paper. Elsevier

Bazooyar F, Momany FA, Bolton K (2012) Validating empirical force fields for molecular-level simulation of cellulose

dissolution. Comput Theor Chem 984:119–127. https://doi.org/10.1016/j.comptc.2012.01.020
Bearchell CA, Heyes DM (2002) Molecular modelling studies of calcium carbonate and its nanoparticles. Mol Simul 28:517–538. https://doi.org/10.1080/08927020290030116
Bering E, Torstensen JØ, Lervik A, de Wijn AS (2022) Computational study of the dissolution of cellulose into single chains: the role of the solvent and agitation. Cellulose 29:1365–1380. https://doi.org/10.1007/s10570-021-04382-9
Bitzek E, Koskinen P, Gähler F et al (2006) Structural relaxation made simple. Phys Rev Lett 97:170201. https://doi.org/10.1103/PhysRevLett.97.170201
Chen W, Lickfield GC, Yang CQ (2004a) Molecular modeling of cellulose in amorphous state. Part I: model building and plastic deformation study. Polymer 45:1063–1071. https://doi.org/10.1016/j.polymer.2003.11.020
Chen W, Lickfield GC, Yang CQ (2004b) Molecular modeling of cellulose in amorphous state part II: effects of rigid and flexible crosslinks on cellulose. Polymer 45:7357–7365. https://doi.org/10.1016/j.polymer.2004.08.023
Chen W, Wang T, Lickfield GC (2007) Molecular modeling of cellulose in amorphous state. III. An innovative elastomeric crosslink system. J Polym Sci Part B Polym Phys 45:1821–1833. https://doi.org/10.1002/polb.21214
Chen X, Qian X, An X (2011) Using calcium carbonate whiskers as papermaking filler. BioResources 6:13
Ciolacu D, Ciolacu F, Popa VI (2010) Amorphous cellulose - structure and characterization. Cellul Chem Technol 9:13–21
Dalas E, Klepetsanis PG, Koutsoukos PG (2000) Calcium carbonate deposition on cellulose. J Colloid Interface Sci 224:56–62. https://doi.org/10.1006/jcis.1999.6670
DeFoe OK, Compton AH (1925) The density of rock salt and calcite. Phys Rev 25:618–620. https://doi.org/10.1103/PhysRev.25.618
Eichhorn SJ, Young RJ (2001) The Young's modulus of a microcrystalline cellulose. Cellulose 8:197–207. https://doi.org/10.1023/A:1013181804540
Fahmy TYA, Mobarak F (2008) Nanocomposites from natural cellulose fibers filled with kaolin in presence of sucrose. Carbohydr Polym 72:751–755. https://doi.org/10.1016/j.carbpol.2008.01.008
Fimbel P, Siffert B (1986) Interaction of calcium carbonate (calcite) with cellulose fibres in aqueous medium. Colloids Surf 20:1–16. https://doi.org/10.1016/0166-6622(86)80224-4
French AD (2017) Glucose, not cellobiose, is the repeating unit of cellulose and why that is important. Cellulose 24:4605–4609. https://doi.org/10.1007/s10570-017-1450-3
French AD, Montgomery DW, Prevost NT et al (2021) Comparison of cellooligosaccharide conformations in complexes with proteins with energy maps for cellobiose. Carbohydr Polym 264:118004. https://doi.org/10.1016/j.carbpol.2021.118004
Ganster J, Fink H, Fraatz J, Nywlt M (1994) Relation between structure and elastic constants of man-made cellulosic fibers. I: a two phase anisotropic model with contiguity parameter. Acta Polym. https://doi.org/10.1002/ACTP.1994.010450405
Garusinghe UM, Raghuwanshi VS, Batchelor W, Garnier G (2018) Water resistant cellulose – titanium dioxide composites for photocatalysis. Sci Rep 8:2306. https://doi.org/10.1038/s41598-018-20569-w
Gebald C, Wurzbacher JA, Borgschulte A et al (2014) Single-component and binary $CO_2$ and $H_2O$ adsorption of amine-functionalized cellulose. Environ Sci Technol 48:2497–2504. https://doi.org/10.1021/es404430g
Hamad H, Bailón-García E, Morales-Torres S et al (2020) 16 - Cellulose–$TiO_2$ composites for the removal of water pollutants. In: Pacheco-Torgal F, Ivanov V, Tsang DCW (eds) Bio-based materials and biotechnologies for eco-efficient construction. pp 329–358. https://doi.org/10.1016/B978-0-12-819481-2.00016-7
Hancock BC, Clas S-D, Christensen K (2000) Micro-scale measurement of the mechanical properties of compressed pharmaceutical powders. 1: the elasticity and fracture behavior of microcrystalline cellulose. Int J Pharm 209:27–35. https://doi.org/10.1016/S0378-5173(00)00541-X
Holik H, Laufmann M, Hubschmid S (2013) Handbook of paper and board. Handbook of paper and board, 1st edn. Wiley, pp 109–143
Hoover WG (1985) Canonical dynamics: equilibrium phase-space distributions. Phys Rev A 31:1695–1697. https://doi.org/10.1103/PhysRevA.31.1695
Hou T, Shu L, Guo K et al (2020) Cellulose membranes with polyethylenimine-modified graphene oxide and zinc ions for promoted gas separation. Cellulose 27:3277–3286. https://doi.org/10.1007/s10570-019-02962-4
Huang K, Wang Y (2022) Recent applications of regenerated cellulose films and hydrogels in food packaging. Curr Opin Food Sci 43:7–17. https://doi.org/10.1016/j.cofs.2021.09.003
Hynninen V, Chandra S, Das S et al (2021) Luminescent gold nanocluster-methylcellulose composite optical fibers with low attenuation coefficient and high photostability. Small 17:2005205. https://doi.org/10.1002/smll.202005205
Isobe N, Noguchi K, Nishiyama Y et al (2013) Role of urea in alkaline dissolution of cellulose. Cellulose 20:97–103. https://doi.org/10.1007/s10570-012-9800-7
Jian C, Gong C, Wang S et al (2014) Multifunctional comb copolymer ethyl cellulose-g-poly(ε-caprolactone)-rhodamine B/folate: synthesis, characterization and targeted bonding application. Eur Polym J 55:235–244. https://doi.org/10.1016/j.eurpolymj.2014.04.003
Kalidhasan S, Santhana KrishnaKumar A, Rajesh V, Rajesh N (2012) Ultrasound-assisted preparation and characterization of crystalline cellulose-ionic liquid blend polymeric material: a prelude to the study of its application toward the effective adsorption of chromium. J Colloid Interface Sci 367:398–408. https://doi.org/10.1016/j.jcis.2011.09.062
Klemm D, Heublein B, Fink H-P, Bohn A (2005) Cellulose: fascinating biopolymer and sustainable raw material. Angew Chem Int Ed 44:3358–3393. https://doi.org/10.1002/anie.200460587
Krysztof M, Olejnik K, Kulpinski P et al (2018) Regenerated cellulose from N-methylmorpholine N-oxide solutions as a coating agent for paper materials. Cellulose 25:3595–3607. https://doi.org/10.1007/s10570-018-1799-y

Kubicki JD, Mohamed MN-A, Watts HD (2013) Quantum mechanical modeling of the structures, energetics and spectral properties of Iα and Iβ cellulose. Cellulose 20:9–23. https://doi.org/10.1007/s10570-012-9838-6

Li W, Huang S, Xu D et al (2017) Molecular dynamics simulations of the characteristics of sodium carboxymethyl cellulose with different degrees of substitution in a salt solution. Cellulose 24:3619–3633. https://doi.org/10.1007/s10570-017-1364-0

Li Y-Y, Wang B, Ma M-G, Wang B (2018) Review of recent development on preparation, properties, and applications of cellulose-based functional materials. Int J Polym Sci 2018:e8973643. https://doi.org/10.1155/2018/8973643

Liu J, Pancera S, Boyko V et al (2010) Evaluation of the particle growth of amorphous calcium carbonate in water by means of the porod invariant from SAXS. Langmuir 26:17405–17412. https://doi.org/10.1021/la101888c

Liu Y, Ahmed S, Sameen DE et al (2021) A review of cellulose and its derivatives in biopolymer-based for food packaging application. Trends Food Sci Technol 112:532–546. https://doi.org/10.1016/j.tifs.2021.04.016

Ma MG, Liu S, Fu LH (2016) Calcium carbonate and cellulose/calcium carbonate composites: synthesis, characterization, and biomedical applications. Mater Sci Forum 875:24–44. https://doi.org/10.4028/www.scientific.net/MSF.875.24

MacLeod JM, Rosei F (2011) 3.02 - Directed assembly of nanostructures. In: Andrews DL, Scholes GD, Wiederrecht GP (eds) Comprehensive nanoscience and technology. Academic Press, Amsterdam, pp 13–68

Maloney TC, Ataide J, Kekkonen J, et al (2005) Changes to PCC structure in papermaking. Lisbon, p 7

McNaught A, Wilkinson A (1997) Compendium of chemical terminology

Mehandzhiyski AY, Zozoulenko I (2021) A review of cellulose coarse-grained models and their applications. Polysaccharides 2:257–270. https://doi.org/10.3390/polysaccharides2020018

Meldrum FC (2003) Calcium carbonate in biomineralisation and biomimetic chemistry. Int Mater Rev 48:187–224. https://doi.org/10.1179/095066003225005836

Mohamadzadeh-Saghavaz K, Resalati H, Ghasemian A (2014) Cellulose-precipitated calcium carbonate composites and their effect on paper properties. Chem Pap. https://doi.org/10.2478/s11696-013-0513-7

Nakamura K, Wada M, Kuga S, Okano T (2004) Poisson's ratio of cellulose I-beta and cellulose II. J Polym Sci Part B-Polym Phys 42:1206–1211. https://doi.org/10.1002/polb.10771

Nishiyama Y, Johnson GP, French AD et al (2008) Neutron crystallography, molecular dynamics, and quantum mechanics studies of the nature of hydrogen bonding in cellulose Iβ. Biomacromol 9:3133–3140. https://doi.org/10.1021/bm800726v

Nivedha AK, Thieker DF, Makeneni S et al (2016) Vina-Carb: improving glycosidic angles during carbohydrate docking. J Chem Theory Comput 12:892–901. https://doi.org/10.1021/acs.jctc.5b00834

Nosé S (1984) A molecular dynamics method for simulations in the canonical ensemble. Mol Phys 52:255–268. https://doi.org/10.1080/00268978400101201

Paajanen A, Rinta-Paavola A, Vaari J (2021) High-temperature decomposition of amorphous and crystalline cellulose: reactive molecular simulations. Cellulose 28:8987–9005. https://doi.org/10.1007/s10570-021-04084-2

Pashmforoush F, Ajori S, Azimi HR (2020) Interfacial characteristics and thermo-mechanical properties of calcium carbonate/polystyrene nanocomposite. Mater Chem Phys 247:122871. https://doi.org/10.1016/j.matchemphys.2020.122871

Phiri J, Johansson L-S, Gane P, Maloney T (2018) A comparative study of mechanical, thermal and electrical properties of graphene-, graphene oxide- and reduced graphene oxide-doped microfibrillated cellulose nanocomposites. Compos Part B Eng 147:104–113. https://doi.org/10.1016/j.compositesb.2018.04.018

Pinto RJB, Marques PAAP, Barros-Timmons AM et al (2008) Novel $SiO_2$/cellulose nanocomposites obtained by in situ synthesis and via polyelectrolytes assembly. Compos Sci Technol 68:1088–1093

Plimpton S (1995) Fast parallel algorithms for short-range molecular dynamics. J Comput Phys 117:1–19. https://doi.org/10.1006/jcph.1995.1039

Quesada Cabrera R, Meersman F, McMillan PF, Dmitriev V (2011) Nanomechanical and structural properties of native cellulose under compressive stress. Biomacromol 12:2178–2183. https://doi.org/10.1021/bm200253h

Raiteri P, Demichelis R, Gale JD (2015) Thermodynamically consistent force field for molecular dynamics simulations of alkaline-earth carbonates and their aqueous speciation. J Phys Chem C 119:24447–24458. https://doi.org/10.1021/acs.jpcc.5b07532

Raiteri P, Gale JD (2010) Water is the key to nonclassical nucleation of amorphous calcium carbonate. https://pubs.acs.org/doi/full/https://doi.org/10.1021/ja108508k. Accessed 24 Apr 2019

Raiteri P, Gale JD, Quigley D, Rodger PM (2010) Derivation of an accurate force-field for simulating the growth of calcium carbonate from aqueous solution: a new model for the calcite-water interface. J Phys Chem 114:5997–6010

Ren Z, Guo R, Zhou X et al (2021) Effect of amorphous cellulose on the deformation behavior of cellulose composites: molecular dynamics simulation. RSC Adv 11:19967–19977. https://doi.org/10.1039/D1RA02625A

Rie JV, Thielemans W (2017) Cellulose–gold nanoparticle hybrid materials. Nanoscale 9:8525–8554. https://doi.org/10.1039/C7NR00400A

Sáenz Ezquerro C, Crespo Miñana C, Izquierdo S, Laspalas M (2019) A molecular dynamics model to measure forces between cellulose fibril surfaces: on the effect of non-covalent polyelectrolyte adsorption. Cellulose 26:1449–1466. https://doi.org/10.1007/s10570-018-2166-8

Sakurada I, Nukushina Y, Ito T (1962) Experimental determination of the elastic modulus of crystalline regions in oriented polymers. J Polym Sci 57:651–660. https://doi.org/10.1002/pol.1962.1205716551

Salama HE, Abdel Aziz MS (2020) Optimized carboxymethyl cellulose and guanidinylated chitosan enriched with titanium oxide nanoparticles of improved UV-barrier properties for the active packaging of green bell pepper. Int J

Biol Macromol 165:1187–1197. https://doi.org/10.1016/j.ijbiomac.2020.09.254

Sankaranarayanan NV, Sarkar A, Desai UR, Mosier PD (2015) Designing "high-affinity, high-specificity" glycosaminoglycan sequences through computerized modeling. In: Balagurunathan K, Nakato H, Desai UR (eds) Glycosaminoglycans. Springer, New York, pp 289–314

Sepahvand S, Jonoobi M, Ashori A et al (2020) A promising process to modify cellulose nanofibers for carbon dioxide ($CO_2$) adsorption. Carbohydr Polym 230:115571. https://doi.org/10.1016/j.carbpol.2019.115571

Shaghaleh H, Hamoud YA, Xu X et al (2021) Thermo-/pH-responsive preservative delivery based on TEMPO cellulose nanofiber/cationic copolymer hydrogel film in fruit packaging. Int J Biol Macromol 183:1911–1924. https://doi.org/10.1016/j.ijbiomac.2021.05.208

Sharma S, Kumar P, Chandra R (2019) Chapter 1 - introduction to molecular dynamics. In: Sharma S (ed) Molecular dynamics simulation of nanocomposites using BIOVIA materials studio. Elsevier, Lammps and Gromacs, pp 1–38

Sheykhnazari S, Tabarsa T, Ashori A, Ghanbari A (2016) Bacterial cellulose composites loaded with $SiO_2$ nanoparticles: dynamic-mechanical and thermal properties. Int J Biol Macromol 93:672–677. https://doi.org/10.1016/j.ijbiomac.2016.09.035

Stukowski A (2009) Visualization and analysis of atomistic simulation data with OVITO–the Open Visualization Tool. Model Simul Mater Sci Eng 18:015012. https://doi.org/10.1088/0965-0393/18/1/015012

Sun H (1998) COMPASS: an ab initio force-field optimized for condensed-phase applications - overview with details on alkane and benzene compounds. J Phys Chem B 102:7338–7364. https://doi.org/10.1021/jp980939v

Tanaka F, Iwata T (2006) Estimation of the elastic modulus of cellulose crystal by molecular mechanics simulation. Cellulose 13:509–517. https://doi.org/10.1007/s10570-006-9068-x

Torvinen K, Pettersson F, Lahtinen P et al (2017) Nanoporous kaolin—cellulose nanofibril composites for printed electronics. Flex Print Electron 2:024004. https://doi.org/10.1088/2058-8585/aa6d97

Ummartyotin S, Manuspiya H (2015) A critical review on cellulose: from fundamental to an approach on sensor technology. Renew Sustain Energy Rev 41:402–412. https://doi.org/10.1016/j.rser.2014.08.050

Uto T, Yui T (2018) DFT optimization of isolated molecular chain sheet models constituting native cellulose crystal structures. ACS Omega 3:8050–8058. https://doi.org/10.1021/acsomega.8b00834

Vilela C, Freire CSR, Marques PAAP et al (2010) Synthesis and characterization of new $CaCO_3$/cellulose nanocomposites prepared by controlled hydrolysis of dimethylcarbonate. Carbohydr Polym 79:1150–1156. https://doi.org/10.1016/j.carbpol.2009.10.056

Wang L, Tang C, Wang X, Zheng W (2019) Molecular dynamics simulation on the thermodynamic properties of insulating paper cellulose modified by silane coupling agent grafted nano-$SiO_2$. AIP Adv 9:125134. https://doi.org/10.1063/1.5131821

Wohlert M, Benselfelt T, Wågberg L et al (2022) Cellulose and the role of hydrogen bonds: not in charge of everything. Cellulose 29:1–23. https://doi.org/10.1007/s10570-021-04325-4

Xu Y, Jiang C, Duan C, Zhang W (2017) In-situ preparation of nano-calcium carbonate/cellulose fiber composite and its application in fluff pulp. J Eng Fibers Fabr 12:155892501701200320. https://doi.org/10.1177/155892501701200306

Xu Y, Liu X, Jiang Q et al (2021) Development and properties of bacterial cellulose, curcumin, and chitosan composite biodegradable films for active packaging materials. Carbohydr Polym 260:117778. https://doi.org/10.1016/j.carbpol.2021.117778

Ylikantola A, Linnanto J, Knuutinen J et al (2013) Molecular modeling studies of interactions between sodium polyacrylate polymer and calcite surface. Appl Surf Sci 276:43–52. https://doi.org/10.1016/j.apsusc.2013.02.122

Zhao Y, Xu Z, Wang B, Wang J (2019) The inhibition of sodium carboxymethyl cellulose on calcite growth by molecular dynamics simulation. Macromol Theory Simul 28:1900019. https://doi.org/10.1002/mats.201900019

Zhu Q, Wang J, Sun J, Wang Q (2020) Preparation and characterization of regenerated cellulose biocomposite film filled with calcium carbonate by in situ precipitation. BioResources 15:7893–7905. https://doi.org/10.15376/biores.15.4.7893-7905

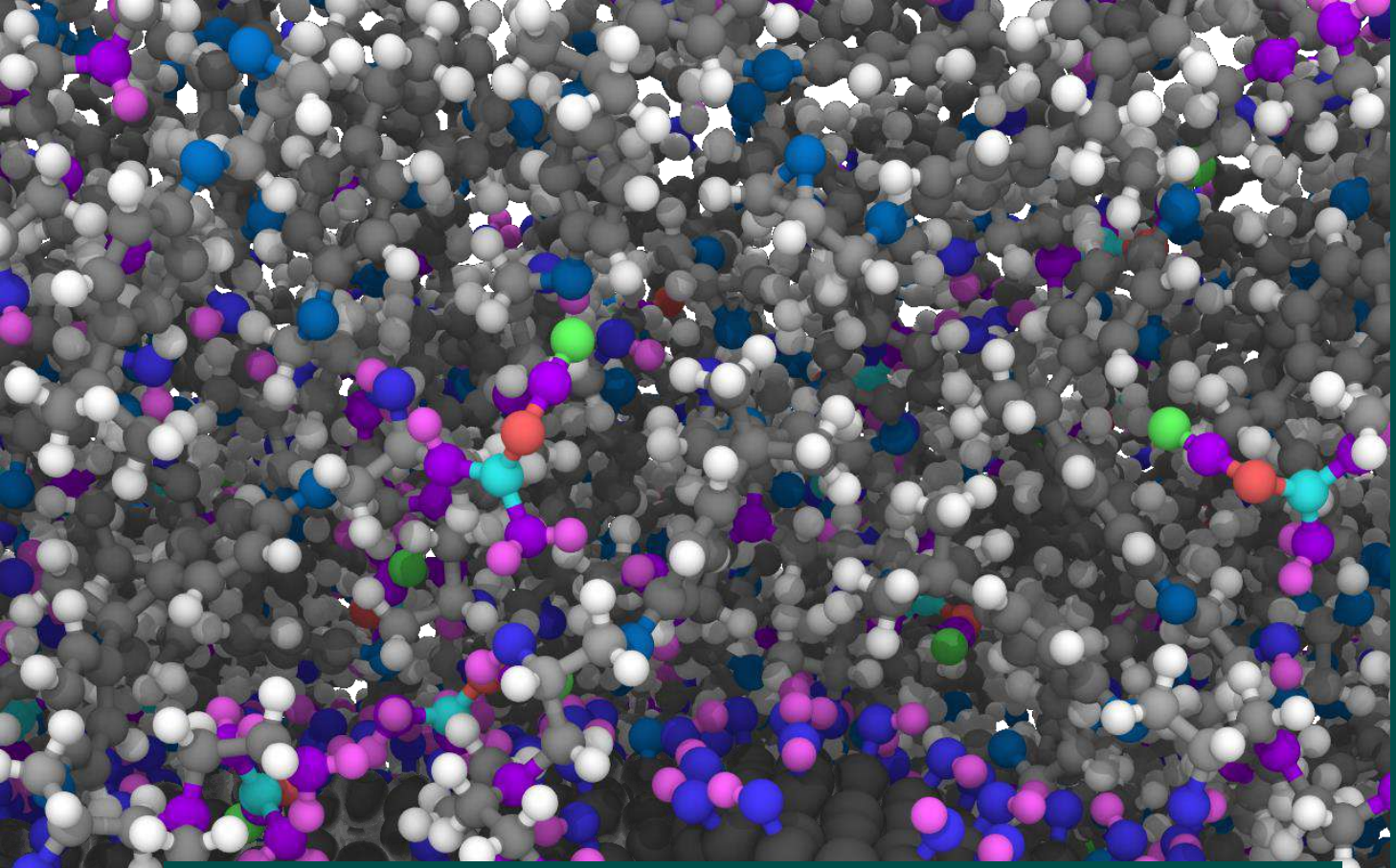

# 8. Publicación III

**Effects of Graphene Oxidation on Interaction Energy and Interfacial Thermal Conductivity of Polymer Nanocomposite: A Molecular Dynamics Approach**

**Fibers,**
**DOI:** 10.3390/nano11071709
**Factor de impacto en 2021**: 3,9
**Área temática**: Materials Science, Multidisciplinary
**Cuartil JCR (2021):** Q3

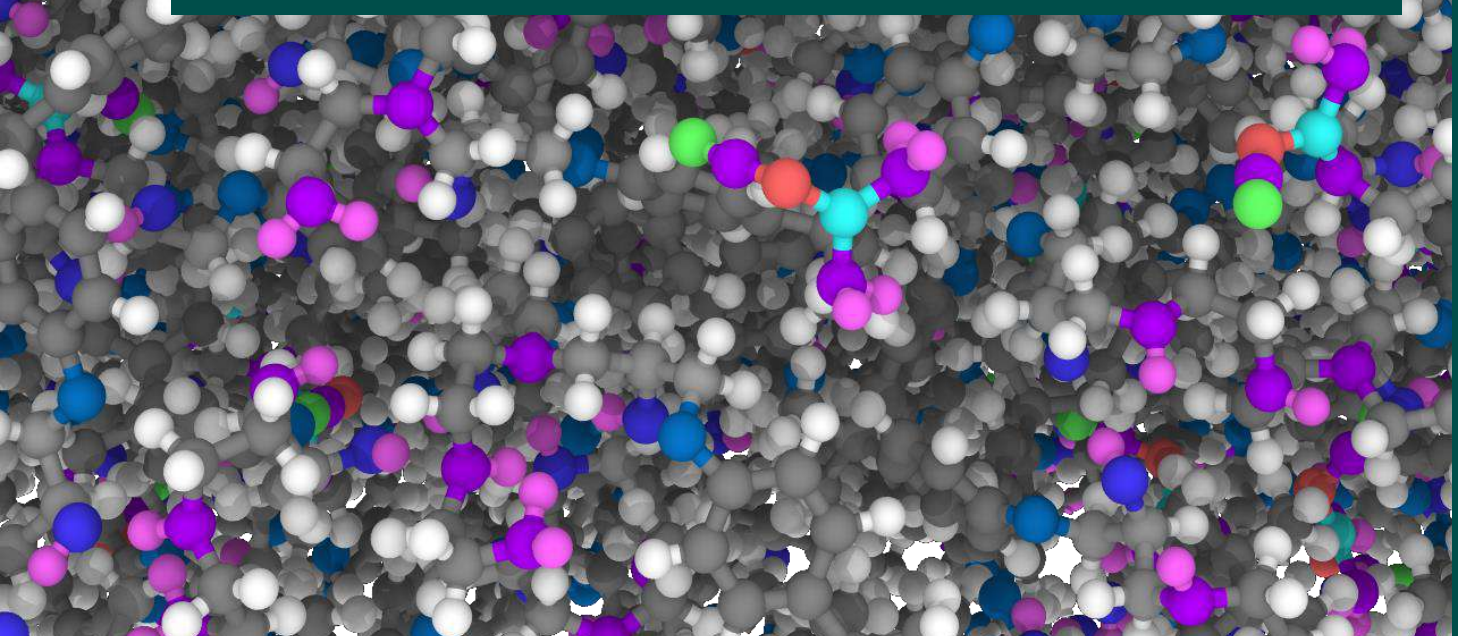

*nanomaterials*

MDPI

*Article*

# Effects of Graphene Oxidation on Interaction Energy and Interfacial Thermal Conductivity of Polymer Nanocomposite: A Molecular Dynamics Approach

**Francesco Maria Bellussi, Carlos Sáenz Ezquerro *, Manuel Laspalas and Agustín Chiminelli**

Aragon Institute of Technology ITAINNOVA, 50018 Zaragoza, Spain; francesco.bellussi@polito.it (F.M.B.); mlaspalas@itainnova.es (M.L.); achiminelli@itainnova.es (A.C.)

* Correspondence: csaenz@itainnova.es

**Abstract:** Interfacial characteristics of polymer nanocomposites represent a crucial aspect to understand their global properties and to evaluate the interaction between nanofillers and matrix. In this work we used a molecular dynamics (MD) approach to characterize the interfacial region at the atomistic scale of graphene-based polymer nanocomposites. Three different polymer matrixes were considered, polylactic acid (PLA), polypropylene (PP) and epoxy resin (EPO), which were reinforced with three types of graphene fillers: pristine graphene (G), graphene oxide (GO) and reduced graphene oxide (rGO). In particular, the compatibility of the nanofillers in polymer matrixes were evaluated in terms of the interaction energy, while the interfacial thermal resistance (Kapitza resistance) between matrices and fillers was calculated with a nonequilibrium molecular dynamics (NEMD) method. Results showed that the oxidation degree plays an important role on the studied properties of the interfacial region. In particular, it was observed that the Kapitza resistance is decreased in the oxidized graphene (GO and rGO), while interaction energy depended on the polarity of the polymer matrix molecules and the contribution of the Coulombic component.

**Keywords:** polymer nanocomposite; graphene; interfacial properties; interaction energy; kapitza resistance; molecular dynamics



**Citation:** Bellussi, F.M.; Sáenz Ezquerro, C.; Laspalas, M.; Chiminelli, A. Effects of Graphene Oxidation on Interaction Energy and Interfacial Thermal Conductivity of Polymer Nanocomposite: A Molecular Dynamics Approach. *Nanomaterials* **2021**, *11*, 1709. https://doi.org/10.3390/nano11071709

Academic Editor: Jin Suk Chung

Received: 2 June 2021
Accepted: 25 June 2021
Published: 29 June 2021



## 1. Introduction

In the last decade, graphene (G) has attracted the attention of both scientists and industry stakeholders for its extraordinary mechanical, electrical and thermal properties [1–4], making it one of the best candidates for the development of nanomaterials in a wide range of applications [3,5,6]. Surface modified derivatives of graphene have been proposed, such as graphene oxide (GO) and reduced graphene oxide (rGO), with the aim of increasing the compatibility with polar matrices [7,8] and improving the composite interface characteristics through surface functionalization [9,10].

Molecular dynamics (MD) simulations have given light to the study and knowledge of the interfacial properties between matrix and filler, which represent key aspects to evaluate the dispersibility and binding capacity of nanofillers in polymer matrix and to understand the effective global characteristic of a nanocomposite. Regarding thermal properties, for example, Su et al. [11] developed a new effective-medium theory introducing both the thermal boundary resistance between matrix and filler (Kapitza resistance, $R_k$) and graphene–graphene contact resistance. By comparing analytical and experimental results these authors demonstrated that the interfacial thermal properties play a relevant role in the global thermal conductivity of a nanocomposite. Similarly, Bigdeli and Fasano [12] and Mohammad Nejad et al. [13] demonstrated, through reverse nonequilibrium molecular dynamics (RNEMD) simulations, that both geometry properties and the thermal boundary resistance between fillers affect significantly the overall thermal properties. In terms of the interactions between the matrices and the fillers, Sáenz et al. [14] evaluated the interface

thickness of composites based on epoxy resin and triple wall carbon nanotubes (TWCNT), by analyzing the density profile. Sun et al. [15] calculated the interaction energy between epoxy resin and GO depending on the content of hydroxyl groups, identifying the range in which the interfacial energy seemed to decrease more sensibly by increasing the number of hydroxyls. MD studies also allow the analysis of the effects of filler surface chemical modification on the interfacial properties. He et al. [16] and Mortazavi et al. [17] found that functionalization and the creation of covalent bonds between matrix and filler reduces sensibly the thermal boundary resistance, thus improving thermal conductivity.

In this study, molecular models of nanocomposites based on different polymer matrices (poly lactic acid, polypropylene and epoxy resin) and graphene fillers (pristine and oxidized) were developed, with the aim of studying some of their interfacial properties. The interface energy between matrix and filler was first evaluated to obtain an estimation of the compatibility, and then the interfacial thermal resistance across the interface (Kapitza resistance) was calculated to quantify the effect of the oxidation degree on interfacial thermal transport.

## 2. Materials and Methods

Three types of nanocomposites were modeled with atomistic detail by considering three different polymer matrices: two thermoplastic polymers, Polylactic acid (PLA) and Polypropylene (PP), and a variety of an epoxy thermoset resin (EPO). The chemical structure of generic PLA and PP chains are shown in Figure 1a,b, where the partial atomic charges are indicated. In all the cases studied, the isotactic variety of the polymers (i.e., with the methyl groups in the same side of the chain in the full extended conformation) was considered. The epoxy resin (EPO) is based on diglycidyl ether of bisphenol-A (DGEBA) with dicyandiamide (DICY) and diethylene triamine (DETA) as hardeners. The chemical structure of DGEBA, DICY and DETA with the partial charge is shown in Figure 1c–e. The COMPASS force field [18] was used to model the interactions between the atoms belonging to the polymer chains. The energy potentials stated in this force field are given in Equation (1).

$$
\begin{aligned}
E_{pot} &= \sum_{b}\left[K_2(r-r_0)^2 + K_3(r-r_0)^3 + K_4(r-r_0)^4\right] \\
&+ \sum_{\theta}\left[H_2(\theta-\theta_0)^2 + H_3(\theta-\theta_0)^3 + H_4(\theta-\theta_0)^4\right] \\
&+ \sum_{\phi}\left[V_1\left[1-cos\left(\phi-\phi_1^0\right)\right] + V_2\left[1-cos\left(2\phi-\phi_2^0\right)\right] + V_3\left[1-cos\left(3\phi-\phi_3^0\right)\right]\right] \\
&+ \sum_{\chi} K_\chi \chi^2 + \sum_{b}\sum_{b'} F_{bb'}(b-b_0)(b'-b'_0) \\
&+ \sum_{b}\sum_{\theta} F_{b\theta}(b-b_0)(\theta-\theta_0) \\
&+ \sum_{b}\sum_{\phi}(b-b_0)[V_1 cos\phi + V_2 cos2\phi + V_3 cos3\phi] \\
&+ \sum_{b'}\sum_{\phi}(b'-b'_0)[V_1 cos\phi + V_2 cos2\phi + V_3 cos3\phi] \\
&+ \sum_{\theta}\sum_{\phi}(\theta-\theta_0)[V_1 cos\phi + V_2 cos2\phi + V_3 cos3\phi] \\
&+ \sum_{\phi}\sum_{\theta}\sum_{\theta'} K_{\phi\theta\theta'} cos\phi(\theta-\theta_0)(\theta'-\theta'_0) \\
&+ \sum_{i>j}\frac{q_i q_j}{\varepsilon r_{ij}} + \sum_{i>j}\left[\frac{A_{ij}}{r_{ij}^9} - \frac{B_{ij}}{r_{ij}^6}\right]
\end{aligned}
\tag{1}
$$

where $K_i$, $H_i$, $V_i$, and $F_i$ are constants; $r$ is the distance between atoms; $b$ is the bond length; $\theta$ and $\varphi$ are the bond angles of bending and torsion; $q_i$ is the partial charge of a given atom; and $A_i$ and $B_i$ are the van de Waals parameters. The value of these parameters were taken as defined in the COMPASS force field according to the work developed by Sun [18].

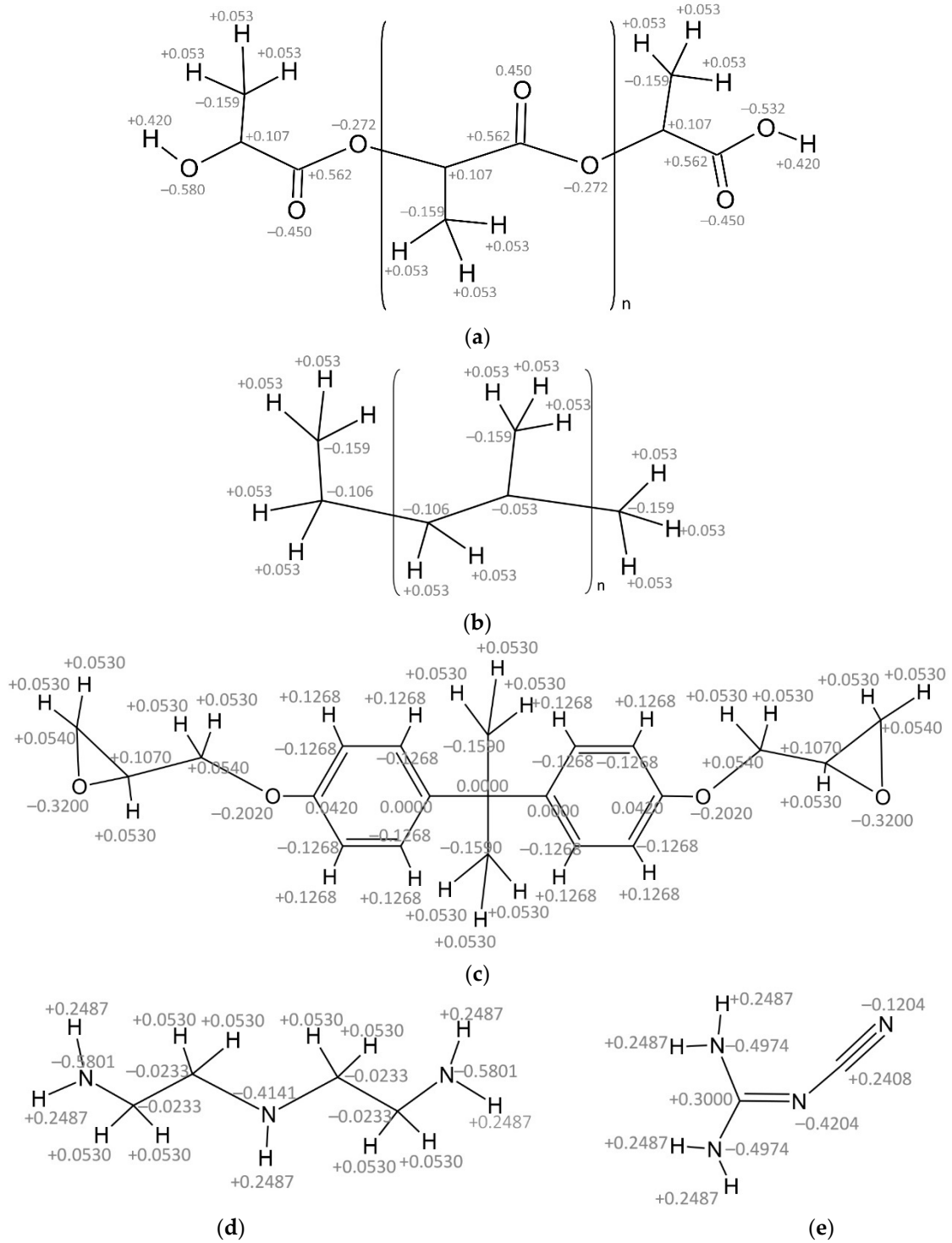


**Figure 1.** Structure and partial atomic charges of polymers: (**a**) polylactic acid (PLA); (**b**) polypropylene (PP); epoxy resin molecules: (**c**) DGEBA, (**d**) DETA and (**e**) DICY.

Three types of graphene fillers (having lateral dimension of 81 × 83 Å, considering periodic boundary conditions in the planar dimensions) were employed to assess the effect of different surface functionalization of the graphene on the interfacial properties (interaction energy and Kapitza resistance) of polymer nanocomposites. In Figure 2, a representative picture of the graphene fillers with details of the type of functionalization and oxidation degree are plotted: neat graphene, graphene oxide (GO) and reduced graphene oxide (rGO). The graphene layer of these fillers was generated using the VMD software [19],

whereas the functionalization was introduced considering a random distribution on the filler surface. The bond interactions between filler and functional groups were introduced using LAMMPS [20]. The molecular structures of the two types of functionalization introduced in the graphene layers are shown in Figure 3, i.e., hydroxyl (C–OH) and oxirane (C–O–C) groups. The graphene oxide (GO) contains both types of groups whereas the reduced graphene oxide (rGO) contains only hydroxyl groups. The interaction potential for these graphene fillers was based on a combination of the Tersoff potential [21] for the interaction between the carbon atoms of the graphene layer, and the COMPASS force field [18] for the description of the functional groups (see Figure 3). In detail, the coefficient for bonds and angles between the functional groups and the graphene layer were chosen according to the COMPASS force field (considering the aromatic structure of carbon atoms in graphene).

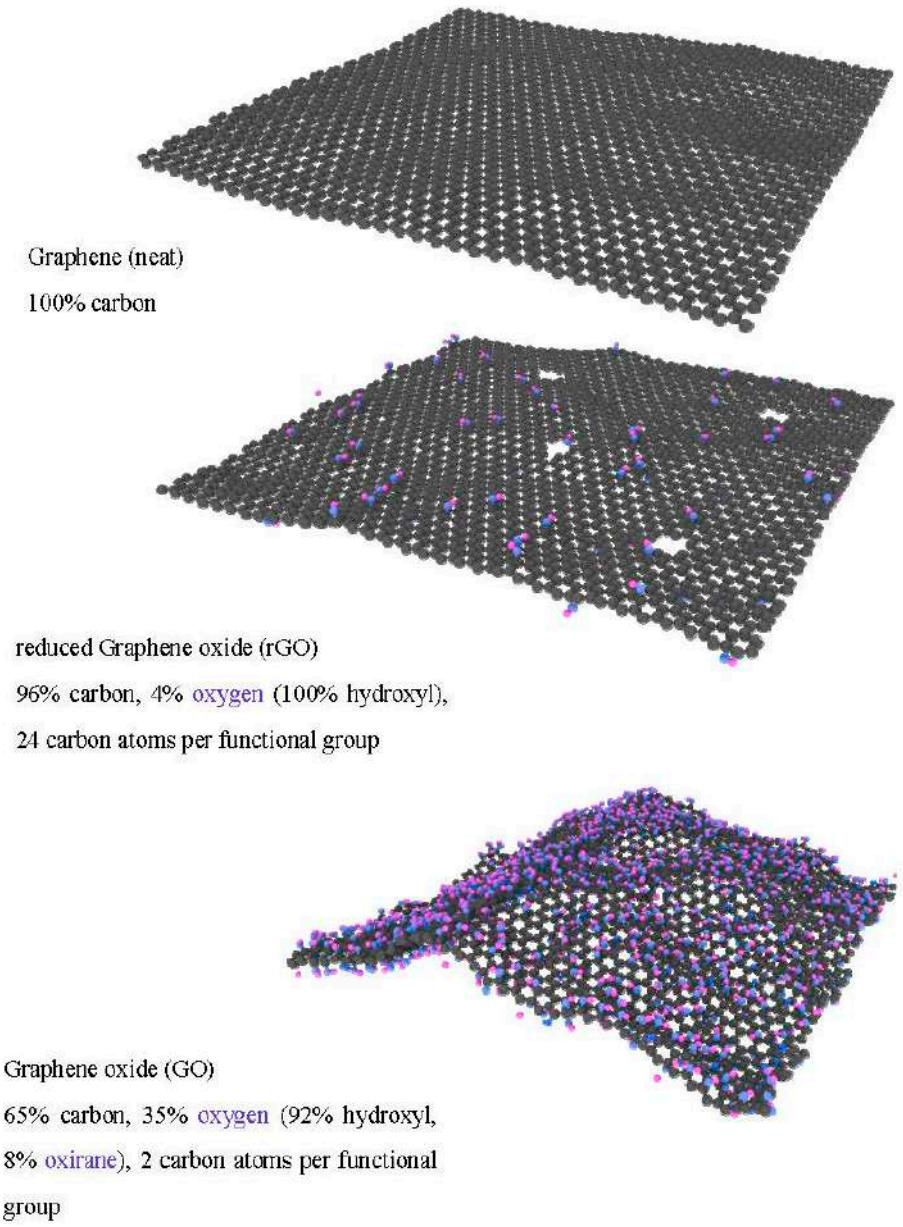


**Figure 2.** Type of graphene models with details of surface functionalization (percentages are atomic).

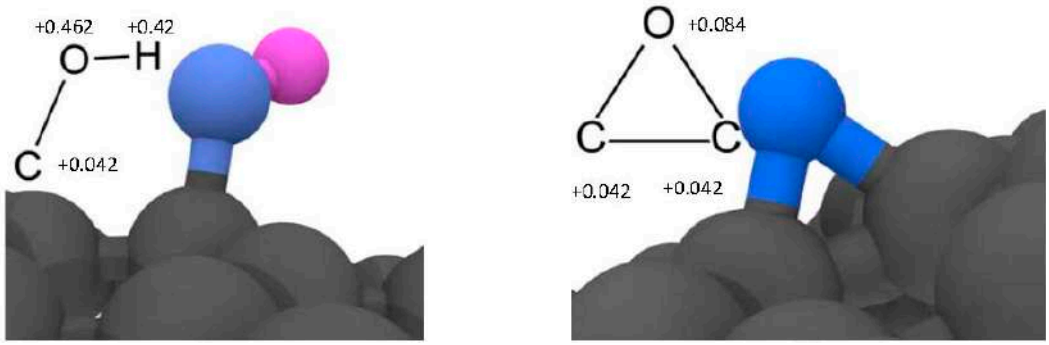


(**a**) (**b**)

**Figure 3.** Types of functionalization introduced on the graphene surface: (**a**) hydroxyl group (C-OH) and (**b**) oxirane group (C-O-C). The bonds and the angles interactions between the functional groups and the carbon atoms of the filler were chosen according to the COMPASS force field and the nonbond interactions between the functional groups and polymer molecules.

The nanocomposite full atom models (Table 1) were generated by adding the polymer molecules to the cell containing the graphene filler (neat G, GO and rGO). In the case of the thermoplastic polymers, polylactic acid (PLA) and polypropylene (PP), 120 chains with a degree of polymerization of 50 for PLA and 42 chains with a degree of polymerization of 150 for PP (which allow for obtaining representative molecular structures with acceptable computational costs) were added to the cell, whilst for the thermosetting epoxy resin (EPO) composites, DGEBA, DICY and DETA molecules were used in stoichiometric proportion. First, a volume adjustment of the cell was performed; in this step the graphene filler atoms were kept fixed to avoid undesired deformation. Then, the models were time integrated in the isobaric–isotherm ensemble (NPT, with the Nosé–Hoover thermobarostat) at 300 K and 1 atm, allowing all atoms to freely move, until reaching the plateau in density (which typically required between 0.5 and 1 ns). In the case of the epoxy resin, the cross-linking procedure, based on methods described in literature [14,20] and performed through consecutive steps of molecular dynamics simulations, was subsequently applied to obtain the desired cross-linking degree of 70%. At the abovementioned conditions used for the systems stabilizations, the PLA and EPO are in the glassy state, while the polypropylene is in the melting state, as reported in previous studies available in the literature [22–24]. The time-step was fixed at 0.5 fs in all simulations and the Verlet algorithm was applied to update the positions of atoms. Periodic boundary conditions (PBC) were applied in all the directions of the simulation cell, which is equivalent to an infinite graphene filler layer (Figure 4). All simulations were performed using the LAMMPS simulation code [20].

**Table 1.** Models studied.

| ID Model | Polymer | Filler | N° Atoms | N° Molecules |
|---|---|---|---|---|
| PLA-G | PLA | G | 56,868 | 120 |
| PLA-GO | PLA | GO | 58,596 | 120 |
| PLA-rGO | PLA | rGO | 57,048 | 120 |
| PP-G | PP | G | 59,216 | 42 |
| PP-GO | PP | GO | 61,320 | 42 |
| PP-rGO | PP | rGO | 59,472 | 42 |
| EPO-G | EPO | G | 57,708 | 1000 + 292 + 164 [(1)] |
| EPO-GO | EPO | rGO | 59,763 | 1000 + 292 + 164 [(1)] |
| EPO-rGO | EPO | GO | 57,888 | 1000 + 292 + 164 [(1)] |

[(1)] DGEBA + DICY + DETA number of initial molecules (before cross-linking).

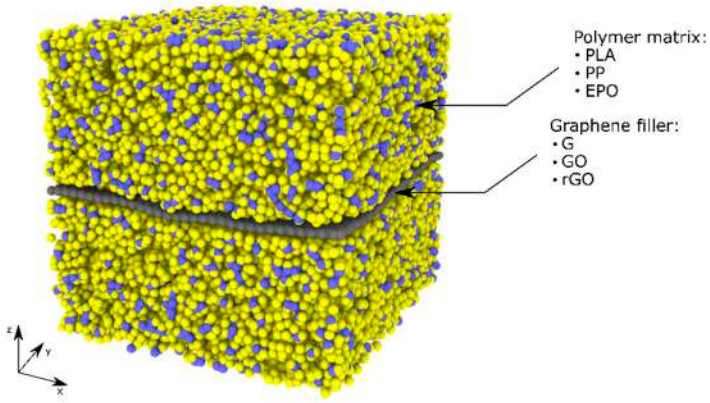


**Figure 4.** Three-dimensional example of an equilibrated system with PBC and graphene filler that crosses the simulation box (infinite length).

### *2.1. Interaction Energy*

The interaction energy defines the energy of the system (in terms of the potential energy) implied in the interaction between the polymer matrix and the graphene filler. The interaction energy ($\Delta E_i$) can be calculated considering the energy of the composite and the energy of the isolated components:

$$\Delta E_i = E_{tot} - E_{polymer} - E_{filler} \quad (2)$$

where $E_{tot}$, $E_{polymer}$ and $E_{filler}$ are the potential energies of the composite, polymer and filler, respectively. The potential energy has contributions of bonds, angles, dihedrals, van der Waals and Coulombic interactions (short- and long-range), but not kinetic energy contribution. Indeed, E could represent the total energy or even only a component of the energy (i.e., van der Waals or Coulombic). After the system equilibration in the isothermal–isobaric (NPT) ensemble, the model is finally minimized with the conjugate gradient method using convergence criterions of 0.0 kcal/mol and $1 \times 10^{-10}$ kcal/mol·Å for energy and force. Then, the energy of the composite ($E_{tot}$), filler ($E_{filler}$) and matrix ($E_{matrix}$) were evaluated, pointing out the electrostatic and dispersive contributions. Each partial contribution was calculated, deleting alternatively the filler and the matrix, which allows for extracting the partial potential energy of each phase at its configurational equilibrium with the other phase, neglecting the interaction contribution between them.

### *2.2. Kapitza Resistance ($R_K$)*

The interfacial thermal resistance, also known as thermal boundary resistance or Kapitza resistance ($R_K$), is a measure of the resistance of the interface to thermal flow. This property is measured from the atomistic models using a transient approach or nonequilibrium molecular dynamics (NEMD). Initially, the simulation box was entirely equilibrated to the equilibrium temperature of 300 K. Once the whole system (polymer + filler) was equilibrated at this temperature, the filler (graphene) was heated to 400 K (i.e., a temperature delta of 100 K was applied). During the heating process of the graphene filler, the temperature of the polymer was kept constant at 300 K using a second thermostat. Finally, when the filler reached the temperature of 400 K, the thermostats were switched off and the system was allowed to relax in the microcanonical NVE ensemble. During this relaxation process, the temperature of the filler and polymer were monitored, from which the temperature difference over time ($\Delta T(t)$) was calculated and plotted (some examples are shown in Figure 5).

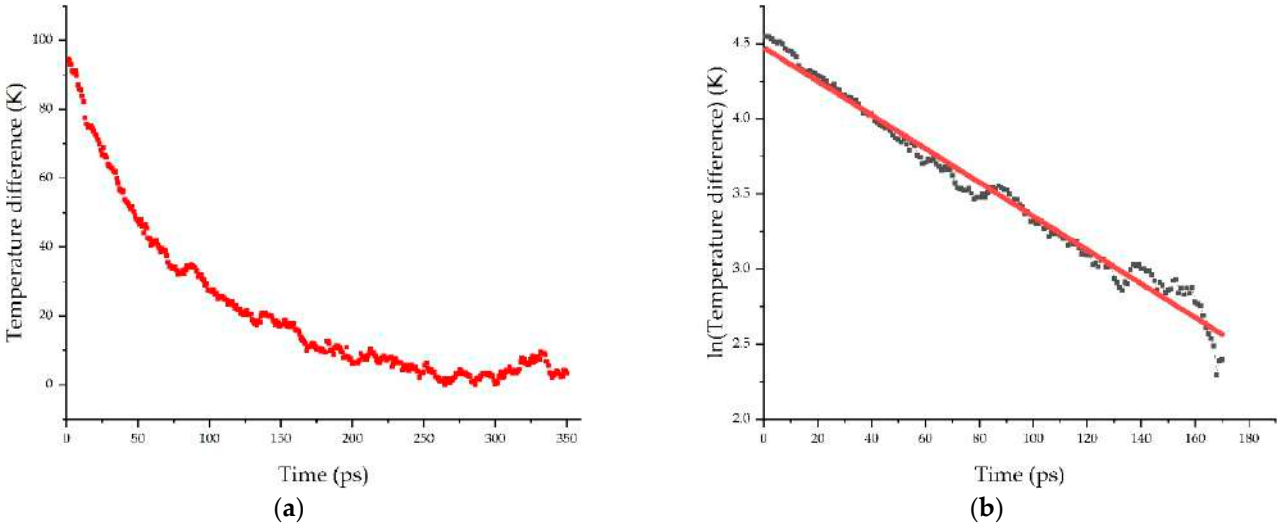


**Figure 5.** Decay of temperature difference between filler and matrix (**a**), with which the relaxation constant is calculated after linearization (**b**). Curves are obtained from model 2a.

The temperature difference ($\Delta T(t)$) can be fitted using an exponential decay:

$$\Delta T(t) = \Delta T(0) \cdot e^{-t/\tau} \tag{3}$$

This expression can be linearized by taking logarithms as follows:

$$ln\Delta T(t) = ln\Delta T(0) - \frac{t}{\tau} \tag{4}$$

The Kapitza resistance ($R_K$) is associated with the relaxation time constant $\tau$ as stated in the next expression:

$$R_K = \frac{A \cdot \tau}{C} \tag{5}$$

where $A$ is the filler surface area and $C$ the filler heat capacity, which were assumed constant for all the models at ambient conditions [17,25].

### *2.3. Phonon Density of State*

The phonon density of states (DOS) of a system describes the proportion of states that are occupied by the system at each energy in the range of modes of vibrations of elastic arrangements of atoms or molecules. The phonons play an important role in the thermal conductivity across the interface between two phases or materials, so the study of this type of vibration mode gives a deep understanding of the influence of atomistic properties on a property such as this [26,27]. The DOS was computed by calculating the Fourier transformation of the atomic velocity autocorrelation functions [28]:

$$\mathrm{DOS}(\omega) = \int_0^{\tau} v(t)v(0)\exp(-i\omega t)dt \tag{6}$$

where $v(0)$ and $v(t)$ are the velocities of each atom at initial time and time $t$, respectively, and $\omega$ is the frequency. The DOS spectra of graphene fillers and polymers were obtained by monitoring the velocity autocorrelation function of the corresponding atoms. The velocity autocorrelation functions were acquired along 5 ps of trajectory with ten repetitions for statistical average.

## 3. Results and Discussions

### *3.1. Interaction Energy*

The interaction energy could be considered as an indicator of the compatibility between two components (in this case between the polymer and the graphene fillers). A negative value of interaction energy means that the interaction produces a release of energy and thus a favorable compatibility between the filler and polymer. The results, which are expressed in terms of average and standard deviation values obtained from three replicas for each system studied, are summarized in Table 2 and plotted in Figure 6 in terms of total ($E$) and van der Waals ($E_{VdW}$) or Coulomb ($E_{Coul}$) components. In the case of PLA and EPO composite models, the interaction energy between matrix and filler increased in the order G < rGO < GO (Figure 6), or, in other words, when increasing the number of functional groups on the filler surface. This tendency was in good agreement with the work of Sun et al. [15], in which they investigated the interface energy between epoxy resin and graphene with an increasing functionalization degree. On the other hand, PP composites do not present tangible variation in the interactions: G ≈ rGO ≈ GO. This behavior reveals better compatibility of the oxidized fillers (with a particular reference to GO, due to its higher oxidation degree compared to rGO) with PLA and EPO when compared with pristine graphene. In the case of PP, the filler surface oxidation did not affect sensibly the interaction energy, due to the nonpolar nature of this polymer (i.e., no polar groups are present in its composition). The contribution of dispersion forces (van der Waals) and Coulombic interaction to the interaction energy were also assessed from the simulation and, as can be seen in Figure 6, in the case of PP composite interactions, the Coulombic energy represents a negligible contribution to interaction energy. On the other hand, in the case of PLA and EPO, the Coulombic contribution increases sensibly with the filler oxidation degree, inducing an increment on the interaction energy. Then, based on these results, both in the case of PLA and EPO, the interaction energy increases when increasing the level of surface filler oxidation (concentration of oxygen groups), due to the presence of polar groups in the matrixes (hydroxyl (-OH) in the case of PLA and hydroxyl (-OH) and amine (-NH) in the case of EPO), which interact with hydroxyl and oxirane groups of the graphene surface. Finally, the differences in value of interaction energy between the two functionalized fillers depend on the different degree of functionalization. In our case, the GO filler was chosen with a higher concentration of functional groups (35%) than the rGO filler (4%). Based on these results, it was observed that the effect of the oxidation of the graphene filler on the interaction energy with a polymer matrix depended on the polarity of the polymer. In nonpolar polymers (such as PP) the interaction energy was not significatively affected by the oxidation of the graphene, whereas in polar polymers (such as PLA and EPO) the interaction energy was affected by the oxidation of the graphene due to the presence of polar groups in the polymer, which contributed to the Coulombic component.

**Table 2.** Interaction energies (in kcal/mol).

| ID Model | Polymer | Filler | $E_{VdW}$ | $E_{Coul}$ | $E_{total}$ | Standard Deviation |
|---|---|---|---|---|---|---|
| PLA-G | PLA | G | −3164 | −3 | −3167 | 14 |
| PLA-GO | PLA | rGO | −3197 | −548 | −3745 | 11 |
| PLA-rGO | PLA | GO | −3091 | −1022 | −4113 | 21 |
| PP-G | PP | G | −3132 | −0.1 | −3132 | 8 |
| PP-GO | PP | GO | −3073 | −24 | −3097 | 17 |
| PP-rGO | PP | rGO | −3151 | −14 | −3165 | 21 |
| EPO-G | EPO | G | −3635 | 1 | −3636 | 4 |
| EPO-GO | EPO | rGO | −3535 | −580 | −4115 | 12 |
| EPO-rGO | EPO | GO | −3395 | −1461 | −4856 | 34 |

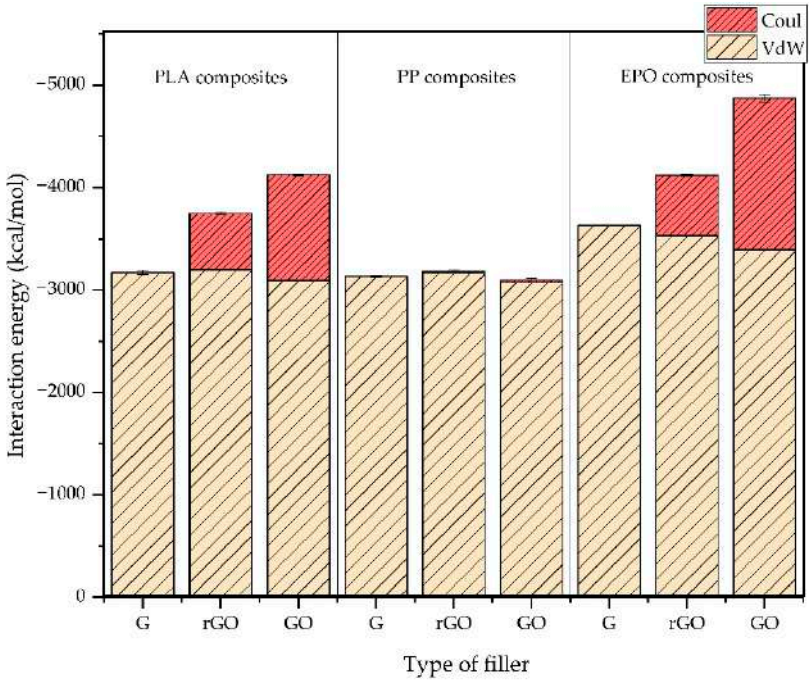


**Figure 6.** Comparison of interaction energy between the different graphene–polymer composite systems (G: neat graphene; GO: graphene oxide; rGO: reduced graphene oxide).

### *3.2. Kapitza Resistance ($R_K$)*

The results of Kapitza resistance ($R_K$) (Table 3), which are expressed in terms of average and standard deviation values obtained from the results of three replicas for each studied system, are in the range 0.5–2 $\times$ $10^{-7}$ $m^2K/W$, which is in good agreement with the values reported in the literature [11,17]. Considering the effect of the oxidation of the graphene in the interface Kapitza resistance, the same tendency was observed for all the polymers studied (PLA, PP, EPO). Systems reinforced with pristine graphene have the highest values of Kapitza resistance, which decreases when the graphene filler is oxidized (G > GO $\approx$ rGO) (Figure 7). This behavior indicates that the presence of functional groups in the graphene filler reduces the resistance to thermal heat flow across the interface, which increases the thermal conductivity across the interface. Finally, it is observed that the polarity of the polymer matrix has a less significant influence on the Kapitza resistance, and just the presence of functional groups in the surface of the graphene in form of oxidation influences the thermal conductivity across the interface. Since the heat flux across interfaces is based on a phonon mechanism [29], the DOS spectrum of the studied composite systems is also studied and is further discussed in the next section in order to support these results of Kapitza resistance.

**Table 3.** Kapitza resistance ($R_K$) of the systems studied (in $m^2K/W$).

| ID Model | Polymer | Filler | $R_K$ | Standard Deviation |
|---|---|---|---|---|
| PLA-G | PLA | G | $1.42 \times 10^{-7}$ | $0.17 \times 10^{-7}$ |
| PLA-GO | PLA | GO | $0.88 \times 10^{-7}$ | $0.12 \times 10^{-7}$ |
| PLA-rGO | PLA | rGO | $0.75 \times 10^{-7}$ | $0.08 \times 10^{-7}$ |
| PP-G | PP | G | $1.58 \times 10^{-7}$ | $0.04 \times 10^{-7}$ |
| PP-GO | PP | GO | $1.01 \times 10^{-7}$ | $0.27 \times 10^{-7}$ |
| PP-rGO | PP | rGO | $0.89 \times 10^{-7}$ | $0.30 \times 10^{-7}$ |
| EPO-G | EPO | G | $1.36 \times 10^{-7}$ | $0.12 \times 10^{-7}$ |
| EPO-GO | EPO | rGO | $0.75 \times 10^{-7}$ | $0.03 \times 10^{-7}$ |
| EPO-rGO | EPO | GO | $0.74 \times 10^{-7}$ | $0.04 \times 10^{-7}$ |

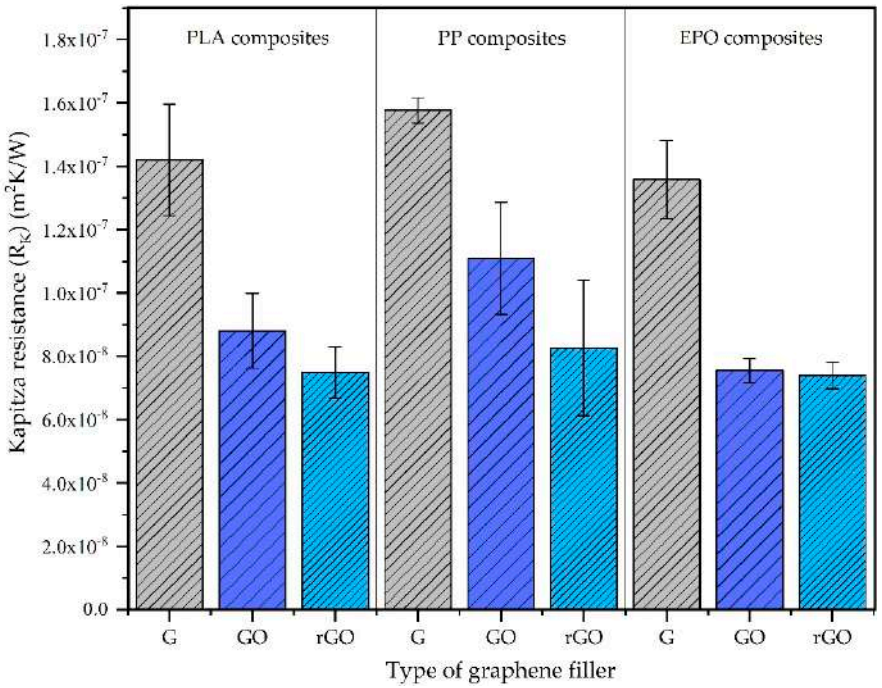


**Figure 7.** Comparison of Kapitza resistance between the different graphene–polymer composite systems (G: neat graphene; GO: graphene oxide; rGO: reduced graphene oxide).

### *3.3. Phonon Density of States (DOS)*

To explain the results of Kapitza resistance, the phonon DOS spectra of graphene fillers and polymers, either in the composite or the neat state, were obtained from the atomic velocity autocorrelation functions after their Fourier transformation (Figure 8). It can be observed that the oxidation clearly alters the phonon vibration modes of the graphene fillers. While the pristine graphene (G) exhibits vibration frequencies below 80 THz, the oxidized graphene fillers exhibit phonon vibration modes at higher frequencies. GO an rGO fillers exhibit an intense phonon vibration mode at near 115 THz, with an additional peak near 90 THz when the graphene was within the PLA or EPO matrices, but not in the case of the PP matrix. These high frequency vibration peaks at 115 THz and 90 THz are both associated with vibrations in which the polar groups (hydroxyl and/or oxirane) are involved, which in the case of the frequency peak at 90 THz presents noncovalent interactions with polar groups of the PLA or EPO matrix that are not present in the PP matrix. The phonon DOS spectra are very similar, in general terms, for the three polymers analyzed. The DOS spectra of the PLA, PP and EPO are dominated by two intense peaks located near 45 THz and 90 THz, with additional vibration peaks at lower frequencies and some extra peaks at higher frequencies in the case of EPO polymer of lower intensity. Whereas the DOS spectra of graphene fillers are affected by the presence of the polymers, as described previously, the DOS spectra of the polymers are practically unaffected by the presence of the graphene fillers.

Heat carriers of high frequency are important to thermal transport across interfaces [28,30,31]. As previously described, the oxidation of graphene (GO and rGO) provided phonon vibrations at high frequencies that are not present in the pristine graphene (G). These high frequency vibrations enhanced the thermal conductivity across the interface between the polymer and the graphene filler, and thus decreased the associated Kapitza resistance. Moreover, given that the three polymers exhibited similar phonon vibrations according to DOS spectra, the Kapitza resistance of the different composite systems studied is not very dependent on the type of polymer and is mainly affected by the type of graphene filler. In the literature, studies presented by Wang et al. [32] and Zabihi et al. [33] established that when the vibrational frequencies of matrix and polymer were much closer, the phonon transmission probability increases

and, thus, the thermal conductivity across the interface increases in the same way. This fact could also explain the results of Kapitza resistance presented in the present study, since the oxidized graphene fillers GO and rGO have phonon vibrations of frequency that are closer to the main polymer phonon vibration frequencies.

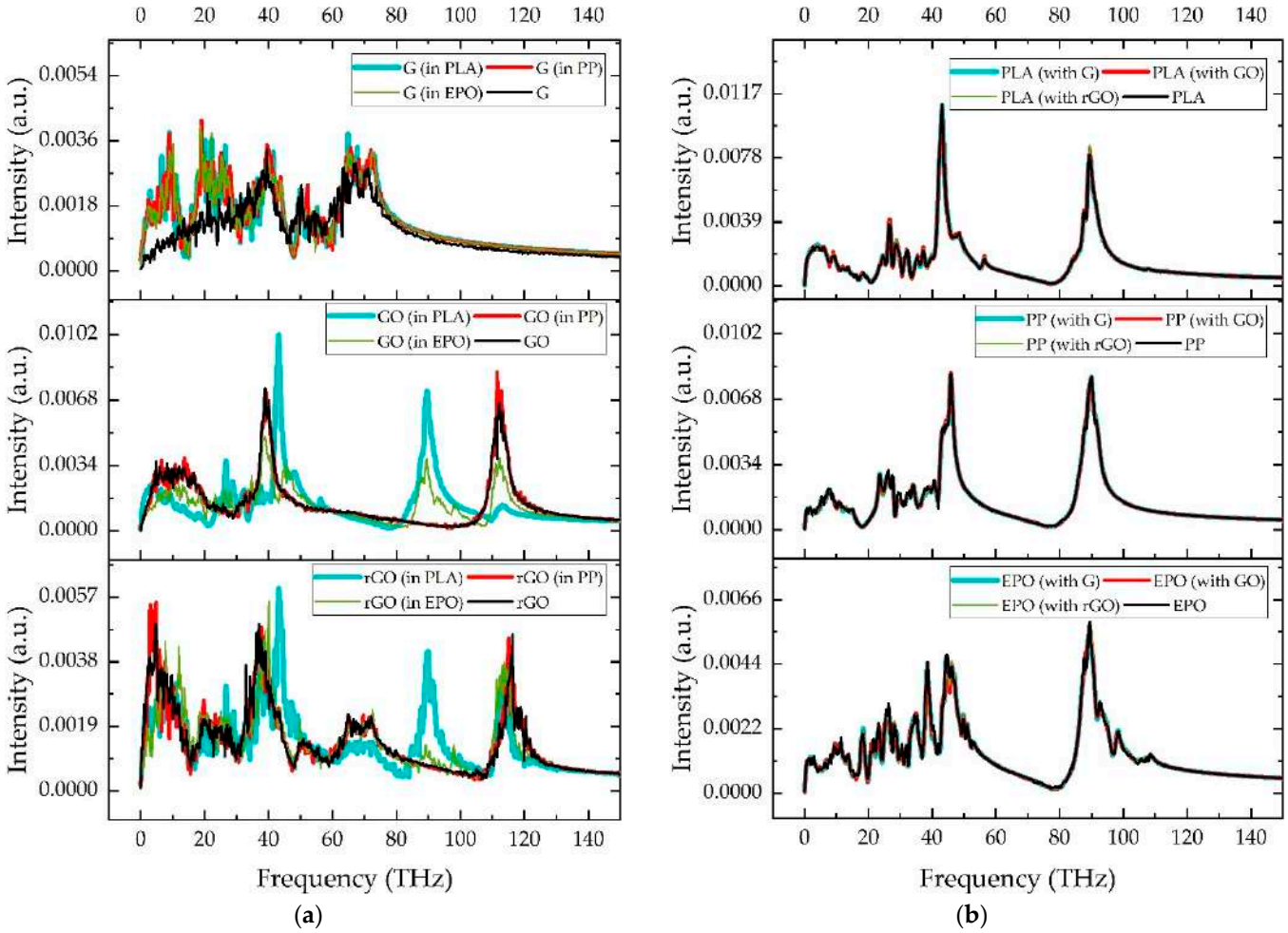


**Figure 8.** Phonon DOS of (**a**) graphene fillers and (**b**) polymers in composite and neat state (G: neat graphene; GO: graphene oxide; rGO: reduced graphene oxide).

## 4. Conclusions

Molecular dynamics (MD) models were developed in order to study the properties of the polymer–graphene fillers interface considering of three different polymer matrices, polylactic acid (PLA), polypropylene (PP) and epoxy resin (EPO) with different graphene derivatives: pristine graphene (G), graphene oxide (GO) and reduced graphene oxide (rGO). From these models, two types of interfacial properties were calculated: the interaction energy and the interfacial thermal resistance (Kapitza resistance). The main conclusions derived from these analyses follow:

- The interaction energy of the three different polymer matrices with the graphene fillers depended on the polarity of the polymer, due to the different contribution of the Coulombic component. Thus, it was observed that the interaction energy increases in the order graphene < rGO < GO for polar polymers such as polylactic acid (PLA) and epoxy resin (EPO), whereas in the case of polypropylene, the functionalization did not affect sensibly its interaction with graphene fillers, due to the negligible Coulombic contribution. These results gave a relevant insight about the matrices–filler compatibility and how it is affected by the different functionalizations considered.

- The Kapitza resistance (RK) exhibited the same behavior/tendency in the three polymers, graphene > rGO ≈ GO. It was observed that the presence of functional groups in the graphene, in the form of oxidation (hydroxyl and oxirane groups) increases the thermal conductivity, which was associated with the appearance of high frequency phonon vibrations in the oxidized graphene fillers, GO and rGO.

**Author Contributions:** C.S.E., F.M.B., M.L. and A.C. collaborated in the definition of the models developed and procedures used, in the results analysis and in writing the manuscript. C.S.E. and F.M.B. performed the simulations. All authors have read and agreed to the published version of the manuscript.

**Funding:** This research was funded by European Union's Horizon 2020 Research and Innovation Programme SMARTFAN grant number 760779.

**Conflicts of Interest:** The authors declare no conflict of interest.

## References

1. Papageorgiou, D.G.; Kinloch, I.A.; Young, R.J. Mechanical properties of graphene and graphene-based nanocomposites. *Prog. Mater. Sci.* **2017**, *90*, 75–127. [CrossRef]
2. Kuilla, T.; Bhadra, S.; Yao, D.; Kim, N.H.; Bose, S.; Lee, J.H. Recent advances in graphene based polymer composites. *Prog. Polym. Sci.* **2010**, *35*, 1350–1375. [CrossRef]
3. Mohan, V.B.; Lau, K.; Hui, D.; Bhattacharyya, D. Graphene-based materials and their composites: A review on production, applications and product limitations. *Compos. Part. B Eng.* **2018**, *142*, 200–220. [CrossRef]
4. Ferrari, A.C.; Bonaccorso, F.; Fal'ko, V.; Novoselov, K.S.; Roche, S.; Bøggild, P.; Borini, S.; Koppens, F.H.L.; Palermo, V.; Pugno, N.; et al. Science and technology roadmap for graphene, related two-dimensional crystals, and hybrid systems. *Nanoscale* **2015**, *7*, 4598–4810. [CrossRef] [PubMed]
5. Stoller, M.D.; Park, S.; Zhu, Y.; An, J.; Ruoff, R.S. Graphene-Based Ultracapacitors. *Nano Lett.* **2008**, *8*, 3498–3502. [CrossRef]
6. Bonaccorso, F.; Sun, Z.; Hasan, T.; Ferrari, A.C. Graphene photonics and optoelectronics. *Nat. Photon.* **2010**, *4*, 611–622. [CrossRef]
7. Ramanathan, T.; Abdala, A.A.; Stankovich, S.; Dikin, D.A.; Herrera-Alonso, M.; Piner, R.D.; Adamson, D.H.; Schniepp, H.C.; Chen, X.; Ruoff, R.S.; et al. Functionalized graphene sheets for polymer nanocomposites. *Nat. Nanotech.* **2008**, *3*, 327–331. [CrossRef] [PubMed]
8. Wan, C.; Chen, B. Reinforcement and interphase of polymer/graphene oxide nanocomposites. *J. Mater. Chem.* **2012**, *22*, 3637. [CrossRef]
9. Smith, A.T.; LaChance, A.M.; Zeng, S.; Liu, B.; Sun, L. Synthesis, properties, and applications of graphene oxide/reduced graphene oxide and their nanocomposites. *Nano Mater. Sci.* **2019**, *1*, 31–47. [CrossRef]
10. Johnson, D.W.; Dobson, B.P.; Coleman, K.S. A manufacturing perspective on graphene dispersions. *Curr. Opin. Colloid Interface Sci.* **2015**, *20*, 367–382. [CrossRef]
11. Su, Y.; Li, J.J.; Weng, G.J. Theory of thermal conductivity of graphene-polymer nanocomposites with interfacial Kapitza resistance and graphene-graphene contact resistance. *Carbon* **2018**, *137*, 222–233. [CrossRef]
12. Bigdeli, M.B.; Fasano, M. Thermal transmittance in graphene based networks for polymer matrix composites. *Int. J. Therm. Sci.* **2017**, *117*, 98–105. [CrossRef]
13. Mohammad Nejad, S.; Bozorg Bigdeli, M.; Srivastava, R.; Fasano, M. Heat Transfer at the Interface of Graphene Nanoribbons with Different Relative Orientations and Gaps. *Energies* **2019**, *12*, 796. [CrossRef]
14. Sáenz Ezquerro, C.; Laspalas, M.; Chiminelli, A.; Serrano, F.; Valero, C. Interface Characterization of Epoxy Resin Nanocomposites: A Molecular Dynamics Approach. *Fibers* **2018**, *6*, 54. [CrossRef]
15. Sun, Y.; Chen, L.; Cui, L.; Zhang, Y.; Du, X. Molecular dynamics simulation of cross-linked epoxy resin and its interaction energy with graphene under two typical force fields. *Comput. Mater. Sci.* **2018**, *143*, 240–247. [CrossRef]
16. He, B.; Mortazavi, B.; Zhuang, X.; Rabczuk, T. Modeling Kapitza resistance of two-phase composite material. *Compos. Struct.* **2016**, *152*, 939–946. [CrossRef]
17. Mortazavi, B.; Benzerara, O.; Meyer, H.; Bardon, J.; Ahzi, S. Combined molecular dynamics-finite element multiscale modeling of thermal conduction in graphene epoxy nanocomposites. *Carbon* **2013**, *60*, 356–365. [CrossRef]
18. Sun, H. COMPASS: An ab initio force-field optimized for condensed-phase applications—Overview with details on alkane and benzene compounds. *J. Phys. Chem. B* **1998**, *102*, 7338–7364. [CrossRef]
19. Humphrey, W.; Dalke, A.; Schulten, K. VMD—Visual Molecular Dynamics. *J. Molec. Graphics* **1996**, *14*, 33–38. [CrossRef]
20. Plimpton, S. Fast parallel algorithms for short-range molecular dynamics. *J. Comput. Phys.* **1995**, *117*, 1–19. [CrossRef]
21. Tersoff, J. Modeling solid-state chemistry: Interatomic potentials for multicomponent systems. *Phys. Rev. B Condens. Matter* **1989**, *39*, 5566–5568. [CrossRef]
22. Yarovsky, I.; Evans, E. Computer simulation of structure and properties of crosslinked polymers: Application to epoxy resins. *Polymer* **2002**, *43*, 963–969. [CrossRef]

23. Yu, K.; Li, Z.; Sun, J. Polymer Structures and Glass Transition: A Molecular Dynamics Simulation Study. *Macromol. Theory Simul.* **2001**, *10*, 624–633. [CrossRef]
24. Xiang, H.; Wang, Y.; Yang, W.; Hu, C.; Mu, Y.; Li, J. Study of the Mechanical and Thermal Properties of Poly(Lactic Acid) and Poly(Ethylene Glycol) Block Copolymer with Molecular Dynamics. *Int. J. Polymer Anal. Charact.* **2010**, *15*, 235–244. [CrossRef]
25. Hadipeykani, M.; Aghadavoudi, F.; Toghraie, D. A molecular dynamics simulation of the glass transition temperature and volumetric thermal expansion coefficient of thermoset polymer based epoxy nanocomposite reinforced by CNT: A statistical study. *Physica A* **2020**, *546*, 123995. [CrossRef]
26. Han, H.; Merabia, S.; Müller-Plathe, F. Thermal Transport at Solid-liquid Interfaces: High Pressure Facilitates Heat Flow through Non-local Liquid Structuring. *J. Phys. Chem. Lett.* **2017**, *9*, 1946–1951. [CrossRef]
27. Merabia, S.; Lombard, J.; Alkurdi, A. Importance of viscoelastic and interface bonding effects in the thermal boundary conductance of solid–water interfaces. *Int. J. Heat Mass Transf.* **2016**, *100*, 287–294. [CrossRef]
28. Chen, S.; Yang, M.; Liu, B.; Xu, M.; Zhang, T.; Zhuang, B.; Ding, D.; Huai, X.; Zhang, H. Enhanced Thermal Conductance at the Graphene–Water Interface Based on Functionalized Alkane Chains. *RSC Adv.* **2019**, *9*, 4563–4570. [CrossRef]
29. Pop, E.; Varshney, V.; Roy, A.K. Thermal properties of graphene: Fundamentals and applications. *MRS Bull.* **2012**, *37*, 1273–1281. [CrossRef]
30. Allen, P.B.; Feldman, J.L.; Fabian, J.; Wooten, F. Diffusons, Locons and Propagons: Character of Atomie Yibrations in Amorphous Si. *Philos. Mag. B* **1999**, *79*, 1715–1731. [CrossRef]
31. Moon, J.; Latour, B.; Minnich, A.J. Propagating Elastic Vibrations Dominate Thermal Conduction in Amorphous Silicon. *Phys. Rev. B* **2018**, *97*, 024201. [CrossRef]
32. Wang, Y.; Zhan, H.F.; Xiang, Y.; Yang, C.; Wang, C.M.; Zhang, Y.Y. Effect of Covalent Functionalization on Thermal Transport across Graphene–Polymer Interfaces. *J. Phys. Chem. C* **2015**, *119*, 12731–12738. [CrossRef]
33. Zabihi, Z.; Araghi, H. Effect of functional groups on thermal conductivity of graphene/paraffin nanocomposite. *Phys. Lett. A* **2016**, *380*, 3828–3831. [CrossRef]

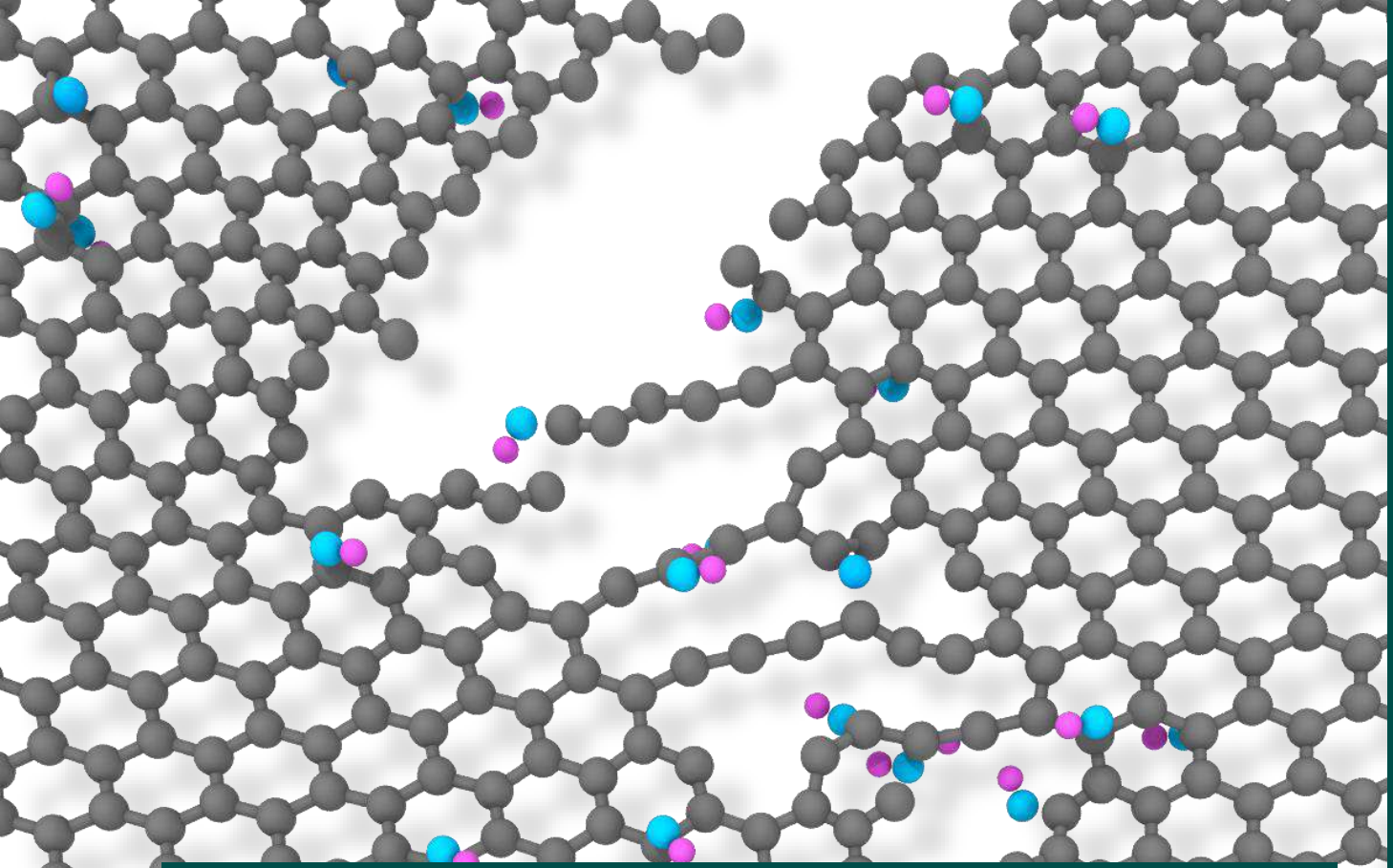

# 9. Publicación IV

**Molecular modelling of graphene nanoribbons on the effect of porosity and oxidation on the mechanical and thermal properties**

**Premio Cahn 2023**

**Journal of Materials Science,**
**DOI:** 10.1007/s10853-023-08810-y
**Factor de impacto en 2023**: 4,5
**Área temática**: Materials Science, Multidisciplinary
**Cuartil JCR (2023):** Q2



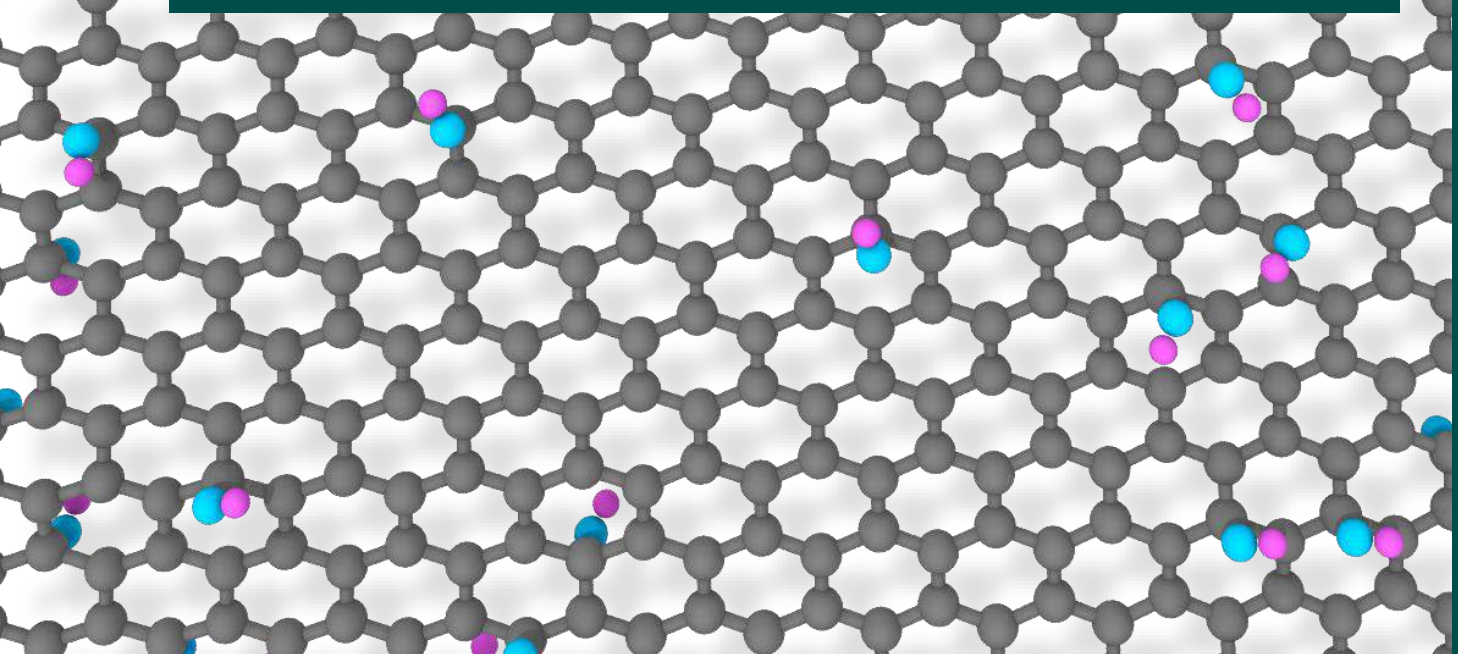

Volume 58 • Number 41
November 2023

# Journal of Materials Science

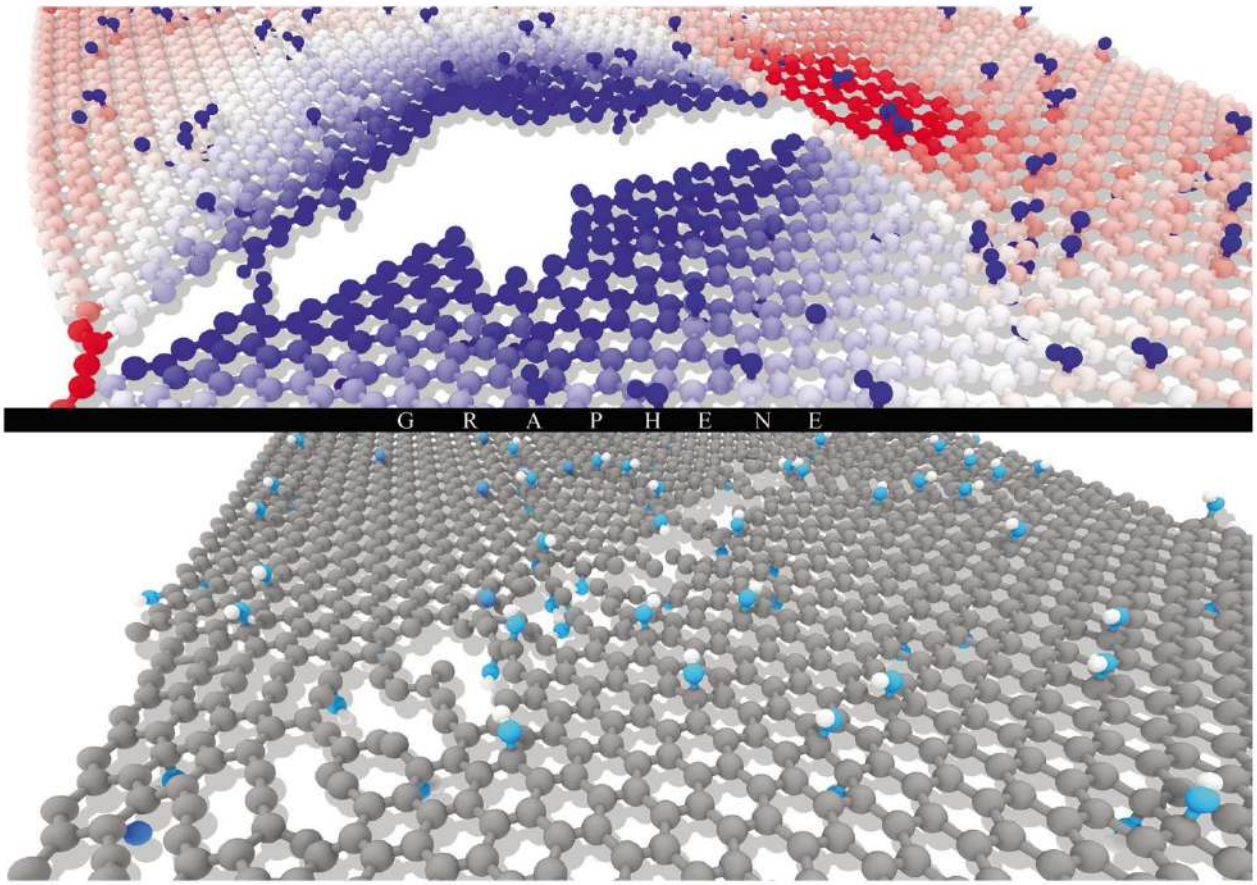


JMS

10853 • 58(41) 15933–16268 (2023)
ISSN 0022-2461 (Print)
ISSN 1573-4803 (Electronic)

Springer

*J Mater Sci*

**Computation & theory**

# Molecular modelling of graphene nanoribbons on the effect of porosity and oxidation on the mechanical and thermal properties

Carlos Sáenz Ezquerro[1], Manuel Laspalas[1], José Manuel García Aznar[2,*], Susana Castelar Ariza[1], and Agustín Chiminelli[1]

[1] *Aragon Institute of Technology ITAINNOVA, María de Luna 7-8, 50018 Saragossa, Spain*

[2] *Multiscale in Mechanical and Biological Engineering (M2BE), Aragon Institute of Engineering Research (I3A), University of Zaragoza, 50018 Saragossa, Spain*

**Received:** 5 June 2023
**Accepted:** 23 July 2023



## ABSTRACT

Graphene is considered as the most promising nanomaterial of the recent decades given the huge amount of studies that have been performed to characterize its outstanding properties and in searching of novel applications. Following this tendency, this study covers the modelling of graphene nanoribbons (GNRs) with the aim of analyzing the effect of porosity and oxidation on the tensile mechanical properties and in-plane thermal conductivity through molecular dynamics (MD). Using quasi-static simulations the mechanical properties were evaluated in first place. A 'hardening' mechanism was observed for GNRs at porosities below 1%, i.e. perfect or near-perfect GNRs, by which the GNRs could withstand higher loading levels. This hardening effect was manifested in the carbon network by the generation of dislocation lines formed by pentagon-heptagon pairs (5–7 defects), which acted as a stress reliever. The failure of GNRs was produced as a tearing mechanism with cracks growing along the armchair or zigzag directions. The porosity affected all the analysed tensile mechanical properties (i.e., Young's modulus, Poisson's ratio, tensile strength and deformation at break), but with different tendency in the fracture properties due to the presence or absence of hardening behaviour in the GNRs. Nevertheless, the oxidation affected only the tensile modulus and Poisson's ratio but not to the tensile strength and deformation at break. The thermal conductivity of the GNRs was affected either by the porosity and oxidation. Pores and oxidation groups acted as phonon scatterers since they disrupted the carbon network by the generation of vacancies or out-of-plane carbons, respectively, which decreased the phonon mean free path and thus the thermal conductivity. In conclusion, the porosity and oxidation of GNRs greatly determine the tensile

Handling Editor: Ghanshyam Pilania.

Address correspondence to E-mail: jmgaraz@unizar.es

https://doi.org/10.1007/s10853-023-08810-y

Published online: 24 August 2023

mechanical properties and in-plane thermal conductivity of such materials and must be considered when tuning the synthetic pathways.

## GRAPHICAL ABSTRACT

The effect of porosity and oxidation on the tensile mechanical and thermal conductivity properties of graphene nanoribbons are evaluated through molecular dynamics simulations.

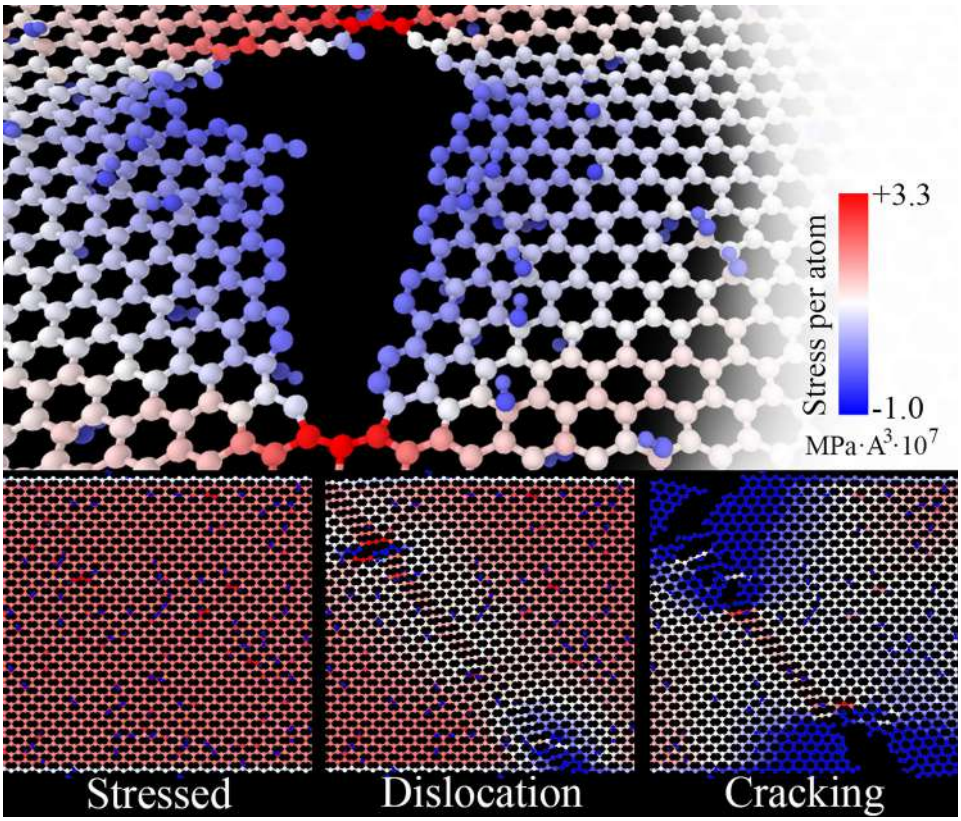


## Introduction

Graphene is an one-atom thick layer of covalently bonded $sp^2$-hybridized carbon atoms that form ideal hexagonal crystal lattices as honeycomb network [1]. This molecular structure originates a long-range π-bonding and is responsible of the outstanding mechanical [2, 3], electric [4, 5] and thermal properties [6] of graphene. The applications and properties of graphene has been intensively studied in the last two decades, after the work published by Geim and Novoselov [7], and covers biomedical engineering [8], electronics [9, 10], aerospace [11], among others. Nevertheless the oxidized forms of graphene, graphene oxide (GO) and reduced graphene oxide (rGO), are usually preferred over the neat structure since they are more active towards chemical modification and have higher interlayer gap than pristine graphene [12] due to the presence of polar groups (i.e., oxygen-containing groups). Improved electrochromic kinetics [13], lower resistance to heat transference through interface [14] and higher

hydrophilicity [15] are reported for the oxidized varieties of graphene compared to the pristine form.

The synthesis of graphene oxide is usually carried out by treating graphene or graphite with strong acids and oxidizers, such as permanganate and sulfuric acid (Hummers method) [16, 17], which delivers hydroxyl (C–OH) and oxirane (C–O–C) groups in the surface of the graphene sheet, together with carboxyl (C–COOH) and carbonyl (C–C = O) groups in the edge positions, as indicated the $^{13}C$ NMR technique [18, 19]. The amount and dispersion of these oxygen-containing groups determines the extension of the unoxidized benzene ring and oxidized aliphatic six-membered ring regions [20], which is identified as L-K structure [12]. Another important structural characteristic of the oxidized forms of graphene is the presence of structural defects in form of pores or holes due to overoxidation and lamellar peeling [21, 22], which also affects the structure of the sheet. Li et al. [23] demonstrated through MD simulations that the presence of hole defects decreased the interfacial strength between polymer and graphene in nanocomposite systems. Thus, the properties and structure of the oxidized graphene derivatives depend on the amount and distribution of the polar groups and the hole defects. While pristine graphene is an hydrophobic material [24–26], the GO and rGO varieties are hydrophilic [27].

The modulation of properties through the amount of such oxygen-containing groups and pores in their structure is a way of tuning the graphene derivatives into the required application. Several methods have been described to synthesize graphene with controlled porosity such as the template approach [28, 29] and the chemical/thermal activation [30, 31]. Lin and Grossman [21] found that there existed a relationship between the size of nanopores and synthesis parameters, such as oxygen and epoxy concentration in the GO, as a potential application for the preparation of selective reverse osmosis membranes. The production of reduced graphene oxide (rGO) through the oxidative exfoliation-reduction of graphite yields a product with a certain degree of defects [1, 32], in contrast with the chemical vapor deposition (CVD) method where the graphene is produced with low defects [33]. Achawi et al. [34] found that the structure of the graphene derivatives directly affected their surface reactivity and cytotoxicity, which revealed the importance of controlling the structure of the graphene materials depending on the desired final properties.

The experimental characterization of nanoparticles commonly is limited to the determination of structural parameters which includes composition, morphology, specific surface and size, among others [35]. Nevertheless, the determination of some properties such as the mechanical (e.g., Young's modulus and strength) or the thermal ones of individual nanoparticles is difficult to carry out experimentally and often requires techniques complex techniques such as atomic force microscopy (AFM) [2, 36–38] or Raman spectroscopy [39, 40], but they generally lack of sufficient certainty and the results are very dependent on the experiment configuration and technician skills. Molecular simulations offer the best alternative to study the properties of nanoparticles [41] and they can also provide a powerful insight into the mechanism that underly complex phenomena such as nucleation of metallic nanoparticles [42, 43] and biologic interactions [44–46]. In the case of graphene nanoparticles molecular dynamics (MD) simulations have been used to study a wide variety of properties such as the mechanical properties [47, 48], thermal stability [49] and conductivity [50–52], interface properties [53, 54], synthesis mechanisms [55] and reinforcing characteristics [56, 57], among others.

In our previous study [14] MD simulations were conducted to compute the thermal conductivity across the interface, i.e. Kapitza resistance, between graphene and different polymeric matrices. Continuing in this line of work in the present study a series of molecular-based models of pristine graphene (G) and graphene oxide (GO) nanoribbons (GNR) with different percentage of pores (i.e. vacancy or hole defects) were developed focusing the characterization on the properties of isolated graphene. With this aim the effect of porosity and oxidation on the tensile mechanical properties and in-plane thermal conductivity were assessed by means of molecular dynamics (MD) simulations. Specifically the Young's modulus, Poisson's ratio, tensile strength and deformation at break were evaluated from quasi-static MD simulations, using the energy minimization approach, from which the failure mechanism was also assessed. Moreover, the thermal conductivity was calculated using the Müller-Plathe method [58], a non-equilibrium approach. Given that the thermal conductivity is fully dependant on the phonon transmission mechanism, the density of states (DOS)

functions together with the mean free path (MFP) were also determined from MD simulations to help understanding the results found of thermal conductivity. The effect of porosity and oxidation on the graphene properties were assessed from a statistical point of view in terms of the *F* parameter (i.e., Fisher factor). This parameter is based on the analysis of the associated errors (i.e., variance) found in the results, in the context of an ANOVA analysis, and is a simple way to check for possible significative effect of factors in a series of results by comparing the variance of each series [59, 60].

## Materials and methods

### Modelling of graphene nanoribbons

A series of pristine graphene (G) and graphene oxide (GO) nanoribbon models having different percentage of pores were prepared. The carbon structure of the graphene sheets was generated using the VMD software [61], using dimensions of 250 Å length and 75 Å width, a C–C distance of 1.4579 Å which constituted 7200 carbon atoms and armchair structure in the edges. Then the oxide functionalities, i.e. hydroxyl and oxirane groups, were randomly bonded to the carbon atoms on both sides of the sheet. A total of 500 hydroxyl groups and 50 oxirane groups were added, which supposed a degree of oxidation (i.e. percentage of oxidized carbon atoms) of 8.3% within the range of experimental values [62]. The pores were generated by taking out a certain number of carbon atoms in the structures in random positions along the length of the nanoribbons. The morphology of the pore was irregular and its sizes varied between 10 and 25 Å of internal length. The carbon atoms at the edges (either at the sides of the nanoribbons or in the pore) were not passivated with hydrogen atoms, which according to Hu and Maroudas [63] doesn't have a significant effect on the thermal conductivity of graphene nanoribbons. The pore percentage was considered in a carbon atom basis, i.e. considering the number of carbon atoms removed in the defective structure respect to the total atoms in the original structure. Models having 0.5, 1, 2, 3, 4 and 6% of pores were prepared both for the pristine (G) and the oxide sheet (G). The carbon structure of the graphene sheets is shown in Fig. 1.

The Tersoff potential [64] was employed to model covalent bonds between carbon atoms in the graphene sheet. As a bond order potential, the Tersoff potential allows for C–C bond formation or dissociation during the course of a simulation, which allows for example to study fracture properties. On the other hand the covalent bonds of the graphene with the oxide functionalities (i.e. hydroxyl and oxirane groups) were modelled through a Class II force field, whose parameters were based on the COMPASS version developed by H. Sun [65]. This type of force fields includes bond, angles and dihedrals interactions, but also cross-terms which increase the accuracy of the force field on the description of the properties of the system [66]. The non-bonded interactions were modelled by the Lennard–Jones 9–6 and Coulomb potentials for distances below the cutoff of 10.5 Å, while the Particle Mesh Ewald (PME) method was used to account for long electrostatic interactions. The partial atomic charges were derived according to bond increments as stated in COMPASS force field (see Fig. 2).

The LAMMPS simulation code [67] was used to perform the MD simulations. Periodic boundary conditions (PBC) were only applied in the x direction of the graphene sheets (i.e. in the 250 Å dimension of the sheet), while the y and z directions were kept non-periodic during the simulations. The graphene models (either G or GO) were equilibrated under the $NP_xT$ ensemble at 1 atm of pressure and 300 K of temperature during at least 0.5 ns until getting zero-stress structures and reaching the plateau in potential energy.

### Characterization of mechanical properties

The tensile mechanical properties of the graphene models were calculated from equilibrium MD simulations, using a quasi-static approach. The equilibrated graphene models, with zero stress, were initially minimized using the FIRE method [68] during 10,000 iterations. The minimized structures were then subjected to subsequent increments of deformation in the x direction of the cell box, controlled by the corresponding strain vector, while keeping the other cell parameters fixed. PBC were only applied to the x direction (direction of loading). After each deformation the structure were re-minimized under the FIRE method without any changes in the cell parameters. The strain was applied in two types of

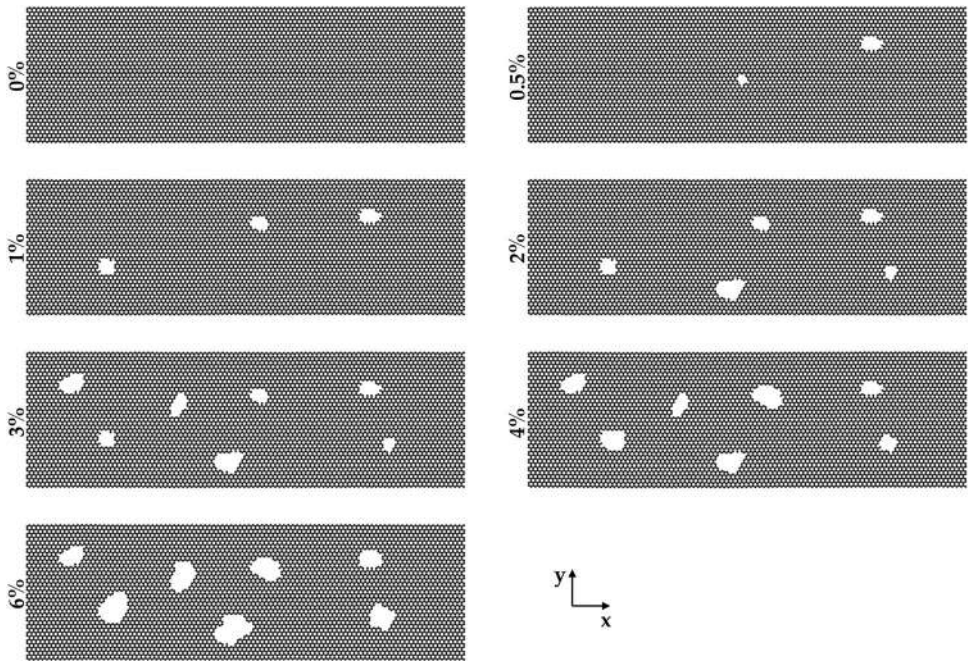


**Figure 1** Structure of carbon atoms in GNRs (either pristine or oxide), showing the morphology of pores.

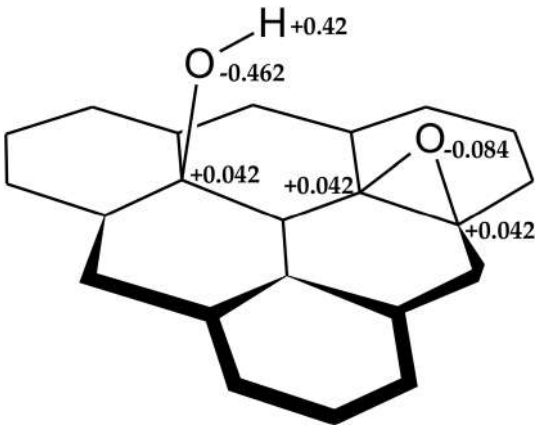


**Figure 2** Schematic showing the structure of oxide groups and partial charges of atoms.

increments: the first 20 increments were of amplitude of 0.002, and the next increments were of 0.008. The response of the system to these increments was monitored as the virial stress calculated with the next expression:

$$\sigma_{ij} = -\frac{1}{V}\sum_{k}\left(m^k u_i^k u_j^k\right) + \frac{1}{2}\sum_{l\neq k}\left(r_i^{kl}\right)\left(f_j^{lk}\right) \quad (1)$$

where $V$ is the total volume of the graphene sheet, $m^k$ and $\boldsymbol{u}^k$ denote the mass and velocity of the $k$th particle, respectively, $\boldsymbol{r}^{kl}$ stands for the distance between $k$th and $l$th particles, and $\boldsymbol{f}^{lk}$ is the force exerted on $l$th particle by $k$th particle. The Young modulus was calculated from the initial slope (i.e. the first derivative of the virial stress respect to the strain) of the stress–strain curve while the tensile strength was calculated as the highest stress registered in the simulation. The thickness of the graphene sheets was considered as 3.35 Å to calculate their corresponding volume, $V$. The in-plane Poisson's ratio, $v_{xy}$, was calculated by monitoring the transversal length of the graphene sheet according to next equation:

$$v_{xy} = -\frac{\varepsilon_y}{\varepsilon_x} \quad (2)$$

where $\varepsilon_x$ and $\varepsilon_y$ refers to the strain of the graphene in x (longitudinal) and y (transverse) direction, respectively. Given that the Poisson's ratio is strain dependant, an average value was compute from the plateau region between the strain range of [0, $\varepsilon_C$], being $\varepsilon_C$ the critical longitudinal strain where the Poisson's ratio changes from negative to positive [69]. In such cases where no $\varepsilon_C$ was observed, due to premature fracture of the graphene, the Poisson's ratio was calculated up to fracture.

## Characterization of thermal conductivity

The thermal conductivity κ of the graphene models was calculated using the Müller-Plathe method [58], which is based on reverse non-equilibrium MD simulations (RNEMD). In this method the simulation box

is divided into slabs along the direction in which the thermal conductivity is being calculated, and a heat flux is imposed between the cold and hot slabs by exchanging the velocity vectors of the hottest atom of the cool slab with the coldest atom of the same mass in the hot slab. This process induces a gradient of temperature between the two slabs, from which thermal conductivity can be calculated as stated in the next formula:

$$\kappa = \frac{-J}{\frac{dT}{dx}} \tag{3}$$

where $J$ is the heat flux and dT/dx is the gradient of temperature in the system along x direction. The heat flux was calculated according to next formula:

$$J = \frac{1}{2tA} \sum_{transfers} \frac{m}{2} \left(v_{hot}^2 - v_{cold}^2\right) \tag{4}$$

where $t$ is the simulation time, A is the cross-sectional area of the graphene model, m is equal to the mass of the atoms transferred, and $v_{hot}$ and $v_{cold}$ are the velocities of the atoms exchanged. The graphene sheets were divided into a total of 20 slabs of about 12.6 Å, the cold slabs were placed in the ends while the hot region was placed in the middle of the graphene sheet. Initially the systems were equilibrated in the canonical ensemble (NVT) during 100 ps, and then the Müller-Plathe algorithm was applied during 1 ns in the microcanonical ensemble (NVE) after getting a steady temperature gradient.

## Characterization of in-plane phonon density of states (DOS)

The thermal conductivity of a system is highly related with the modes and frequencies of vibration of its constitutive atoms, i.e. the phonons. The phonon density of states (DOS), which describes the proportion of states that are occupied by the system at each energy in the range of modes of vibrations, was calculated for each graphene nanoribbon. The DOS was computed by applying the Fourier transformation to the velocity autocorrelation functions (VACF) as stated next:

$$DOS(\omega) = \int_0^{\tau} \langle v(t)v(0)\rangle exp(-i\omega t)dt \tag{5}$$

where $v(0)$ and $v(t)$ are the velocities of each atom at initial time and at time t, respectively. The VACF functions were acquired along 1 ps trajectories with five repetitions for statistical average. Only the x and y components of the velocity of atoms were considered for the calculation to get in-plane DOS, since the z component doesn't contribute to thermal conductivity of graphene nanoribbons due to their planar or sheet geometry.

## Statistical analysis

With the aim of analysing the results from a statistical point of view, the statistical $F$-value was calculated according to next formula:

$$F = \frac{s_{series}^2}{s_{error}^2} \tag{6}$$

where $s_{series}$ is the standard deviation associated to a series of results in which an associated factor could be acting (i.e. the effect of oxidation or the effect of pores) and $s_{error}$ is the standard deviation associated to the MD method itself due to random errors. The $F$-value compares if two standard deviations (i.e., variances) are statistically equal or not, and thus the existence of a factor which produces variations in the results in addition to random errors. If the null hypothesis $H_0$ was true, then the standard deviation in the results would only be associated to random errors ($s_{series} = s_{error}$). On the other hand, if the alternative hypothesis $H_1$ was true then there would be an additional factor which produced the differences found in the results in addition to random errors ($s_{series} = s_{factor} + s_{error}$). The $F$-value was compared to a critical $F$-value, considering a statistical significance of 95%, in order to accept or reject the null hypothesis $H_0$.

# Results and discussion

## Mechanism of failure under tensile stress of graphene nanoribbons

The stress–strain curves obtained during the tensile simulations of the graphene models are plotted in Fig. 3 and Fig. 4 for pristine graphene (G) and graphene oxide (GO), respectively, with a comparison between the different pore percentages. It was observed that the stress–strain curves of some of the models, depending on the percentage of pores, exhibited a complex behaviour with two steps of deformation in which after the initial linear elastic

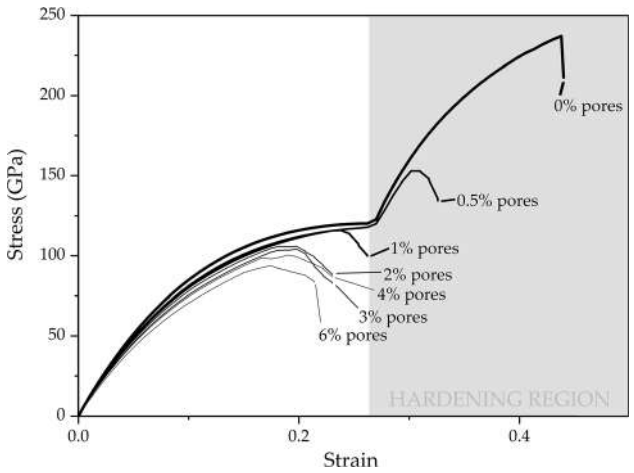


**Figure 3** Stress–strain curves for pristine graphene (G) models for different pore percentages.

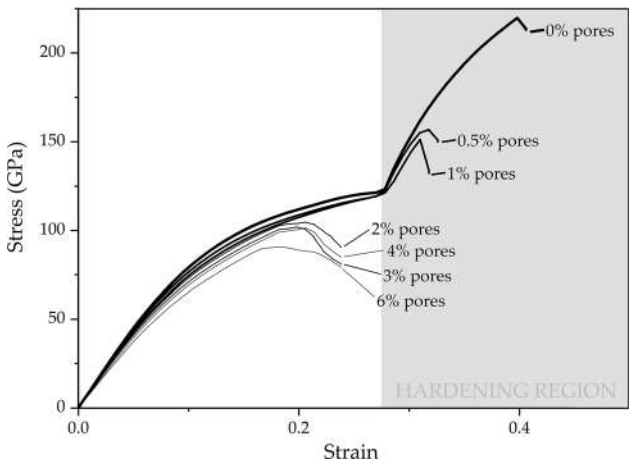


**Figure 4** Stress–strain curves for graphene oxide (GO) models for different pore percentages.

response and plastic yield there was a sharp increase of stress at deformations around 0.28. This 'hardening' behaviour [70] associated to high strain was produced in the pristine graphene (G) models of 0 and 0.5% pores (Fig. 3), whereas in the graphene oxide (GO) it was also observed for the 1% pore model (Fig. 4). When analysing the snapshots from MD simulations in these models it was observed that, around 0.28 of deformation, it was produced the reorganization of some atoms in form of dislocations. In Fig. 5 a series of snapshots from the tensile simulation of the GO model with 0.5% pores have been selected to show a graphic schematic. The dislocations appeared in the structure as pentagon-heptagon pairs due to the breakage of one C–C bond and later displacement of the atoms. This pentagon-heptagon pairs have also been identified in the literature as '5–7' defects [71] or Stone–Wales defects [23]. It was observed that these dislocations started preferably at the borders of the pores, which acted someway as nucleation points of this type of defects. While increasing the deformation of the sheet, new pentagon-heptagon pairs were created next to the previous ones and the dislocation grew in a straight line which followed the armchair or zigzag directions of the crystal lattice of the graphene sheet. In Fig. 6 a snapshot showing the formation of a dislocation line with detail is plotted, while in Fig. 7 the stress map of snapshots before dislocation of atoms, during the generation of a dislocation line and after cracking are represented. As it can be observed from the stress maps, the dislocation of atoms decreased the stress of the atoms just besides the dislocation line, i.e. the dislocation acted as a stress reliever, and helped the GNR sheet to accommodate higher degrees of deformation before failure. Other authors such as Mao et al. [72] and Liang and Huan [73] also reported this 'hardening' behaviour, while the presence of such dislocations has also been demonstrated experimentally using sophisticated TEM microscopy [74, 75].

When the pore percentage was higher than the one indicated previously for each type of graphene (i.e., higher than 0.5% for pristine GNRs and higher than 1.0% for GO), it was observed that the graphene sheet broke at lower deformations without the previous formation of such dislocation defects. Thus, no 'hardening' behavior was observed in the stress–strain curves for these GNRs. At a certain stress, the structure finally collapsed and tore with even the production of monoatomic carbon chains at certain points of the crack [76]. It was also observed that the crack growth was predominantly produced along straight lines aligned with the armchair or zigzag directions of the hexagonal crystal lattice of graphene (Fig. 8), which was in agreement with other studies [77, 78]. These cracks were produced in form of tears (i.e. tearing mechanism) which occurred in the direction perpendicular to the direction of loading. In some cases, the direction of the tear occurred with some tilt respect to the direction of loading, and it

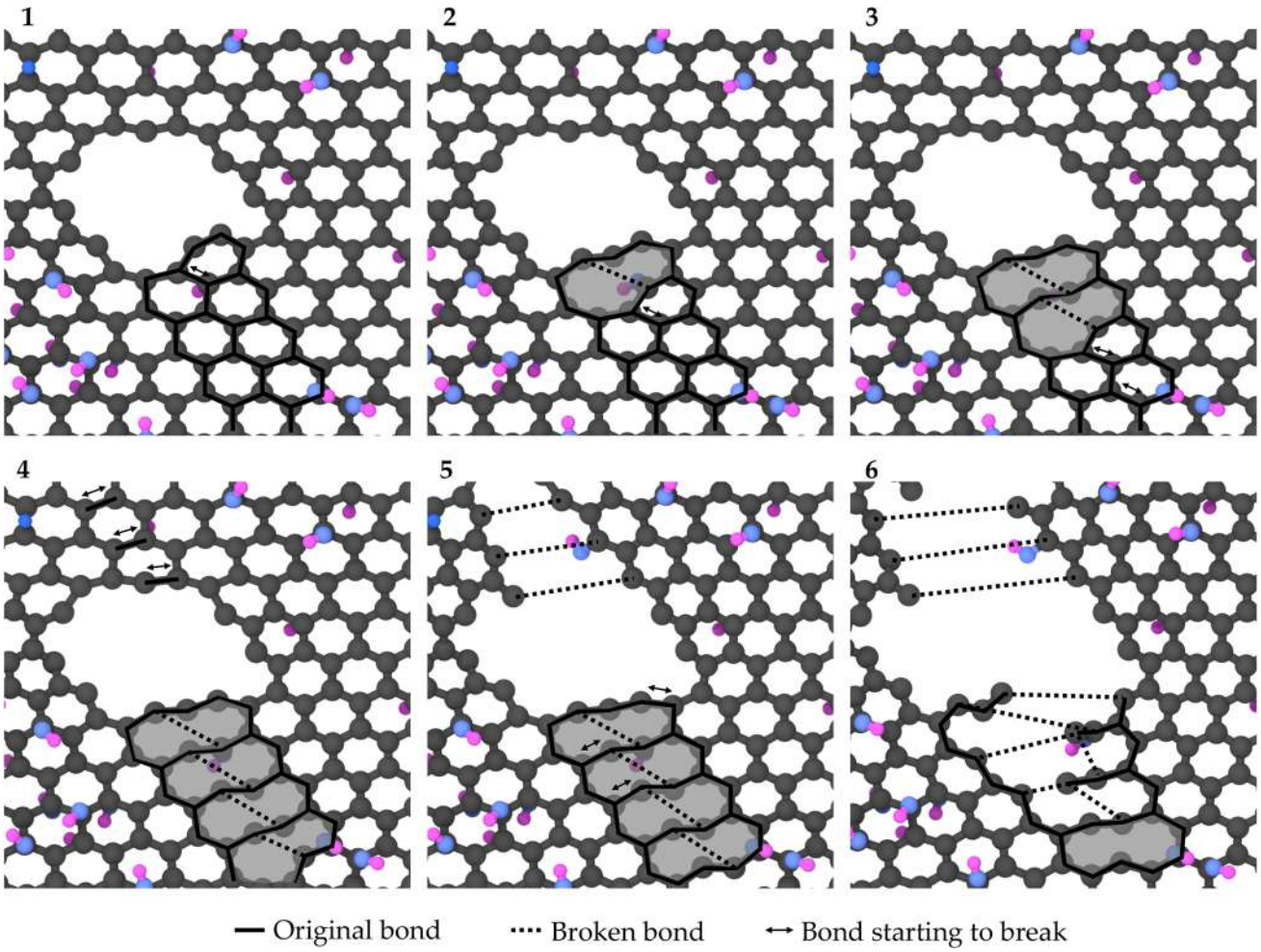


**Figure 5** Snapshots showing the formation of dislocations during stretching simulation (GO model with 0.5% of pores).

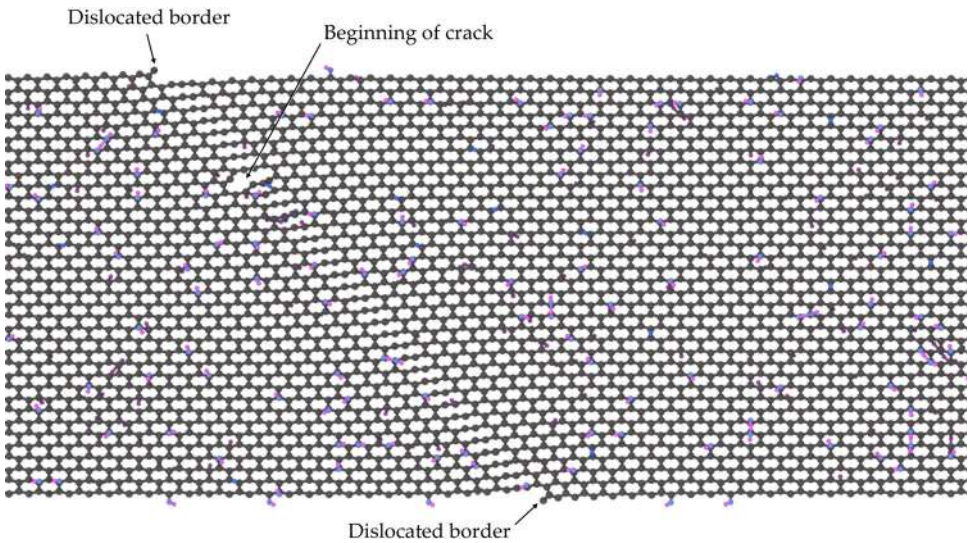


**Figure 6** Snapshot showing a complete dislocation and beginning of crack in the 0% porosity GO nanoribbon.

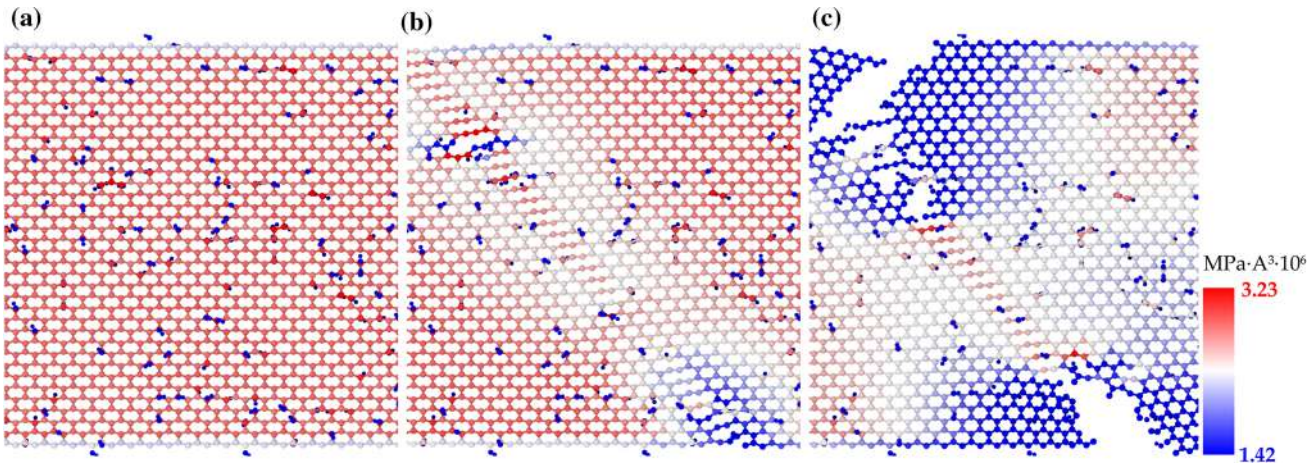


**Figure 7** Stress map of 0% porosity GO nanoribbon **a** before dislocation, **b** during generation of dislocation and **c** after cracking.

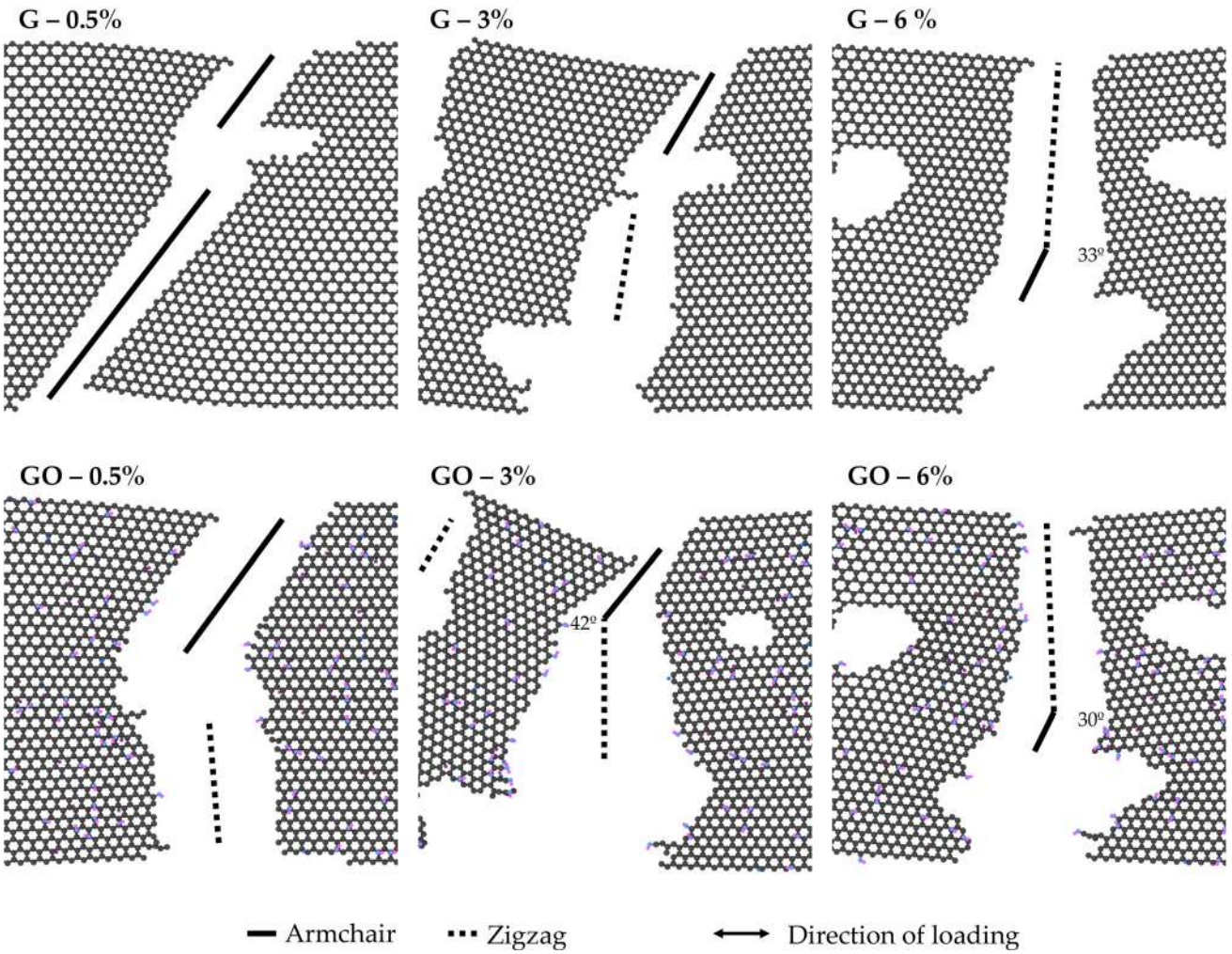


**Figure 8** Snapshots showing the region of failure in selected GNR models.

was observed that even it occasionally changed the direction from armchair to zigzag (or vice versa). This mechanism of deformation and failure of graphene sheets, through the formation of dislocations and ripping, has also been observed for carbon nanotubes [71].

## Tensile mechanical properties of GNRs

A summary of the main tensile mechanical properties of the pristine graphene (G) and graphene oxide (GO) models in terms of Young's modulus, tensile strength, deformation at break and Poisson's ratio is shown in Table 1 and Table 2. Graphic representations of these properties versus the porosity are plotted in Fig. 9 and Fig. 10. The Young modulus of pristine graphene (G) without pores (0% model) was calculated as 1.17 TPa, which was near the value of 1 TPa reported experimentally [2] and by ab initio simulations [79]. Nevertheless, the intrinsic strength (i.e. tensile strength) was overestimated for this model (238 GPa) in comparison with that reported in the literature of 130 GPa [2] or even lower [80], which would be closer to the values of tensile strength obtained for the models with pores. In the same way, the values of deformation at break were higher than those reported in the literature [79], which indicated that the MD method tended to overestimate the value of properties at high levels of deformation. Liang et al. [81], which conducted a similar study on pristine graphene sheets using the AIREBO potential, obtain equivalent results either in terms of the stress–strain curve and tensile strength. In the case of the graphene oxide (GO), the reported values for Young's modulus are dependant on the degree and type of oxidation (i.e., oxirane and/or hydroxyl). Kang et al. [82] obtained from experimental measurements a Young's modulus of about 700 GPa for a graphene sheet with 25% oxidation, while Suk et al. reported a modulus of 207 GPa for a graphene sheet of 40% oxidation. On the other hand, Khoei et al. [83], who also studied the mechanical properties of graphene oxide through MD simulations, found a Young's modulus of around 950 GPa for a graphene sheet with 10% degree of oxidation. In the present study a value of 903 GPa was obtained for the 0% porosity model and 8.3% degree of oxidation, which was consistent with the results found in the literature.

According to previous studies, the Poisson's ratio depends on the size and chirality of the sheet [84], but also on the applied strain [69]. The values of Poisson's ratio reported in Table 1 and Table 2 were calculated in the range of deformation [0, $\varepsilon_C$] as explained before, and were negative in all the cases, either G or GO, indicating thus an auxetic behaviour for these nanoribbons [85, 86]. According to the study by Jiang and Park [69], the negative Poisson's ratio phenomenon can be observed in graphene sheets with widths up to about 10 nm, which agrees with the results found in the present study. The 'hardening' mechanism explained previously also affected the transversal deformation of the graphene nanoribbons and thus to the value of the associated Poisson's ratio. It was observed that at deformation levels below 0.28 the Poisson's ratio had negative and approximately constant values but, at higher deformations (i.e., in those cases where no failure was produced before) the Poisson's ratio tended to increase linearly and even turned to positive values (see Fig. 10). Besides, a graphic comparative of the snapshots between the longitudinal section of the graphene nanoribbon at different deformation states have been plotted in Fig. 11 to illustrate this behaviour.

**Table 1** Tensile mechanical properties for pristine graphene (G) nanoribbons (variation percentages are in brackets)

| Porosity (%) | Young's modulus (GPa) | Tensile strength (GPa) | Deformation at break (%) | Poisson's ratio |
|---|---|---|---|---|
| 0 | 1170 ± 14 | 238.2 ± 3.3 | 0.442 ± 0.006 | −0.151 ± 0.001 |
| 0.5 | 1121 ± 15 (−4%) | 154.0 ± 0.2 (−35%) | 0.310 ± 0.000 (−30%) | −0.148 ± 0.000 (+ 2%) |
| 1 | 1107 ± 13 (−5%) | 115.9 ± 2.8 (−51%) | 0.234 ± 0.006 (−47%) | −0.144 ± 0.001 (+ 5%) |
| 2 | 1081 ± 13 (−8%) | 105.9 ± 2.4 (−56%) | 0.198 ± 0.000 (−55%) | −0.126 ± 0.000 (+ 16%) |
| 3 | 1050 ± 12 (−10%) | 104.1 ± 1.9 (−56%) | 0.198 ± 0.000 (−55%) | −0.109 ± 0.000 (+ 28%) |
| 4 | 1035 ± 13 (−12%) | 100.5 ± 1.5 (−58%) | 0.190 ± 0.000 (−57%) | −0.096 ± 0.000 (+ 36%) |
| 6 | 980 ± 13 (−16%) | 93.9 ± 1.4 (−61%) | 0.174 ± 0.000 (−61%) | −0.064 ± 0.001 (+ 57%) |

**Table 2** Tensile mechanical properties for graphene oxide (GO) nanoribbons (variation percentages are in brackets)

| Porosity (%) | Young's modulus (GPa) | Tensile strength (GPa) | Deformation at break (%) | Poisson's ratio |
|---|---|---|---|---|
| 0 | 903 ± 20 | 216.6 ± 4.6 | 0.398 ± 0.000 | −0.147 ± 0.001 |
| 0.5 | 893 ± 7 (−1%) | 156.6 ± 0.4 (−28%) | 0.318 ± 0.000 (−20%) | −0.146 ± 0.002 (+ 1%) |
| 1 | 856 ± 2 (−5%) | 151.2 ± 0.1 (−30%) | 0.310 ± 0.000 (−22%) | −0.135 ± 0.001 (+ 8%) |
| 2 | 840 ± 32 (−7%) | 104.7 ± 0.2 (−52%) | 0.210 ± 0.006 (−47%) | −0.123 ± 0.002 (+ 16%) |
| 3 | 825 ± 20 (−9%) | 102.0 ± 1.6 (−53%) | 0.202 ± 0.006 (−49%) | −0.103 ± 0.007 (+ 30%) |
| 4 | 786 ± 19 (−13%) | 101.4 ± 1.3 (−53%) | 0.206 ± 0.000 (−48%) | −0.081 ± 0.002 (+ 45%) |
| 6 | 751 ± 29 (−17%) | 90.8 ± 1.1 (−58%) | 0.182 ± 0.011 (−54%) | −0.044 ± 0.001 (+ 70%) |

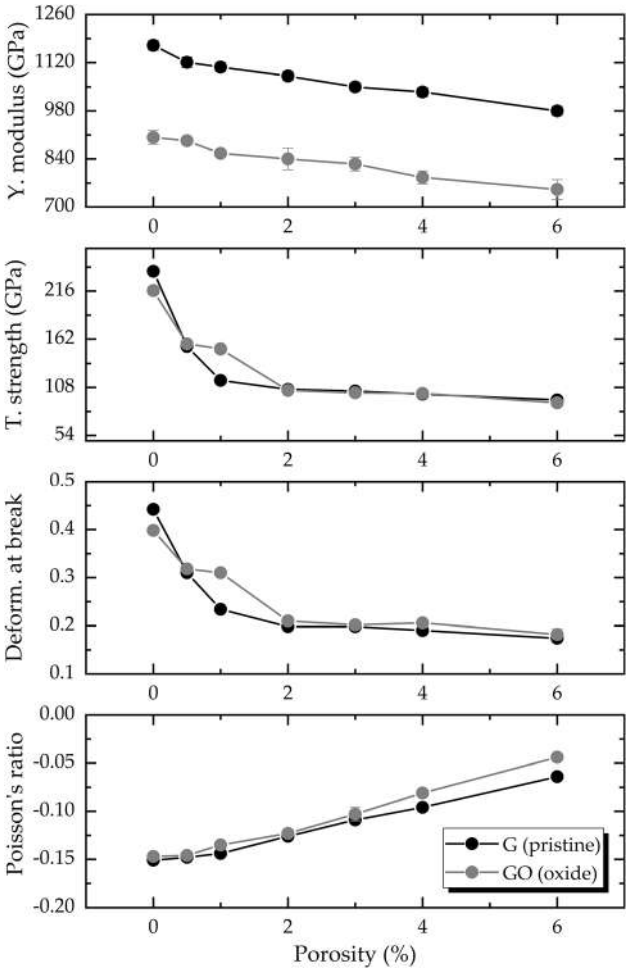


**Figure 9** Plots of tensile mechanical properties versus porosity.

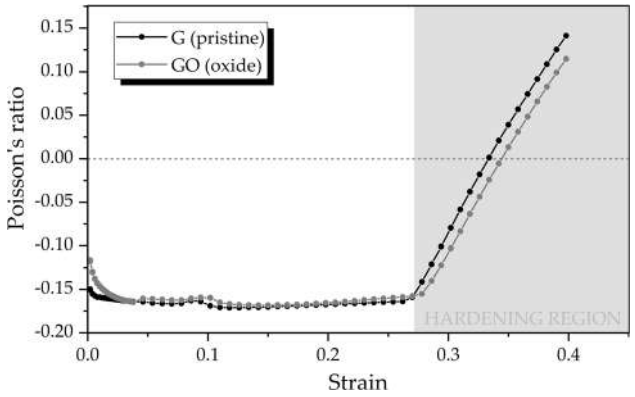


**Figure 10** Poisson's ratio versus strain for 0% pores G and GO nanoribbons.

The values of the parameter $F$ were calculated from the standard deviation associated to the results to analyse, from a statistical point of view, the effect of porosity and oxidation of the graphene nanoribbons on its tensile mechanical properties. The results are summarized in Table 3, in which bold values indicate that the value of $F$ was higher than the critical value, and thus the alternative hypothesis $H_1$ was accepted, i.e., there was an effect of the factor. The first analysed factor, i.e. porosity, had a significative effect in all the assessed tensile mechanical properties and either the Young modulus, tensile strength, deformation at break or Poisson's ratio were statistically affected due to the presence of pores in the graphene sheet. The tendencies versus porosity found on these properties (see Fig. 9) were similar in both types of graphene nanoribbons (G and GO), although different for each analysed property. In the case of the Young's modulus it decreased approximately in a linear fashion when the porosity increased, up to a decrease of around 16–17% when the porosity was 6%. The tendency found in Poisson's ratio also

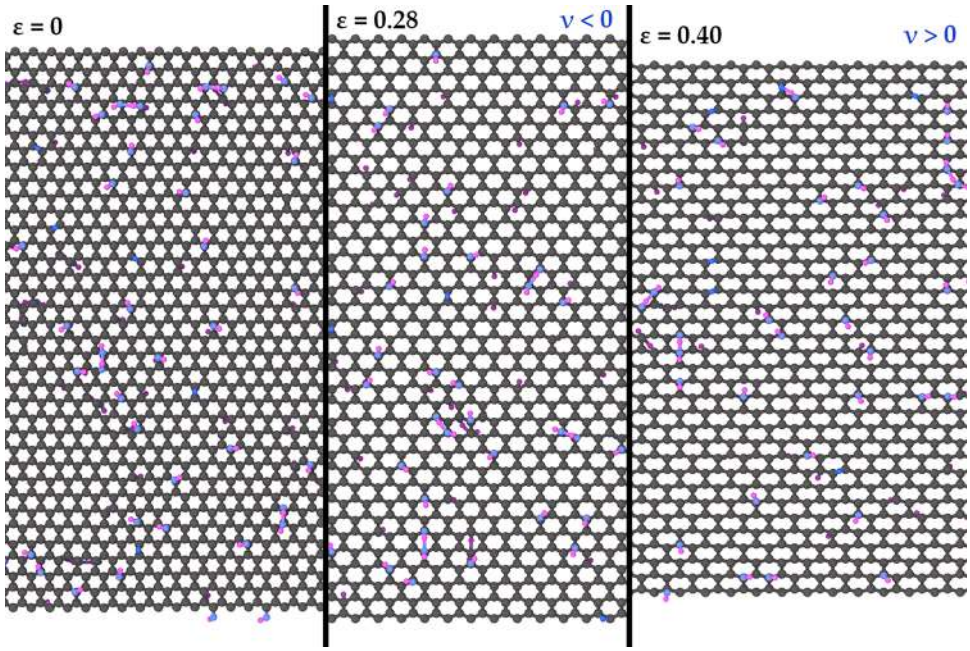


**Figure 11** Snapshots showing a comparative of the longitudinal section of the 0% pores GO nanoribbon during the tensile deformation at different deformation states.

**Table 3** *F*-values[a] for the tensile mechanical properties

| Factor | Young's modulus (GPa) | Tensile strength (GPa) | Deformation at break (%) | Poisson's ratio | Critical F-value |
|---|---|---|---|---|---|
| Porosity | **47.7** | **103.2** | **80.6** | **283.0** | 2.6 |
| Oxidation | **1431.0** | *0.19* | *2.4* | **28.5** | 4.3 |

[a]In bold: $H_0$ is refused (significative effect of factor)/In italics: $H_0$ is accepted (no effect of factor)

followed a linear trend, although for this property the porosity produced an increase in its value, reaching up to 70% for a 6% porosity respect to the non porosity nanoribbon. For the tensile strength and deformation at break, both properties related with fracture parameters, the tendency followed a exponential decrease. At porosities below 2% there was produced a dramatic decrease either in the tensile strength and deformation at break (with maximum decreases of about 54–51%), but at higher porosities it was observed an asymptotic behaviour where the porosity had a lower impact on the values of such properties. This different tendency versus porosity found in one hand in the Young's modulus and Poisson's ratio, and on the other hand on the tensile strength and deformation at break could be explained by the hardening mechanism described before. The hardening behaviour, by which the graphene nanoribbons could afford higher stress and deformations (see Fig. 3 and Fig. 4), was only produced in perfect (i.e., 0% porosity) or practically perfect (i.e., below 1% porosity) graphene nanoribbons, but at porosities higher than 1% this mechanism was not produced. The absence of this hardening mechanism in the graphene nanoribbons produced the sharp decrease observed in the properties related with fracture, i.e. tensile strength and deformation at break. The Young's modulus and Poisson's ratio were not affected by this mechanism since these properties are calculated in the elastic region.

Regarding the second analysed factor, i.e. the oxidation of the graphene nanoribbons, the *F* values indicated that only the Young's modulus and Poisson's ratio were significatively affected, whereas the tensile strength and deformation at break were not modified due to this factor. As can be seen in Fig. 9, the oxidation decreased the values of Young's

modulus by around 240 GPa (around 20–24%) respect to the G nanoribbons, which was in agreement with a 8.3% degree of oxidation or functionalization [87]. This decrease in the rigidity of the graphene sheet due to the oxidation can be explained considering the disruption of the $sp^2$ network due to the presence of hydroxyls and oxirane groups [88]. As was described by Zheng et al. [87], the $sp^3$ hybridization of carbon atoms breaks the local π bond of the graphene sheet and also makes the $sp^3$ with an off-plane structure easier to be bent by tension, which weaken the graphene structure. The fact that the oxidation has no significant effect either in the tensile strength and deformation at break, i.e. tensile fracture properties, indicated that at high deformations the effect of oxidation was negligible. Zandiatashbar et al. [89], who also studied the effect of defects on the mechanical properties of graphene, found that the porosity govern the mechanical properties over the $sp^3$ defects (i.e. oxidation) in the vacancy-defect regime. In the present study it was observed that this statement applied essentially to the fracture properties, but in the case of tensile mechanical properties in the elastic region (i.e. at low strains) the effect of oxidation was comparable to the effect of porosity and both factors contributed significatively to the Young's modulus and Poisson's ratio.

## Thermal conductivity of graphene nanoribbons

A summary of the results of thermal conductivity (κ) measured in the pristine (G) and graphene oxide (GO) nanoribbons can be found in Tables 4 and 5, respectively. The thermal conductivity of non-porous pristine graphene (G) nanoribbon (0% model) was calculated as 160.5 W/m·K, according to the RNEMD simulations performed in this study. This value was in agreement with the values reported for armchair edge graphene nanoribbons in other MD studies [90, 91] as well with the experimental range found for suspended graphene of 100–300 W/m·K [92]. The thermal conductivity of graphene nanoribbons is usually reported an order of magnitude lower than that of graphene [93], which is a consequence of the edge and defect scattering due to its narrow width (7.5 nm width in the present study) [94]. Besides, Li and Zhang [95] demonstrated that the Tersoff potential, i.e., the potential used in the present study, produced similar heat flux distribution along graphene nanoribbons than the AIREBO potential.

**Table 4** Thermal conductivity (300 K) for pristine graphene (G) nanoribbons (variation percentages are in brackets)

| Porosity (%) | Thermal conductivity κ (W/m K) |
|---|---|
| 0 | 160.5 ± 11.8 |
| 0.5 | 142.6 ± 2.2 (−11%) |
| 1 | 125.4 ± 1.4 (−22%) |
| 2 | 111.1 ± 1.6 (−31%) |
| 3 | 103.6 ± 2.2 (−35%) |
| 4 | 95.0 ± 2.3 (−41%) |
| 6 | 77.0 ± 0.9 (−52%) |

**Table 5** Thermal conductivity (300 K) for graphene oxide (GO) nanoribbons (variation percentages are in brackets)

| Porosity (%) | Thermal conductivity κ (W/m·K) |
|---|---|
| 0 | 43.6 ± 2.8 |
| 0.5 | 40.2 ± 0.8 (−8%) |
| 1 | 38.8 ± 0.5 (−11%) |
| 2 | 36.6 ± 0.8 (−16%) |
| 3 | 34.1 ± 0.9 (−22%) |
| 4 | 32.3 ± 1.5 (−26%) |
| 6 | 28.9 ± 0.2 (−34%) |

**Table 6** *F*-values[a] for the thermal conductivity results

| Factor | Thermal conductivity κ (W/m·K) | Critical F-value |
|---|---|---|
| Porosity | **6.4** | 2.6 |
| Oxidation | **254.1** | 4.3 |

[a]In bold: $H_0$ is refused (significative effect of factor)/In italics: $H_0$ is accepted (no effect of factor)

The statistical analysis results made in terms of parameter *F* are summarized in Table 6. It was found that either the porosity or oxidation had a significative effect on the calculated thermal conductivity, since the determined parameter *F* was higher than the critical value in each case. The curves of thermal conductivity versus porosity plotted in Fig. 12 showed a linear trend in both types of nanoribbons, although two regions with different slope were observed in both types of graphene nanoribbons. Below 1% porosity, the thermal conductivity exhibited a higher slope versus porosity, but at higher porosities, the curve had a lower slope, i.e. a lower

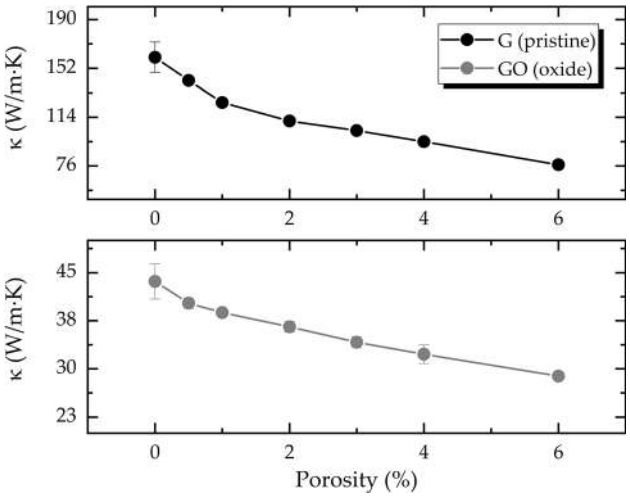


**Figure 12** Plots of thermal conductivity κ versus porosity.

dependence of porosity. This double-side linear behaviour of thermal conductivity versus porosity was also obtained by other authors [96, 97] for graphene sheets. In addition, other studies found an exponential decay of thermal conductivity when increasing porosity in pristine GNR [98, 99]. Given that the thermal conductivity is based on the transmission of phonons through the net of carbon atoms, the presence of pores acted as phonon scattering points where the transmission of vibrations was cancelled. Nevertheless, the scattering effect is more significant in small pores (i.e., lower porosity) than in longer pores (i.e., higher porosity) [97, 100]. The analysis of the phonons and its connection with thermal conductivity is discussed in next section.

The oxidation of GNRs approximately decreased their thermal conductivity for about 60–70% respect to that found for the pristine GNR, indicating thus that GO nanoribbons were worst heat conductors than their non-oxidized version (i.e., are better insulators). This sharp decrease of thermal conductivity was in the order as calculated by other studies for a 8.3% of oxidation of the graphene sheet [91, 101]. The oxidation of GNR through the introduction of hydroxyl and oxirane groups produced a change in the hybridization of the implied carbon atoms from $sp^2$ to $sp^3$, which generated structural or morphological changes in the graphene sheet. These structural changes were due to variations found in the C–C bond distances and C–C–C–C dihedral angles produced in the environment of the oxidation groups, as can be seen from the representations shown in Figs. 13 and 14. The C–C bond distance in a non-oxidated environment (i.e., in pristine GNR) was of 1.46 Å (Fig. 13a), but this distance increased in the first neighbour atoms of the C atoms involved in the oxidation groups. When a hydroxyl or oxirane group was attached to the C atoms, the C–C bond distance of the first neighbours increased to around 1.51 Å (Fig. 13b) and 1.48 Å (Fig. 13c), respectively, or even to 1.52 Å in the C atoms directly bonded to the oxirane group. Consequently, the C atoms bonded to the oxidative groups had to get out of the plane to accommodate these bond increments, as were manifested in the dihedral angle values (Fig. 14). The alteration of the structure of the GNR sheet, either by an increase of the bond distance or by a change in the dihedral angles, generated points were a phonon-defect scattering mechanism was produced, which finally manifested in a lower thermal conductivity. Mu et al. [101] also indicated that the change in mass that produced the oxidation also perturbed the vibration of the C atoms, but the change produced in the structure affected more significatively to the thermal conductivity than the change in mass. On the other hand, Lin and Buehler [91] explained that the decrease found in the in-plane thermal conductivity after the oxidation of GNR was also due by a reduction of the phonon mean free path, as it is discussed in the next section.

## In-plane phonon density of states (DOS)

According to Balandin et al. [102], acoustic phonons are the main heat carriers in carbon materials such as graphene, thanks to the exceptionally strong $sp^2$ covalent C–C bonds of its lattice structure. In this way, the results of thermal conductivity can be explained from the analysis of in-plane phonon density of states (DOS), which were obtained from the Fourier transformation of the atomic velocity autocorrelation functions (VACF). According to the kinetic theory [91, 101], the thermal conductivity can be related with phonons through the next expression:

$$\kappa \sim \sum_i C_i v_i l_i = l_{eff} \sum_i C_i v_i \tag{7}$$

where $C_i$ is the volumetric specific heat of the vibration mode, $v_i$ the group velocity, $l_i$ the mean free path of the phonon mode i (with an angular frequency ω), and $l_{eff}$ the effective phonon mean free path. The

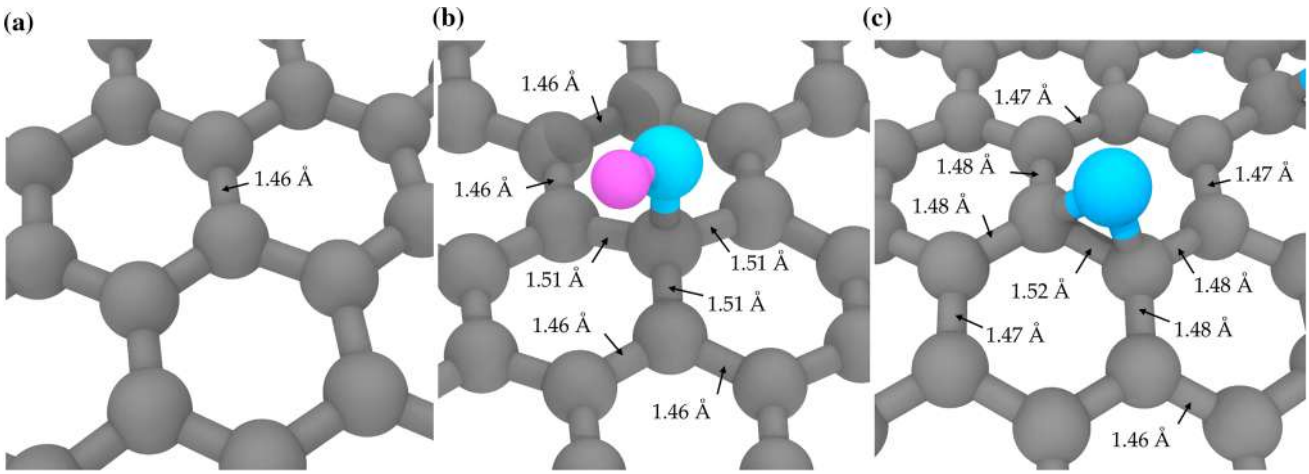


**Figure 13** C–C bond distances determined in **a** pristine GNR and in oxide GNR at **b** hydroxyl and **c** oxirane environments.

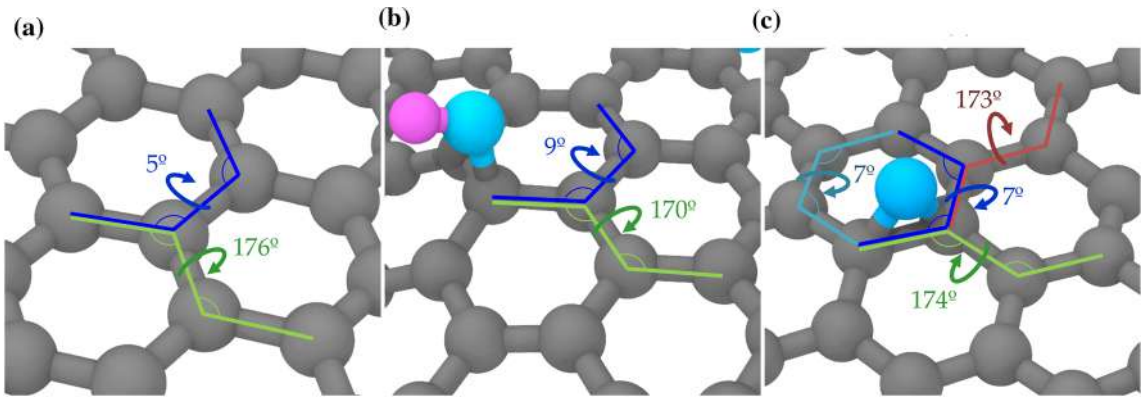


**Figure 14** C–C–C–C dihedral angles determined in **a** pristine GNR and in oxide GNR at **b** hydroxyl and **c** oxirane environments (associated uncertainty is equal to ± 5° in all cases).

previous relation establishes that the thermal conductivity is proportional to the phonon mean free path, the heat capacity and the phonon velocity. On the other hand, according to the Debye model, the specific heat capacity $C_i$ is related with the phonons as:

$$C_i = C(\omega) = \hbar\omega D(\omega)\frac{\partial f(T,\omega)}{\partial T} \quad (8)$$

where $\hbar$ is the Planck constant, $D(\omega)$ is the DOS for phonon mode i with frequency $\omega$, T is the absolute temperature and $f(T,\omega)$ is the Bose–Einstein distribution function. Given that the derivative term is constant for a fixed phonon mode i with frequency $\omega$ at constant T [91], Eq. 8 states that the specific heat capacity $C_i$ of a phonon mode is mainly dependant on the product of frequency and DOS function. Considering thus the previous relationships, the DOS multiplied by the frequency spectra and the phonon mean free path were calculated to get a better understanding of the effect of the porosity and oxidation on these parameters and therefore in the conductivity. The phonon DOS spectra are plotted in Fig. S15 (see Supplementary Material) whereas the product of frequency and DOS function spectra are plotted in Fig. 15. In first place, the porosity had negligible effect on the DOS spectra of either G and GO nanoribbons, which indicated that the presence of pores did not affected the vibrational modes of the graphene. Nevertheless, when comparing the DOS spectra of G and GO (see Fig. 16), the oxidation produced the apparition of a new in-plane vibrational mode at high frequencies, around 120 THz, associated to the C–O bonds. According to Eq. 8,

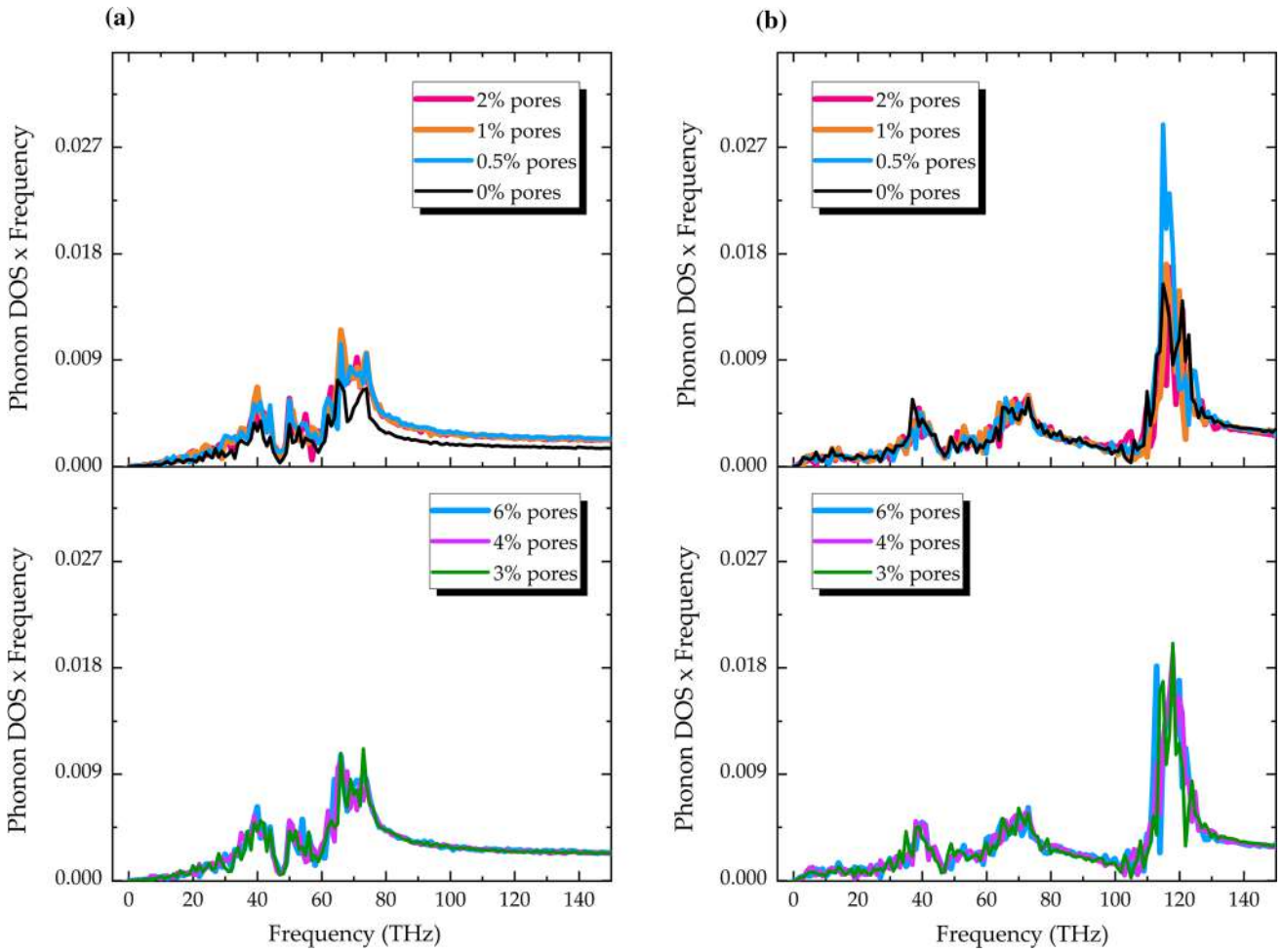


**Figure 15** In-plane phonon DOS multiplied by the frequency of **a** pristine graphene (G) and **b** graphene oxide (GO) nanoribbons.

these high frequency phonons contributed increasing the in-plane thermal conductivity of the GO nanoribbons, nevertheless their contribution was not enough since the thermal conductivity of the GO structures was lower than the G structures as was described in previous section. At this point, the modification of the mean free path of the phonons due to the oxidation played a major role in the thermal conductivity of the nanoribbons than the vibration frequencies. The effective phonon mean free path $l_{eff}$ can be expressed through the Matthiessen's rule as:

$$\frac{1}{l_{eff}} = \frac{1}{l_{ph-ph}} + \frac{1}{l_{ph-b}} \tag{9}$$

where $l_{ph\text{-}ph}$ is the intrinsic mean free path due to the phonon–phonon scattering and $l_{ph\text{-}b}$ is the phonon

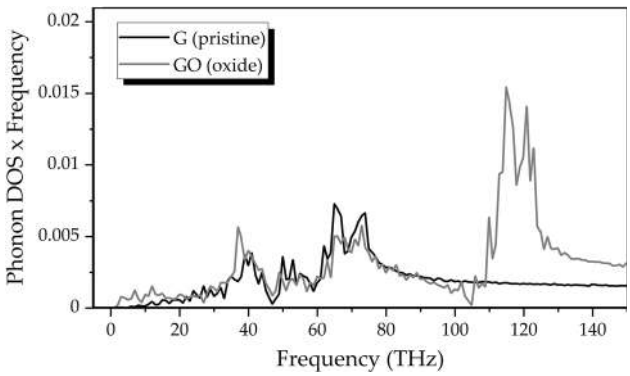


**Figure 16** Comparative of in-plane phonon DOS multiplied by the frequency between pristine graphene (G) and (b) graphene oxide (GO) (0% porosity).

free path due to boundary scattering, which is the nanoribbon length, $L$ (i.e., $l_{ph\text{-}b} = L$). Combining Eqs. (7) and (9) the thermal conductivity can be related with the nanoribbon length as:

$$\frac{1}{\kappa} = \frac{1}{\sum_i C_i v_i}\left(\frac{1}{l_{ph-ph}} + \frac{1}{L}\right) \tag{10}$$

According to Eq. (10), from the linear plot of $1/\kappa$ against $1/L$ the thermal conductivity for an infinitely long nanoribbon can be obtained from the intercept of the extrapolation whereas $l_{ph\text{-}ph}$ from the slope of the fitting. With the aim of calculating the intrinsic mean free path $l_{ph\text{-}ph}$ at each porosity, a series of models were generated by replicating twice or three times the models presented in Fig. 1 along the longitudinal direction to obtain doubled (2L) and tripled length (3L) graphene nanoribbons. After their equilibration, the thermal conductivity of each model was calculated according to the Müller-Plathe method. The individual results of thermal conductivity for these 2L and 3L models can be found in the Supplementary Material. From the linear plots of $1/\kappa$ against $1/L$ the intrinsic mean free path $l_{ph\text{-}ph}$ was calculated for each porosity level on each type of graphene nanoribbon, G and GO, and the results are summarized in Fig. 17. When analysing in first place the effect of porosity, in the case of G nanoribbons it was observed that $l_{ph\text{-}ph}$ decay rapidly with the porosity from 2000 Å at 0% porosity to around 240 Å at 3% porosity, from which $l_{ph\text{-}ph}$ maintained constant with no further decrease. For the GO nanoribbons there were observed two regions of $l_{ph\text{-}ph}$ versus porosity: between 0 and 1% the value of $l_{ph\text{-}ph}$ was around 180 Å, while at porosities higher than 2% the $l_{ph\text{-}ph}$ decreased and took values around 115 Å. In comparison with G nanoribbons, the effect of porosity had less impact on GO nanoribbons. On the other hand, it can also be observed that $l_{ph\text{-}ph}$ was an order of magnitude higher in G nanorribons compared to GO nanoribbons at porosities below 1%, and approximately twofold higher in G nanorribons at porosities over 2%. This higher values of $l_{ph\text{-}ph}$ for G nanoribbons would explained their higher thermal conductivity and the effect of oxidation was mainly manifested in a sharp decrease of the $l_{ph\text{-}ph}$ parameter. Although was not the purpose of the present study to analyse different oxidation degree levels, Chen and Li [103] determined that the degree of oxidation was directly proportional to the inverse of the phonon mean free path. In summary, either the porosity and the oxidation affected mainly the phonon mean free path, and either the pores and the oxidized groups (i.e., hydroxyl and oxirane) acted as scattering points for the transmission of the phonons throughout the graphene sheet.

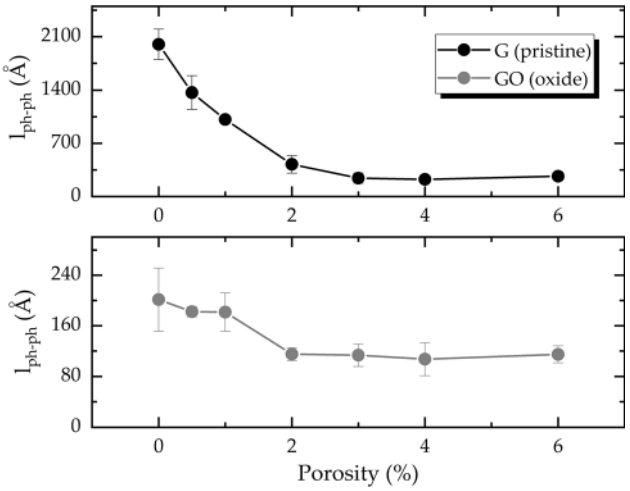


**Figure 17** Plots of intrinsic mean free path $l_{ph\text{-}ph}$ versus porosity.

## Conclusions

A series of molecular simulation models of graphene nanoribbons (GNRs) were constructed with different degrees of porosity and with or without oxidation, i.e. neat (G) or oxide (GO), to assess the effect of such parameters in the tensile mechanical and thermal conductivity properties. In first place, regarding the failure mechanism of graphene nanoribbons under tensile loadings, it was observed that at low porosity levels and around 0.28 deformations a 'hardening' behaviour was manifested in the structures as dislocations lines formed by pentagon-heptagon pairs (i.e., 5–7 defects) which helped the nanoribbons to accommodate higher tensile stress and acted as stress reliever. Such GNRs exhibited a complex stress–strain curve with two steps of deformation. This 'hardening' behaviour required of near perfect or non-defective graphene nanoribbons, so that at porosities higher than around 1% the nanoribbons broke at deformations below 0.28 with no hardening effect. The breaking of the nanoribbons was produced as a tearing mechanism in which the crack growth predominantly along straight lines perpendicular to the direction of loading and aligned with the armchair

or zigzag directions of the hexagonal crystal lattice of graphene. The porosity affected all the analysed tensile mechanical properties (i.e., Young's modulus, tensile strength, deformation at break and Poisson's ratio), but with different tendency in the fracture properties (tensile strength and deformation at break) which was explained by the presence or absence of hardening behaviour at high deformations in the graphene nanoribbons. Nevertheless, the oxidation affected only the tensile and Poisson's ratio but not to the tensile strength and deformation at break. On the other hand, the thermal conductivity of the GNRs was affected either by the porosity and oxidation according to the F analysis. Pores and oxidation groups (i.e., hydroxyl and oxirane) acted as phonon scatterers since they disrupted the carbon network by the generation of vacancies or out-of-plane carbons, respectively, which decreased the phonon mean free path and thus the thermal conductivity. In conclusion, the porosity and oxidation of GNRs must be considered when tuning the tensile mechanical properties and thermal conductivity of such materials through the synthetic pathways. Moreover, it can also be established that the MD methodology is a valid technique to compute the mechanical and thermal properties of graphene derivatives.

## Acknowledgements

We thank Dr. Pablo González for its support with the statistical analysis. The technical activities presented have been carried out under the SMARTFAN project framework ("Smart by Design and Intelligent by Architecture for turbine blade fan and structural components systems", grant agreement no. 750779) funded by the European Union's Horizon 2020 research and innovation program. The writing of the article has been done as a dissemination activity with the support of the European Regional Development Fund (ERDF).

## Author contributions

All authors contributed to the study conception and design. Modeling, data collection and analysis were performed by CSE. The first draft of the manuscript was written by CSE and all authors commented on previous versions of the manuscript. All authors read and approved the final manuscript.

## Funding

Open Access funding provided thanks to the CRUE-CSIC agreement with Springer Nature.

## Data and code availability

The raw data is available upon request to the authors.

## Declarations

**Conflicts of interests** The authors have no relevant financial or non-financial interests to disclose.

**Ethical approval** Not Applicable.

**Supplementary Information:** The online version contains supplementary material available at https://doi.org/10.1007/s10853-023-08810-y.



## References

[1] Lee XJ et al (2019) Review on graphene and its derivatives: synthesis methods and potential industrial implementation. J Taiwan Inst Chem Eng 98:163–180. https://doi.org/10.1016/j.jtice.2018.10.028

[2] Lee C, Wei X, Kysar JW, Hone J (2008) Measurement of the elastic properties and intrinsic strength of monolayer graphene. Science 321:385–388. https://doi.org/10.1126/science.1157996

[3] Papageorgiou DG, Kinloch IA, Young RJ (2017) Mechanical properties of graphene and graphene-based

nanocomposites. Prog Mater Sci 90:75–127. https://doi.org/10.1016/j.pmatsci.2017.07.004

[4] Lee JH, Park SJ, Choi JW (2019) Electrical property of graphene and its application to electrochemical biosensing. Nanomaterials 9:297. https://doi.org/10.3390/nano9020297

[5] Stoller MD, Park S, Zhu Y, An J, Ruoff RS (2008) Graphene-based ultracapacitors. Nano Lett 8:3498–3502. https://doi.org/10.1021/nl802558y

[6] Sang M, Shin J, Kim K, Yu KJ (2019) Electronic and thermal properties of graphene and recent advances in graphene based electronics applications. Nanomaterials 9:374. https://doi.org/10.3390/nano9030374

[7] Novoselov KS, Geim AK, Morozov SV, Jiang DE, Zhang Y, Dubonos SV, Firsov AA (2004) Electric field effect in atomically thin carbon films. Science 306:666–669. https://doi.org/10.1126/science.1102896

[8] Goenka S, Sant V, Sant S (2014) Graphene-based nanomaterials for drug delivery and tissue engineering. J Controll Release 173:75–88. https://doi.org/10.1016/j.jconrel.2013.10.017

[9] Perruisseau-Carrier J (2012) Graphene for antenna applications: opportunities and challenges from microwaves to THz. In: 2012 Loughborough Antennas and Propagation Conference (LAPC) (pp 1-4). IEEE https://doi.org/10.1109/LAPC.2012.6402934.

[10] Kang M, Kim J, Jang B, Chae Y, Kim JH, Ahn JH (2017) Graphene-based three-dimensional capacitive touch sensor for wearable electronics. ACS Nano 11:7950–7957. https://doi.org/10.1021/acsnano.7b02474

[11] Kausar A, Rafique I, Muhammad B (2017) Aerospace application of polymer nanocomposite with carbon nanotube, graphite, graphene oxide, and Nanoclay. Polym Plast Technol Eng 56:1438–1456. https://doi.org/10.1080/03602559.2016.1276594

[12] Yu W, Sisi L, Haiyan Y, Jie L (2020) Progress in the functional modification of graphene/graphene oxide: a review. RSC Adv 10:15328–15345. https://doi.org/10.1039/D0RA01068E

[13] Gadgil B, Damlin P, Kvarnström C (2016) Graphene vs. reduced graphene oxide: a comparative study of graphene-based nanoplatforms on electrochromic switching kinetics. Carbon 96:377–381. https://doi.org/10.1016/j.carbon.2015.09.065

[14] Bellussi FM, Sáenz Ezquerro C, Laspalas M, Chiminelli A (2021) Effects of graphene oxidation on interaction energy and interfacial thermal conductivity of polymer nanocomposite: a molecular dynamics approach. Nanomaterials 11:1709. https://doi.org/10.3390/nano11071709

[15] Yoon Y, Kye H, Yang WS, Kang JW (2020) Comparing graphene oxide and reduced graphene oxide as blending materials for polysulfone and polyvinylidene difluoride membranes. Appl Sci 10:2015. https://doi.org/10.3390/app10062015

[16] William S, Hummers JREO, Offeman RE (1958) Preparation of Graphitic Oxide. J Am Chem Soc 80:1339. https://doi.org/10.1021/ja01539a017

[17] Marcano DC, Kosynkin DV, Berlin JM, Sinitskii A, Sun Z, Slesarev A, Tour JM (2010) Improved synthesis of graphene oxide. ACS Nano 4:4806–4814. https://doi.org/10.1021/nn1006368

[18] He H, Riedl T, Lerf A, Klinowski J (1996) Solid-state NMR studies of the structure of graphite oxide. J Phys Chem 100:19954–19958. https://doi.org/10.1021/jp961563t

[19] Lerf A, He H, Forster M, Klinowski J (1998) Structure of graphite oxide revisited. J Phys Chem B 102:4477–4482. https://doi.org/10.1021/jp9731821

[20] Erickson K, Erni R, Lee Z, Alem N, Gannett W, Zettl A (2010) Determination of the local chemical structure of graphene oxide and reduced graphene oxide. Adv Mater 22:4467–4472. https://doi.org/10.1002/adma.201000732

[21] Lin LC, Grossman JC (2015) Atomistic understandings of reduced graphene oxide as an ultrathin-film nanoporous membrane for separations. Nat Commun 6:8335. https://doi.org/10.1038/ncomms9335

[22] Volfkovich YM, Lobach AS, Spitsyna NG, Baskakov SA, Sosenkin VE, Rychagov AY, Shulga YM (2019) Hydrophilic and hydrophobic pores in reduced graphene oxide aerogel. J Porous Mater 26:1111–1119. https://doi.org/10.1007/s10934-018-0712-2

[23] Li M, Zhou H, Zhang Y, Liao Y, Zhou H (2017) The effect of defects on the interfacial mechanical properties of graphene/epoxy composites. RSC Adv 7:46101–46108. https://doi.org/10.1039/C7RA08243F

[24] Chang W, Peng B, Egab K, Zhang Y, Cheng Y, Li X, Li C (2021) Few-layer graphene on nickel enabled sustainable dropwise condensation. Sci Bull 66:1877–1884. https://doi.org/10.1016/j.scib.2021.06.006

[25] Raj R, Maroo SC, Wang EN (2013) Wettability of graphene. Nano Lett 13:1509–1515. https://doi.org/10.1021/nl304647t

[26] Munz M, Giusca CE, Myers-Ward RL, Gaskill DK, Kazakova O (2015) Thickness-dependent hydrophobicity of epitaxial graphene. ACS Nano 9:8401–8411. https://doi.org/10.1021/acsnano.5b03220

[27] Wang G, Wang B, Park J, Yang J, Shen X, Yao J (2009) Synthesis of enhanced hydrophilic and hydrophobic graphene oxide nanosheets by a solvothermal method. Carbon 47:68–72. https://doi.org/10.1016/j.carbon.2008.09.002

[28] Huang X, Qian K, Yang J, Zhang J, Li L, Yu C, Zhao D (2012) Functional nanoporous graphene foams with

controlled pore sizes. Adv Mater 24:4419–4423. https://doi.org/10.1002/adma.201201680

[29] Tang C, Li BQ, Zhang Q, Zhu L, Wang HF, Shi JL, Wei F (2016) CaO-templated growth of hierarchical porous graphene for high-power lithium–sulfur battery applications. Adv Funct Mater 26:577–585. https://doi.org/10.1002/adfm.201503726

[30] Zhu Y, Murali S, Stoller MD, Ganesh KJ, Cai W, Ferreira PJ, Ruoff RS (2011) Carbon-based supercapacitors produced by activation of graphene. Science 332:1537–1541. https://doi.org/10.1126/science.1200770

[31] Kim DW, Choi J, Kim D, Jung HT (2016) Enhanced water permeation based on nanoporous multilayer graphene membranes: the role of pore size and density. J Mater Chem A 4:17773–17781. https://doi.org/10.1039/C6TA06381K

[32] Chua CK, Pumera M (2014) Chemical reduction of graphene oxide: a synthetic chemistry viewpoint. Chem Soc Rev 43:291–312. https://doi.org/10.1039/C3CS60303B

[33] Min BH, Kim DW, Kim KH, Choi HO, Jang SW, Jung HT (2014) Bulk scale growth of CVD graphene on Ni nanowire foams for a highly dense and elastic 3D conducting electrode. Carbon 80:446–452. https://doi.org/10.1016/j.carbon.2014.08.084

[34] Achawi S, Feneon B, Pourchez J, Forest V (2021) Structure-activity relationship of graphene-based materials: impact of the surface chemistry, surface specific area and lateral size on their in vitro toxicity. Nanomaterials 11:2963. https://doi.org/10.3390/nano11112963

[35] Ealia SAM, Saravanakumar MP (2017) A review on the classification, characterisation, synthesis of nanoparticles and their application. In: IOP conference series: materials science and engineering (Vol. 263, No. 3, p 032019). IOP Publishing. https://doi.org/10.1088/1757-899X/263/3/032019.

[36] Dietzel D, Marsaudon S, Aimé JP, Nguyen CV, Couturier G (2005) Mechanical properties of a carbon nanotube fixed at a tip apex: a frequency-modulated atomic force microscopy study. Phys Rev B 72:035445. https://doi.org/10.1103/PhysRevB.72.035445

[37] Barber AH, Cohen SR, Eitan A, Schadler LS, Wagner HD (2006) Fracture transitions at a carbon-nanotube/polymer interface. Adv Mater 18:83–87. https://doi.org/10.1002/adma.200501033

[38] Teklu A, Barry C, Palumbo M, Weiwadel C, Kuthirummal N, Flagg J (2019) Mechanical characterization of reduced graphene oxide using AFM. Adv Condens Matter Phys. https://doi.org/10.1155/2019/8713965

[39] Lee JU, Yoon D, Cheong H (2012) Estimation of Young's modulus of graphene by raman spectroscopy. Nano Lett 12:4444–4448. https://doi.org/10.1021/nl301073q

[40] Liu B, Pavlou C, Wang Z, Cang Y, Galiotis C, Fytas G (2021) Determination of the elastic moduli of CVD graphene by probing graphene/polymer Bragg stacks. 2D Materials 8:035040. https://doi.org/10.1088/2053-1583/abfedb

[41] Jónsson H, Mills G, Jacobsen KW (1998) Nudged elastic band method for finding minimum energy paths of transitions. In: Classical and quantum dynamics in condensed phase simulations (pp 385-404). https://doi.org/10.5802/crphys.70

[42] Milek T, Zahn D (2014) Molecular simulation of Ag nanoparticle nucleation from solution: redox-reactions direct the evolution of shape and structure. Nano Lett 14:4913–4917. https://doi.org/10.1021/nl502503t

[43] Zhang H, Waychunas GA, Banfield JF (2015) Molecular dynamics simulation study of the early stages of nucleation of iron oxyhydroxide nanoparticles in aqueous solutions. J Phys Chem B 119:10630–10642. https://doi.org/10.1021/acs.jpcb.5b03801

[44] Casalini T et al (2019) Molecular modeling for nanomaterial–biology interactions: opportunities, challenges, and perspectives. Bioeng. Biotechnol, Front. https://doi.org/10.3389/fbioe.2019.00268

[45] Das M, Dahal U, Mesele O, Liang D, Cui yQ (2019) Molecular dynamics simulation of interaction between functionalized nanoparticles with lipid membranes: analysis of coarse-grained models. J Phys Chem B 123(49):10547–10561 https://doi.org/10.1021/acs.jpcb.9b08259.

[46] Panczyk T, Nieszporek J, Nieszporek K (2022) Molecular dynamics simulations of interactions between human telomeric I-motif deoxyribonucleic acid and functionalized graphene. J Phys Chem B 126:6671–6681. https://doi.org/10.1021/acs.jpcb.2c04327

[47] Kang JW, Lee S (2013) Molecular dynamics study on the bending rigidity of graphene nanoribbons. Comput Mater Sci 74:107–113. https://doi.org/10.1016/j.commatsci.2013.03.009

[48] Javvaji B, Budarapu PR, Sutrakar VK, Mahapatra DR, Paggi M, Zi G, Rabczuk T (2016) Mechanical properties of Graphene: Molecular dynamics simulations correlated to continuum based scaling laws. Comput Mater Sci 125:319–327. https://doi.org/10.1016/j.commatsci.2016.08.016

[49] Dugan N, Erkoc S (2008) Stability analysis of graphene nanoribbons by molecular dynamics simulations. Phys Status Solidi (B) 245:695–700. https://doi.org/10.1002/pssb.200743461

[50] Hu J et al (2009) Molecular dynamics calculation of thermal conductivity of graphene nanoribbons. In: En AIP

Conference Proceedings, Albany (New York): AIP pp 135–138. https://doi.org/10.1063/1.3251208

[51] Hu J, Ruan X, Chen YP (2009) Thermal conductivity and thermal rectification in graphene nanoribbons: a molecular dynamics study. Nano Lett 9:2730–2735. https://doi.org/10.1021/nl901231s

[52] Muhammad A, Sáenz Ezquerro C, Srivastava R, Asinari P, Laspalas M, Chiminelli A, Fasano M (2023) Atomistic to mesoscopic modelling of thermophysical properties of graphene-reinforced epoxy nanocomposites. Nanomaterials 13:1960. https://doi.org/10.3390/nano13131960

[53] Mohammad Nejad S, Bozorg Bigdeli M, Srivastava R, Fasano M (2019) Heat transfer at the interface of graphene nanoribbons with different relative orientations and gaps. Energies 12:796. https://doi.org/10.3390/en12050796

[54] Fonseca AF, Liang T, Zhang D, Choudhary K, Phillpot SR, Sinnott SB (2017) Graphene–titanium interfaces from molecular dynamics simulations. ACS Appl Mater Interfaces 9:33288–33297. https://doi.org/10.1021/acsami.7b09469

[55] Xu Z, Yan T, Liu G, Qiao G, Ding F (2016) Large scale atomistic simulation of single-layer graphene growth on Ni (111) surface: molecular dynamics simulation based on a new generation of carbon–metal potential. Nanoscale 8:921–929. https://doi.org/10.1039/C5NR06016H

[56] Shariatinia Z, Mazloom-Jalali A (2020) Molecular dynamics simulations on chitosan/graphene nanocomposites as anticancer drug delivery using systems. Chin J Phys 66:362–382. https://doi.org/10.1016/j.cjph.2020.04.012

[57] Zhang Q, Mortazavi B, Aldakheel F (2021) Molecular dynamics modeling of mechanical properties of polymer nanocomposites reinforced by C 7 N 6 nanosheet. Surfaces 4:240–254

[58] Müller-Plathe F (1997) A simple nonequilibrium molecular dynamics method for calculating the thermal conductivity. J Chem Phys 106:6082–6085. https://doi.org/10.1063/1.473271

[59] Siegel AF (2016) Practical business statistics. Academic Press

[60] Farbodi M (2017) Application of taguchi method for optimizing of mechanical properties of polystyrene-carbon nanotube nanocomposite. Polym Polym Compos 25:177–184. https://doi.org/10.1177/096739111702500208

[61] William H (1996) VMD-visual molecular dynamics. J Mol Graph 14:33–38. https://doi.org/10.1016/0263-7855(96)00018-5

[62] Carvalho A, Costa MCF, Marangoni VS, Ng PR, Nguyen TLH, Neto C, yAH, (2021) The degree of oxidation of graphene oxide. Nanomaterials 11:560. https://doi.org/10.3390/nano11030560

[63] Hu L, Maroudas D (2014) Thermal transport properties of graphene nanomeshes. J Appl Phys 10:4901335

[64] Tersoff JJPRB (1989) Modeling solid-state chemistry: interatomic potentials for multicomponent systems. Phys Rev B 39:5566

[65] Sun H (1998) COMPASS: an ab initio force-field optimized for condensed-phase applications overview with details on alkane and benzene compounds. J Phys Chem B 102:7338–7364. https://doi.org/10.1021/jp980939v

[66] Hwang SW et al (2011) Grafting of maleic anhydride on poly(L-lactic acid) effects on physical and mechanical properties. Polym Test. https://doi.org/10.1016/j.polymertesting.2011.12.005

[67] Plimpton S (1995) Fast parallel algorithms for short-range molecular dynamics. J Comput Phys 117:1–19. https://doi.org/10.1006/jcph.1995.1039

[68] Bitzek E, Koskinen P, Gähler F, Moseler M, y P. Gumbsch, (2006) Structural relaxation made simple. Phys Rev Lett 97:170201. https://doi.org/10.1103/PhysRevLett.97.170201

[69] Jiang JW, Park HS (2016) Negative Poisson's Ratio in Single-Layer Graphene Ribbons. Nano Lett 16:2657–2662. https://doi.org/10.1021/acs.nanolett.6b00311

[70] Dowling NE (2007) Mechanical Behavior of materials: engineering methods for deformation, fracture, and fatigue. Pearson Prentice Hall

[71] Ruoff RS, Qian D, Liu WK (2003) Mechanical properties of carbon nanotubes: theoretical predictions and experimental measurements. Comptes Rendus Phys 4:993–1008. https://doi.org/10.1016/j.crhy.2003.08.001

[72] Mao JJ, Liu S, Li L, Chen J (2022) Molecular dynamic simulation of defective graphene nanoribbons for tension and vibration. Nanomaterials 12:2407. https://doi.org/10.3390/nano12142407

[73] Liang Y, Huan S (2020) Research on strain rate effect of the mechanical properties of graphene sheet containing randomly distributed defects. Iran J Sci Technol Trans Civil Eng 44:1171–1177. https://doi.org/10.1007/s40996-019-00309-4

[74] Bonilla LL, Carpio yA (2012) Driving dislocations in graphene. Science 337:161–162. https://doi.org/10.1126/science.1224681

[75] Warner JH, Margine ER, Mukai M, Robertson AW, Giustino F, Kirkland AI (2012) Dislocation-driven deformations in graphene. Science 337:209–212. https://doi.org/10.1126/science.1217529

[76] I. A. Ovid'ko, (2013) Mechanical properties of graphene. Rev Adv Mater Sci 34:1–11

[77] Kim K, Artyukhov VI, Regan W, Liu Y, Crommie MF, Yakobson BI, Zettl A (2012) Ripping graphene: preferred directions. Nano Lett 12:293–297. https://doi.org/10.1021/nl203547z

[78] Sen D, Novoselov KS, Reis PM, Buehler MJ (2010) Tearing graphene sheets from adhesive substrates produces tapered nanoribbons. Small 6:1108–1116. https://doi.org/10.1002/smll.201000097

[79] Liu F, Ming P, Li J (2007) Ab initio calculation of ideal strength and phonon instability of graphene under tension. Phys Rev B 76:064120. https://doi.org/10.1103/PhysRevB.76.064120

[80] Ruiz-Vargas CS, Zhuang HL, Huang PY, Van Der Zande AM, Garg S, McEuen PL, Park J (2011) Softened elastic response and unzipping in chemical vapor deposition graphene membranes. Nano Lett 11:2259–2263. https://doi.org/10.1021/nl200429f

[81] Liang Y (2019) Research on strain rate effect of the mechanical properties of graphene sheet containing randomly distributed defects. Iran J Sci Technol, p 7

[82] Kang SH, Fang TH, Hong ZH, Chuang CH (2013) Mechanical properties of free-standing graphene oxide. Diam Relat Mater 38:73–78. https://doi.org/10.1016/j.diamond.2013.06.016

[83] A. R. Khoei y M. S. Khorrami, (2016) Mechanical properties of graphene oxide: a molecular dynamics study. Fuller Nanotub Carbon Nanostruct 24:594–603. https://doi.org/10.1080/1536383X.2016.1208180

[84] Zhao H, Min K, Aluru NR (2009) Size and chirality dependent elastic properties of graphene nanoribbons under uniaxial tension. Nano Lett 9:3012–3015. https://doi.org/10.1021/nl901448z

[85] Mir M, Ali MN, Sami J, Ansari U (2014) Review of mechanics and applications of auxetic structures. Adv Mater Sci Eng. https://doi.org/10.1155/2014/753496

[86] Zhang C, Lu C, Pei L, Li J, Wang R (2019) Molecular dynamics simulation of the negative poisson's ratio in graphene/Cu nanolayered composites: implications for scaffold design and telecommunication cables. ACS Appl Nano Mater 3:496–505. https://doi.org/10.1021/acsanm.9b02063

[87] Zheng Q, Geng Y, Wang S, Li Z, Kim JK (2010) Effects of functional groups on the mechanical and wrinkling properties of graphene sheets. Carbon 48:4315–4322. https://doi.org/10.1016/j.carbon.2010.07.044

[88] Liu L, Zhang J, Zhao J, y F. Liu, (2012) Mechanical properties of graphene oxides. Nanoscale 4:5910–5916. https://doi.org/10.1039/C2NR31164J

[89] Zandiatashbar A, Lee GH, An SJ, Lee S, Mathew N, Terrones M, Koratkar N (2014) Effect of defects on the intrinsic strength and stiffness of graphene. Nature Commun 5:3186. https://doi.org/10.1038/ncomms4186

[90] Guo Z, Zhang D, Gong XG (2009) Thermal conductivity of graphene nanoribbons. Appl Phys Lett 10:3246155

[91] Lin S, Buehler MJ (2014) Thermal transport in monolayer graphene oxide: atomistic insights into phonon engineering through surface chemistry. Carbon 77:351–359. https://doi.org/10.1016/j.carbon.2014.05.038

[92] Wang Z, Xie R, Bui CT, Liu D, Ni X, Li B, Thong JT (2011) Thermal transport in suspended and supported few-layer graphene. Nano Lett 11:113–118. https://doi.org/10.1021/nl102923q

[93] Pop E, Varshney V, Roy AK (2012) Thermal properties of graphene: fundamentals and applications. MRS Bull 37:1273–1281. https://doi.org/10.1557/mrs.2012.203

[94] Liao AD, Wu JZ, Wang X, Tahy K, Jena D, Dai H, Pop E (2011) Thermally limited current carrying ability of graphene nanoribbons. Phys Rev Lett 106:256801. https://doi.org/10.1103/PhysRevLett.106.256801

[95] Li X, Zhang G (2013) Enhancing the extremely high thermal conduction of graphene nanoribbons. Front Phys 1:19. https://doi.org/10.3389/fphy.2013.00019

[96] Shahadat MRB, Alam MF, Mandal MNA, Ali MM (2018) Thermal transportation behaviour prediction of defective graphene sheet at various temperature: a molecular dynamics study. Am. J. Nanomater 6:34–40

[97] Fang TH, Lee ZW, Chang WJ, Huang CC (2019) Determining porosity effect on the thermal conductivity of single-layer graphene using a molecular dynamics simulation. Phys E Low-Dimens Syst Nanostruct 106:90–94. https://doi.org/10.1016/j.physe.2018.10.017

[98] Yarifard M, Davoodi J, Rafii-Tabar H (2016) In-plane thermal conductivity of graphene nanomesh: a molecular dynamics study. Comput Mater Sci 111:247–251. https://doi.org/10.1016/j.commatsci.2015.09.033

[99] Zhan N, Chen B, Li C, Shen PK (2018) Molecular dynamics simulations of the thermal conductivity of graphene for application in wearable devices. Nanotechnology 30:025705. https://doi.org/10.1088/1361-6528/aae98b

[100] Sumirat I, Yamamoto N, Shimamura S (2011) Optimization of thermal and mechanical properties in nanoporous materials. Trans Mater Res Soc Japan 36:281–284

[101] Mu X, Wu X, Zhang T, Go DB, Luo T (2014) Thermal transport in graphene oxide–from ballistic extreme to amorphous limit. Sci Rep 4:3909. https://doi.org/10.1038/srep03909

[102] Balandin AA Nika yDL (2012) Phononics in low-dimensional materials. Mater Today 15:266–275. https://doi.org/10.1016/S1369-7021(12)70117-7

[103] Chen J, Li L (2020) Effect of oxidation degree on the thermal properties of graphene oxide. J Mater Res Technol 9:13740–13748. https://doi.org/10.1016/j.jmrt.2020.09.092

# 10. Discusión y conclusiones globales

Esta tesis ha abordado la descripción de la metodología, el desarrollo y los resultados obtenidos de la aplicación de la simulación mediante dinámica molecular (MD) a cuatro casos particulares basados en nanomateriales, bien en su refuerzo con polímeros o bien en forma de nanopartícula. Estos estudios se han centrado fundamentalmente en el análisis de propiedades interfaciales, propiedades mecánicas y propiedades térmicas de difícil caracterización experimental o bien en el establecimiento de relaciones entre estas propiedades y la estructura a nivel molecular del material. Las conclusiones que se han obtenido tras la conclusión de los cuatro capítulos expuestos se describen en los siguientes apartados.

# 10.1. Discusión global

En el desarrollo de los diferentes estudios que componen esta tesis, se ha seguido una metodología de trabajo sistemática y consistente, la cual se describió de forma general en el apartado 2.3 de la Introducción y de forma particular en cada uno de los diferentes casos de estudio. De forma resumida, esta metodología inicialmente contempla el modelado atomístico del material, seguido de su equilibrado en las condiciones objeto de estudio para finalmente realizar su caracterización en cuanto a las propiedades mecánicas y/o térmicas. La metodología de trabajo concluía en todos los casos con una comparativa de los resultados obtenidos en cada estudio con datos experimentales relevantes encontrados en bibliografía. Esta verificación de resultados obtenidos a través de simulaciones atomísticas y su comparativa con resultados experimentales ha permitido avalar la metodología de trabajo desarrollada y sus aplicaciones al estudio de nanocomposites poliméricos y sus nanopartículas.

Algunas de las propiedades determinadas son de fácil acceso experimental (datos ampliamente disponibles en bibliografía y de fácil caracterización), tales como el módulo de Young, resistencias de tracción o conductividad térmica, por citar algunas, de polímeros y/o sus materiales nanocompuestos. Sin embargo, se han calculado otras propiedades de estos materiales que son de difícil acceso experimental, como son las propiedades de la interfase nanopartícula-polímero o las propias propiedades de las nanopartículas. Esta caracterización *ultra* de los materiales ha permitido obtener valores de propiedades especiales tales como el módulo de Young, resistencia, coeficiente de Poisson o conductividad térmica de interfases nanopartícula-polímero y de las propias nanopartículas, las cuales se pueden considerar bien simplemente como ayuda para el desarrollo experimental, o bien para alimentar modelos de material de escalas superiores (en

aproximaciones multiescala) que incluyen en su formulación la propia interfase o requieren de introducir propiedades de la fase dispersa (esto es, de las nanopartículas).

## 10.2. Conclusiones particulares

Las conclusiones particulares que se han podido extraer se enumeran a continuación:

- La modificación química superficial en las nanopartículas da lugar a cambios en la energía de interacción con el polímero (fase continua). Si esta modificación se realiza en la dirección adecuada, permiten incrementar la interacción nanopartícula-polímero. En general, se puede establecer que para polímeros con grupos polares o presencia de átomos electronegativos en su estructura, las modificaciones superficiales de la nanopartícula deberían ser de esta misma naturaleza para aumentar la energía de interacción tal y como se observó en el caso de la nanopartícula de sílice modificada con PEG (polietilenglicol) y su interacción con policaprolactona (PCL), o nanopartículas de grafeno oxidadas y su interacción con resina epoxi o ácido poliláctico (PLA).

- La presencia de la nanopartícula se manifiesta en forma de perturbaciones de la densidad polimérica en las zonas inmediatamente próximas o en contacto con la superficie de la nanopartícula. Estas perturbaciones de densidad permiten estimar el espesor de la región de la interfase, a través del método ASD (*accumulated standard deviation*), y posteriormente generar perfiles de propiedades mecánicas a lo largo de la interfase a través de su relación con la densidad.

- Las simulaciones de extensión-deformación permiten determinar el porcentaje de deformación plástica remanente que experimenta un material tras la aplicación de una tensión o nivel de deformación. A partir de estas simulaciones se pudo comprobar que la presencia de la nanopartícula de carbonato de calcio en el nanocompuesto de celulosa daba lugar a un aumento de la deformación plástica del material.

- El análisis de la conformación de ángulos diedros (torsión) permite evaluar los posibles cambios a nivel estructural/molecular que se producen en el material ante la aplicación de deformaciones o esfuerzos, y relacionarlo con la elasticidad del material y la presencia de deformaciones plásticas permanentes tras la aplicación del esfuerzo.

- La evaluación visual detallada de los fotogramas de simulación permitió establecer el mecanismo de fallo bajo tensión de tracción de nanopartículas de grafeno (nanocintas) así como el del fenómeno de endurecimiento (en inglés *hardening*) o endurecimiento por el cual las nanopartículas son capaces de acomodar mayores niveles de tensión. Así, la formación de dislocaciones en la lámina a través de pares pentágono-heptágono (defectos "5-7" tipo Stone-Wales) actúa como liberadores de tensión que permiten acomodar a las nanopartículas de grafeno mayores niveles de tensión, aunque para que este mecanismo tenga lugar se requiere de láminas prácticamente perfectas (porosidades menores a 1%). Por otro lado, la rotura de las nanocintas se produce como un mecanismo de desgarro en el que el crecimiento de la grieta tiene lugar, predominantemente, a lo largo de líneas rectas perpendiculares a la dirección de carga y alineadas con las direcciones *armchair* o *zigzag* de la red cristalina hexagonal del grafeno.

- Atendiendo a las propiedades mecánicas de las nanopartículas de grafeno, la porosidad afectó a todas las propiedades evaluadas (módulo de Young, resistencia a la tracción, deformación a la rotura y coeficiente de Poisson), pero con diferente tendencia en las propiedades de fractura (resistencia a la tracción y deformación a la rotura), lo que se explica por la presencia del fenómeno de endurecimiento a altas deformaciones. Sin embargo, la oxidación sólo afectó al módulo de Young y al coeficiente Poisson, pero no a la resistencia a la tracción y a la deformación a la rotura.

- La conductividad térmica en las nanopartículas de grafeno se encuentra íntimamente ligada a la transmisión de fonones (modos de vibración), de tal modo que perturbaciones en la estructura tales como poros (vacantes) y/o oxidación (que da lugar a cambios de hibridación de los átomos de carbono) disminuyen el tiempo medio de vida de los fonones (lph-ph) y, por tanto, la conductividad térmica.

- En el caso de nanocomposites poliméricos, la conductividad térmica a través de la interfase grafeno-polímero se vio favorecida y, por tanto, disminuyó la resistencia de Kapitza (RK) asociada, por la presencia de modos de vibración de fonones de altas frecuencias en la nanopartícula (especialmente fuera del plano), independientemente de cuál fuera la interacción con el polímero. En los casos en los que existió interacción específica con el polímero (por ejemplo, mediante puentes de hidrógeno), aparecieron nuevos modos de vibración de fonones que pueden contribuir en la misma dirección, aunque, si son de frecuencias más bajas, su contribución será menor.

## 10.3. Conclusiones globales

Considerando los objetivos inicialmente planteados, tras el desarrollo de la tesis se pueden extraer las siguientes conclusiones globales:

- La técnica de dinámica molecular se puede aplicar a una amplia variedad de sistemas materiales para la obtención de resultados verosímiles con los datos experimentales. En esta tesis, la técnica se ha aplicado a la caracterización de nanocompuestos poliméricos, con diferentes combinaciones de polímero y nanopartícula, y sus nanopartículas, dando lugar a resultados comparables con los datos experimentales disponibles.

- La técnica de dinámica molecular permite predecir las propiedades de interfases nanopartícula-polímero en nanocompuestos poliméricos. En esta tesis se caracterizaron los perfiles de propiedades mecánicas junto con valores promedios, y el valor la resistencia térmica de Kapitza.

- La técnica permite predecir el efecto en las propiedades mecánicas y térmicas de nanocompuestos poliméricos tras la adición de nanopartículas al sistema material. En esta tesis se estudió el efecto de la adición de nanopartículas de sílice a policaprolactona, de carbonato de calcio a celulosa, y de nanopartículas de grafeno a diferentes materiales poliméricos.

- La técnica permite analizar los cambios estructurales/moleculares que se producen en el material como consecuencia de la aplicación de deformaciones. En esta tesis se han relacionado los cambios estructurales que se producen en el material, a nivel molecular, con la deformación plástica de nanocompuestos de celulosa y carbonato de calcio.

- La técnica permite caracterizar las propiedades mecánicas y térmicas de nanopartículas, y evaluar el efecto de su modificación química y/o física. En esta tesis se relacionó el efecto de la porosidad y la oxidación en las propiedades mecánicas y térmicas de nanocintas de grafeno.

## 10.4. Aportaciones originales

En esta tesis doctoral, uno de los puntos en los que se ha querido profundizar ha sido en el de estudiar el potencial de aplicación de la dinámica molecular para determinar propiedades de difícil caracterización experimental, principalmente las relacionadas con la interfase y las nanopartículas. En este sentido esta tesis ha realizado las siguientes aportaciones originales:

- La generación de perfiles de propiedades mecánicas en función de la longitud de la interfase (o distancia a la nanopartícula) empleando para ello una estrategia de correlación con perfiles de densidad. Este tipo de perfiles permiten tener una idea de la distribución a lo largo de la interfase y de la heterogeneidad de esta, así como el cálculo de un valor promedio de la propiedad.

- El análisis de los mecanismos moleculares que dan lugar a los fenómenos de elasticidad y deformación plástica, evaluado para el caso concreto de nanocompuestos de celulosa, empleando para ello la monitorización de la conformación de los ángulos diedros y su variación con la deformación aplicada (representaciones delta-φ o ψ versus deformación). Esta metodología de análisis permite evaluar los cambios que tienen lugar en la conformación de los ángulos diedros que definen las diferentes moléculas, y su morfología, de una forma global y en un único gráfico.

- Explicación teórica al mecanismo por el que tiene lugar el fenómeno de endurecimiento de nanopartículas de grafeno (nanocintas), a través de la formación de dislocaciones en la estructura cristalina de la lámina mediante la generación de defectos pentágono-heptágono tipo Stone-Wales.

Aunque no forma parte del trabajo de esta tesis, también debe destacarse el trabajo previo desarrollado y publicado en la revista Fibers [162], en el que se estableció una metodología para la caracterización del espesor de la interfase mediante el análisis de los perfiles de densidad poliméricos alrededor de la nanopartícula.

## 10.5. Resultados de la tesis

Esta tesis ha permitido establecer unos procedimientos de trabajo para el estudio de las propiedades mecánicas y térmicas de materiales nanocompuestos y sus nanopartículas empleando para ello simulaciones atomísticas. De esta manera, se han descrito, en cada uno de los diferentes casos de estudio, los siguientes procedimientos:

- Procedimiento para la determinación de propiedades mecánicas elásticas de la interfase nanopartícula-polímero y generación de gradientes de propiedad en función de la distancia a la nanopartícula.

- Procedimiento para la determinación del porcentaje de deformación plástica remanente tras la aplicación de tensiones y monitorización de cambios estructurales en el material.

- Procedimiento para la determinación de propiedades mecánicas y térmicas de grafeno (nanopartículas de geometría laminar o 2D).

Los resultados de esta tesis han permitido la elaboración y publicación de cuatro artículos originales en revistas científicas recogidas dentro del índice Journal Citation Reports (JCR).

También hay que destacar, como parte de los méritos logrados en el desarrollo de la tesis, la selección como **portada** para el volumen de noviembre de 2023 [163] (**Figura 1**) y, posteriormente, la consecución del **Premio Cahn 2023** [164] (**Figura 2**) como mejor artículo en investigación del año 2023 en la revista *Journal of Materials Science*, de la editorial

Springer Nature, al artículo «*Molecular modelling of graphene nanoribbons on the effect of porosity and oxidation on the mechanical and thermal properties*» [4].


**Figura 1 –** *Portada del volumen de noviembre de 2023 en la revista Journal of Materials Science* [163].

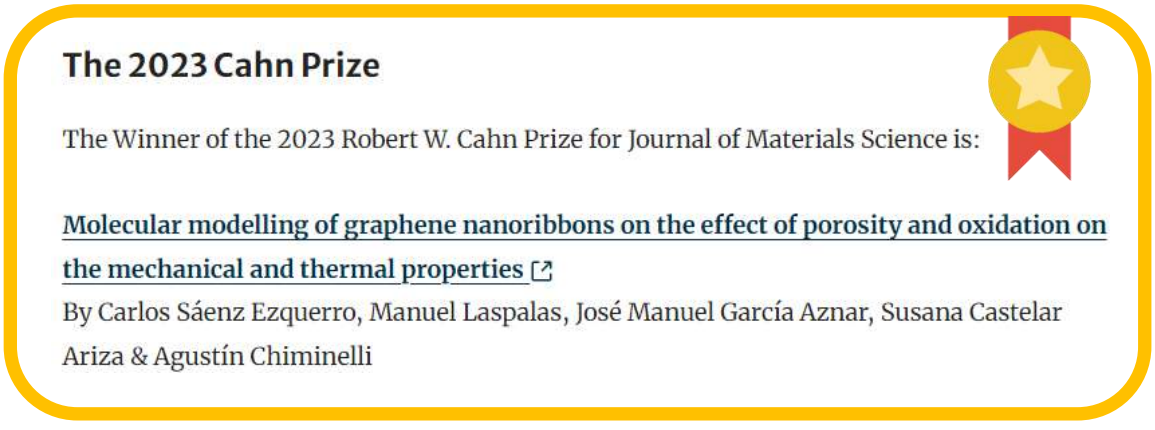


**Figura 2 –** *Premio Robert W. Cahn 2023 al Mejor Artículo del Año 2023 en la revista Journal of Materials Science* [164].

## 10.6. Trabajo futuro

Los casos de estudio considerados en esta tesis se han centrado principalmente en materiales nanocompuestos poliméricos y nanopartículas relacionadas con éstos. En un futuro se pretende ampliar la metodología de trabajo desarrollada a otro tipo de materiales, tales como materiales metálicos y cerámicos, así como al estudio de otro tipo de propiedades entre las que se incluiría el cálculo de coeficientes de difusión y magnitudes relacionadas (tales como la permeabilidad y migración de moléculas en el seno de un material).

En una línea de trabajo futura también se pretende explorar en la aplicación del campo reactivo ReaxFF [165]. Esta nueva formulación de campos de fuerza, introducida por Adri C.T. van Duin en 2001, supone un salto cuantitativo en el paradigma de la dinámica molecular ya que permite la formación y rotura de enlaces durante el transcurso de una simulación, esto es, de reacciones químicas. ReaxFF se establece además como un nexo entre la química cuántica computacional (DFT) y la dinámica molecular al permitir el estudio de propiedades habitualmente solo reservadas a los métodos *ab initio* (tales como energías de formación, de reacción, etc.) pero en sistemas más grandes.

Mencionar finalmente que los resultados que se generan de las simulaciones atomísticas, también pueden servir para alimentar modelos de material a escalas superiores, tales como modelos de micromecánica y/o modelos de elementos finitos (FEM), lo que daría lugar a un análisis multiescala del material.

# Referencias


[1] C. S. Ezquerro, J. M. G. Aznar, y M. Laspalas, «Prediction of the structure and mechanical properties of polycaprolactone–silica nanocomposites and the interphase region by molecular dynamics simulations: the effect of PEGylation», *Soft Matter*, vol. 18, n.º 14, pp. 2800-2813, abr. 2022, doi: 10.1039/D1SM01794B.

[2] C. Sáenz Ezquerro, M. Laspalas, J. M. García Aznar, y C. Crespo Miñana, «Monitoring interactions through molecular dynamics simulations: effect of calcium carbonate on the mechanical properties of cellulose composites», *Cellulose*, vol. 30, n.º 2, pp. 705-726, ene. 2023, doi: 10.1007/s10570-022-04902-1.

[3] F. M. Bellussi, C. Sáenz Ezquerro, M. Laspalas, y A. Chiminelli, «Effects of Graphene Oxidation on Interaction Energy and Interfacial Thermal Conductivity of Polymer Nanocomposite: A Molecular Dynamics Approach», *Nanomaterials*, vol. 11, n.º 7, Art. n.º 7, jul. 2021, doi: 10.3390/nano11071709.

[4] C. Sáenz Ezquerro, M. Laspalas, J. M. García Aznar, S. Castelar Ariza, y A. Chiminelli, «Molecular modelling of graphene nanoribbons on the effect of porosity and oxidation on the mechanical and thermal properties», *J. Mater. Sci.*, vol. 58, n.º 33, pp. 13295-13316, sep. 2023, doi: 10.1007/s10853-023-08810-y.

[5] S. A. Hollingsworth y R. O. Dror, «Molecular Dynamics Simulation for All», *Neuron*, vol. 99, n.º 6, pp. 1129-1143, sep. 2018, doi: 10.1016/j.neuron.2018.08.011.

[6] L. Verlet, «Computer "Experiments" on Classical Fluids. I. Thermodynamical Properties of Lennard-Jones Molecules», *Phys. Rev.*, vol. 159, n.º 1, pp. 98-103, jul. 1967, doi: 10.1103/PhysRev.159.98.

[7] T. E. I. Gartner y A. Jayaraman, «Modeling and Simulations of Polymers: A Roadmap», *Macromolecules*, vol. 52, n.º 3, pp. 755-786, feb. 2019, doi: 10.1021/acs.macromol.8b01836.

[8] A. Ylikantola, J. Linnanto, J. Knuutinen, A. Oravilahti, y M. Toivakka, «Molecular modeling studies of interactions between sodium polyacrylate polymer and calcite surface», *Appl. Surf. Sci.*, vol. 276, pp. 43-52, jul. 2013, doi: 10.1016/j.apsusc.2013.02.122.

[9] Y. Zhao, Z. Xu, B. Wang, y J. Wang, «The Inhibition of Sodium Carboxymethyl Cellulose on Calcite Growth by Molecular Dynamics Simulation», *Macromol. Theory Simul.*, vol. 28, n.º 5, p. 1900019, 2019, doi: https://doi.org/10.1002/mats.201900019.

[10] F. Pashmforoush, S. Ajori, y H. R. Azimi, «Interfacial characteristics and thermo-mechanical properties of calcium carbonate/polystyrene nanocomposite», *Mater. Chem. Phys.*, vol. 247, p. 122871, jun. 2020, doi: 10.1016/j.matchemphys.2020.122871.

[11] D. N. Theodorou y U. W. Suter, «Atomistic modeling of mechanical properties of polymeric glasses», *Macromolecules*, vol. 19, n.º 1, pp. 139-154, ene. 1986, doi: 10.1021/ma00155a022.

[12] E. Bitzek, P. Koskinen, F. Gähler, M. Moseler, y P. Gumbsch, «Structural Relaxation Made Simple», *Phys. Rev. Lett.*, vol. 97, n.º 17, p. 170201, oct. 2006, doi: 10.1103/PhysRevLett.97.170201.

[13] F. Müller-Plathe, «A simple nonequilibrium molecular dynamics method for calculating the thermal conductivity», *J. Chem. Phys.*, vol. 106, n.º 14, pp. 6082-6085, abr. 1997, doi: 10.1063/1.473271.

[14] R. Salomon-Ferrer, D. A. Case, y R. C. Walker, «An overview of the Amber biomolecular simulation package», *WIREs Comput. Mol. Sci.*, vol. 3, n.º 2, pp. 198-210, 2013, doi: 10.1002/wcms.1121.

[15] M. J. Abraham *et al.*, «GROMACS: High performance molecular simulations through multi-level parallelism from laptops to supercomputers», *SoftwareX*, vol. 1-2, pp. 19-25, sep. 2015, doi: 10.1016/j.softx.2015.06.001.

[16] A. P. Thompson *et al.*, «LAMMPS - a flexible simulation tool for particle-based materials modeling at the atomic, meso, and continuum scales», *Comput. Phys. Commun.*, vol. 271, p. 108171, feb. 2022, doi: 10.1016/j.cpc.2021.108171.

[17] S. Gowthaman, «A review on mechanical and material characterisation through molecular dynamics using large-scale atomic/molecular massively parallel simulator (LAMMPS)», *Funct. Compos. Struct.*, vol. 5, n.º 1, p. 012005, mar. 2023, doi: 10.1088/2631-6331/acc3d5.

[18] K. Cha, «Performance Evaluation of LAMMPS on Multi-core Systems», en *2013 IEEE 10th International Conference on High Performance Computing and Communications & 2013 IEEE International Conference on Embedded and Ubiquitous Computing*, Zhangjiajie, China: IEEE, nov. 2013, pp. 812-819. doi: 10.1109/HPCC.and.EUC.2013.117.

[19] U. Landman, «Molecular Dynamics Simulations in Material Science and Condensed Matter Physics», en *Computer Simulation Studies in Condensed Matter Physics*, D. P. Landau, K. K. Mon, y H.-B. Schüttler, Eds., en Springer Proceedings in Physics. Berlin, Heidelberg: Springer, 1988, pp. 108-123. doi: 10.1007/978-3-642-93400-1_12.

[20] M. O. Steinhauser y S. Hiermaier, «A Review of Computational Methods in Materials Science: Examples from Shock-Wave and Polymer Physics», *Int. J. Mol. Sci.*, vol. 10, n.º 12, pp. 5135-5216, dic. 2009, doi: 10.3390/ijms10125135.

[21] J. L. Klepeis, K. Lindorff-Larsen, R. O. Dror, y D. E. Shaw, «Long-timescale molecular dynamics simulations of protein structure and function», *Curr. Opin. Struct. Biol.*, vol. 19, n.º 2, pp. 120-127, abr. 2009, doi: 10.1016/j.sbi.2009.03.004.

[22] H. Sun, «COMPASS: An ab initio force-field optimized for condensed-phase applications - Overview with details on alkane and benzene compounds», *J. Phys. Chem. B*, vol. 102, n.º 38, pp. 7338-7364, sep. 1998, doi: 10.1021/jp980939v.

[23] V. Hornak, R. Abel, A. Okur, B. Strockbine, A. Roitberg, y C. Simmerling, «Comparison of multiple AMBER force fields and development of improved protein backbone parameters», *Proteins*, vol. 65, n.º 3, pp. 712-725, nov. 2006, doi: 10.1002/prot.21123.

[24] W. L. Jorgensen, D. S. Maxwell, y J. TiradoRives, «Development and testing of the OPLS all-atom force field on conformational energetics and properties of organic liquids», *J. Am. Chem. Soc.*, vol. 118, n.º 45, pp. 11225-11236, nov. 1996, doi: 10.1021/ja9621760.

[25] B. J. Alder y T. E. Wainwright, «Studies in Molecular Dynamics. I. General Method», *J. Chem. Phys.*, vol. 31, n.º 2, pp. 459-466, ago. 1959, doi: 10.1063/1.1730376.

[26] B. J. Alder y T. E. Wainwright, «Phase Transition for a Hard Sphere System», *J. Chem. Phys.*, vol. 27, n.º 5, pp. 1208-1209, 1957, doi: 10.1063/1.1743957.

[27] J. A. McCammon, B. R. Gelin, y M. Karplus, «Dynamics of folded proteins», *Nature*, vol. 267, n.º 5612, pp. 585-590, jun. 1977.

[28] G. Ciccotti, C. Dellago, M. Ferrario, E. R. Hernández, y M. E. Tuckerman, «Molecular simulations: past, present, and future (a Topical Issue in EPJB)», *Eur. Phys. J. B*, vol. 95, n.º 1, p. 3, ene. 2022, doi: 10.1140/epjb/s10051-021-00249-x.

[29] A. Rahman y F. H. Stillinger, «Molecular dynamics study of liquid water», *J. Chem. Phys.*, vol. 55, n.º 7, pp. 3336-3359, 1971.

[30] J. E. Stone, M. J. Hallock, J. C. Phillips, J. R. Peterson, Z. Luthey-Schulten, y K. Schulten, «Evaluation of Emerging Energy-Efficient Heterogeneous Computing Platforms for Biomolecular and Cellular Simulation Workloads», en *2016 IEEE International Parallel and Distributed Processing Symposium Workshops (IPDPSW)*, Chicago, IL, USA: IEEE, may 2016, pp. 89-100. doi: 10.1109/IPDPSW.2016.130.

[31] K. Kremer y G. S. Grest, «Molecular dynamics (MD) simulations for polymers», *J. Phys. Condens. Matter*, vol. 2, n.º S, p. SA295, dic. 1990, doi: 10.1088/0953-8984/2/S/045.

[32] Y. Li, C. Chen, Z. He, Y. Wang, M. Xiao, y Y. Zhou, «Molecular Dynamics Simulation in Compatibility and Mechanical Properties of Chloroprene Rubber/Polyurethane Blends», *Adv. Theory Simul.*, vol. 6, n.º 9, p. 2300249, 2023, doi: 10.1002/adts.202300249.

[33] Q. Wei, Y. Wang, Y. Che, M. Yang, X. Li, y Y. Zhang, «Molecular mechanisms in compatibility and mechanical properties of Polyacrylamide/Polyvinyl alcohol blends», *J. Mech. Behav. Biomed. Mater.*, vol. 65, pp. 565-573, ene. 2017, doi: 10.1016/j.jmbbm.2016.09.011.

[34] Q. Wei, Y. Wang, W. Chai, T. Wang, y Y. Zhang, «Effects of composition ratio on the properties of poly(vinyl alcohol)/poly(acrylic acid) blend membrane: A molecular dynamics simulation study», *Mater. Des.*, vol. 89, pp. 848-855, ene. 2016, doi: 10.1016/j.matdes.2015.10.048.

[35] M. Gao, Y. Chen, C. Fan, y M. Li, «Molecular Dynamics Study on the Compatibility of Asphalt and Rubber Powder with Different Component Contents», *ACS Omega*, vol. 7, n.º 41, pp. 36157-36164, oct. 2022, doi: 10.1021/acsomega.2c02813.

[36] F. M. Bellussi *et al.*, «Wettability of soft PLGA surfaces predicted by experimentally augmented atomistic models», *MRS Bull.*, vol. 48, n.º 2, pp. 108-117, feb. 2023, doi: 10.1557/s43577-022-00380-9.

[37] B. M. Rice y T. D. Sewell, «Equilibrium Molecular Dynamics Simulations», en *Static Compression of Energetic Materials*, S. M. Peiris y G. J. Piermarini, Eds., en Shock Wave and High Pressure Phenomena. , Berlin, Heidelberg: Springer, 2008, pp. 255-290. doi: 10.1007/978-3-540-68151-9_7.

[38] «Ergodic Hypothesis - an overview | ScienceDirect Topics». Accedido: 11 de enero de 2024. [En línea]. Disponible en: https://www-sciencedirect-com.cuarzo.unizar.es:9443/topics/engineering/ergodic-hypothesis

[39] P. V. Coveney y S. Wan, «On the calculation of equilibrium thermodynamic properties from molecular dynamics», *Phys. Chem. Chem. Phys.*, vol. 18, n.º 44, pp. 30236-30240, nov. 2016, doi: 10.1039/C6CP02349E.

[40] Q. Yang, W. Li, S. T. Stober, A. B. Burns, M. Gopinadhan, y A. Martini, «Molecular Dynamics Simulation of the Stress–Strain Behavior of Polyamide Crystals», *Macromolecules*, vol. 54, n.º 18, pp. 8289-8302, sep. 2021, doi: 10.1021/acs.macromol.1c00974.

[41] X. Wu, R. J. Moon, y A. Martini, «Tensile strength of Iβ crystalline cellulose predicted by molecular dynamics simulation», *Cellulose*, vol. 21, n.º 4, pp. 2233-2245, ago. 2014, doi: 10.1007/s10570-014-0325-0.

[42] J. Konrad, D. Zahn, y Lehrstuhl für Theoretische Chemie/Computer Chemie Centrum, Friedrich-Alexander Universität Erlangen-Nürnberg, Nägelsbachstraße 25, 91052 Erlangen, Germany, «Assessing the mechanical properties of molecular materials from atomic simulation», *AIMS Mater. Sci.*, vol. 8, n.º 6, pp. 867-880, 2021, doi: 10.3934/matersci.2021053.

[43] X. Wu, R. J. Moon, y A. Martini, «Crystalline cellulose elastic modulus predicted by atomistic models of uniform deformation and nanoscale indentation», *Cellulose*, vol. 20, n.º 1, pp. 43-55, feb. 2013, doi: 10.1007/s10570-012-9823-0.

[44] J. Li *et al.*, «Molecular dynamics simulation of mechanical properties of nanocrystalline platinum: Grain-size and temperature effects», *Phys. Lett. A*, vol. 383, n.º 16, pp. 1922-1928, jun. 2019, doi: 10.1016/j.physleta.2018.10.053.

[45] D. Huang, Q. Zhang, y P. Qiao, «Molecular dynamics evaluation of strain rate and size effects on mechanical properties of FCC nickel nanowires», *Comput. Mater. Sci.*, vol. 50, n.º 3, pp. 903-910, ene. 2011, doi: 10.1016/j.commatsci.2010.10.028.

[46] M. S. Green, «Markoff Random Processes and the Statistical Mechanics of Time-Dependent Phenomena. II. Irreversible Processes in Fluids», *J. Chem. Phys.*, vol. 22, pp. 398-413, mar. 1954, doi: 10.1063/1.1740082.

[47] R. Kubo, «Statistical-Mechanical Theory of Irreversible Processes. I», *J. Phys. Soc. Jpn.*, vol. 12, pp. 570-586, jun. 1957, doi: 10.1143/JPSJ.12.570.

[48] O. Adeyemi, S. Zhu, y L. Xi, «Equilibrium and non-equilibrium molecular dynamics approaches for the linear viscoelasticity of polymer melts», *Phys. Fluids*, vol. 34, n.º 5, p. 053107, may 2022, doi: 10.1063/5.0090540.

[49] S. Saber-Samandari y A. Afaghi Khatibi, «The effect of interphase on the elastic modulus of polymer based nanocomposites», *Key Eng. Mater.*, vol. 312, pp. 199-204, 2006.

[50] K. L. Reifsnider, «Modelling of the interphase in polymer-matrix composite material systems», *Composites*, vol. 25, n.º 7, pp. 461-469, ene. 1994, doi: 10.1016/0010-4361(94)90170-8.

[51] A. Kusmin *et al.*, «Polymer Dynamics in Nanochannels of Porous Silicon: A Neutron Spin Echo Study», *Macromolecules*, vol. 43, n.º 19, pp. 8162-8169, oct. 2010, doi: 10.1021/ma1004925.
[52] S. Y. Kim, H. W. Meyer, K. Saalwächter, y C. F. Zukoski, «Polymer Dynamics in PEG-Silica Nanocomposites: Effects of Polymer Molecular Weight, Temperature and Solvent Dilution», *Macromolecules*, vol. 45, n.º 10, pp. 4225-4237, may 2012, doi: 10.1021/ma300439k.
[53] S. Ok, M. Steinhart, A. Şerbescu, C. Franz, F. Vaca Chávez, y K. Saalwächter, «Confinement Effects on Chain Dynamics and Local Chain Order in Entangled Polymer Melts», *Macromolecules*, vol. 43, n.º 10, pp. 4429-4434, may 2010, doi: 10.1021/ma1003248.
[54] J. Segurado Escudero, «Micromecánica computacional de materiales compuestos reforzados con partículas», Universidad politécnica de Madrid, Madrid, 2004.
[55] H. L. Duan, J. Wang, Z. P. Huang, y B. L. Karihaloo, «Eshelby formalism for nano-inhomogeneities», *Proc. R. Soc. Math. Phys. Eng. Sci.*, vol. 461, n.º 2062, pp. 3335-3353, oct. 2005, doi: 10.1098/rspa.2005.1520.
[56] N. Sheng, M. C. Boyce, D. M. Parks, G. C. Rutledge, J. I. Abes, y R. E. Cohen, «Multiscale micromechanical modeling of polymer/clay nanocomposites and the effective clay particle», *Polymer*, vol. 45, n.º 2, pp. 487-506, ene. 2004, doi: 10.1016/j.polymer.2003.10.100.
[57] Y. Golitsyn, G. J. Schneider, y K. Saalwächter, «Reduced-mobility layers with high internal mobility in poly(ethylene oxide)–silica nanocomposites», *J. Chem. Phys.*, vol. 146, n.º 20, p. 203303, may 2017, doi: 10.1063/1.4974768.
[58] M. Krutyeva *et al.*, «Effect of Nanoconfinement on Polymer Dynamics: Surface Layers and Interphases», *Phys. Rev. Lett.*, vol. 110, n.º 10, p. 108303, mar. 2013, doi: 10.1103/PhysRevLett.110.108303.
[59] T. Glomann *et al.*, «Microscopic Dynamics of Polyethylene Glycol Chains Interacting with Silica Nanoparticles», *Phys. Rev. Lett.*, vol. 110, n.º 17, p. 178001, abr. 2013, doi: 10.1103/PhysRevLett.110.178001.
[60] P. Klonos, A. Kyritsis, y P. Pissis, «Interfacial and confined dynamics of PDMS adsorbed at the interfaces and in the pores of silica–gel: Effects of surface modification and thermal annealing», 2016, doi: 10.1016/J.POLYMER.2015.12.045.
[61] W. Xu, Q. H. Zeng, A. B. Yu, y D. R. Paul, «Determination of Interphase Thickness and Mechanical Properties of Effective Nanofillers in Polymer Nanocomposites by Molecular Dynamic Simulation», *Mater. Sci. Forum*, vol. 654-656, pp. 1654-1657, 2010, doi: 10.4028/www.scientific.net/MSF.654-656.1654.
[62] M. Cho, S. Yang, S. Chang, y S. Yu, «A study on the prediction of the mechanical properties of nanoparticulate composites using the homogenization method with the effective interface concept», *Int. J. Numer. Methods Eng.*, vol. 85, n.º 12, pp. 1564-1583, 2011, doi: 10.1002/nme.3039.
[63] H. Shin, S. Yang, J. Choi, S. Chang, y M. Cho, «Effect of interphase percolation on mechanical behavior of nanoparticle-reinforced polymer nanocomposite with filler agglomeration: A multiscale approach», *Chem. Phys. Lett.*, vol. 635, pp. 80-85, ago. 2015, doi: 10.1016/j.cplett.2015.06.054.
[64] G. M. Odegard, T. C. Clancy, y T. S. Gates, «Modeling of the mechanical properties of nanoparticle/polymer composites», *Polymer*, vol. 46, n.º 2, pp. 553-562, ene. 2005, doi: 10.1016/j.polymer.2004.11.022.
[65] M. Malagù, M. Goudarzi, A. Lyulin, E. Benvenuti, y A. Simone, «Diameter-dependent elastic properties of carbon nanotube-polymer composites: Emergence of size effects from atomistic-scale simulations», *Compos. Part B Eng.*, vol. 131, pp. 260-281, dic. 2017, doi: 10.1016/j.compositesb.2017.07.029.
[66] B. Arash, Q. Wang, y V. K. Varadan, «Mechanical properties of carbon nanotube/polymer composites», *Sci. Rep.*, vol. 4, oct. 2014, doi: 10.1038/srep06479.
[67] J. Gou, B. Minaie, B. Wang, Z. Liang, y C. Zhang, «Computational and experimental study of interfacial bonding of single-walled nanotube reinforced composites», *Comput. Mater. Sci.*, vol. 31, n.º 3–4, pp. 225-236, nov. 2004, doi: 10.1016/j.commatsci.2004.03.002.

[68] D. Liu, X. Chen, Y. Yue, M. Chen, y Q. Wu, «Structure and rheology of nanocrystalline cellulose», *Carbohydr. Polym.*, vol. 84, n.º 1, pp. 316-322, feb. 2011, doi: 10.1016/j.carbpol.2010.11.039.

[69] T. V. M. Ndoro, E. Voyiatzis, A. Ghanbari, D. N. Theodorou, M. C. Böhm, y F. Müller-Plathe, «Interface of Grafted and Ungrafted Silica Nanoparticles with a Polystyrene Matrix: Atomistic Molecular Dynamics Simulations», *Macromolecules*, vol. 44, n.º 7, pp. 2316-2327, abr. 2011, doi: 10.1021/ma102833u.

[70] A. Ghanbari, T. V. M. Ndoro, F. Leroy, M. Rahimi, M. C. Böhm, y F. Müller-Plathe, «Interphase Structure in Silica–Polystyrene Nanocomposites: A Coarse-Grained Molecular Dynamics Study», *Macromolecules*, vol. 45, n.º 1, pp. 572-584, ene. 2012, doi: 10.1021/ma202044e.

[71] J. S. Smith, O. Borodin, G. D. Smith, y E. M. Kober, «A molecular dynamics simulation and quantum chemistry study of poly(dimethylsiloxane)–silica nanoparticle interactions», *J. Polym. Sci. Part B Polym. Phys.*, vol. 45, n.º 13, pp. 1599-1615, jul. 2007, doi: 10.1002/polb.21119.

[72] H. Eslami, M. Rahimi, y F. Müller-Plathe, «Molecular Dynamics Simulation of a Silica Nanoparticle in Oligomeric Poly(methyl methacrylate): A Model System for Studying the Interphase Thickness in a Polymer–Nanocomposite via Different Properties», *Macromolecules*, vol. 46, n.º 21, pp. 8680-8692, nov. 2013, doi: 10.1021/ma401443v.

[73] J. C. Suárez, S. Miguel, P. Pinilla, y F. López, «Molecular Dynamics Simulation of Polymer–Metal Bonds», *J. Adhes. Sci. Technol.*, vol. 22, n.º 13, pp. 1387-1400, ene. 2008, doi: 10.1163/156856108X305732.

[74] T. Wang, D. Li, y G. Zhang, «Molecular Dynamics Simulations of Interface Properties and Key Physical Properties of Nanodielectrics Manufactured With Epoxy Resin Doped With Metal Nanoparticles», *IEEE Access*, vol. 9, pp. 34231-34239, 2021, doi: 10.1109/ACCESS.2021.3061824.

[75] J. Fankhänel, B. Arash, y R. Rolfes, «Elastic interphase properties of nanoparticle/epoxy nanocomposites: A molecular dynamics study», *Compos. Part B Eng.*, vol. 176, p. 107211, nov. 2019, doi: 10.1016/j.compositesb.2019.107211.

[76] C. E. Plazas Bonilla, S. Trujillo, B. Demirdögen, J. E. Perilla, Y. Murat Elcin, y J. L. Gómez Ribelles, «New porous polycaprolactone–silica composites for bone regeneration», *Mater. Sci. Eng. C*, vol. 40, pp. 418-426, jul. 2014, doi: 10.1016/j.msec.2014.04.024.

[77] A. Liberman, N. Mendez, W. C. Trogler, y A. C. Kummel, «Synthesis and surface functionalization of silica nanoparticles for nanomedicine», *Surf. Sci. Rep.*, vol. 69, n.º 2, pp. 132-158, sep. 2014, doi: 10.1016/j.surfrep.2014.07.001.

[78] D. Klemm, B. Heublein, H.-P. Fink, y A. Bohn, «Cellulose: Fascinating Biopolymer and Sustainable Raw Material», *Angew. Chem. Int. Ed.*, vol. 44, n.º 22, pp. 3358-3393, may 2005, doi: 10.1002/anie.200460587.

[79] S. Ummartyotin y H. Manuspiya, «A critical review on cellulose: From fundamental to an approach on sensor technology», *Renew. Sustain. Energy Rev.*, vol. 41, pp. 402-412, ene. 2015, doi: 10.1016/j.rser.2014.08.050.

[80] Y.-Q. Niu *et al.*, «Calcium carbonate: controlled synthesis, surface functionalization, and nanostructured materials», *Chem. Soc. Rev.*, vol. 51, n.º 18, pp. 7883-7943, sep. 2022, doi: 10.1039/D1CS00519G.

[81] F. C. Meldrum, «Calcium carbonate in biomineralisation and biomimetic chemistry», *Int. Mater. Rev.*, vol. 48, n.º 3, pp. 187-224, jun. 2003, doi: 10.1179/095066003225005836.

[82] C. Vilela, C. S. R. Freire, P. A. A. P. Marques, T. Trindade, C. Pascoal Neto, y P. Fardim, «Synthesis and characterization of new CaCO3/cellulose nanocomposites prepared by controlled hydrolysis of dimethylcarbonate», *Carbohydr. Polym.*, vol. 79, n.º 4, pp. 1150-1156, mar. 2010, doi: 10.1016/j.carbpol.2009.10.056.

[83] Y. Liu *et al.*, «A review of cellulose and its derivatives in biopolymer-based for food packaging application», *Trends Food Sci. Technol.*, vol. 112, pp. 532-546, jun. 2021, doi: 10.1016/j.tifs.2021.04.016.

[84] C. Jian *et al.*, «Multifunctional comb copolymer ethyl cellulose-g-poly(ε-caprolactone)-rhodamine B/folate: Synthesis, characterization and targeted bonding application», *Eur. Polym. J.*, vol. 55, pp. 235-244, jun. 2014, doi: 10.1016/j.eurpolymj.2014.04.003.

[85] S. Kalidhasan, A. Santhana KrishnaKumar, V. Rajesh, y N. Rajesh, «Ultrasound-assisted preparation and characterization of crystalline cellulose-ionic liquid blend polymeric material: a prelude to the study of its application toward the effective adsorption of chromium», *J. Colloid Interface Sci.*, vol. 367, n.º 1, pp. 398-408, feb. 2012, doi: 10.1016/j.jcis.2011.09.062.

[86] C. Gebald, J. A. Wurzbacher, A. Borgschulte, T. Zimmermann, y A. Steinfeld, «Single-Component and Binary CO2 and H2O Adsorption of Amine-Functionalized Cellulose», *Environ. Sci. Technol.*, vol. 48, n.º 4, pp. 2497-2504, feb. 2014, doi: 10.1021/es404430g.

[87] S. Sepahvand *et al.*, «A promising process to modify cellulose nanofibers for carbon dioxide (CO2) adsorption», *Carbohydr. Polym.*, vol. 230, p. 115571, feb. 2020, doi: 10.1016/j.carbpol.2019.115571.

[88] T. Hou *et al.*, «Cellulose membranes with polyethylenimine-modified graphene oxide and zinc ions for promoted gas separation», *Cellulose*, vol. 27, n.º 6, pp. 3277-3286, abr. 2020, doi: 10.1007/s10570-019-02962-4.

[89] R. J. B. Pinto, P. A. A. P. Marques, A. M. Barros-Timmons, T. Trindade, y C. P. Neto, «Novel SiO2/cellulose nanocomposites obtained by in situ synthesis and via polyelectrolytes assembly», *Compos. Sci. Technol.*, vol. 68, n.º 3-4, pp. 1088-1093, 2008.

[90] S. Sheykhnazari, T. Tabarsa, A. Ashori, y A. Ghanbari, «Bacterial cellulose composites loaded with SiO2 nanoparticles: Dynamic-mechanical and thermal properties», *Int. J. Biol. Macromol.*, vol. 93, pp. 672-677, dic. 2016, doi: 10.1016/j.ijbiomac.2016.09.035.

[91] U. M. Garusinghe, V. S. Raghuwanshi, W. Batchelor, y G. Garnier, «Water Resistant Cellulose – Titanium Dioxide Composites for Photocatalysis», *Sci. Rep.*, vol. 8, n.º 1, p. 2306, feb. 2018, doi: 10.1038/s41598-018-20569-w.

[92] H. Hamad, E. Bailón-García, S. Morales-Torres, A. F. Pérez-Cadenas, F. Carrasco-Marín, y F. J. Maldonado-Hódar, «16 - Cellulose–TiO2 composites for the removal of water pollutants», en *Bio-Based Materials and Biotechnologies for Eco-Efficient Construction*, F. Pacheco-Torgal, V. Ivanov, y D. C. W. Tsang, Eds., en Woodhead Publishing Series in Civil and Structural Engineering. , Woodhead Publishing, 2020, pp. 329-358. doi: 10.1016/B978-0-12-819481-2.00016-7.

[93] J. V. Rie y W. Thielemans, «Cellulose–gold nanoparticle hybrid materials», *Nanoscale*, vol. 9, n.º 25, pp. 8525-8554, jun. 2017, doi: 10.1039/C7NR00400A.

[94] T. Y. A. Fahmy y F. Mobarak, «Nanocomposites from natural cellulose fibers filled with kaolin in presence of sucrose», *Carbohydr. Polym.*, vol. 72, n.º 4, pp. 751-755, jun. 2008, doi: 10.1016/j.carbpol.2008.01.008.

[95] K. Torvinen *et al.*, «Nanoporous kaolin—cellulose nanofibril composites for printed electronics», *Flex. Print. Electron.*, vol. 2, n.º 2, p. 024004, may 2017, doi: 10.1088/2058-8585/aa6d97.

[96] L. Alves, E. Ferraz, y J. A. F. Gamelas, «Composites of nanofibrillated cellulose with clay minerals: A review», *Adv. Colloid Interface Sci.*, vol. 272, p. 101994, oct. 2019, doi: 10.1016/j.cis.2019.101994.

[97] V. Hynninen *et al.*, «Luminescent Gold Nanocluster-Methylcellulose Composite Optical Fibers with Low Attenuation Coefficient and High Photostability», *Small*, vol. 17, n.º 27, p. 2005205, 2021, doi: 10.1002/smll.202005205.

[98] J. Phiri, L.-S. Johansson, P. Gane, y T. Maloney, «A comparative study of mechanical, thermal and electrical properties of graphene-, graphene oxide- and reduced graphene oxide-doped microfibrillated cellulose nanocomposites», *Compos. Part B Eng.*, vol. 147, pp. 104-113, ago. 2018, doi: 10.1016/j.compositesb.2018.04.018.

[99] J. Liuyun, L. Yubao, y X. Chengdong, «Preparation and biological properties of a novel composite scaffold of nano-hydroxyapatite/chitosan/carboxymethyl cellulose for bone tissue engineering», *J. Biomed. Sci.*, vol. 16, n.º 1, p. 65, jul. 2009, doi: 10.1186/1423-0127-16-65.

[100] N. Jia, S.-M. Li, M.-G. Ma, R.-C. Sun, y J.-F. Zhu, «Hydrothermal fabrication, characterization, and biological activity of cellulose/CaCO3 bionanocomposites», *Carbohydr. Polym.*, vol. 88, n.º 1, pp. 179-184, mar. 2012, doi: 10.1016/j.carbpol.2011.11.086.

[101] M.-G. Ma, Y.-Y. Dong, L.-H. Fu, S.-M. Li, y R.-C. Sun, «Cellulose/CaCO3 nanocomposites: microwave ionic liquid synthesis, characterization, and biological activity», *Carbohydr. Polym.*, vol. 92, n.º 2, pp. 1669-1676, feb. 2013, doi: 10.1016/j.carbpol.2012.11.034.

[102] M. G. Ma, S. Liu, y L. H. Fu, «Calcium Carbonate and Cellulose/Calcium Carbonate Composites: Synthesis, Characterization, and Biomedical Applications», *Mater. Sci. Forum*, vol. 875, pp. 24-44, oct. 2016, doi: 10.4028/www.scientific.net/MSF.875.24.

[103] H.-X. Zhao *et al.*, «Treatment of heavy metal ions-polluted water into drinkable water: Capture and recovery of Pb2+ by cellulose@CaCO3 bio-composite filter via spatial confinement effect», *Chem. Eng. J.*, vol. 454, p. 140297, feb. 2023, doi: 10.1016/j.cej.2022.140297.

[104] A. Salama, R. Abouzeid, B. Prelot, M. Diab, M. Assaf, y P. Hesemann, «Preparation and Adsorption Performance of Cellulose Nanofibers/Silica/Calcium Carbonate Composites for Water Purification», *Chem. Afr.*, vol. 6, n.º 5, pp. 2357-2367, oct. 2023, doi: 10.1007/s42250-023-00741-0.

[105] R.-J. Shi, J.-Q. Lang, T. Wang, N. Zhou, y M.-G. Ma, «Fabrication, Properties, and Biomedical Applications of Calcium-Containing Cellulose-Based Composites», *Front. Bioeng. Biotechnol.*, vol. 10, p. 937266, jun. 2022, doi: 10.3389/fbioe.2022.937266.

[106] T. C. Maloney, J. Ataide, J. Kekkonen, H. Fordsmand, y H. Hoeg-Petersen, «Changes to PCC structure in papermaking», presentado en Proceeding of XIX National Technicelpa Conference, Lisbon, 2005, p. 7.

[107] X. Chen, X. Qian, y X. An, «Using calcium carbonate whiskers as papermaking filler», *BioResources*, vol. 6, n.º 3, p. 13, 2011.

[108] K. Mohamadzadeh-Saghavaz, H. Resalati, y A. Ghasemian, «Cellulose-precipitated calcium carbonate composites and their effect on paper properties», *Chem. Pap.*, vol. 68, n.º 6, ene. 2014, doi: 10.2478/s11696-013-0513-7.

[109] K. S. Novoselov *et al.*, «Electric Field Effect in Atomically Thin Carbon Films», *Science*, vol. 306, n.º 5696, pp. 666-669, oct. 2004, doi: 10.1126/science.1102896.

[110] X. J. Lee *et al.*, «Review on graphene and its derivatives: Synthesis methods and potential industrial implementation», *J. Taiwan Inst. Chem. Eng.*, vol. 98, pp. 163-180, may 2019, doi: 10.1016/j.jtice.2018.10.028.

[111] A. R. Urade, I. Lahiri, y K. S. Suresh, «Graphene Properties, Synthesis and Applications: A Review», *JOM*, vol. 75, n.º 3, pp. 614-630, mar. 2023, doi: 10.1007/s11837-022-05505-8.

[112] C. Lee, X. Wei, J. W. Kysar, y J. Hone, «Measurement of the Elastic Properties and Intrinsic Strength of Monolayer Graphene», *Science*, vol. 321, n.º 5887, pp. 385-388, jul. 2008, doi: 10.1126/science.1157996.

[113] D. G. Papageorgiou, I. A. Kinloch, y R. J. Young, «Mechanical properties of graphene and graphene-based nanocomposites», *Prog. Mater. Sci.*, vol. 90, pp. 75-127, oct. 2017, doi: 10.1016/j.pmatsci.2017.07.004.

[114] J.-H. Lee, S.-J. Park, y J.-W. Choi, «Electrical Property of Graphene and Its Application to Electrochemical Biosensing», *Nanomaterials*, vol. 9, n.º 2, p. 297, feb. 2019, doi: 10.3390/nano9020297.

[115] M. D. Stoller, S. Park, Y. Zhu, J. An, y R. S. Ruoff, «Graphene-Based Ultracapacitors», *Nano Lett.*, vol. 8, n.º 10, pp. 3498-3502, oct. 2008, doi: 10.1021/nl802558y.

[116] M. Sang, J. Shin, K. Kim, y K. J. Yu, «Electronic and Thermal Properties of Graphene and Recent Advances in Graphene Based Electronics Applications», *Nanomaterials*, vol. 9, n.º 3, p. 374, mar. 2019, doi: 10.3390/nano9030374.

[117] S. Goenka, V. Sant, y S. Sant, «Graphene-based nanomaterials for drug delivery and tissue engineering», *J. Controlled Release*, vol. 173, pp. 75-88, ene. 2014, doi: 10.1016/j.jconrel.2013.10.017.

[118] J. Perruisseau-Carrier, «Graphene for antenna applications: Opportunities and challenges from microwaves to THz», en *2012 Loughborough Antennas & Propagation Conference (LAPC)*, nov. 2012, pp. 1-4. doi: 10.1109/LAPC.2012.6402934.

[119] M. Kang, J. Kim, B. Jang, Y. Chae, J.-H. Kim, y J.-H. Ahn, «Graphene-Based Three-Dimensional Capacitive Touch Sensor for Wearable Electronics», *ACS Nano*, vol. 11, n.º 8, pp. 7950-7957, ago. 2017, doi: 10.1021/acsnano.7b02474.

[120] A. Kausar, I. Rafique, y B. Muhammad, «Aerospace Application of Polymer Nanocomposite with Carbon Nanotube, Graphite, Graphene Oxide, and Nanoclay», *Polym.-Plast. Technol. Eng.*, vol. 56, n.º 13, pp. 1438-1456, sep. 2017, doi: 10.1080/03602559.2016.1276594.

[121] W. Yu, L. Sisi, Y. Haiyan, y L. Jie, «Progress in the functional modification of graphene/graphene oxide: a review», *RSC Adv.*, vol. 10, n.º 26, pp. 15328-15345, abr. 2020, doi: 10.1039/D0RA01068E.

[122] B. Gadgil, P. Damlin, y C. Kvarnström, «Graphene vs. reduced graphene oxide: A comparative study of graphene-based nanoplatforms on electrochromic switching kinetics», *Carbon*, vol. 96, pp. 377-381, ene. 2016, doi: 10.1016/j.carbon.2015.09.065.

[123] Y. Yoon, H. Kye, W. S. Yang, y J.-W. Kang, «Comparing Graphene Oxide and Reduced Graphene Oxide as Blending Materials for Polysulfone and Polyvinylidene Difluoride Membranes», *Appl. Sci.*, vol. 10, n.º 6, Art. n.º 6, ene. 2020, doi: 10.3390/app10062015.

[124] G. Wang, B. Wang, J. Park, J. Yang, X. Shen, y J. Yao, «Synthesis of enhanced hydrophilic and hydrophobic graphene oxide nanosheets by a solvothermal method», *Carbon*, vol. 47, n.º 1, pp. 68-72, ene. 2009, doi: 10.1016/j.carbon.2008.09.002.

[125] W. Chang *et al.*, «Few-layer graphene on nickel enabled sustainable dropwise condensation», *Sci. Bull.*, vol. 66, n.º 18, pp. 1877-1884, sep. 2021, doi: 10.1016/j.scib.2021.06.006.

[126] R. Raj, S. C. Maroo, y E. N. Wang, «Wettability of Graphene», *Nano Lett.*, vol. 13, n.º 4, pp. 1509-1515, abr. 2013, doi: 10.1021/nl304647t.

[127] M. Munz, C. E. Giusca, R. L. Myers-Ward, D. K. Gaskill, y O. Kazakova, «Thickness-Dependent Hydrophobicity of Epitaxial Graphene», *ACS Nano*, vol. 9, n.º 8, pp. 8401-8411, ago. 2015, doi: 10.1021/acsnano.5b03220.

[128] A. T. Lawal, «Graphene-based nano composites and their applications. A review», *Biosens. Bioelectron.*, vol. 141, p. 111384, sep. 2019, doi: 10.1016/j.bios.2019.111384.

[129] L. Yang *et al.*, «Polydopamine-coated graphene as multifunctional nanofillers in polyurethane», *RSC Adv.*, vol. 3, n.º 18, pp. 6377-6385, abr. 2013, doi: 10.1039/C3RA23307C.

[130] E. Pop, V. Varshney, y A. K. Roy, «Thermal properties of graphene: Fundamentals and applications», *MRS Bull.*, vol. 37, n.º 12, pp. 1273-1281, dic. 2012, doi: 10.1557/mrs.2012.203.

[131] W. Cai *et al.*, «Thermal Transport in Suspended and Supported Monolayer Graphene Grown by Chemical Vapor Deposition», *Nano Lett.*, vol. 10, n.º 5, pp. 1645-1651, may 2010, doi: 10.1021/nl9041966.

[132] E. Muñoz, J. Lu, y B. I. Yakobson, «Ballistic Thermal Conductance of Graphene Ribbons», *Nano Lett.*, vol. 10, n.º 5, pp. 1652-1656, may 2010, doi: 10.1021/nl904206d.

[133] X. Huang *et al.*, «Thermal conductivity of graphene-based polymer nanocomposites», *Mater. Sci. Eng. R Rep.*, vol. 142, p. 100577, oct. 2020, doi: 10.1016/j.mser.2020.100577.

[134] I. Y. Forero-Sandoval *et al.*, «Electrical and thermal percolation in two-phase materials: A perspective», *J. Appl. Phys.*, vol. 131, n.º 23, p. 230901, jun. 2022, doi: 10.1063/5.0091291.

[135] A. J. Marsden *et al.*, «Electrical percolation in graphene–polymer composites», *2D Mater.*, vol. 5, n.º 3, p. 032003, jun. 2018, doi: 10.1088/2053-1583/aac055.

[136] N. Jović, D. Dudić, A. Montone, M. V. Antisari, M. Mitrić, y V. Djoković, «Temperature dependence of the electrical conductivity of epoxy/expanded graphite nanosheet composites», *Scr. Mater.*, vol. 58, n.º 10, pp. 846-849, may 2008, doi: 10.1016/j.scriptamat.2007.12.041.

[137] I. Balberg, D. Azulay, D. Toker, y O. Millo, «Percolation and tunneling in composite materials», *Int. J. Mod. Phys. B*, vol. 18, n.º 15, pp. 2091-2121, jun. 2004, doi: 10.1142/S0217979204025336.

[138] G. Ambrosetti, C. Grimaldi, I. Balberg, T. Maeder, A. Danani, y P. Ryser, «Solution of the tunneling-percolation problem in the nanocomposite regime», *Phys. Rev. B*, vol. 81, n.º 15, p. 155434, abr. 2010, doi: 10.1103/PhysRevB.81.155434.

[139] F. Kargar *et al.*, «Thermal Percolation Threshold and Thermal Properties of Composites with High Loading of Graphene and Boron Nitride Fillers», *ACS Appl. Mater. Interfaces*, vol. 10, n.º 43, pp. 37555-37565, oct. 2018, doi: 10.1021/acsami.8b16616.

[140] L. Joly-Pottuz *et al.*, «Mechanical Properties of Nanoparticles: Characterization by In situ Nanoindentation Inside a Transmission Electron Microscope», en *Handbook of Mechanical Nanostructuring*, M. Aliofkhazraei, Ed., Wiley, 2015, pp. 163-180. doi: 10.1002/9783527674947.ch8.

[141] A. Al Sheikh Omar, F. M. Salehi, M. Bai, B. J. Inkson, y A. Morina, «In situ nanocompression of carbon black to understand the tribology of contaminated diesel engine oils», *Carbon*, vol. 212, p. 118170, ago. 2023, doi: 10.1016/j.carbon.2023.118170.

[142] J. Amodeo y L. Pizzagalli, «Modeling the mechanical properties of nanoparticles: a review», *Comptes Rendus Phys.*, vol. 22, n.º S3, pp. 1-32, may 2021, doi: 10.5802/crphys.70.

[143] L. Patra y R. Pandey, «Mechanical properties of 2D materials: A review on molecular dynamics based nanoindentation simulations», *Mater. Today Commun.*, vol. 31, p. 103623, jun. 2022, doi: 10.1016/j.mtcomm.2022.103623.

[144] W. S. Jr. Hummers y R. E. Offeman, «Preparation of Graphitic Oxide», *J. Am. Chem. Soc.*, vol. 80, n.º 6, pp. 1339-1339, mar. 1958, doi: 10.1021/ja01539a017.

[145] D. C. Marcano *et al.*, «Improved Synthesis of Graphene Oxide», *ACS Nano*, vol. 4, n.º 8, pp. 4806-4814, ago. 2010, doi: 10.1021/nn1006368.

[146] H. He, T. Riedl, A. Lerf, y J. Klinowski, «Solid-State NMR Studies of the Structure of Graphite Oxide», *J. Phys. Chem.*, vol. 100, n.º 51, pp. 19954-19958, ene. 1996, doi: 10.1021/jp961563t.

[147] A. Lerf, H. He, M. Forster, y J. Klinowski, «Structure of Graphite Oxide Revisited», *J. Phys. Chem. B*, vol. 102, n.º 23, pp. 4477-4482, jun. 1998, doi: 10.1021/jp9731821.

[148] L.-C. Lin y J. C. Grossman, «Atomistic understandings of reduced graphene oxide as an ultrathin-film nanoporous membrane for separations», *Nat. Commun.*, vol. 6, p. 8335, sep. 2015, doi: 10.1038/ncomms9335.

[149] Y. M. Volfkovich *et al.*, «Hydrophilic and hydrophobic pores in reduced graphene oxide aerogel», *J. Porous Mater.*, vol. 26, n.º 4, pp. 1111-1119, ago. 2019, doi: 10.1007/s10934-018-0712-2.

[150] M. Li, H. Zhou, Y. Zhang, Y. Liao, y H. Zhou, «The effect of defects on the interfacial mechanical properties of graphene/epoxy composites», *RSC Adv.*, vol. 7, n.º 73, pp. 46101-46108, sep. 2017, doi: 10.1039/C7RA08243F.

[151] X. Huang *et al.*, «Functional nanoporous graphene foams with controlled pore sizes», *Adv. Mater. Deerfield Beach Fla*, vol. 24, n.º 32, pp. 4419-4423, ago. 2012, doi: 10.1002/adma.201201680.

[152] C. Tang *et al.*, «CaO-Templated Growth of Hierarchical Porous Graphene for High-Power Lithium–Sulfur Battery Applications», *Adv. Funct. Mater.*, vol. 26, n.º 4, pp. 577-585, 2016, doi: 10.1002/adfm.201503726.

[153] Y. Zhu *et al.*, «Carbon-based supercapacitors produced by activation of graphene», *Science*, vol. 332, n.º 6037, pp. 1537-1541, jun. 2011, doi: 10.1126/science.1200770.

[154] D. W. Kim, J. Choi, D. Kim, y H.-T. Jung, «Enhanced water permeation based on nanoporous multilayer graphene membranes: the role of pore size and density», *J. Mater. Chem. A*, vol. 4, n.º 45, pp. 17773-17781, nov. 2016, doi: 10.1039/C6TA06381K.

[155] X. Mu, X. Wu, T. Zhang, D. B. Go, y T. Luo, «Thermal Transport in Graphene Oxide – From Ballistic Extreme to Amorphous Limit», *Sci. Rep.*, vol. 4, n.º 1, Art. n.º 1, ene. 2014, doi: 10.1038/srep03909.

[156] D. A. Dikin *et al.*, «Preparation and characterization of graphene oxide paper», *Nature*, vol. 448, n.º 7152, Art. n.º 7152, jul. 2007, doi: 10.1038/nature06016.

[157] C. Tian, W. Miao, L. Zhao, y J. Wang, «Graphene nanoribbons: Current status and challenges as quasi-one-dimensional nanomaterials», *Rev. Phys.*, vol. 10, p. 100082, jun. 2023, doi: 10.1016/j.revip.2023.100082.

[158] K. Bang *et al.*, «Effect of ribbon width on electrical transport properties of graphene nanoribbons», *Nano Converg.*, vol. 5, n.º 1, p. 7, mar. 2018, doi: 10.1186/s40580-018-0139-0.

[159] Y.-W. Son, M. L. Cohen, y S. G. Louie, «Energy Gaps in Graphene Nanoribbons», *Phys. Rev. Lett.*, vol. 97, n.º 21, p. 216803, nov. 2006, doi: 10.1103/PhysRevLett.97.216803.

[160] O. Gröning *et al.*, «Engineering of robust topological quantum phases in graphene nanoribbons», *Nature*, vol. 560, n.º 7717, Art. n.º 7717, ago. 2018, doi: 10.1038/s41586-018-0375-9.

[161] G. Soavi *et al.*, «Exciton–exciton annihilation and biexciton stimulated emission in graphene nanoribbons», *Nat. Commun.*, vol. 7, n.º 1, Art. n.º 1, mar. 2016, doi: 10.1038/ncomms11010.

[162] C. Sáenz Ezquerro, M. Laspalas, A. Chiminelli, F. Serrano, y C. Valero, «Interface Characterization of Epoxy Resin Nanocomposites: A Molecular Dynamics Approach», *Fibers*, vol. 6, n.º 3, p. 54, sep. 2018, doi: 10.3390/fib6030054.

[163] M. Jimenez, «The November 2023 cover paper», *J. Mater. Sci.*, vol. 58, n.º 41, pp. 15933-15935, nov. 2023, doi: 10.1007/s10853-023-09015-z.

[164] «The Robert W. Cahn Prize for Best Research Paper | Journal of Materials Science». [En línea]. Disponible en: https://link.springer.com/journal/10853/updates/17557656

[165] A. C. T. van Duin, S. Dasgupta, F. Lorant, y W. A. Goddard, «ReaxFF: A Reactive Force Field for Hydrocarbons», *J. Phys. Chem. A*, vol. 105, n.º 41, pp. 9396-9409, oct. 2001, doi: 10.1021/jp004368u.

# Anexo A

## Área temática y factor de impacto de las revistas

A continuación, se indican el área temática y el factor de impacto de las revistas en las que se realizaron las diferentes publicaciones, en el año en el que fueron publicadas (datos extraídos de *Journal Citation Reports*, JCR):

| PUBLICACIÓN | REVISTA | AÑO PUBLICACIÓN | ÁREA TEMÁTICA | CUARTIL | FACTOR IMPACTO |
|---|---|---|---|---|---|
| Prediction of the structure and mechanical properties of polycaprolactone-silica nanocomposites and the interphase region by molecular dynamics simulations: the effect of PEGylation | Soft Matter | 2022 | Materials science, Multidisciplinary | Q3 | 3,4 |
| Monitoring interactions through molecular dynamics simulations: effect of calcium carbonate on the mechanical properties of cellulose composites | Cellulose | 2022 | Materials science, Paper & Wood | Q1 | 5,7 |
| Effects of Graphene Oxidation on Interaction Energy and Interfacial Thermal Conductivity of Polymer Nanocomposite: A Molecular Dynamics Approach | Fibers | 2021 | Materials science, Multidisciplinary | Q3 | 3,9 |
| Molecular modelling of graphene nanoribbons on the effect of porosity and oxidation on the mechanical and thermal properties | Journal of Materials Science | 2023 | Materials science, Multidisciplinary | Q2 | 4,5 |

# Anexo B

## Justificación de contribución del doctorando

El autor de la tesis ha sido el principal contribuyente de las publicaciones que componen esta tesis, realizando tanto la preparación de los modelos moleculares (*modelling*), de los códigos de cálculo (*scripts*) con procedimientos para su caracterización e interpretación de resultados, así como la redacción de las publicaciones, en la cual se incluye la revisión bibliográfica correspondiente.

En el caso de la publicación "Effects of graphene oxidation on Interaction Energy and Interfacial Thermal Conductivity of Polymer Nanocomposite: A Molecular Dynamics Approach", el autor de la tesis realizó el modelado de los sistemas nanocompuestos basados en resina epoxi y poli(ácido láctico), y de nanopartículas de grafeno (G, GO y rGO), incluyendo su caracterización. Del mismo modo, contribuyó en la redacción del artículo, edición de gráficas de resultados (empleando *OriginLab*), así como fue el principal contribuyente en la interpretación y análisis de resultados de los espectros de fonones (espectros DOS, *density of states*).

Todos los coautores de las publicaciones que componen la tesis son doctores ya titulados.